

Understanding the structure and emission processes in AGN using blazar variability

A thesis submitted in partial fulfillment of
the requirements for the degree of

Doctor of Philosophy

by

Navpreet Kaur

(Roll No. 13330001)

Under the guidance of

Prof. Kiran S. Baliyan

Astronomy & Astrophysics Division

Physical Research Laboratory, Ahmedabad, India.



DEPARTMENT OF PHYSICS

INDIAN INSTITUTE OF TECHNOLOGY GANDHINAGAR

2017

*To my grandfather Late S. Tara Singh,
and
my parents*

Declaration

I, Navpreet Kaur, declare that this written submission represents my ideas in my own words and where others' ideas or words have been included, I have adequately cited and referenced the original sources. I also declare that I have adhered to all principles of academic honesty and integrity and have not misrepresented or fabricated or falsified any idea/data/fact/source in my submission. I understand that any violation of the above will be cause for disciplinary action by the Institute and can also evoke penal action from the sources which have thus not been properly cited or from whom proper permission has not been taken when needed.

(Navpreet Kaur)

Roll No: 13330001

Date:

Certificate

It is certified that the work contained in the thesis entitled, “**Understanding the Structure and Emission Processes in AGN using Blazar Variability**”, by **Ms. Navpreet Kaur** (Roll No. 13330001), has been carried out under my supervision and that this work has not been submitted elsewhere for any degree or diploma.

(Kiran Singh Baliyan)

Thesis Supervisor

Professor,

Astronomy & Astrophysics Division,

Physical Research Laboratory,

Unit of Department of Space, Government of India,

Ahmedabad- 380009, Gujarat, India.

Date:

Acknowledgement

The journey of these four years remained memorable and cherishable with many ups and downs and maintaining peace with my mind remained really a challenging task, to achieve the desired targets. This would have not been possible without the support of the lovely people around. Words fall short to express my deepest appreciation for their ever lasting support, encouragement, motivation and most importantly, for believing in me.

I owe all of the research work to my grandfather, Late S. Tara Singh, who remained my life coach and always encouraged me to choose the research field. My sincere thanks and love to my parents Mr. Kulwinder Singh and Mrs. Lakhbir Kaur, my brothers, Sehajpreet & his wife Mrs. Manjusha, and Deepkaran (aka Deepu), for being the strongest pillars of my life. Their constant support and encouragement led me to carry out my research without much anxiety and stress.

Words are not enough to express my sincere gratitude to my supervisor, Prof. Kiran Singh Baliyan, for his continuous support, immense patience, and motivation during my Ph.D. research programme. I would like to acknowledge all his efforts for making me familiar with the field of research to the large extent, from the basics as well as an independent thinking to scientific writing. His constant encouragement, timely and far-sighted guidance, broad scientific experience, friendly nature, and enthusiasm for the work kept me going all these years of my research endeavor. His approach to think critically upon any matter is remarkable and I learned a lot from him during many scientific and non-scientific discussions. It is a great privilege for me to get a companionship with him. Being personally connected with Baliyan family, I would like to thank my supervisor, Ma'm (Mrs. Dharam Baliyan) and Ritu for inviting me for several parties, and making me feel more comfortable with such a lively and homely environment. I consider myself fortunate to have him as a supervisor, a guardian, a friend and thank him for everything.

I am also thankful to our present Director, Dr. Anil Bhardwaj, for providing all the facilities necessary to pursue my research work. I am also thankful to our former directors, Drs. Tapan Mishra, Utpal Sarkar, and J.N. Goswami. I wish to express my sincere thanks to our Dean, Prof. P. Janardhan; academic chairman, Prof. S. Ramachandran, and academic Committee members for their help and support. I am thankful to our present area chairman, Dr. A. Chakraborty and the former area chairman, Prof. Kiran S Baliyan, for the help, encouragement and financial support in attending several conferences and national/international meetings and other facilities.

Besides my supervisor, I wish to sincerely thank my Doctoral Studies Committee (DSC) member-cum-mentor, Dr. Shashikiran Ganesh, for his insightful inputs and critical comments at every stage of my doctoral programme. His kind guidance really helped me in learning to take the observations and data analysis. I am grateful to him for listening all my doubts and patiently answering them. I thank him for several discussions and giving the critical checking to my thesis. I feel glad to work with him as a mentor and a good friend. I like the traditional food made by Abhi Ma'm and her lively smile and talks, and feel delighted receiving the blessings and encouraging words from Shashi ji's mother and the sweet talks with Gayatri. I am grateful to my another DSC member, Dr. Som Kumar Sharma, for his timely inputs and critical suggestions during my research progress, seminars which were very fruitful in shaping my research work.

I take this opportunity to thank Dr. Sunil Chandra, my collaborator and a nice senior, for the help in understanding the subject in more depth. I really enjoyed the scientific discussions with him at several occasions, conferences, meetings etc. His dedication towards his work is tremendous, which gave the encouragement to juniors, like me, to work harder and in more efficient way. I wish him many more academic successes in his post doctoral career and the future ahead. I am thankful to Mr. Sameer for all the help, encouragement, and the good times we had during his stay in PRL. We really enjoyed working together on blazars, a wonderful field of research!

I am grateful to Dr. Massimo Cappi at INAF-Bologna, Italy for hosting me to learn the high energy data analysis techniques under AHEAD program. I had a great time in learning X-ray and γ -ray data reduction and analysis from Drs. Paola Grandi, Eleonora Terrosi, Andrea Bulgarelli and Carlotta Pittori. My stay at INAF-Bologna was really comfortable and I enjoyed participating in various scientific group discussions there. I would also like to thank Dr. Frank Rieger and Dr. Nachiketa Chakraborty for the scientific discussions during my first visit abroad to MPIK, Hiedelberg (Germany) in the early stage (2015) of my research endeavor.

I have spent a significant time in carrying out optical observations, for my research work, from Mount Abu InfraRed Observatory (MIRO), Rajasthan. I am thankful to Mr. Kothari ji, and all the supporting staff at the Mount Abu guest house (Hill View) for their amazing hospitality. I would like to thank Mr. J.K. Jain, Mr. Nafees, and Mr. G.S. Rajpurohit for teaching, helping and accompanying me during the observations with different instruments. I express my sincere regards to Mr. S.N. Mathur, Mr Patwal and Mr. R.R. Shah for their efforts in maintaining the telescope and instruments to enable continuous uninterrupted

observations. I would also like to express my sincere thanks to Mr. Prakash, Mr. Akshay Desai, Mr. Prashant, Mr. Jatin, Mr. Mukesh, telescope operator trainees, for helping me during observations over the years.

I am thankful for the support from members of the Astronomy & Astrophysics Division, including Prof. U.C. Joshi, Dr. A.K. Singal, Prof. N.M. Ashok, Dr. Sachinder Naik, Dr. Santosh Vadawale, Dr. Aveek Sarkar, Dr. Arvind Rajpurohit, Dr. Mudit Srivastava, Dr. Veeresh Singh, Dr. V. Venkatraman and Dr. Vishal Joshi. I would like to thank Mr. A.B. Shah, Miss Deekshya and Mr. Prashant for their nice company.

I feel lucky to meet such a wonderful bunch of people at PRL in my life, my batch-2013. My life at PRL would have never been so joyful and happening without their presence. Each one is unique in their own way and makes the environment colorful with so much of laughter, humor. I really enjoyed being in their company and the never ending tea and coffee parties. I feel delighted to acknowledge all of them: Santosh, Rupa, Rukmnai, Satish, Jabir, Kumar, Prahlad, Kuldeep, Chandan, Ali, Hemant, Yasir, Sonam, Ashish. I am grateful to Shweta for bearing my non-sense talks and being my consulter in past two years. I feel lucky to have Santosh as my soul sister who remained my strength all these years. I express my sincere thanks to Mr. Dharmpreet Singh for all the fruitful discussions and motivating me in the academics.

The journey would have never been so comfortable and enjoyable with all the seniors, colleagues, and friends. The PRL Thaltej Hostel is like a second home to me and I cherish each and every moment spent here. My seniors in the hostel have always supported, guided and helped me in need. I am thankful to Priyanka, Bhavya, Anjali, Ikshu, Shraddha, Deepak, Dipti, Bivin, Tanmoy Chattopadhyay, Arko, Tanomy Mondal, Monojit, Amrendra for all sort of discussions. It feels great to have a company of the juniors and share happy moments with them either at workplace or in hostel. I would like to thank Archita, Akanksha, Aarthy, Shefali, Richa, Nidhi, Shivangi, Subir, Kaustav, Varun, Deepika, Varun, Abdur, Priyank, Harish, Shivani, Aayan, Sandeep, Nisha, and Deepika, and wish them good luck for their bright future.

Apart from the academics, I am thankful to my entire Ubhi family: Taaya ji, Taayi ji, my cousin brothers and bhaabi- Rajbir Singh & Harpreet bhaabi, Preeturinder Singh & Preeti bhaabi, and Vikram Singh for their support and love. My niece, Navleen Kaur, and my nephews, Yuvraj, Harkaran, Abhay, and Manraj, are the best and charming part of my life. I express my love and affection to the kids and wish them good luck for their future ahead.

Abstract

Active galactic nuclei (AGN) are centers of galaxies majority of which are 10^2 to 10^5 times more luminous than a normal galaxy and show signs of non-thermal activity. Since AGN are very compact and at relatively large redshift, they are non-resolvable by any existing facility. Therefore, understanding their structure and processes responsible for such high energy output is a big challenge. These are now broadly known to be powered by a supermassive black hole (SMBH) accreting matter through a disk surrounding it. An important diagnostic to investigate AGN phenomenon is temporal variability in blazars- a subclass of AGN. The emission in blazars is dominated by non-thermal radiation which is extremely variable at time scales ranging from a few tens of minutes to several tens of years across the whole electromagnetic spectrum (EMS). Rapid flux variability is capable of resolving features close to the central engine. In the present work, we have used variability of blazars to improve our understanding of the AGN in general and blazars in particular. The thesis is organized as follows.

We introduce the AGN phenomena, blazar properties and observational facilities which are used to obtain data at several energy regimes. The data reduction and analysis methods along with statistical techniques used to facilitate extraction of science from the data are also described. To address the microvariability (intra-night variations; INV) and long term variations in optical domain, we have carried out optical observations from the Mt Abu InfraRed Observatory (MIRO), complementing these with data from Steward Observatory, where available. Instances of INV and their time scales are determined for IBL 3C66A and S5 0716+71, duly verified using statistical techniques. The duty cycle of variation (DCV), sizes of the emission regions and possible mechanisms of emissions are discussed. The long-term behaviour of the source brightness, major outbursts and spectral properties of the two sources have been addressed using the entire dataset. The shock-in-jet model appears to be explaining the long term behaviour. We also studied the extent of variability as a function of source brightness and found opposite trends in the two IBLs. Though blazars are valuable sources of information, they become wonderful probes when in outburst. During these outbursts,

source is normally detected across the EMS, providing opportunity to study the correlated variations among different energy bands. Two sources which exhibited unprecedented outbursts during last three years or so, 1ES 1959+650 (HBL) and CTA 102 (FSRQ), were studied using the multiwavelength data from optical observatories, Swift-XRT/UVOT (X-ray/UV/optical), Fermi-LAT(γ -rays) and 15GHz radio data from OVRO. The data were analyzed using standard techniques and multiwavelength light curves were generated. Both sources were at their historically brightest levels with several major outbursts and a number of rapid flares with significant amplitudes. It was possible to put constraints on the sizes of emission regions, distance of the high energy emitting region from the black hole and infer processes responsible for flares. For CTA 102, we used 3-hour binned data to estimate the flux doubling time scale. The spectral energy distributions were constructed to study their spectral behaviour during pre-, post- and flaring periods. We infer that the jet has multiple emission regions in almost all the energy regimes, DCV depends on the duration of monitoring, variations at shorter time scales are stochastic in nature and long term outbursts are probably caused by shock moving down the jet, interacting with plasma over-densities (shocks/knots) or the changes in the viewing angle. The variability amplitudes appear to increase with frequency. The INV and LTV are possibly connected but such inference needs to be strengthened by an extensive study with densely sampled data.

Contents

Acknowledgement	i
Abstract	vii
Contents	ix
List of Figures	xv
List of Tables	xxiii
1 Introduction	1
1.1 Fascinating Quasars Ever Since	1
1.2 Active Galactic Nuclei	3
1.2.1 The Central Engine	4
1.3 Classification of AGN	6
1.3.1 Seyfert galaxies	7
1.3.2 Quasars	9
1.3.3 Radio galaxies	9
1.3.4 LINERs	10
1.3.5 Blazars	10
1.4 AGN Unification	10
1.5 Jet Phenomenon	13
1.5.1 Relativistic beaming	13
1.5.2 Superluminal Motion	14
1.6 Standard Model of Blazars	17
1.6.1 Particle Acceleration	17

1.6.2	Emission Mechanisms	18
1.7	Blazars	23
1.7.1	Continuum spectral energy distribution (SED)	24
1.7.2	Variability- A Multiwavelength Perspective	28
1.8	Models for the blazar variability	32
1.8.1	Intrinsic models for the variability	33
1.8.2	Extrinsic Models	35
1.9	Motivation and objective of the present work	37
1.10	Plan of the Thesis	39
2	Observations, Data Reduction and Analysis	42
2.1	An Overview of Telescope Facilities Used	43
2.1.1	Mount Abu InfraRed Observatory (MIRO)	43
2.1.2	Swift	46
2.1.3	Fermi Observatory	47
2.1.4	Archival data	53
2.2	Data Reduction and Analysis	54
2.2.1	Optical Data	55
2.2.2	X-rays and UV	59
2.2.3	Gamma-rays	60
2.3	Statistical techniques	63
2.3.1	C-test	63
2.3.2	F-test	64
2.3.3	Amplitude of Variability	64
2.3.4	Fractional Variability	65
2.3.5	Duty cycle of variation (DCV)	65
2.3.6	Structure function	66
2.3.7	Discrete Correlation Function	67
2.3.8	Lomb-Scargle Periodogram Analysis	68
3	Intra-night and Long-term Optical Variability in 3C 66A	70
3.1	Introduction	71

3.2	Observations and Data reduction	74
3.2.1	Observation strategy	74
3.2.2	Data reduction using IRAF	75
3.3	Data analysis	76
3.3.1	INV detection using statistical methods	76
3.3.2	Quasi-periodic variations (QPV) and variability timescales	77
3.4	Results & Discussion	78
3.4.1	Intra-night flux Variability (INV)	81
3.4.2	Variability time-scales and size of the emission region	86
3.4.3	Quasi-periodic variations in 3C 66A	89
3.4.4	Amplitude of variability and source brightness	93
3.4.5	Average brightness trend during 2005–2016	94
3.4.6	Spectral variability during 2005-2016	98
3.5	Summary	107
4	Optical Study of Flaring S5 0716+714	110
4.1	Introduction	111
4.2	Observations and Data Reduction/Analysis	113
4.3	Results and discussion	115
4.3.1	Intra-night variability	116
4.3.2	Long-term variability	137
4.4	Conclusions	149
5	HBL 1ES 1959+650 in Outburst: A Multiwavelength Study	152
5.1	Introduction	153
5.2	1ES 1959+650	154
5.3	Multi-wavelength Observations and Data Reduction	156
5.3.1	Gamma-ray : Fermi-LAT	156
5.3.2	X-ray, UV, optical : Swift-XRT/UVOT	157
5.3.3	Optical observations : MIRO	159
5.3.4	Supplementary data : Optical (Steward Observatory); Radio(OVRO)	160

5.4	Results and Discussion	161
5.4.1	Multi-wavelength light curve	161
5.4.2	MWLC: Outburst 1 (March 2015)	164
5.4.3	MWLC: Outburst 2 (October 2015- June 2016)	166
5.4.4	Twin flares during October 2015 outburst: Optical/ γ -ray light-curve	180
5.4.5	DP and PA change during October 2015 outburst	182
5.4.6	Injection of a new component in the jet	183
5.4.7	Time-averaged Spectral Energy Distribution	185
5.5	Summary and conclusions	188
6	Unprecedented Outbursts in FSRQ CTA 102	192
6.1	Introduction	193
6.2	Multiwavelength Observations and Data Analysis	195
6.2.1	Fermi-LAT Observations	195
6.2.2	Swift X-ray, UV & optical Observations	195
6.2.3	Optical Observations from MIRO	196
6.2.4	Steward Optical Observatory data	196
6.3	Results & Discussion	196
6.3.1	Multiwavelength light curves	199
6.3.2	Correlated variations using zDCF	210
6.4	Conclusions	213
7	Summary and Future Scope	216
7.1	Summary	216
7.2	Work carried out in this thesis	217
7.2.1	Main findings of the study	220
7.3	Challenges and Scope of the AGN Research	222
7.3.1	AGN & origin of VHE γ -rays, neutrino and cosmic rays	224
8	List of Publications	228
8.1	Publications in Journals	228
8.2	Published Reports (ATels)	229

References

List of Figures

1.1	Shown are the approximate spatial locations from black hole, densities and ionization parameters of various AGN components. Credits: Netzer (1990)	4
1.2	A heterogeneous group of various AGN: FR I FR II: Fanaroff-Riley type 1 & 2; Sey xx: Seyferts; NLXG: Narrow Line X-ray Galaxy; HPQ/LPQ: High & low polarization quasars; GPS: GigaHertz Peaked Spectrum source; CDQ: Core Dominated quasars; OVV: Optically Violently Variable quasars; CSS: Compact Steep Spectrum sources; QSR: Quasi-Stellar Radio sources	7
1.3	(Top) The AGN classification based on the radio loudness parameter. (Bottom) The geometry of AGN under the unified model, where the classification is based on the viewing angle. Credits: (Zackrisson 2005).	8
1.4	(Left) A phenomenological unification model of AGN, proposed by Urry and Padovani (1995), suggesting similar intrinsic structure for AGN sources and their orientation dependency. (Right) Accretion rate–Eddington ratio plane showing the AGN unification scheme (Boroson 2002) based on the physical parameters–accretion rates, Eddington ratio and black hole mass. The diagonal lines, from left to right, represent constant black hole masses with $10^6, 10^8, 10^{10} M_{\odot}$. 11	11

1.5	A schematic diagram showing the typical structure of Active Galactic Nuclei (not to scale). A bipolar jet (not shown here) emanates perpendicular to the disk. Image credits: http://www.isdc.unige.ch/\protect\unhbox\voidb@x\penalty\@M\{}ricci/Website/Active_Galactic_Nuclei.html	12
1.6	A schematic showing the superluminal motion from the nucleus of AGN. The plasma blob (in blue color) is emitted towards the line of sight of the observer. Image Credits: Garret Cotter (http://www.astro.physics.ox.ac.uk/\protect\unhbox\voidb@x\penalty\@M\{}garret/teaching/lecture10-2011.pdf).	16
1.7	An observational example of the nearest AGN, M87, which is seen to exhibit superluminal motion.	16
1.8	The synchrotron radiation, emitted when a charged particle gyrates in the presence of magnetic field.	19
1.9	The up-scattering of low energy photons (say, IR photons) by the higher energy electrons under inverse Compton, leading to high energy emission (e.g., X-rays).	21
1.10	A schematic of the synchrotron radiation and inverse-Compton radiation spectra, up-scattered by the power-law distribution of electrons. Image Credits: Kolb (2010).	22
1.11	The schematic shows the blazar sequence, proposed first by Fossati et al. (1998) and later by Abdo et al. (2010b).	29
1.12	A schematic showing the acceleration of electrons at the shock front (left) and the evolution of the synchrotron spectra (right). Figure is taken from the article by Marscher (2016).	34
2.1	Mount Abu InfraRed Observatory (MIRO) is situated at 1680 m above the sea level, on the highest peak of Aravali mountain range in Mount Abu, Rajasthan, India.	44
2.2	A schematic of Swift satellite, a multiwavelength observatory, showing three instruments onboard- BAT, XRT and UVOT. Credits: http://www.swift.psu.edu	48

2.3	A schematic explaining the γ -ray detection in the Large Area Telescope (LAT) instrument, on board Fermi satellite. Concept Credit: https://www-glast.stanford.edu/instrument.html . . .	52
2.4	The Owens Valley Radio Telescope, 40 meter dish antenna, located near Big Pine, California, US. It is dedicated for blazar monitoring at 15 GHz.	54
2.5	Flowchart showing procedure to correct the raw science images using bias and flat frames.	58
3.1	The light curves of 3C 66A in optical R-band	73
3.2	Intra-night variability (INV) light-curves for 3C 66A during 2005-2016	82
3.3	Intra-night variability (INV) light-curves for 3C 66A during 2005-2016	83
3.4	Intra-night variability (INV) light-curves for 3C 66A during 2005-2016	84
3.5	Structure function corresponding to INV detected nights during 2005-2016	87
3.6	Detection and confirmation of a quasi-periodic variation (QPV) on 2015 December, 30	91
3.7	Amplitude of variation as a function of source brightness	94
3.8	Light-curves in B, V, R, and I bands during 2005-2016	96
3.9	Long-term spectral trend as a function of the source brightness . . .	100
3.10	Long-term spectral trend as a function of the source brightness . . .	101
3.11	Spectral evolution with time	102
3.12	Spectral evolution with time	103
3.13	Color trend as a function of bright and faint state of the source . .	104
3.14	Color trend as a function of bright and faint state of the source . .	105
4.1	Intra-night light curves for the source S5 0716+714 during January, 2013 to June, 2015.	124
4.2	Same as for Fig. 4.1, but for 2013 March 7 & March 12 INV nights	125

4.3	Same as for Fig. 4.1, but for 2013 November 11 & December 28 INV nights.	126
4.4	Same as for Fig. 4.1, but for 2013 December 30 & 2014 December 02 INV nights.	127
4.5	Same as for Fig. 4.1, but for 2014 December 03 INV night.	128
4.6	Structure functions for the INV nights are plotted for the source S5 0716+714 during 2013-2015.	128
4.7	Structure functions for the INV nights are plotted for the source S5 0716+714 during 2013-2015.	129
4.8	Structure functions for the INV nights are plotted for the source S5 0716+714 during 2013-2015.	130
4.9	Structure functions for the INV nights are plotted for the source S5 0716+714 during 2013-2015.	130
4.10	Power spectrum density for source S5 0716+714, plotted for the nights showing indication of periodic component in their SFs & LCs.	134
4.11	The amplitude of variability as a function of the average R-band brightness during 2013-2015. The linear regression fit at 95% con- fidence level (0.05 significance) gives p value of 0.049 but Pearson correlation coefficient is low (0.313), showing a weak correlation.	136
4.12	Long-term B,V,R & I band light curves of S5 0716+714 for the duration 2013 January - 2015 May. Data used are from MIRO and Steward observatory.	140
4.13	Color-magnitude plot for source S5 0716+714 during 2013-2015 showing bluer when brighter trend. The statistical significance parameters are given in Table 4.6	145
4.14	Color-magnitude plot for source S5 0716+714 during 2013-2015 showing bluer when brighter trend. The statistical significance parameters are given in Table 4.6.	146
4.15	The color of source S5 0716+714 is plotted with time (MJD). B-V v/s time shows a bluer trend with time while B-R v/s time trend is not significant.	147

- 4.16 The color of source S5 0716+714 is plotted with time (MJD). The trend is not significant at 95% confidence level. 148
- 5.1 Multi-wavelength light curve (MWLC) for 1ES 1959+650 from January 2015 to June 2016, showing three major flaring episodes. Flare 1 (March 2015), Flare 2 (October 2015) and Flare 3 (June 2016) in γ -rays are clearly visible in the MWLC. Time is in MJD, plotted along X-axis and Y-axis has the fluxes/magnitudes. Top panel shows Fermi-LAT fluxes with 3σ statistical error bars. The second panel is soft X-ray (XRT-Swift) with three energy bands (0.3-3.0 KeV, 3.0-10 KeV, and 0.3-10 KeV). Third panel shows UV flux (in mJy; W1 band) from UVOT onboard Swift. Fourth panel display optical V-band magnitudes obtained from Swift, MIRO and Steward Observatory. Last panel shows radio flux at 15 GHz taken from OVRO public archive. 162
- 5.2 (Top): Detailed light curves in γ -ray, X-ray, UV, optical and radio with optical polarization (DP) and position angle (PA) for the duration between MJD 57250 - 57450 (August 2015 to March 2016). (Bottom) : Zoomed version of the light curve in γ -ray and optical showing rapid changes in DP and PA occurred within five days (MJD: 57306.5 - 57311.5) before the onset of major outburst in γ -ray. 165
- 5.3 Discrete correlation plots for 1ES 1959+650, during October 2015 outburst between (Left) γ -ray & UV, (Right) γ -ray & V-band. Top two panels show light curves in respective energies (X-axis : MJD; Y-axis : Flux/Mag) while the bottom panel shows correlation between them (X-axis: Lag in days; Y-axis: zDCF). 171

- 5.4 Discrete correlation plots of 1ES 1959+650, during October 2015 outburst between UV (UVW1 band) & optical (V-band). Top two panels show light curves in respective bands (X-axis : MJD; Y-axis : Flux/Mag) while the bottom panel shows correlation between them (X-axis: Lag in days; Y-axis: zDCF). Correlation is significant at 95% confidence. 172
- 5.5 The X-ray light curve (Time in MJD along X-axis; Counts/sec along Y-axis) shows the similar flux trend in blazar 1ES 1959+650 using three different energy bins, i.e., 0.3–10keV: first panel (from top); 0.3–3keV: third panel; 3–10keV: fourth panel. The second panel shows the spectral index in 0.3-10 keV range. The bottom panel shows the hardness ratio obtained from fluxes at 3.0-10.0 keV and 0.3-3.0 keV. 175
- 5.6 The plot shows correlation between the soft X-rays (0.3–3 keV) and the hard X-rays (3–10 keV) flux in 1ES 1959+650 during its bright state. A strong correlation is seen using the quadratic fit in violet ($R^2 = 0.91$) along with linear fit indicating a common origin of two emissions. The lower panel shows residuals of the fitting. 176
- 5.7 Optical color-magnitude plot of 1ES 1959+650 during 2015–2016. The X-axis shows the B-magnitude and the colors, U-B (top panel), U-V (middle panel) and B-V (bottom panel), are plotted along Y-axis. The legend on the top-right corner shows the average color and the grey dashed line shows the best fit to the data. 184
- 5.8 Time averaged spectral energy distribution for HBL 1ES 1959+650 during 2015-2016. The combined spectra during different epochs covering the flare (filled down-triangles; red), pre-flare (filled circles; cyan) and post-flare (cross symbols; blue) periods. The low-flux phase data collected over the period 2007-2011 are plotted with grey filled circles. The low energy synchrotron component during pre-flare and post-flare periods are seen to overlap (for details, see the text). 186

6.1	Multi-wavelength light curves for CTA 102 during the 2016 Nov - 2017 Jan outburst. From top to bottom: 1d binned Fermi-LAT γ -ray flux ($E > 100$ MeV); Swift-XRT flux (2.0-10.0 keV) ; X-ray photon index (Γ) Swift-XRT; Swift-UVOT UV-band magnitudes (W1, M2, W2); Swift-UVOT and Steward Observatory optical magnitudes; Degree of Polarization (DP%) and position angle (PA in degrees) taken from Steward Observatory.	198
6.2	γ -ray light curve of FSRQ CTA 102 showing flaring activity during November 2016-January 2017. Time in MJD is plotted along X-axis and flux along Y-axis. The grey dashed line shows the average flux level.	200
6.3	γ -ray intra-day flux variability in CTA 102 using 3 hrs and 6 hrs binned data, for the two major flares on MJD 57750-57752 (December 2016) and MJD 57759-57761 (January 2017).	204
6.4	The fractional variability amplitudes of CTA 102 in various energy bands.	208
6.5	γ -ray spectra fitted with a simple power-law ($E > 100$ MeV) for whole duration, 2016 November - 2017 January (green), during the MJD 57751 (red) and the MJD 57760 (blue) major flares.	209
6.6	Discrete correlations (zDCF) for CTA 102 between γ -rays and X-ray, UV and optical fluxes, respectively, during 2016 November-2017 January.	212

List of Tables

2.1	The technical description of X-Ray and UV-Optical telescopes on-board Swift satellite.	49
3.1	A complete log of confirmed INV nights for 3C 66A with the statistical parameter estimation.	80
4.1	Details of the rate of rise/fall in the magnitude for INV nights. Δm_+ , Δm_- represent the source brightening or dimming, respectively.	120
4.2	Details of INV nights for the source S5 0716+714 during 2013-2015. The statistical parameters mentioned, i.e., C and A_{var} , have been calculated at 99% confidence level, N is no of data points and σ is standard deviation in nightly averaged magnitude.	122
4.3	The table shows the structure function parameters for INV nights, k and β , along with time scale of variability. All the parameters have been calculated at more than 99% confidence level.	129
4.4	Observation log and photometric results for S5 0716+714 in R-band during 2013 January-2015 May. Columns are: Date of observation, Time (UT) & MJD, No. of data points, average magnitude with standard deviation & Photometric errors, variable (Y/N)	141
4.5	Brightest and faintest magnitudes of the S5 0716+714 during two & half year period.	142
4.6	The average color values with statistical parameters for color versus magnitude of the source S5 0716+714 during 2013-2015. The plots show a mild bluer when brighter trend.	142

- 5.1 Column 1 represents the different energy regime and the energy ranges are given in column 2. The fractional root mean square variability estimate for each energy range is calculated in column 3 along with the associated errors in column 4, using the prescription given in [Vaughan et al. \(2003\)](#). 178
- 6.1 Nightly averaged R-band optical magnitudes for the blazar CTA 102 obtained using 1.2 m telescope of MIRO, during December 2016. . 202

Chapter 1

Introduction

The energetics and structure of the active galactic nuclei (AGN) remain illusive even after almost 6-decades of their formal discovery. It is because of their compact, un-resolvable dimension and complex energy generation mechanisms, which are non-stellar in nature. The phenomenological model consists of a super-massive blackhole (SMBH; $10^6 - 10^{10} M_{\odot}$), an accretion disk, broad line region clouds (BLR; $10^3 - 10^5$ km/s), narrow line region clouds (NLR; $10^2 - 10^3$ km/s), two bipolar plasma jets and a dusty torus. Because of their large distances and extreme compactness, the jets are resolvable only upto sub-parsec scales using VLBI in nearby AGN. The work presented in this thesis attempts to study these aspects using the variability in blazars—a subclass of AGN- which promises to resolve the small structures based on the observed rapid variations at different wavelengths. The shortest time scales of variations put upper limit on the size of emission regions and are also indicative of their location in the jet. This chapter gives an overview of active galactic nuclei, their properties and classification, and proposed physical emission models to study variability.

1.1 Fascinating Quasars Ever Since

The discovery of quasars was made at radio wavelength in the late 60s. Marteen Schmidt detected the object 3C 273 with a magnitude of 13 in V band with a large redshift ($z=0.37$). The interpretation of such large redshifts was a challenge

at that time. Marteen and Greenstein gave the alternative explanation of 3C 273 and 3C 48 in terms of cosmological redshifts, large distances and enormous luminosities, albeit any strong arguments for it was illusive. The results for both the studies were published in four articles in *Nature*. The appearance of quasars did not initially suggest association with galaxies and they were likely to be found as rare objects only at great distances. At such distances, only the star-like nuclear source is seen in a quasar, and the light from the surrounding galaxy is lost in the glare of the nucleus because of its relative faintness. These sources, therefore, were called quasi-stellar objects (QSOs). With advancement of technology, a large number of such sources were detected and this field developed hugely but the nature of their detailed structure and emission mechanisms still pose a lot of questions which astronomers are trying to answer.

The discovery of these enigmatic sources itself has been fascinating and challenging at those times, when the picture of Universe was considered to be almost complete. The quasar discovery, however, questioned the existing theory of the Universe being a “steady-state Universe” ([Marziani et al. 2012](#), for more details), which considered the infinite (and uniform) expansion of Universe. That convinced Dr. Fred Hoyle to shun his theory of steady state Universe. Researchers all over the world were puzzled to see such high redshift sources and began to question their existence billions light years away from us - the time after the Universe was just reasonably young (Big bang?). It was the era, when many young scientists found the field attractive and switched their field of research in order to unravel the misery behind these enigmatic sources.

For the sake of curiosity, we narrate one incident that lead Dr. Suzi Collins to change her research field, leading to the discovery of the variability in these sources over the years. During her graduate studies, she was aware of the discovery made by Greenstein and Schmidt on 3C273 and 3C48—where they provided the possible explanation on the redshift of these sources using Hubble law. She abandoned the solar flare investigation and started working on quasars. She found the evidences of variability seen in the broad- and narrow-line regions. Also, since these sources were so enigmatically powerful, a comic series was started known as, “Protectors

of Cosmos”, with a character named, ‘Quasar’, mandated to save the Universe, which continued to publish 60 issues. The discovery was so fascinating that, “quasars” became popular name among people. The Byrds, an American band group, even composed a song on one of the quasar, named CTA 102.

In late fifties, after the second world war, radio window enabled the astronomers to look for the pulsars, quasars and many other sources. The quasars and QSOs looked like point sources—just like stars but emitted huge radio emission and other properties unlike stars. Soon the astronomers realized that the process that powers the stars (thermonuclear reactions), was not enough to power quasars. Much later, it was proposed that at the core there is a massive black hole, attracting matter by its huge gravity. The matter is compressed, heated and then partly emitted as radiation. The X-ray studies from, “The Uhuru, Ariel 5, HEAO-1” and “Einstein” satellites show that all kind of quasars were strong X-ray emitters. The third qualitative jump in their study was with the interferometric technique in radio band in the early seventies.

In the following sections we briefly discuss AGN, their classification schemes and blazar phenomenon.

1.2 Active Galactic Nuclei

At the heart of active galaxies lies a very compact structure, known as active galactic nuclei (AGN), which are rare objects in the Universe. A huge energy budget from these compact centers makes these sources spectacular and enigmatic. They are so powerful and luminous that they outshine their entire host galaxy. AGN alone are capable of producing the luminosity which, normally, is of the order of $10^2 - 10^5$ times the luminosity of our Milky Way galaxy. Most of the emission produced is non-thermal, unlike the normal galaxies that radiate as a blackbody due to nuclear emission from the stars. The typical luminosity range for AGN lies between $10^{44} - 10^{49} \text{ erg s}^{-1}$ (Padovani et al. 2017), whereas for normal galaxies it is $10^{38} - 10^{43} \text{ erg s}^{-1}$. What mechanism powers such sources which are very compact in size but emit such huge energy, was the main challenge

Component	Location	Density	Ionization Parameter
Accretion disk	10^{-3} pc	$\sim 10^{15}$ cm $^{-3}$	$U(\text{oxygen}) = 10^{-3} - 10^{-1}$
BLR	0.01–1 pc	$\sim 10^{10}$ cm $^{-3}$	$U(\text{hydrogen}) \sim 10^{-2}$
Torus	1–10 pc	10^{3-6} cm $^{-3}$	$U(\text{oxygen}) \sim 10^{-2}$
HIG	~ 1 pc	$10^3 - 10^5$ cm $^{-3}$	$U(\text{oxygen}) \sim 10^{-2}$
NLR	100–1000 pc	10^{3-5} cm $^{-3}$	$U(\text{hydrogen}) \sim 10^{-2}$
Starburst	~ 1000 pc	$10^0 - 10^3$ cm $^{-3}$	$U(\text{oxygen}) = 10^{-2} - 10^{-4}$

Figure 1.1: Shown are the approximate spatial locations from black hole, densities and ionization parameters of various AGN components. Credits: [Netzer \(1990\)](#).

in front of the physicists and astrophysicists alike. After considerable theoretical and observational efforts, it was accepted that these sources are powered by a central engine, which converts gravitational energy into the radiation.

1.2.1 The Central Engine

The unresolved compact cores of AGN are often referred to as AGN central engine, which is responsible for the extremely high energy output from these sources. The extreme luminosities emitted by AGN indicated that the energy extraction could be possible only through the release of gravitational energy. Around 1960s, when the idea of supermassive blackhole surrounded by a viscous disk emerged ([Zel'dovich & Novikov 1964](#); [Lynden-Bell 1969](#)), it became the standard model of AGN. The accretion efficiency in case of SMBH is nearly 10% ($0.1 m_p c^2$; with luminosity 10^{20} erg/g) and for nuclear fusion reaction (i.e., stars) it is 0.7% ($0.007 m_p c^2$; with luminosity 6×10^8 erg/g). The standard supermassive blackhole model proposed by [Rees \(1984\)](#) easily solved the energy problem in these sources. He proposed that the accretion onto a SMBH is the most efficient source of energy. The Figure 1.1 shows the parameters of different AGN components, given in a tabular format.

Following are considered as components of the central engine.

Supermassive blackhole (SMBH):

The existence of black hole was postulated way back in 1783 by John Michell who mentioned that there might be an object so massive that even light might not

escape! It took Einstein to theoretically declare the existence of such an object through his theory of general relativity. The term, “Black Hole” was coined by John Wheeler in 1968. The blackholes are probably the most mysterious objects in the Universe and mostly occur in the giant ellipticals (for example, Messier 87 (or, M87) at the center of Virgo cluster, and NGC 5128). The basic properties of SMBH are defined by its mass and spin and are expressed in terms of the gravitational radii (r_g) and Schwarzschild radii (r_{sh}). It is now believed that AGN are powered by accretion onto supermassive black hole which converts matter into energy efficiently ($E = mc^2$). The process converts 10% of matter into light (i.e., radiation), leaving behind the typical remnant masses between $10^6 - 10^9$ solar mass. The radiation carries most of the angular momentum and can exert pressure preventing the in-falling of matter into the BH, only if the source is sufficiently bright. This maximum observed luminosity is related to the BH mass and is termed as, “Eddington luminosity”.

Accretion Disk (AD):

The accretion disk surrounding the SMBH, is highly dense (10^{10} cm^{-3}) and has extremely large column density at 1–100 gravitational radii (r_g). The velocity of the accreted matter is nearly 0.3 times the speed of light. The continuum emission from the disk dominates at IR–optical–UV–X-rays energy ranges in the spectral energy distribution curve (SED). Also, various emission and absorption features are observed when a part of disk is illuminated by the central bright source. The accretion disk is present at 0.001 pc away from the central SMBH. The disk geometry is not well understood but based on the predictions of low and high ionization parameters, it is supposed to show the strong spectral signatures of Fe line at 6.4 keV, and resonance transitions in H-like and He-like sequences. These lines, if coming from the vicinity of SMBH, tend to get broadened because of the strong gravitational field and large rotational velocity of the gas.

Broad Line Region (BLR):

The broad line region is thought to be a very dense region of clouds rapidly rotating around the center at the typical velocity range of $10^3 - 10^4$ km/s, with a large column density ($\approx 10^{23} \text{ cm}^{-2}$). The high density ($\approx 10^{10} \text{ cm}^{-3}$) gas clouds

are located at about 1 parsec (1 pc) with an isotropic flux of $10^9 \text{ erg cm}^{-2}\text{s}^{-1}$. These regions produce strong emission lines. i.e., H I, Mg II, Fe II and due to the low covering factor, the absorption lines are weak. Because of the low magnetic field, the magnetic confinement of these sources is possible upto 1G.

Narrow Line Region (NLR):

The physical conditions of NLR are considerably different from BLR, even for the same level of ionization. The narrow line region is a rarer region of clouds which are slowly rotating around the center with a typical velocity of $10^1 - 10^2 \text{ km/s}$, a smaller column density ($10^{20} - 10^{21} \text{ cm}^{-2}$), low density ($\approx 10^4 \text{ cm}^{-3}$) gas clouds located at about 3 kpc with an isotropic flux of $10^2 \text{ erg cm}^{-2} \text{ s}^{-1}$. Due to small covering factor (0.01–0.1), the intense forbidden lines weakens the semi-forbidden and permitted lines. This region also produces coronal lines which are observed in infrared regime.

Dusty Torus (DT):

A dusty torus is a highly dense region ($\approx 10^4 - 10^6 \text{ cm}^{-3}$) of clouds at low temperatures, with equatorial motion in a plane. It has a large column density ($\approx 10^{25} \text{ cm}^{-2}$ or higher), a flat geometry and extends from 1–100 pc from the central BH. These regions contain large amount of dust and can be studied using the spectral properties of the infrared emission and absorption along with the strong dust features.

1.3 Classification of AGN

The sources belonging to AGN family are like a zoo, with a large number of sources having some distinct properties. It was noticed observationally that a set of sources share some common properties and therefore, to facilitate their study, attempts were made to group them together. The major classification of AGN is done based on their radio properties which splits AGN family into two main classes, radio-quiet (RQ) AGN and radio-loud (RL) AGN. The classification forming a heterogeneous group is shown in Figure 1.2 and Figure 1.3.

1. In the radio-loud AGN the radio emission from the jets and the radio lobes

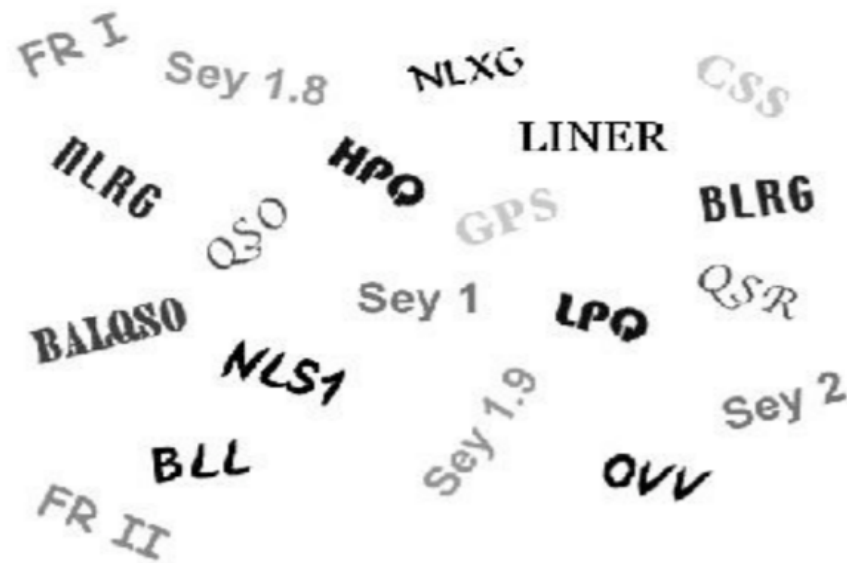


Figure 1.2: A heterogeneous group of various AGN: FR I FR II: Fanaroff-Riley type 1 & 2; Sey xx: Seyferts; NLXG: Narrow Line X-ray Galaxy; HPQ/LPQ: High & low polarization quasars; GPS: GigaHertz Peaked Spectrum source; CDQ: Core Dominated quasars; OVV: Optically Violently Variable quasars; CSS: Compact Steep Spectrum sources; QSR: Quasi-Stellar Radio sources

dominates the luminosity of the AGN, especially at radio wavelengths but these emit in other wavelengths also. It includes blazars (BL-Lac objects and OVV quasars) and Radio galaxies.

2. In the radio-quiet AGN, jet and jet-related emission are negligible/non-existent, radio emission is weak in comparison to the optical emission. These mainly include LINERs, Seyfert galaxies, QSOs.

1.3.1 Seyfert galaxies

Carl Seyfert discovered the first class of AGN having high surface brightness, which is now named after him. To distinguish them from quasars, they have absolute blue magnitude $M_B > -21.5$ and bolometric luminosity is $L_{Bol} = 10^{43} - 10^{45}$ erg/s. The classic Seyferts show the redshift of about $z < 0.1$. The nuclei of Seyfert galaxies show broad and narrow emission lines. Type-I Seyfert galaxies

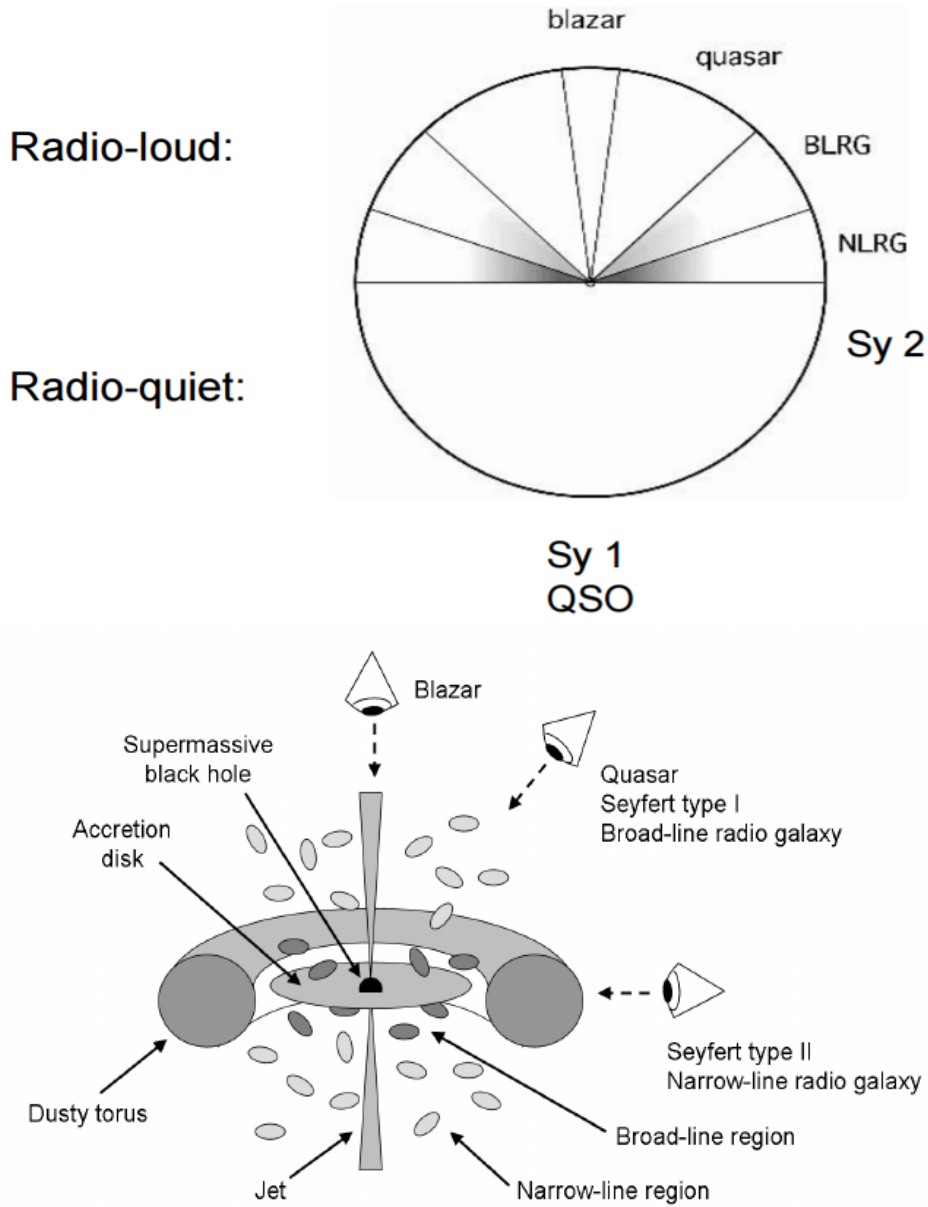


Figure 1.3: (Top) The AGN classification based on the radio loudness parameter. (Bottom) The geometry of AGN under the unified model, where the classification is based on the viewing angle. Credits: ([Zackrisson 2005](#)).

have both narrow and broadened optical spectral emission lines. The broad lines imply gas velocities of 1000-5000 km/s very close to the nucleus. Seyfert type-II galaxies have narrow emission lines only (but still wider than emission lines in normal galaxies) implying gas velocities of 500–1000 km/s. These narrow lines are due to low density gas clouds at larger distances from the nucleus. These galaxies are generally radio–quiet and show broad hydrogen lines. Later on, Seyfert type-I galaxies showed intermediate outburst properties which were divided into sub–classes like Seyfert 1.5, Seyfert 1.8, Seyfert 1.9. Seyfert 1.5 has broad and narrow $H\beta(486\text{ nm})$ emission line components which are similar. Seyfert 1.8 shows weak $H\alpha(653\text{nm})$ and $H\beta(486\text{nm})$ lines and Seyfert 1.9 shows only weak but broad $H\alpha(653\text{nm})$ lines.

1.3.2 Quasars

Quasars were discovered as quasi stellar radio sources in 1963 and have strong optical spectra similar to type-I Seyfert galaxies, but are more powerful and show strong non-thermal emission. Most of them are observed to have jets and lobes like radio galaxies that carry significant amount of energy in the form of particles moving at relativistic speeds. They differ in stellar absorption features and their narrow emission lines are weak. They show variation in brightness over a period of a few weeks to years.

1.3.3 Radio galaxies

Radio galaxies are strong emitters in radio band. They have extended and compact components. Most of the extended sources have linear double structure (single or twin radio lobes extending at Mpc–scale) straddling a giant elliptical galaxy or a quasar near the centre. Compact components coincide with nuclei of galaxies. The radio emission is non–thermal, due to the fast moving electrons that spiral in magnetic field producing synchrotron emission. Sometimes the radio lobes and the nuclear radio emission are seen connected through narrow radio jet features.

1.3.4 LINERs

These objects show only weak nuclear emission-line regions, and no other signatures of the AGN phenomena. A very low nuclear-luminosity class of low ionization nuclear emission-line region galaxies (LINERs) were identified by Heckman (1980). Spectroscopically, they resemble Seyfert 2 galaxies, except that their low-ionization lines, e.g., [OI], $\lambda = 630$ nm and [NII], $\lambda = 654.8$ nm, 658.3 nm, are relatively strong. LINERs are very common, and might be present at detectable levels in nearly half of all the spiral galaxies. It is debatable whether all such systems are true AGN powered by accretion on to a supermassive black hole.

1.3.5 Blazars

The blazars are characterized by a relativistic jet almost aligned towards the line of sight with an angle $< 10^\circ$. Their continuum emission is dominated by non-thermal emission which is highly polarized ($> 3\%$) and variable. They are variable across the whole spectrum and are discussed in the section 1.7. The work presented in the thesis would focus mainly on studying their temporal and spectral variability properties.

All these sub-classes of AGN were found to have one or other properties common with some other class of objects. For example, R. Antonucci & J Miller (1985) detected broad emission lines in NGC 1068, a Seyfert 2 galaxy, in polarized flux. It was inferred to be BLR emission scattered at a large distance from the nuclear region avoiding its obscuration by the torus and detected as polarized emission from a Seyfert 2. Thus, Seyfert-1 and Seyfert-2 were considered belonging to same type of sources. In order to facilitate their study, it was felt to look for ways to unify them based on the common properties and/or structures.

1.4 AGN Unification

Several attempts were made by many workers to unify the objects belonging to various sub-classes of AGN. This led to the emergence of two different unification

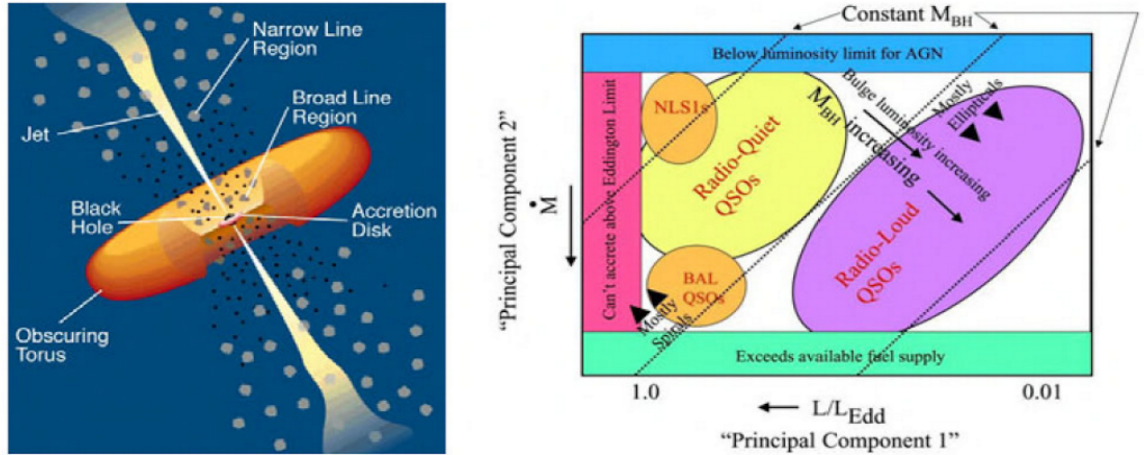


Figure 1.4: (Left) A phenomenological unification model of AGN, proposed by Urry and Padovani (1995), suggesting similar intrinsic structure for AGN sources and their orientation dependency. (Right) Accretion rate–Eddington ratio plane showing the AGN unification scheme (Boroson 2002) based on the physical parameters–accretion rates, Eddington ratio and black hole mass. The diagonal lines, from left to right, represent constant black hole masses with 10^6 , 10^8 , $10^{10} M_{\odot}$.

schemes as shown in Figure 1.4. According to the first approach (Figure 1.4; left), proposed by C. Megan Urry (Yale University) and Paola Padovani (University of Rome), a phenomenological model was developed. According to this model, a supermassive black hole is residing at the center of the AGN which is surrounded by an accretion disk that produces a big blue bump (BBB) and perhaps, broad line clouds also. These are surrounded by an obscuring dusty torus along with narrow line region clouds and a bipolar jet emanating from the center perpendicular to the disk plane (Urry & Padovani 1995). According to this, difference in the properties of various sub–classes is largely based on the way they are oriented in the sky with respect to the observer.

The second approach (Figure 1.4; right) was proposed by Todd Boroson of NOAO (Boroson 2002). It is based on the direct observations and their analysis unifying the AGN sub–classes based on the black hole mass, accretion rate (extracted from luminosity), and ‘Eddington Ratio’ (using mass and luminosity,

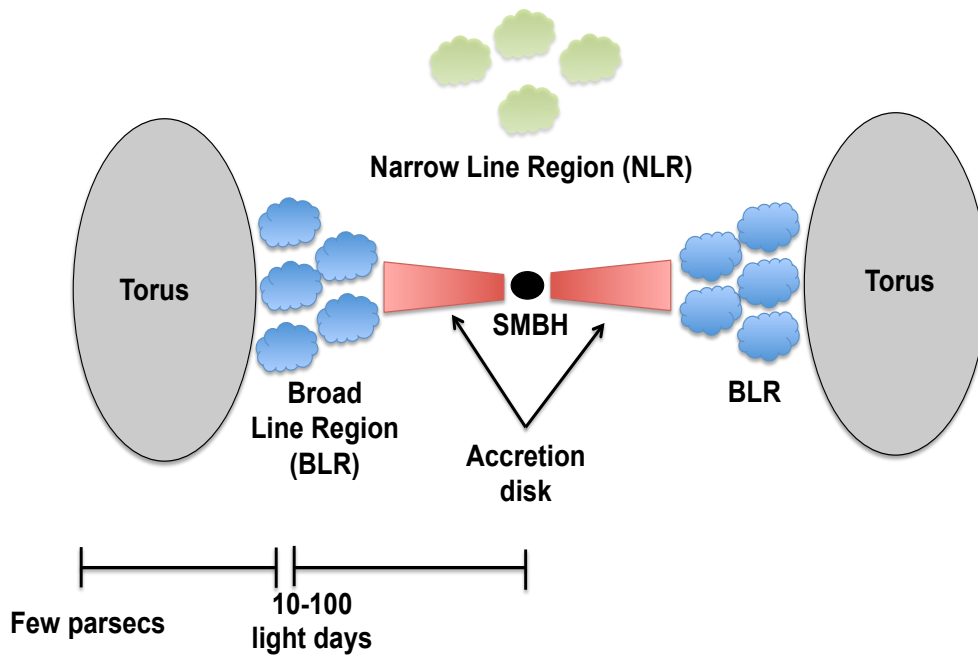


Figure 1.5: A schematic diagram showing the typical structure of Active Galactic Nuclei (not to scale). A bipolar jet (not shown here) emanates perpendicular to the disk. Image credits: http://www.isdc.unige.ch/~ricci/Website/Active_Galactic_Nuclei.html.

both). The radio-loud quasars have larger black hole mass as compared to radio-quiet quasars and due to their similar absolute accretion rates, the accretion rates in radio-loud AGN are somewhat lower than the Eddington limit.

A standard model of AGN is defined based on their observational properties and an assumption that all AGNs are intrinsically similar. The different observational properties seen in a zoo of AGN are due to their orientation effect. A general schematic of AGN is shown in the Figure 1.5.

1.5 Jet Phenomenon

The black holes are powerful drivers of the supersonic flows in the form of jets. The speeds of these outflows in AGN jets become relativistic, indicated by the superluminal motion as observed in the radio. The shocks in the jet may be precipitated by entrainment of the material at the jet-ISM interface or inhomogeneities in the driving stimulus at the base of the jet where these are launched. In both cases, the collision of fast, relativistic blobs with the slower ones forms shock discontinuities and also lead to emission. The blazar phenomenon is the boosted anisotropic radiation emitted in the direction of motion, at a small angle to the LOS, making the jet to look brighter with larger apparent luminosity at all the frequencies. The direct observations of relativistic motion are imaged at radio frequencies. Since the jet is observed very close to our line of sight, it compresses the time resulting in the apparent superluminal motion ([Kellermann et al. 2003](#)).

1.5.1 Relativistic beaming

Relativistic beaming is the result of the bulk relativistic motion of the emitting plasma which is Doppler boosted towards the observer. It has enormous effect on the observed luminosity and easily explains the superluminal motion inside the astrophysical jets. Consider a blob of jet material emitting radiation at some angle θ towards the line of sight of the observer, the Doppler factor can be written as follows,

$$\delta = \frac{1}{\gamma(1 - \beta \cos\theta)} \quad (1.1)$$

where, γ is the Lorentz factor and $\beta = \frac{v}{c}$. Owing to the time dilation introduced due to the relativistic effects, the number of photons in the observer's frame of reference are δ times the number of photons in its rest frame. The emitted radiation is beamed towards the observer that transforms both, viewing angle (θ) and the subtended solid angle (Ω) as,

$$\sin\theta' = \delta \sin\theta \quad (1.2)$$

$$d\Omega' = \delta^2 d\Omega \quad (1.3)$$

After taking into account the cosmological redshift (z), the observed luminosity is order of three more than that intrinsically emitted. It is to be noted that, the frequency at which the radiation is emitted is not same as the received one. We denote the observed and emitted flux as F_{obs} and F respectively. When the blob is traveling towards the observer, the flux (or, brightness) increases by a factor of δ^p (Eq.1.4), while it is Doppler de-boosted when moving away from an observer leading to a flux decreases by the same factor. The observed flux is a function of the jet speed and the viewing angle through Doppler boosting. The equation 1.4 embodies three effects, i.e., relativistic aberration, time dilation and redshift or blueshift.

$$F_{obs} = \delta^{p+\alpha} F \quad (1.4)$$

where, α is the spectral index and $p=2$ for the continuous jet and $p=3$ for a moving sphere (eg, in blazar jets) (Urry & Padovani 1995). Other values of α are also possible (Lind & Blandford 1985).

In the relativistic jets, more energy is transmitted forward towards the observer due to beaming effect. Under the simple homogeneous jet model, spherical blobs of plasma, emit energy isotropically. The beaming aberration is responsible for the δ^2 factor. Another term is the effect of the special relativity-time dilation which is responsible for the flux change by a factor of δ . The third term (α) is the blueshift (or, redshift) of the emitted radiation at a particular frequency which is independent of the beaming factor and contributes to the beaming equations by the factor of $\frac{1}{\delta^\alpha}$. Due to beaming effect in the blazars, it is possible to detect even a small intrinsic variation, which makes these sources very important tools for studying AGN phenomena.

1.5.2 Superluminal Motion

The superluminal motion is a proper motion of the source and their apparent speeds always appear greater than the speed of light ($v_{app} > c$). In 1966, Rees

explained that this phenomenon occurs when the emitting regions move at speeds close to speed of light at small angles to the line of sight (Rees 1966). Blazar jets are relativistic in nature and the moving jet plasma (or blobs) follow the photons they have emitted. This greatly reduces the time interval between the two photon events in the observer's frame of reference leading to the impression of faster than light speeds. Consider a blazar lying at a distance R from the observer (Figure 1.6) with jet inclination angle θ to the LOS. Suppose at time t_1 , a blob is ejected from the nucleus that moves down the jet at a speed βc . In the observer's frame of reference, the blob is seen by observer at t_1 ,

$$t_1 = \frac{R}{c} \quad (1.5)$$

where, c is the speed of light. The ejected blob travels down the jet for some time T in the blazar frame of reference. The transverse separation of the blob after this time is,

$$\Delta X = \beta c T \sin \theta \quad (1.6)$$

Now, at time t_2 , the observer sees the blob reaching a distance ΔX from the center. The light emitted at time T , travels a distance of $R - \beta c T \cos \theta$. The time t_2 is calculated as follows,

$$t_2 = \frac{R}{c} + T(1 - \beta \cos \theta). \quad (1.7)$$

Therefore, the apparent transverse velocity is calculated as,

$$\beta_{app} c = \frac{\Delta X}{t_2 - t_1} \quad (1.8)$$

or,

$$\beta_{app} = \frac{\beta \sin \theta}{1 - \beta \cos \theta} \quad (1.9)$$

where, $\beta = \frac{v}{c}$.

For small θ , β is close to 1 and $\beta_{app} > 1$. For $\cos \theta = \beta$ or $\sin \theta = \gamma^{-1}$, the maximum value of apparent velocity reaches as, $\beta_{app,max} = \sqrt{\gamma^2 - 1}$, where, $\gamma = \frac{1}{\sqrt{1-\beta^2}}$ is Lorentz factor. The values of β_{app} up to 5 to 10 are observed in many sources (3C 279, M87 etc.) using Very Large Baseline Interferometer (VLBI). Figure 1.7 shows the superluminal motion as detected using VLBI in the nearby AGN, M87.

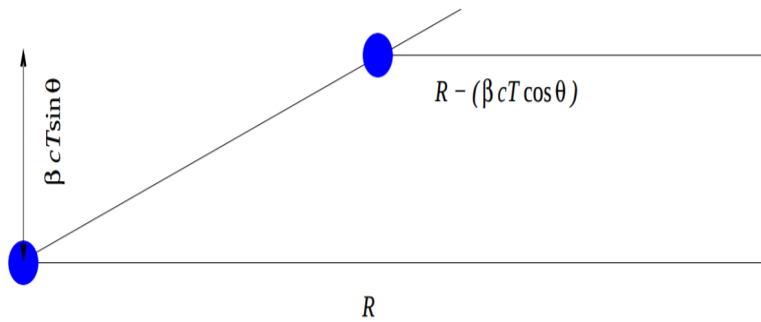


Figure 1.6: A schematic showing the superluminal motion from the nucleus of AGN. The plasma blob (in blue color) is emitted towards the line of sight of the observer. Image Credits: Garret Cotter (<http://www.astro.physics.ox.ac.uk/~garret/teaching/lecture10-2011.pdf>).

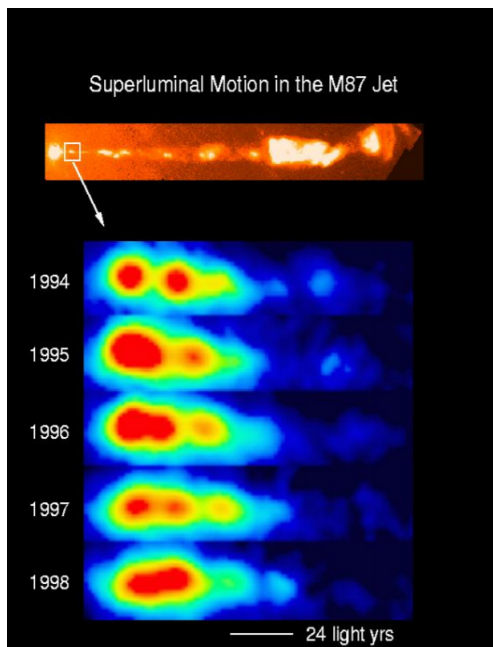


Figure 1.7: An observational example of the nearest AGN, M87, which is seen to exhibit superluminal motion.

1.6 Standard Model of Blazars

The standard model of blazar can be described by the two main processes which explain the non-thermal emission from these sources. The first process is the particle acceleration and the second one is the radiation mechanisms. We briefly discuss these two processes in the following.

1.6.1 Particle Acceleration

It is known that the jet emission, in blazars, is dominated by the non-thermal emission process due to the particle accelerated in the jet ambient magnetic field. The energy losses are rapid and require efficient acceleration/injection at the sites of their dissipation. The most preferred scenario to explain the particle acceleration is to invoke the strong shocks in the mildly relativistic jet ([Marscher & Gear 1985](#); [Marscher et al. 2010](#)). According to this picture, the shock front propagates down the jet, a part of energy is converted in energizing the particles (electrons/positrons) upto relativistic speeds, and dissipation occurs when the shock interacts with the local inhomogeneities present inside the jet ([Blandford & Königl 1979](#)). The basic mechanism behind the fast particle acceleration is possible through the Fermi I acceleration process.

Fermi Processes

In the optically-thin plasma, the shock front carries a high flux of high energy particles on either side of the shock (front and back). When the particles with very high energy are injected into the jet, they interact with the shock front which has relatively low energy as compared to the energy of injected particles. There is an isotropic velocity distribution of particles inside the jet and the total mass is conserved through the shock. Each time the particles cross the shock front, they only gain the energy which is of the order of v/c . In case of strong shocks, the collision is always head-on and energy is transferred to the particles, unlike in the standard Fermi mechanism (i.e., Fermi II process). This scattering process ensures the isotropic power-law particle distribution producing flat spectrum,

i.e., $N(E)dE = E^{-\alpha}dE$, where, $\alpha=2$. Therefore, Fermi I acceleration process is considered to be a *clever acceleration* mechanism where the particles only gain energy each time they cross the shock front.

On the other hand, the original Fermi mechanism (also known as Fermi II process) was proposed by Fermi in 1949 to explain the stochastic acceleration of the cosmic rays. This process is relatively slow process compared to the Fermi I process with the $(v/c)^2$ dependence on the rate of energy losses. It assumes that the particles and the *in-situ* inhomogeneities undergo an elastic collision and produce a power-law distribution of the particles.

Magnetic Reconnection

Apart from the Fermi acceleration processes, a model that could explain the fast and highly variable flares in the blazars, is via magnetic reconnection model. This model can be used to produce a single power-law distribution of particles but fails to produce the break energy spectrum in the low- and high-energy components. Several authors have tried to explain the high energy particle acceleration using magnetic reconnection models without invoking shocks. They argue that this process alone could produce rapid high energy flares more efficiently (see the discussions by [Nalewajko et al. \(2011\)](#); [Narayan & Piran \(2012a\)](#); [Guo et al. \(2015\)](#); [Sironi & Spitkovsky \(2014\)](#); [Nalewajko et al. \(2015\)](#)). They also claim that even efficient shocks are not able to accelerate particles far beyond thermal energy. Magnetic reconnection can supply about 50% of the dissipated energy into non-thermal leptons.

1.6.2 Emission Mechanisms

The blazar jets accelerate the particles upto (ultra-)relativistic velocities, much above the thermal energy of the environment, which then cool down emitting radiation at respective energies. The knowledge of their emitting regions are inferred by studying the radiation they produce through radiation mechanisms ([Kolb 2010](#)). We discuss two main radiative processes that are responsible for the emission at low and high energies and the spectral features in the blazars.

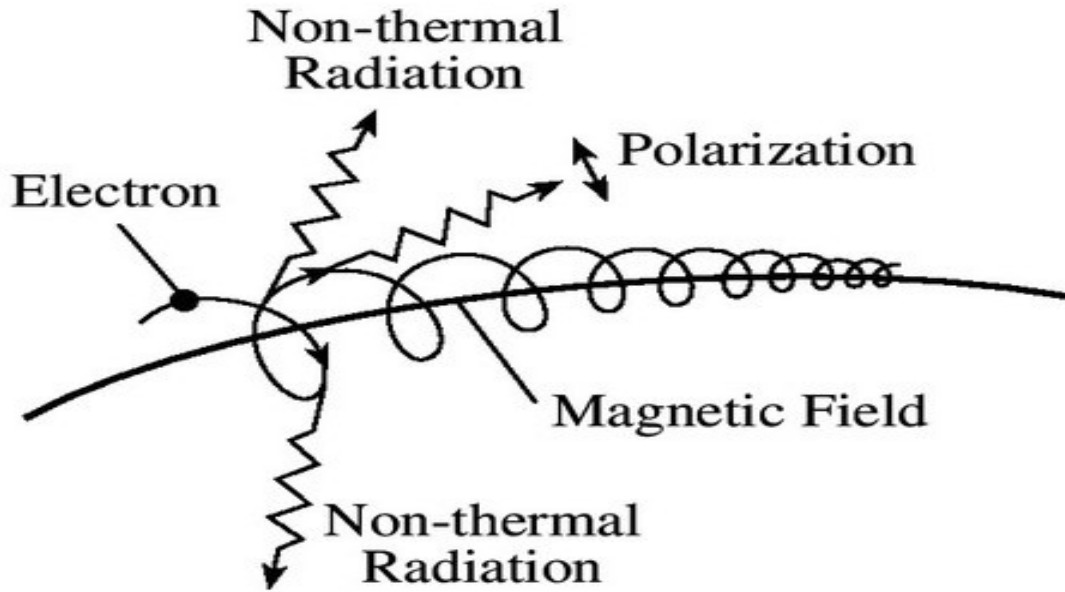


Figure 1.8: The synchrotron radiation, emitted when a charged particle gyrates in the presence of magnetic field.

Synchrotron Radiation

The synchrotron radiation is predominantly produced by the acceleration of electrons (or positrons), because of their small masses compared to mass of a proton ($m_p/m_e = 1836$) and are easy to get accelerated in the presence of the magnetic field (Figure 1.8). When an electron with velocity v enters a magnetic field B , it experiences a Lorentz force $ev \times B$. This force accelerates the particles in the direction perpendicular to the vB -plane. The electron propagates in a helical path around the magnetic field and radiates with frequency of its revolving motion (cyclotron radiation). The cyclotron frequency is obtained as

$$\nu_{cy} = \frac{eB_{\perp}}{2\pi m_e} \quad (1.10)$$

where, B_{\perp} is the magnetic field strength perpendicular to the direction of motion of the electron.

The synchrotron radiation is highly polarized in nature and is observed in most of the high energy astrophysical sources. We consider the particle energy distribution following a simple power-law, $F_{\nu} \propto \nu^{-\alpha}$, producing non-thermal synchrotron radiation,

$$N(E)dE = KE^{-\alpha}dE \quad (1.11)$$

where, α is an index varying from 2-2.5 and K is the normalization constant. The energy spectrum for an ensemble of electrons with a power-law distribution (p) obeys a power-law (with index, α), as shown in Figure 1.10, and their indices are related as,

$$\alpha = \frac{(p-1)}{2} \quad (1.12)$$

For a single particle, frequency dependent scenario, the total synchrotron power is given as

$$P_{sync,tot}(\nu) \propto B^{(\alpha+1)/2}\nu^{-(\alpha-1)/2} \quad (1.13)$$

The most important property of non-thermal synchrotron radiation is that a power-law particle distribution with index α produces the spectrum obeying the power-law distribution with index $p = (\alpha - 1)$. The optically thin synchrotron spectrum increases towards lower frequencies (Rayleigh-Jeans criterion), i.e., below the critical frequency and hence, is self-absorbed as the emission rate exceeds that of the blackbody radiation. The critical frequency depends on the energy of the electrons as, $\nu_c \propto E^2$. At lower energies, the spectrum behaves as $P_{sync,tot} \propto \nu^p$, where $p=5/2$, which gives a clear indication that the radiation is non-thermal and the critical frequency is a measure of the optical depth of the emitting region. The total power depends upon the density of the photons and the energy density of the magnetic field, i.e., $U_B = B^2/8\pi$. The equation 1.13 tells that the more energetic particles (electrons) contribute more to the emitted power and radiate at higher frequencies. From the total power, the cooling timescales of the electrons are calculated as follows,

$$t_{cool} = \frac{E}{P} \quad (1.14)$$

$$t_{cool} = \frac{\gamma_e^2 mc^2}{(4/3)\sigma_T c U_B \gamma^2 \beta^2} = \frac{24.57}{B^2 \gamma} yr \quad (1.15)$$

The magnetic field, B, is in Gauss. One can, therefore, estimate strength of the magnetic field if one knows cooling time and Lorentz factor.

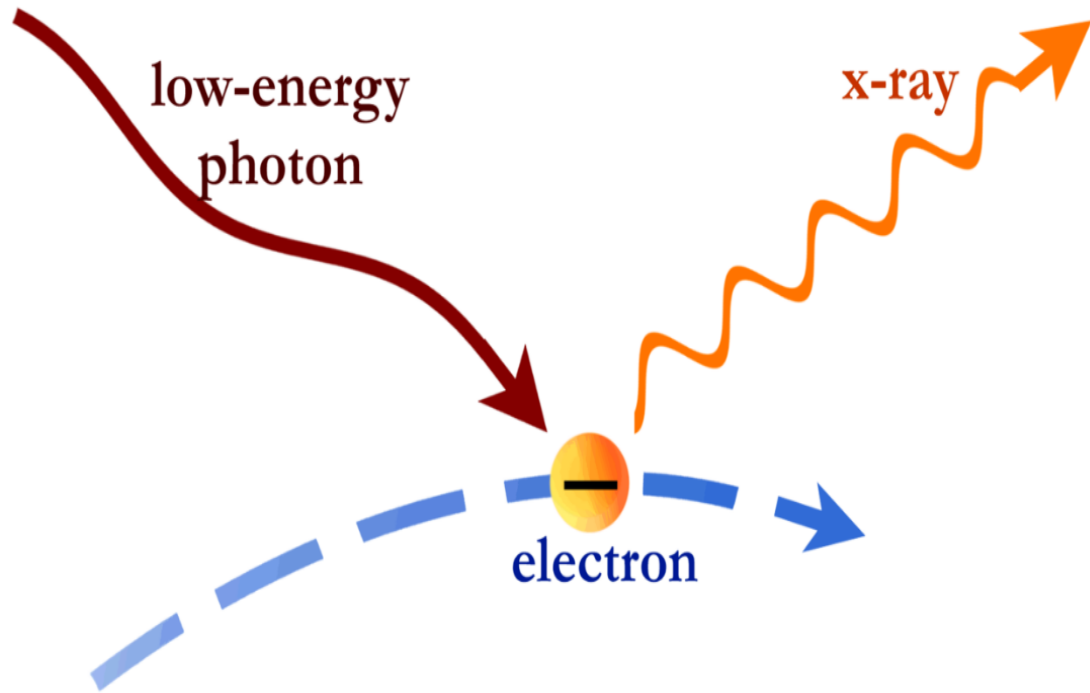


Figure 1.9: The up-scattering of low energy photons (say, IR photons) by the higher energy electrons under inverse Compton, leading to high energy emission (e.g., X-rays).

Inverse Compton Radiation

In conjunction with the synchrotron emission, the inverse-Compton (IC) radiation is predominantly present in almost all high-energy astrophysical sources. The interaction or collision of electron with photon gives rise to Compton radiation where the energetic photons lose their energy to the less energetic electrons. The high energy relativistic electrons, on the other hand, impart their energy to the photon resulting in high energy emission (photon gains, instead of losing energy). This process is called the IC scattering.

The frequency of the scattered photon, ν_{IC} , is calculated based on the relativistic energy-momentum conservation as,

$$\nu_{IC} = \frac{4}{3}(\gamma_e^2 - 1)\nu_0 \quad (1.16)$$

where, ν_0 is the photon frequency before scattering. This follows the same scenario of the synchrotron radiation, that more energetic electrons tend to emit at higher

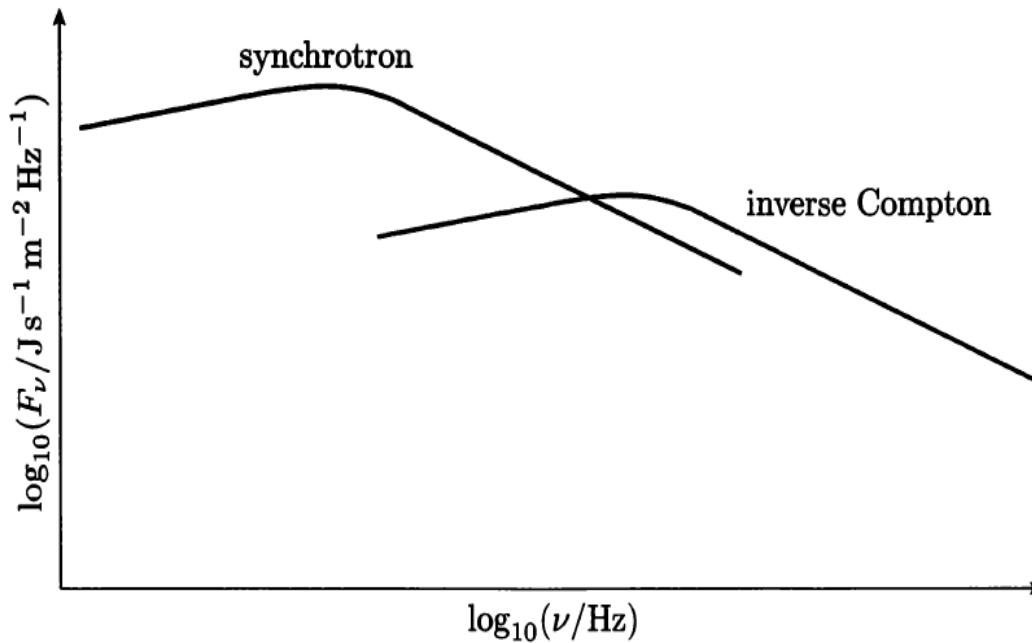


Figure 1.10: A schematic of the synchrotron radiation and inverse-Compton radiation spectra, up-scattered by the power-law distribution of electrons. Image Credits: [Kolb \(2010\)](#).

frequencies. For a single electron, the power emitted is,

$$P_{IC} = \frac{4}{3} \sigma_{TC} (\gamma_e^2 - 1) U_{rad} \quad (1.17)$$

where, U_{rad} is the available energy density of the photons for scattering. The equations describing both the processes share a very close resemblance with each other. It is because they are derived from the equivalent physical processes, i.e., scattering between the electron and a photon. The ratio of total power emitted as a the synchrotron and inverse-Compton radiation gives the relative intensity which depends upon the radiation field and magnetic field energy densities,

$$\frac{P_{sync}}{P_{IC}} = \frac{U_B}{U_{rad}} \quad (1.18)$$

The IC process is very important in the case of AGN as higher energy emissions, X-ray and gamma-ray, are produced through this process.

The inverse Compton scattering takes place through two main processes which contribute to the high energy emission– self-synchrotron Compton (SSC) and/or

external Compton (EC). The brief description of these processes is given in the section 1.7.1.

1.7 Blazars

Briefly defined in the section 1.3.5, blazars are extremely violently variable sources among all AGN. They show featureless continuum spectrum (Biermann et al. 1981) or a continuum with very weak emission lines (with equivalent width less than 5 \AA). The extreme properties seen in blazars are due to non-thermal emission from a relativistic jet which almost points towards the line of sight (Blandford & Königl 1979; Urry & Padovani 1995) and hence flux is Doppler boosted as discussed earlier. Due to their orientation, it is possible to probe the central regions of the AGN and study the events happening very close to the black hole. Many blazars are detected with features (knots) moving at apparent superluminal velocities within the first few tens of parsecs of their jets. The blazars exhibit following properties:

1. Compact and core-dominated sources responsible for the blazar phenomenon.
2. Strong millimeter emitters, accompanied by flat/inverted radio spectrum.
3. High and variable optical ($P > 3\%$) and radio ($P > 2\%$) polarization.
4. Highly variable at time scales ranging from sub-day to tens of years at all the energies.
5. Strong γ -ray emission upto TeV energies which is extremely variable.
6. Exhibits superluminal motion of VLBI components.

The current VLBI network is able to resolve the nearby blazar jets only upto sub-parsec scales at sub-mm wavelengths (Marscher 2008) which can image the core upstream the jet. Due to the opacity effects and the limitations of the current telescope resolution, we can not probe the jet structure upstream this VLBI core. These unresolved regions are thought to be the production sites of very high energy γ -rays as they are very close to the central engine. However, this lack

of resolution can be addressed, at least partly, by variability in flux which puts constraints on the size of the emission regions and structure in the jet.

1.7.1 Continuum spectral energy distribution (SED)

The spectral energy distribution (SED) of blazars shows two broad peaked structures, the nature of which has been widely discussed in the literature (Fossati et al. 1998; Abdo et al. 2010b, and references there-in). The first peak in SED corresponds to the synchrotron radiation process which is believed to originate from the gyration of relativistic electrons around the strong magnetic field present inside the jet and covers radio to UV/X-ray frequencies. The second peak corresponds to inverse Compton (IC) process, in which the low energy photons (*seed photons*) are being up-scattered to very high energies by the high energy charged particles. There are two possible scenarios under consideration which are responsible for the emission at higher energies. Under the first scenario, the same population of relativistic electrons up-scatter the photons which are being produced through the synchrotron process itself, upto very high (TeV) energies (Jones et al. 1974; Ghisellini et al. 1985; Bloom & Marscher 1996). This process is known as Self-synchrotron Compton process (SSC). According to the second scenario, the low-energy seed photons, which are external (Begelman & Sikora 1987) to the jet either from AD (Dermer & Schlickeiser 1993), BLR (Sikora et al. 1994), or dusty torus (Błażejowski et al. 2000), are up-scattered to very high energies and the process is called the external Compton (EC). The origin of the seed photons is not well understood and so is the production mechanism of the high energy component. In addition to the above mentioned ‘leptonic’ processes which produce high energy emission, such emission is also proposed to be produced via hadronic processes (Mannheim & Biermann 1992; Aharonian 2000; Mücke & Protheroe 2001; Mücke et al. 2003; Böttcher 2006; Boettcher 2010). The issue whether it is the leptonic, hadronic or a hybrid (leptonic and hadronic, both) model which is responsible for such high emission, is yet to be settled. Presently, though most of the observational data agree with the leptonic origin of the photons, there are shortcomings of these simplistic models to explain, for example, the high en-

energy phenomenon like the occurrence of the orphan flares at GeV-TeV energies, softer spectra at higher energies, sites of high energy production, the evidences of neutrino detection from AGN, and many more.

Depending upon the position of the synchrotron peak frequency ν_{sync}^{peak} in SED, blazars have been classified into three categories [Abdo et al. \(2010b\)](#).

1. LBLs (low energy peaked BL Lacs) - $\nu_{sync}^{peak} < 10^{14}$ Hz.
2. IBLs (intermediate energy peaked BL Lacs) - 10^{14} Hz $< \nu_{sync}^{peak} < 10^{15}$ Hz.
3. HBLs (high-energy peaked BL Lacs) - $\nu_{sync}^{peak} > 10^{15}$ Hz.

where, ν_{sync}^{peak} represents the synchrotron peak frequency. Figure 1.11 shows a general schematic of the spectral energy distributions of these sources. The flat spectrum radio quasars (FSRQ) which are part of the blazar class and differ in that they have broad emission lines also have low synchrotron frequency and high polarization. In addition to the peak frequency, the blazar sub-classes (FSRQs, LBLs, IBLs, HBLs) are also seen to differ in luminosities. Fossati1998 reported anti-correlation between luminosity and synchrotron peak frequency- FSRQs being the most luminous blazars. However, several sources were detected which violate the sequence; e.g. luminosity of PKS 1424+240 is at the same level as FSRQ 3C279, but the peak frequency is two orders of magnitude higher.

Several comprehensive models are proposed by [Blandford & Königl \(1979\)](#); [Marscher \(1979\)](#); [Konigl \(1981\)](#); [Marscher & Gear \(1985\)](#); [Ghisellini et al. \(1985\)](#), to explain intrinsic radiation mechanisms in blazars. According to these, the synchrotron radiation is responsible for low-energy component and inverse-Compton for the high-energy component in the spectral energy distribution. The origin of synchrotron emission is due to the gyration of electrons (preferably) in the magnetic field and inverse-Compton emission is due to the upscattering of low-energy photons (internal or external to the jet) by the same population of electrons emitting synchrotron radiation. All these models include the possibility of internal (SSC) as well as external (external radiation Compton; ERC) seed photons for the high energy component.

In case of FSRQs, it has been generally seen that the jet luminosity is dominated by the Compton component and the ratio (Compton component to synchrotron component), in some cases, reaches upto 100 during the flares (for e.g., in case of 3C 279; [Hayashida et al. \(2012\)](#)). This means that the high energy flux is much higher than the synchrotron one which has implications on the magnetization of the jets. The jet collimation, acceleration and radiative models invoke the strong magnetic fields to explain the radiation at all frequencies. During the rapid flares, one possibility of particle acceleration is through the magnetic reconnection process, under the “jets inside a jet” scenario, as shocks become less efficient in high magnetic field environment.

Spine-Sheath Model:

Another scenario of spine-sheath structure of the blazar jet is proposed by [Sikora et al. \(2016\)](#), in which spine moves at higher Lorentz factor as compared to the sheath. This model is valid for blazars having significant particle density, like FSRQs, where ERC is a dominant process which produces the high energy radiation with or without any counterpart at the lower-energies. Studying their high energy component, in detail, leads to a better understanding of the particle acceleration and the jet structure.

Mirror model:

A canonical picture addresses the emission from FSRQs by using one-zone SSC modeling, where the synchrotron and IC emission originate from a single region. The recent results by [Vittorini et al. \(2014\)](#) for the blazar 3C 454.3, and [Hayashida et al. \(2015\)](#), for 3C 279, pose serious challenges for these simplistic models while explaining high luminosities and uncorrelated γ -ray emission. Recently, [Tavani et al. \(2015\)](#) introduced version of their mirror geometry model to explain above mentioned problems. In addition, this model is able to produce the hard energy spectra (100 MeV–10 GeV) which otherwise is not possible using the standard SSC approach.

In HBLs, the low energy component peaks near X-rays and high energy near

TeV range in the SED. The correlation between these two energy ranges provides a viable tool to study their emission processes. Recently, [Furniss et al. \(2015\)](#) for Mrk 501 and [Baloković et al. \(2016\)](#) for Mrk 421, studied the broadband spectral properties of HBLs and found the time series correlation between X-rays and VHE γ -ray energy bands, suggesting their emission to originate from the same population. Under the simplest synchrotron and SSC approach, the amplitude of variability in SSC component follows the quadratic relation with that at synchrotron fluxes for Mrk 421 ([Baloković et al. 2016](#)) but it follows linear trend (possible under EC scenario) in case of Mrk 501 [Furniss et al. \(2015\)](#). This poses a challenge in explaining the variability properties in these objects using SSC and perhaps involves the larger variable magnetic field during the flares to explain second case ([Katarzyński et al. 2005](#)). [Madejski et al. \(2017\)](#) reported that the different correlations between X-rays and VHE γ -rays cannot be solely attributed to the Klien–Nishina (KN) effect, because the variability at TeV, for both the cases, is seen in KN regime.

Leptonic or Hadronic Model

The existing leptonic radiative models, with some modifications, are able to broadly explain the low and high energy, including γ -ray, observational data. The major difficulty lies in explaining the γ -ray variability seen in those sources where no correlation between low-energy and high-energy component is seen (for example, orphan flare in case of 1ES 1959+650; [Krawczynski et al. \(2004\)](#); [Aliu et al. \(2014\)](#)). The models invoke hadronic processes to explain the un-correlated γ -ray variability during a flare. [Mannheim & Biermann \(1992\)](#); [Aharonian \(2000\)](#) specifically introduced hadronic models in which the protons play a major role in IC emission process. Under this scenario, the emission is produced by direct synchrotron emission from protons and mesons, and, via synchrotron emission of pair cascades triggered by photo-meson process. In case of proton-proton model, protons are accelerated via the shocks in SNe, gamma-ray burst and AGN jets in the presence of strong magnetic fields. The accelerated protons interact with ISM or other ambient protons and create neutral pions or eta mesons, which

quickly decay by emitting gamma-rays. However, these models have limitations and are not favored because they are radiatively inefficient (Sikora et al. 2013) and require the acceleration of protons to very high (more than 10^{19} eV) energies (Zdziarski & Böttcher 2015). It puts requirement of very high magnetic field (30G or higher) and restricting photon field largely to synchrotron photons to produce gamma-ray by photon-pion process.

Considering the large total kinetic energy in FSRQ-jets, the pure leptonic scenario falls short (Sikora & Madejski 2000) of explaining the bulk motion and radiation mechanisms. It is because of the over estimation of the soft X-ray emission produced by the IC process in leptonic scenario, is located at the lower energy side of the particle distribution. The study conducted by Ghisellini (2012) indicates that in FSRQ, matter in the jet is dominated by the protons. A general picture of radiation mechanisms in blazar jet has emerged where, the SSC models work relatively well for HBLs and ERC models are required for FSRQs. The SED modeling suggests that the FSRQs have sufficient circumnuclear material present in their environment that produces the strong radiation field, which is lacking in the case of HBLs.

Though there are several attempts to interpret the observed data using various models, not a single model is able to uniformly and satisfactorily explain observational data even from a single source taken at different epochs. A large number of parameters are tweaked to fit the data with additional approximations. Therefore, situation on theoretical modeling is far from satisfactory.

1.7.2 Variability- A Multiwavelength Perspective

The most striking property of blazars is their variability. The patterns seen in their light curves are really complex throughout electromagnetic spectrum. However, lightcurves carry a lot of information on the variability mechanisms, particularly during the flares. It has been observed that the amplitude of variability increases towards the higher energies. The higher variability amplitude is observed just after the two respective peaks in their SED, indicative of spectral hardening towards higher frequencies.

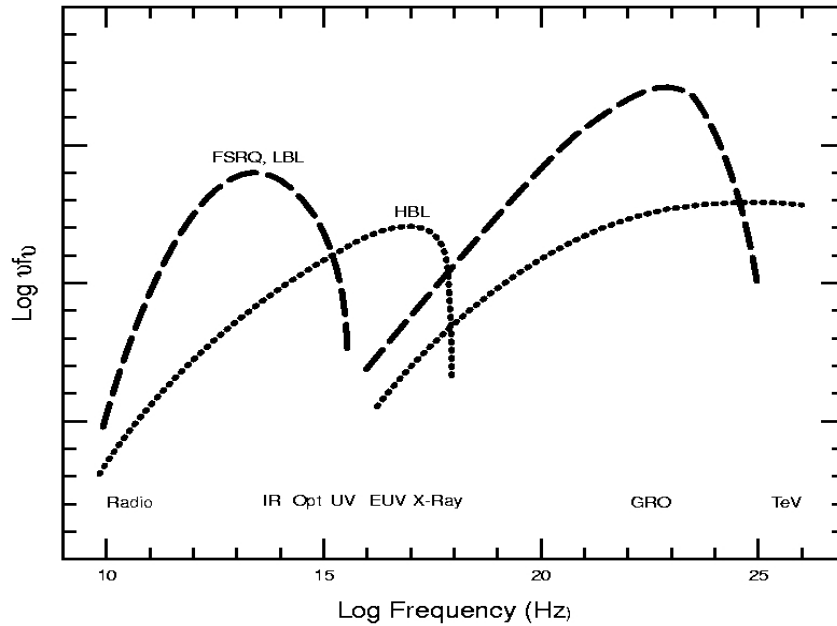


Figure 1.11: The schematic shows the blazar sequence, proposed first by [Fossati et al. \(1998\)](#) and later by [Abdo et al. \(2010b\)](#).

Blazars are one of the most luminous distant sources in the Universe showing extreme variability in their flux. Variability in blazars is a powerful diagnostic tool to study the activities near to the central blackhole system due to very close alignment of the jet to the line-of-sight. Therefore, they prove to be the ideal sources to study the jet physics and to interpret the physical processes leading to the emissions at all the timescales. The variability, being a characteristic feature of blazars, is manifested at all wavelengths with different variability time-scales ([Wierzcholska & Siejkowski 2015](#)). Based on the time scale of variation, the variability is categorized as in the following.

1. **Intra-night variability:-** The rapid variability over the span of few hours to minutes is termed as intra-night optical variability (INV) or micro-variability. The term rapid means that the rate of change of brightness is a few tenths of magnitude over the span of a day or less ([Wagner & Witzel 1995](#)). The INV puts strong constraints on the size of the emitting volume and has been used extensively for this purpose as the sources are not otherwise resolved. The reasons behind such rapid variations are not clear at all and various propositions are made in the literature. The INV

was first detected at radio wavelengths, in 3C 279 (Oke 1967). Later, with the detection of variability at other wavelengths, it became the generic feature of the blazars and was reported by several authors (e.g., Miller et al. (1989); Wagner & Witzel (1995); Jang & Miller (1997); Wu et al. (2005); Fan (2005); Montagni et al. (2006a); Fan et al. (2009); Poon et al. (2009); Rani et al. (2010); Chandra et al. (2011); Bachev et al. (2012); Wierzcholska & Siejkowski (2015); Kaur et al. (2017c)).

The optical flares on time scales of few hours were reported by Miller et al. (1989); Carini et al. (1992) with change in brightness by 0.5 mag in ten minutes which puts stringent limits on the size of the emission region. However, it also posed challenges to explain such rapid variations vis-a-vis brightness temperatures. There are other recent studies carried out to understand the intra-night flux and spectral variability as reported by several authors on different blazar sources (e.g. Qian et al. 2000; Villata et al. 2002; Papadakis et al. 2004; Poon et al. 2009; Wu et al. 2009; Stalin et al. 2009; Hao et al. 2010; Chandra et al. 2011; Larionov et al. 2016a; Gaur et al. 2012; Agarwal et al. 2015; Raiteri et al. 2015; Kaur et al. 2017c, and references there-in). Recently, Bachev et al. (2017) reported the instances of rapid variability on intra-night timescales for FSRQ CTA 102 in its outburst phase, showing 0.2 magnitude enhancements in 30 minutes and overall changes of about 0.4-0.5 mag spanning few hours. The authors found asymmetric flare profiles in their light curves and suggested the cause behind intra-night variability as the change in the Doppler factor due to the helical motion of a blob, leading to boosting of the observed flux by a factor of δ^3 .

After their detection in high energy gamma-rays by EGRET (Hughes et al. 1980) a kind of revolution was witnessed with a large number of blazars being detected in several surveys (Jorstad et al. 2001; Romani et al. 2005; Healey et al. 2008). These exhibited extreme variability in the γ -rays (GeV-TeV) at shorter and shorter time scales. The most spectacular result was reported by Aharonian et al. (2007), with source PKS 2155-304 showing

γ -ray variability within 200 seconds (≈ 3 min) as detected by H.E.S.S.¹. The authors suggested that such dramatic variability could arise either due to the large Doppler factor or its origin is not associated with the central black hole system and these are being produced at larger distances from black hole. A recent study conducted on PKS 0736+017 (Cerruti et al. 2017) could locate the γ -ray production site, based on the opacity effects, variability timescales, and the cooling timescales.

2. **Short-term variability:-** The variability over the timescales from a few days to weeks and months is termed as short-term variability (STV). The amplitude of variation is expected to be more than a few tenths of a magnitude or more. These can be caused by instability in the disk or the interaction of plasma blobs with inhomogeneities in the jet (Ghisellini et al. 1997; Villata et al. 1998, 2002; Gaur et al. 2015; Baliyan et al. 2016; Zhang & Li 2017, and references there-in).
3. **Long-term variability:-** The variability in flux or polarization with the timescales ranging from several years to months, is called long-term variability (LTV). These are often caused by large outbursts of the source which last for several years and cause a change in the brightness by several magnitudes (1.5-5 or so). The reasons behind such variability could be perturbation in the accretion disk, injection of plasma at random intervals which cause formation of shocks. These shocks move down the jet and interact with randomly distributed particle over densities (stationary shocks). These could also be caused by precession of the jet leading to quasi-periodicities in the flux.

Montagni et al. (2006a) reported the optical variability in the blazar S5 0716+714 in their ten years of observations. The source varied about 2 magnitudes in R-band at an average rate of change of brightness, $\delta m/\delta t = 0.027$ mag/hr. The fastest variation rate was found to be 0.1 mag/h over the span of about 2 hours. Sandrinelli et al. (2013) presented the results of

¹H.E.S.S. is an acronym for The High Energy Stereoscopic System, that detects high energy cosmic photons between 0.03-100 TeV energy range.

optical-NIR variability based on the data from 2005-2012, on the six blazars and found three sources, PKS 0537-441, PKS 1510-089 and PKS 2155-304, showing dramatic variability with >3 magnitudes in the IR bands.

To understand the structure and emission processes in blazars, variability time-scales, correlations between different energy fluxes, color variation etc (Marscher 2008; Marscher et al. 2010; Jorstad et al. 2010; Dai et al. 2015; Ciprini et al. 2007) are used as tools. Short-term variability shows faster and rapid fluctuations, which lead to spectral changes and maybe caused by different physical mechanisms (Ghisellini et al. 1997; Villata et al. 1998, 2002). Long-term variability in these sources are due to superposition of emissions from a number of components located randomly in the large scale jet.

As seen in several sources, the source brightness varies significantly over few months to years (Nesci et al. 2005; Dai et al. 2015; Kaur et al. 2017c). These long term changes are suggested to be associated with the helical motion of the jet, in which the blob of plasma travels in the ambient helical magnetic field, causing the enhanced flux whenever the blob comes in the line-of-sight. On the other hand, the rapid variations, which are now of main interest, are believed to arise due to the interaction of the blobs with the small scale particle over-densities or knots inside the relativistic jet. The detection of very rapid variations across the EMS (optical to TeV emission domain) have posed questions on the production mechanism and site of these variable emission, whether very close to base of the jet (as their timescales are at times faster than light crossing time of the gravitational radius of the black hole) or far away in the jet. Several models are proposed to answer these questions.

1.8 Models for the blazar variability

Understanding the variability of blazars has become an important part of AGN study as these are not resolvable by any of the present telescope facility. The variability proves to be one of the most viable tools to study the features and emission processes in blazars. However, the physical processes responsible for

the variability, particularly at intra-night time scale, are not understood well. There are some models addressing intrinsic (those due to the physical process in the source) and extrinsic (due to effects outside the source, including geometrical origins) variability. Some of them are discussed here. More details can be found in several reviews on variability ([Miller et al. 1989](#); [Wagner & Witzel 1995](#); [Boettcher 2010](#); [Marscher 2014](#)).

1.8.1 Intrinsic models for the variability

The nature of variability in blazars is significantly different as compared to other AGN, due to their mostly random nature, extreme extent and rapid features detected at all the frequencies. The strong Doppler boosting of the intrinsic variations in the jet makes them significant. The intrinsic variability is caused by changes in the particle acceleration, shocks, particle and magnetic field densities including reconnection events etc. We briefly discuss various models proposed to explain the observed variability in the flux.

Shock-in-jet model

Most of the observational features, till now, could be explained by the shock-in-jet model which is one of the most used models to study variability in blazars. [Blandford & Königl \(1979\)](#) proposed the idea that the knots seen in the VLBI images of the jet could be the shocks propagating down the jet. [Marscher & Gear \(1985\)](#) developed a model that could explain the variability in flux, polarization, and continuum emission. According to this model, the shocks moving in the jet at relativistic speeds align the magnetic field perpendicular to the jet flow. At the shock front, the highly energetic electrons are accelerated via Fermi shock acceleration. Just behind the shock front, where the particles get accelerated, these electrons lose their energy either via radiative processes or through adiabatic expansion. This results in strong frequency stratification, where highest energy emission comes from a thin layer behind the shock front and the lower energy emission from a larger volume (see [Figure 1.12](#)). The reason behind this is that the high energy electrons cool down faster than the lower energy electrons which

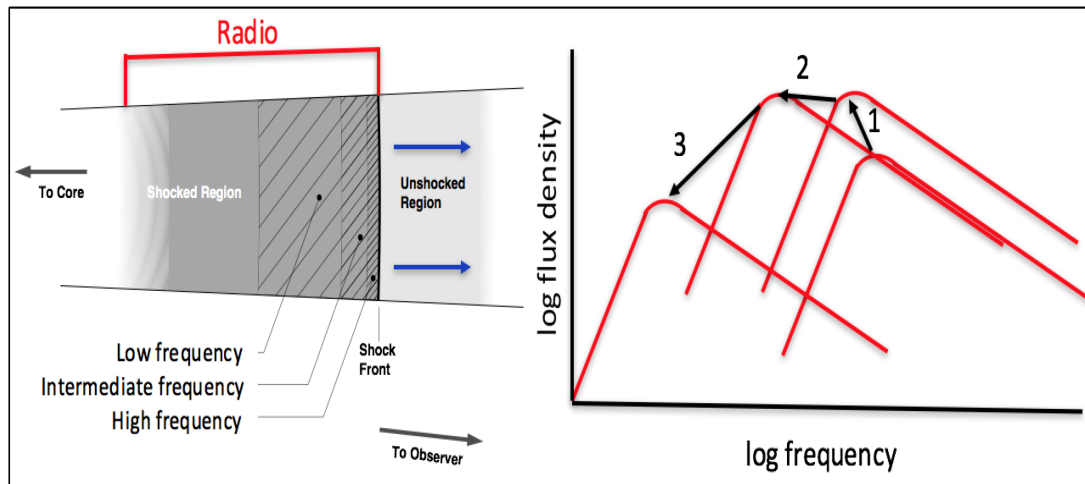


Figure 1.12: A schematic showing the acceleration of electrons at the shock front (left) and the evolution of the synchrotron spectra (right). Figure is taken from the article by [Marscher \(2016\)](#).

travel longer distance before they radiate at lower frequencies. The model, thus, is able to explain the lags between emissions at different frequencies, softer/harder spectra etc.

This model is the basic template model for all other advanced shock-in-jet models. For example, to explain the flickering and low amplitude flux variations [Marscher et al. \(1992\)](#), incorporated the idea of shocks propagating downstream the jet and giving rise to these variable features evolving over the time. Another later version of the model is the, Turbulent, Extreme Multi-zone Model or TEMZ, in short ([Marscher 2014](#)). For more details, please refer to the recent review article by [Marscher \(2016\)](#).

Disk model

It is known that the thermal radiation from the accretion disk, in the blazars, is either very feeble or gets washed away by the jet emission. But there are few cases in which the thermal radiation is observed. Recently, [Ghisellini et al. \(2014\)](#) conducted a comprehensive study on 200 blazars to study connection between the jet and disk radiation, if any. They studied the time-averaged spectra of all the sources and found a correlation between jet power and accretion disk luminosity.

This result directly gives a hint of their mass accretion rates. Another striking result is the higher jet luminosity than the disk luminosity that agrees with the Blandford-Znajek (BZ) process. In BZ-process (Blandford & Znajek 1977), the central black hole is rotating and most of the jet power is extracted via the trapped rotational energy in the central region via Blandford-Znajek process. This model has a direct implication on the historical evolution of the SMBHs. There are recent studies by various authors that explain these observations via numerical simulations through accretion onto a blackhole in presence of the strong BH magnetic fields. Also, any hotspot or irregularities in the accretion disk itself could introduce the periodic variations in the optical-UV flux (Mangalam & Wiita 1993; Rani et al. 2010). These are more easily detectable when the source is in low brightness phase.

1.8.2 Extrinsic Models

The extrinsic variations are seen due to the geometrical effects and are not originated from the source itself. We briefly list the possible models or effects that account for such extrinsic variations in the source.

Helical jet model

The helical jet model, proposed by Villata & Raiteri (1999), to explain the X-ray brightness state and hard X-ray spectra in Mrk 501. The model assumes the inhomogeneous curved jet trajectory without invoking any intrinsic variations. The emitting feature moves down the jet in helical motion which causes changes in the viewing angle and hence beaming factor. This introduces changes in the apparent flux detected by the observer. The model has been used to explain long term as well as short term variations (Zhang et al. 2012; Camenzind & Krokenberger 1992). It also supports the hypothesis of binary black hole (BBH) systems in the blazars. The orbital motion in the binary black hole system causes the variation in the jet orientation and hence the beaming factor. There are several observational evidences that support the periodic variations associated with the disk precession. For example, OJ 287: Sillanpaa et al. (1988); Pihajoki et al.

(2013); Valtonen et al. (2016), AO 0235+16: Ostorero et al. (2004), S5 0716+71: Nesci et al. (2005). The predicted variability timescales span over few months to years.

Microensing

The microlensing model detects the variability of the magnification factor (μ) ratio on the timescales of few days to hundreds of days. This ratio is inversely proportional to the smallest structures of the source. The overall flux variations are achromatic (energy-independent) in nature and should lead to symmetric profile. A recent study by (Vovk & Neronov 2016) puts constraints on the gamma-ray emitting region of the order of $10^{14} - 10^{15}$ cm, using Fermi-LAT data for gravitationally lensed blazar B0218+357, consistent with the time variability studies. The similar results are proposed for another blazar, PKS 1830-211 studied by Neronov (2015). It seems that the small size and location close to SMBH are the generic features of γ -ray emission from blazars.

Interstellar Scintillation (ISS)

Wagner & Witzel (1995) proposed that the interstellar scintillation mechanisms are due to the density inhomogeneities of electrons in the interstellar medium (ISM) which cause diffraction and refraction and are likely to lead to the variability at longer wavelengths. The variability due to ISS is strongly wavelength dependent (i.e., chromatic in nature) and does not affect the frequencies above the radio regime. The timescales involved from ISS effects are a few days. If the variations at shorter and longer wavelengths are correlated, ISS can not be the reason behind such variation.

Since the blazar lightcurves are very complex having unpredictable shapes and features, it is a difficult task to associate one or other mechanism as the cause of variation. Indeed there are certain signatures which help to rule out some mechanisms, e.g., asymmetrical flares with chromatic behaviour are generally produced by the intrinsic mechanism, such as shock propagating down the jet, periodic, symmetric and achromatic variability feature indicate to geometric and

extrinsic mechanisms to be responsible. There are several nice reviews which provide detailed information on variability (Wagner & Witzel 1995; Ulrich et al. 1997; Boettcher 2010; Marscher 2014) .

1.9 Motivation and objective of the present work

We now know that active galactic nuclei (AGN) are centers of galaxies which show strong activity. The AGN are very compact in size but emit huge amount of energy, which not only outshines the host galaxy, but in some cases emit more than hundred to thousand times a normal galaxy. The structure and emission processes leading to such enormous energy output from such compact regions posed great challenge to physicists and astrophysicists. A considerable amount of theoretical and observational efforts over decades led to most acceptable basic model as mentioned above. Here, the accretion of matter onto supermassive black hole through accretion disk is responsible for energy generation. A bipolar jet ejected perpendicular to the disk carries energetic flow to long distances. However, since the central engine is not resolvable, details about the energy mechanisms and their structure are not understood. Here, blazars, a subclass of AGN come to the rescue. The blazars are the radio-loud AGNs which form less than 10% of the entire AGN population. Their jets are pointed towards observer's line of sight and therefor the emission is highly boosted due to the relativistic effects (Blandford & Königl 1979; Urry & Padovani 1995). Their emission is jet-dominated and shows strong flux and spectral variability, high polarization ($>3\%$) and a flat continuum spectra (Biermann et al. 1981). The radiation processes of blazars are highly complex and non-thermal in nature, characterized by a power-law distribution of the accelerated particles in the jet. The blazars show dramatic variability over the whole electromagnetic spectrum (EMS; from radio, IR, optical, UV, X-rays and γ -rays) and at all the timescales, from years to months, and days to a few hours/minutes (Wagner & Witzel 1995). Their rapid flux variability is capable of resolving the small features near the central engine which is not possible even by present day VLBI imaging. Various time scales of variability have been detected

by several workers (Fan 2005; Fan et al. 2009; Wierzcholska & Siejkowski 2015; Nair et al. 2005).

The blazar variability has been used to understand their structure and emission processes. Several coordinated multiwavelength campaigns, using ground and space based observatories, have been carried out in the past to gain a deeper understanding of these issues (Raiteri et al. 1998; Pihajoki et al. 2013; Böttcher et al. 2005; Bach et al. 2007; Osterman Meyer et al. 2009; Marscher et al. 2010). There are several models proposed to explain variability and spectral energy distribution (Boettcher 2010; Marscher 2014). Broadly, the plasma is injected into the relativistic jet having strong magnetic field, which leads to acceleration of charged particles which, in turn, cool down emitting synchrotron radiation. The faster moving plasma interacts with slower moving or stationary features, distributed randomly in the parsec scale jet, creating shocks which are sites of efficient particle acceleration. These processes are able to accelerate particles to very high energies leading to emissions ranging from very high energy (TeV or higher) and down to radio (Marscher et al. 2010). The emission processes involved in the low and high energy emissions are briefly discussed in earlier section. However, how the jet is launched and how the particles are accelerated to attain very high energies, are not very clear.

After decades of the considerable efforts, our understanding about these sources has been improved considerably, but still many fundamental questions remain unanswered, i.e., how the matter is being accreted, how exactly the shocks are formed, the structure of the jet, its constituents (protons or electrons, or both), the sites of high-energy particles, origin of the seed photons to be upscattered to high energy is not known (Böttcher et al. 2005), why at times emissions at different energy domains are correlated while they are not at other epoch, what exactly causes orphan flares and several other related questions. The present work is an effort to improve upon our understanding of the blazar jet structure and emission processes, which lead to the huge energy emission across EMS.

We address these issues using the flux and spectral variability in a blazars as

tool. To achieve our objective, high temporal observations at various wavelengths, preferably simultaneous, are required to generate high quality multiwavelength light curves and SEDs. These two products are necessary to extract information on INV, STV, & LTV timescales and the spectral properties. The information thus gained is utilized in determining the sizes and locations of the emission regions in the jet with respect to the central engine and the magnetic field strength. The correlated variations between the fluxes at various energies and SED in association with existing models help us to infer the mechanisms responsible for variability and the physical processes involved in the emission. We also aimed at capturing our sources when they were flaring or in outburst phase because then they provide great opportunity to study correlated variations across the EMS – an important tool to get clues to the emission processes, spectral changes and spatial separation of various emitting regions which empower us to constrain AGN models.

To achieve the proposed objective, we required long term multifrequency data on selected blazar sources. We extensively used Mt Abu Infrared Observatory's 1.2m and 0.5m telescopes to obtain multi-band optical data along with several space and ground based observatories covering almost complete EMS (for example, γ -ray raw data from Fermi-LAT; X-ray/UV/optical data from Swift-XRT/UVOT and radio data from Owens Valley Radio Observatory; OVRO). The data analysis procedures for all the wavebands, including those for high energy X- & γ -ray, are non-trivial and require a considerable efforts and understanding.

1.10 Plan of the Thesis

The thesis has been organized in seven chapters. Chapter I (the present chapter) provides a brief introduction about the Active Galactic Nuclei–blazars in particular, the variability and its classification, and proposed theoretical framework for the emission processes. Since the multiwavelength results obtained from the present work are completely dependent upon the observational data from

ground-based and space-based observatories, and the data reduction & analysis techniques are non-trivial, we will discuss them in some detail in Chapter II. Chapter III will present the results on the intra-night and the decade long optical flux and spectral variability in the blazar 3C 66A. Chapter IV describes the optical flux and spectral properties of one of the most active and well studied IBL blazar, S5 0716+714, addressing IDV and STV. It also provides a comparative framework for 3C 66A emission processes at different timescales, as they belong to the same blazar class. Chapter V will present a comprehensive multiwavelength study on HBL 1ES 1959+650 during its outburst phases, a detailed study during the major outburst and the variability in its spectral energy distribution during the various flux-states. The blazars in their outbursts have always been interesting and provide a great opportunity to study their correlated variations across the EMS, flare strengths, changes in the spectral indices, the shape of the spectrum, sizes and the location of the high-energy emission regions and the magnetic field. Chapter VI will present the multiwavelength results of the recent unprecedented flaring activity in CTA 102 indicating strong correlation between γ -rays and other lower frequencies. The study provides insight into the location of high energy emission region from the central supermassive black hole, using the shortest variability timescales. In addition to the unprecedented flux values, the average levels reported in our study are the highest ever reported for CTA 102 in its history. And, finally Chapter VII will give a brief summary of thesis work with a future outlook of the AGN study.

Chapter 2

Observations, Data Reduction and Analysis

The night sky has always fascinated and awed the mankind with the mysterious cosmic objects (e.g., stars, planets, clusters, constellations, galaxies etc.) which were only seen through a narrow visible window (optical) of the electromagnetic spectrum (EMS). The curiosity to know more about these sources led mankind to explore this further and resulted in the invention of telescopes. The photons (*cosmic messengers*) coming from different sources revealed whether their origin is galactic or extra-galactic. With the advancement in telescope and detector technology, the understanding of these sources had improved further. The observations were mainly in optical, IR and radio windows of EMS as due to the non-transparency, higher energy (UV, X-rays, γ -rays) emissions were blocked by earth's atmosphere. The field further advanced to make it possible to access these observing windows, initially with balloon experiments followed by the space-based satellite missions. Presently, both ground- and space-based observatories are capable of collecting data for many cosmic sources and also helping in the new detections (e.g., variable transients, gamma-ray bursts, supernovae etc.).

The prolonged efforts in astronomy contributed hugely to our understanding of several classes of cosmic objects. However, there are few powerful sources at large distances, whose energetics is still poorly understood since their discovery in early 60s. These sources are called blazars which are a sub-class of the active

galaxies and the prime focus of our study. This work focuses on the detailed investigation and understanding of these enigmatic sources¹ in a temporal and spectral domain. This required acquiring the data in all the accessible windows of EMS with best possible temporal resolution as normally these sources are faint. We, therefore, used all the facilities, both at ground and space, at our disposal for carrying out observations. The collected data need to be reduced and analyzed which required sophisticated non-trivial techniques. For the interpretation of the scientific data several statistical techniques are essential. The present chapter provides the overview about the observing facilities and instruments used, observation strategy, the data reduction techniques and various statistical techniques used.

2.1 An Overview of Telescope Facilities Used

The data are collected in all the energy bands using various national and international telescope facilities. For the optical observations, Mount Abu InfraRed Observatory (MIRO) facilities were extensively used. The archival data are obtained from Fermi-LAT (γ -rays), Swift-XRT/UVOT (X-rays, UV, optical), OVRO (radio) and Steward Observatory (optical) and are reduced. These telescope facilities and instruments used are briefly described in the following.

2.1.1 Mount Abu InfraRed Observatory (MIRO)

Mount Abu InfraRed Observatory is operated by Astronomy & Astrophysics division of Physical Research Laboratory, a unit of Government of India, India. It is situated at 1680 m above the sea level, near the highest mountain peak of Aravali range, Gurushikhar, in Mount Abu, Rajasthan, India (see Figure 2.1). Its geographical location is $24^{\circ}39'17.34''N$ and $72^{\circ}46'45.18''E$, which represents its latitude and longitude, respectively. The location is ideal to carry out optical and infrared observations, because of very low water vapor content (1-2 mm during winters) that makes the site dry. For the astronomical observations,

¹For more details, please refer to Chapter 1

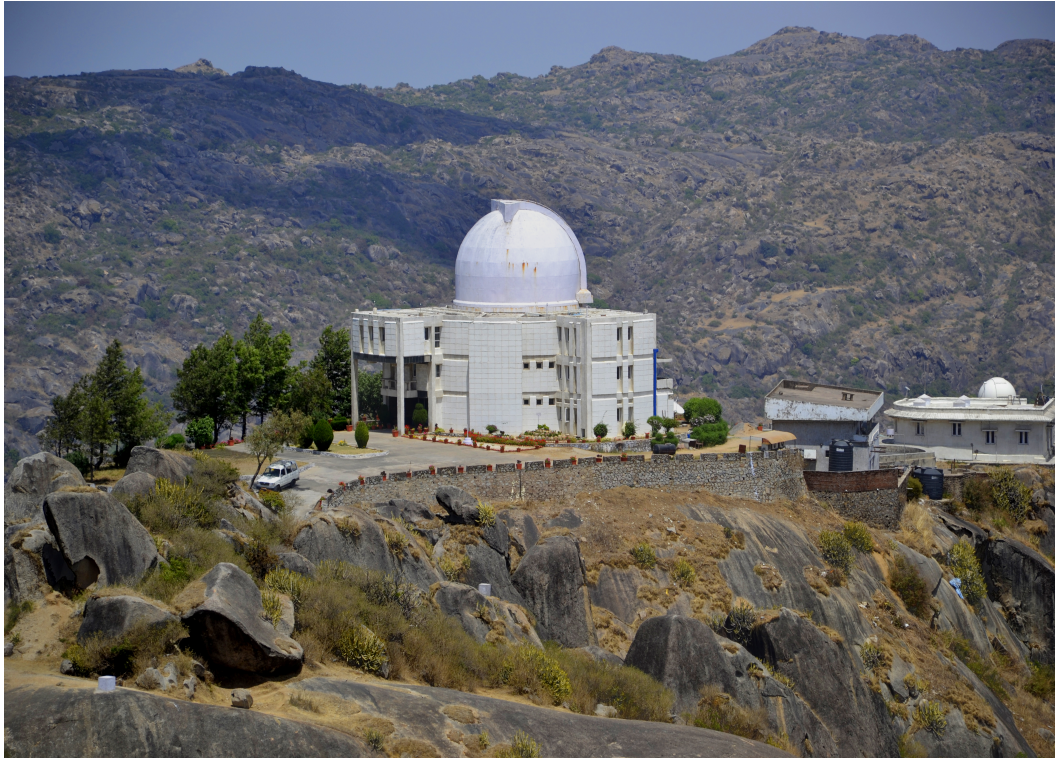


Figure 2.1: Mount Abu InfraRed Observatory (MIRO) is situated at 1680 m above the sea level, on the highest peak of Aravali mountain range in Mount Abu, Rajasthan, India.

nearly 180 photometric nights are available during the full observing cycle, from mid-September to May (extended upto June), with a typical seeing of 1.2 arcsecond. The observatory is operational since December 1994 and contributed largely in carrying out the astronomical observations that resulted in over 150 peer-reviewed research articles. It is also involved in several observing campaigns, in national or international collaborations, and several other science programs are conducted using this facility.

The observatory has two moderate sized telescopes- 1.2m and 0.5m, which are operational since 1994 and 2009, respectively. Both telescopes are equatorial mount systems. The larger telescope has a parabolic mirror with aperture size of 1.21 m and focal ratio, $f/3$. The secondary mirror is hyperbolic with the size of about 0.3 m. The combination of two surface design, i.e., primary parabolic and secondary hyperbolic arrangement (Ritchey-Chretien telescope configuration or RCT), helps to reduce the third order coma and spherical aberrations and

provides wide field of view with final effective focal ratio of $f/13$. The plate scale of 1.2 m telescope is $13.2''/\text{mm}$ at the Cassegrain focus and is calculated by using the relation, $206265/f$ (in mm) arcseconds. The 0.51 m telescope is used for monitoring AGN (specifically, blazars), comets or transient studies. Being equatorial mounted, this telescope has a Cassegrain unit, with primary and secondary mirror arrangement. This is a CDK20 system with $f/6.8$ corrected Dall-Kirkham Astrograph Telescope, provided by PlaneWave Instruments. The primary mirror is prolate ellipsoidal mirror whereas, the geometry of the secondary mirror is a spherical. Along the light path, inside the baffle tube, there is a group of lenses that makes the structure free of astigmatism and also corrects the sky image from various aberration effects, like off-axis coma, field curvature effect etc. This minimizes the optical aberrations to carry out the astronomical observations.

Backend Instruments

The 1.2 m telescope has several backend instruments regularly used for the observations and are listed below:

- Liquid Nitrogen (LN_2) cooled optical CCD camera
- ANDOR CCD optical camera
- Near Infrared Camera and Spectrograph (NICS)
- Optical imaging and polarimeter
- PRL Advanced Radial-velocity All sky Search (PARAS).

Here, we describe the specifications of two optical CCD cameras (or, detectors) used to conduct the astronomical observations, which are presented in this work.

1. Optical CCD camera (LN_2 cooled):

This detector (dewar and controller) is made by M/s Pixcellent (formely Astrocams of Cambridge, UK). The dimension of the optical CCD Camera is 1296×1152 pixels (nearly, $1K \times 1K$) and each pixel size is 22 microns.

The optical camera is installed at the focal point of 1.2 m Cassegrain telescope with f/13 focal ratio. With 0.29 arcsec per pixel, the total field of view (FOV) is about $6.5' \times 5.5'$. The CCD-photometric system is equipped with the Johnson-Cousin UBVRI (Johnson & Morgan 1951; Bessell 2005) filter set, in a filter wheel just above the detector plane (outside the dewar). The control of the filter wheel is integrated into the pixcellent camera control software. This software also interfaces with the 1.2 m telescope control system to get instantaneous telescope parameters at the time of observations. This allows us to include all observational parameters (filter, pointing, timing etc.) into appropriate keywords in the FITS format headers of individual images. Liquid nitrogen cooling is used to actively control the detector temperature to about -100°C , resulting in negligible dark current in the system.

2. ANDOR CCD:

The observations during October 2014 were made with thermo-electrically cooled iKon ANDOR CCD camera having 2048×2048 pixels ($2\text{K} \times 2\text{K}$). The ANDOR camera has four stage thermo-electric cooling and reaches -70°C . The software allows for on chip binning in various modes as well as several readout rates. It also has capability to take sequence of images at regular intervals. This camera is also equipped with a large number of filters in a 12 position filter wheel. However, the filter wheel information as well as the telescope parameters need to be tabulated separately for further use during analysis of the observations. This camera and filter wheel can also be controlled using linux based software from the RTS2 (Remote Telescope System 2). In that case, various parameters are added to the header in relevant keywords automatically.

2.1.2 Swift

Swift is a multi-wavelength observatory, a part of NASA's MIDEX (medium explorer) program. It was developed under the principal investigation of Neil

Gehrels, with an international team from United States, the United Kingdom, and Italy, with additional involvement by other countries, i.e., France, Japan, Germany, Denmark, Spain, and South Africa. The mission was launched on November 20, 2004 and primarily designed for the detection of gamma-ray burst (GRB) and to study their afterglows ([Burrows et al. 2005](#)).

The satellite is comprised of three main instruments on: BAT (Burst Alert Telescope; 15-150 keV), XRT (X-Ray Telescope; 0.3-10 keV), and UVOT (ultra-violet and optical telescope), which work in a co-ordinated manner to rapidly identify and conduct the multi-wavelength follow up observations of GRBs. The field of view (FOV) of XRT and UVOT are co-aligned and falls within the wide FOV of BAT instrument, as shown in the [Figure 2.2](#). The XRT and UVOT are focusing telescopes which produce sub-arcsecond positions in the sky, whereas BAT has wide FOV with coded-aperture gamma ray imager that can produce sub-arcmin positions for GRBs.

The motivation to launch Swift was to detect and study the GRBs and their afterglows, in detail. But, the satellite became very important in blazar science program because of its ability to simultaneously monitor them in optical, UV and X-rays. The observational results thus obtained help us to study the connection between low-energy and high-energy component in their SEDs, which represents the turn-over region. This information could shed light on their physical processes responsible for the emission in its various flux states. Therefore, Swift is one unique multiwavelength observatory of its kind, still operational and monitors hundreds of blazars. In the present study, we have used data from XRT and UVOT instruments to study a few blazars. Here, we brief the specifications of these two instruments, given in the [Table 2.1](#).

2.1.3 Fermi Observatory

The high energy gamma-ray emission from AGN, GRBs, black hole binaries etc. plays a major role in their understanding of energy mechanisms. The importance of high energy gamma-ray emission was established by the role played by the Compton Gamma-ray Observatory which had EGRET ([Hughes et al.](#)

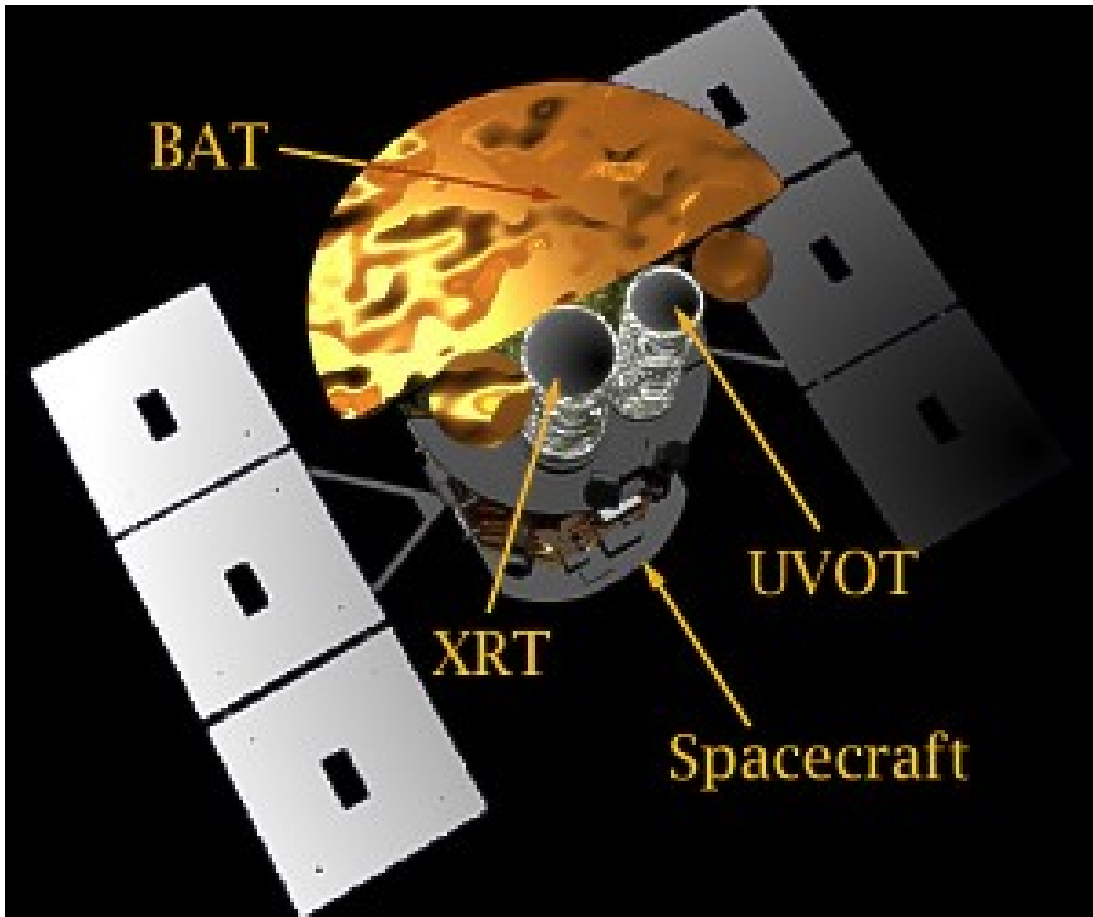


Figure 2.2: A schematic of Swift satellite, a multiwavelength observatory, showing three instruments onboard- BAT, XRT and UVOT. Credits: <http://www.swift.psu.edu>

Table 2.1: The technical description of X-Ray and UV-Optical telescopes onboard Swift satellite.

Parameter	XRT	UVOT
Telescope	JET-X Wolter I	Modified Ritchey-Chretien
Range	0.3-10keV	170-650 nm (7.2eV to 1.8eV)
FOV	23.6 x 23.6 arcmin	17 x 17 arcmin
Pixel Scale	2.36 arcsec/pixel	0.5 arcsec/pixel
PSF	18 arcsec at 1.5 keV	2.5 arcsec at 350 nm
Sensitivity	$4 \times 10^{-14} \text{erg cm}^{-2} \text{s}^{-1}$ in 10^4 sec	B-mag=22 in 1000 sec
Detector	EEV CCD-22, 600×600 pixels	CCD, 2048×2048 pixels
Mode of operation	Imaging, Photon Counting, and Timing	Photon Counting

1980), Energetic Gamma-Ray Experiment Telescope, detecting a large number of sources emitting gamma-rays, particularly AGN. With Fermi operational since 2008, thousands of sources have been monitored for gamma-ray emission to extract wealth of information, majority of which are blazars.

Fermi, formally known as Gamma-ray Large Area Telescope, or GLAST (Atwood et al. 2009), is a space based observatory that conducts gamma-ray observations of the cosmic sources. It was launched on 11 June 2008 (UTC 16:05). It is an international project of NASA in collaboration with U.S. Department of Energy, and the government agencies in France, Japan, Germany, Sweden, Italy. The main aim of this mission is to study gamma-ray Universe by performing observations on the diverse high-energy gamma-ray sources that would help in understanding the astrophysical and the cosmological phenomena of the enigmatic Universe. The diverse source list includes the massive accelerators of the Universe i.e., Active Galactic Nuclei, pulsars, gamma-ray bursts, solar flares and dark matter. Fermi satellite has two main instruments on board. The principal scientific instrument is Large Area Telescope (LAT) and another one is Gamma-

ray Burst Monitor (GBM).

Large Area Telescope (LAT)

LAT is an imaging high-energy gamma-ray telescope which provides unprecedented sensitivity to gamma-rays, detects photons of energy from about 20 MeV to more than 300 GeV. Such gamma rays are emitted only in the most extreme conditions, by particles moving nearly at the speed of light. The LAT's field of view covers about 20% of the sky at any time, and it scans continuously, covering the whole sky every three hours. This instrument may be thought of as a sequel to the Energetic Gamma Ray Experiment Telescope (EGRET) instrument onboard Compton Gamma-Ray Observatory (CGRO) albeit with much better sensitivity. Several operations for the scientific observations carried out by LAT are listed below. Data obtained with the LAT are intended;

1. To permit rapid notification of high-energy gamma-ray bursts (GRBs) and transients and facilitate monitoring of variable sources.
2. To create an extensive catalog of several thousand high-energy sources obtained from all-sky survey.
3. To measure spectra from 20 MeV to more than 50 GeV for several hundred sources.
4. To localize point sources to within 0.3 - 2 arc minutes.
5. To map and obtain spectra of extended sources such as SNRs, molecular clouds, and nearby galaxies.
6. To measure the diffuse isotropic gamma-ray background up to TeV energies.
7. To understand particle acceleration processes in Active Galactic Nuclei, pulsars and supernova Remnants (SNRs).
8. To explore the discovery space for dark matter ([Atwood et al. 2009](#)).

Mode of satellite operation

The Fermi spacecraft orbits the earth in about 96 minutes. It is oriented to point the LAT upward at all time, so the earth does not block the view. On

alternate orbits Fermi moves to the left and right, allowing the LAT to cover more of the sky. Thus the whole sky can be surveyed in two orbits. This mode of operation allows for constant monitoring of any gamma-ray emitter over days, weeks, months and years. Fermi point itself at the location of the burst for a few hours to collect extra data, when a strong gamma-ray burst occurs.

Technical description of LAT instrument

This section provides a brief description of LAT instrument. The LAT works on the similar principles as any terrestrial high energy particle detectors, to detect high energy particles. The gamma-rays cannot be refracted or focused using mirrors and lenses and it requires the four sub-systems to detect the incoming high energy particles (see Figure 2.3). The LAT is 0.72 m deep and 1.8 m square with a total mass is 2789 kg. It uses 650 W of electric power. The whole instrument is comprised of

1. Anticoincidence detector
2. Tracker/Convertor
3. Calorimeter, and
4. Data Acquisition system.

Working of LAT

Incoming gamma rays pass through the thin plastic anti-coincidence detector, on the top of the module, and the charged cosmic rays cause a flash of light that allows LAT to identify the gamma rays. A gamma ray continues until it interacts with an atom in one of the thin tungsten foils, producing two charged particles: an electron and a positron. They proceed on, creating ions in thin silicon strip detectors. The silicon strips alternate in the perpendicular directions, allowing the progress of the particles to be tracked. Finally the particles are stopped by a cesium iodide calorimeter which measures the total energy deposited. A sophisticated, flexible data acquisition system combines information from all the components to decide when a likely gamma-ray has been detected and to

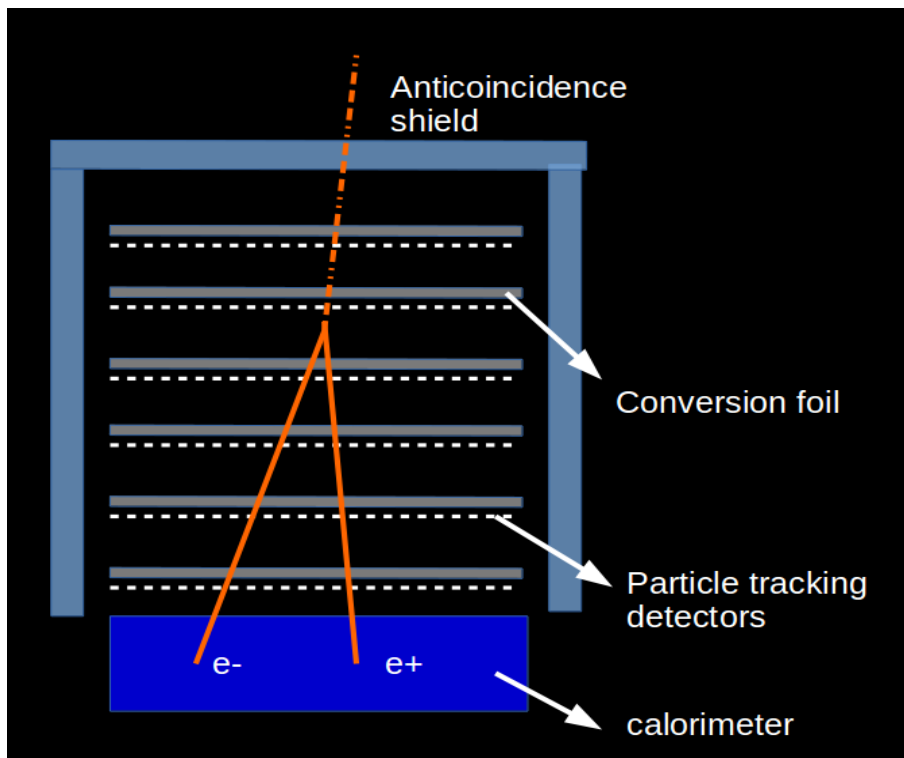


Figure 2.3: A schematic explaining the γ -ray detection in the Large Area Telescope (LAT) instrument, on board Fermi satellite. Concept Credit: <https://www-glast.stanford.edu/instrument.html>

choose what information to send to the ground. The high energy gamma-ray data acquired from the satellite is used to probe the non-thermal Universe.

2.1.4 Archival data

The detection of several gamma-ray blazars from Fermi motivated various ground-based observatories (in optical, IR, radio) to regularly monitor blazars. To study the temporal evolution and variability in these sources, every epoch information is valuable to know about the status or behavior of the source over long-term or short-term. Therefore, to keep an eye on several promising candidates, there are few observatories which regularly monitor such sources and make the data public for the use to the blazar community. In the present study, we used the optical and radio archival data, whenever needed, from two such observatories— Steward Observatory and Owens Valley Radio Observatory, respectively. We give a brief description of these facilities below.

Owens Valley Radio Observatory

The Owens Valley Radio Observatory is a radio observatory founded in late 1940s in Owens Valley, California, US (Figure 2.4). This site is situated at 1222 m above the sea level and operated by California Institute of Technology (Caltech).

Radio Telescope- 40 meter: After the launch of Fermi in 2008, it was discovered that most of the gamma-ray sky is dominated by blazars. OVRO–40m supported this mission and is regularly monitoring nearly 1800 blazars twice per week. The sources are monitored in radio energy regime at 15GHz frequency, using OVRO 40 meter radio telescope. The telescope is used either as a single dish antenna for conducting interferometric observations with VLBI (Very Long Baseline Interferometry) program. We have collected and used the data from OVRO 40m telescope in order to conduct the multiwavelength studies on two important blazars of our interest.



Figure 2.4: The Owens Valley Radio Telescope, 40 meter dish antenna, located near Big Pine, California, US. It is dedicated for blazar monitoring at 15 GHz.

Steward Observatory

The Kuiper telescope, operated by Steward Observatory, is located at Mount Bigelow in the Santa Catalina Mountains, near Tucson, Arizona at an altitude of 2510 meter above sea level. It is a 1.54 meter Cassegrain telescope with two secondary reflectors, one with $f/13.5$ secondary focal ratio (10 arcsec/mm) and other with $f/45$ having plate scale of 3 arcsec/mm. The optical observations are performed using $2K \times 2K$ CCD camera. We have used the optical archival data, if available, for the sources of interest.

2.2 Data Reduction and Analysis

The astronomical data and their reduction procedure are crucial steps albeit, time consuming and non-trivial tasks and requires informed decisions, based on a good understanding of the instrumentation. Before getting into the details of the data reduction procedure, it is vital to know about the format of the astronomical data.

Most of the astronomical data, if not all, is stored in the most conventional format, called FITS format. It stands for the Flexible Image Transport System (with extension, .FITS, .FIT, or .FITS) and is a standard digital file format designed specifically for the scientific purpose in astronomy. This format was standardized in 1981 and is useful for archiving, transmission, and processing the astronomical data. The major advantage of this format is its user readable headers written in ASCII code and the ability to store non-image data, for example, spectra, data cubes, photon lists and even multi-dimensional database. The details of each parameter of the observations are stored in its header. FITS supports tabular format and is used by several programming languages like, C, C++, IDL, Fortran, R, Tcl, Python, MATLAB, Mathematica etc.

2.2.1 Optical Data

The observations from MIRO are presented in this study and the data are reduced using standard routines in IRAF² software. The details about the observations, the strategy adopted and the data reduction steps are briefly mentioned in the next sections.

Observations and Techniques

An extensive amount of observations are carried out to obtain optical data in several bands from MIRO. Here, we will describe the strategy adopted to carry out the optical observations in order to get a consistent data coverage on a set of blazars addressing the long-term, short-term and intra-night variability timescales. The general observation strategy, we adopted, was to take about a few frames (four or five) in B, V, R and I bands and monitor the source in the R-band for a few hours (at least two to four hours) depending upon its availability in the sky. This way, we get a longer coverage throughout the observing night. Since this strategy has been adopted for long term studies. we could obtain long

²IRAF is distributed by the National Optical Astronomy Observatories, which are operated by the Association of Universities for Research in Astronomy, Inc., under cooperative agreement with the National Science Foundation.

term data series on a number of blazars. Before taking the observations of the source of our interest, it is necessary to obtain several auxiliary frames along with the source frame. We briefly describe the types of CCD frames needed that help in the data reduction procedure, later on. These frames are needed to calibrate the science CCD images that help in removing the instrumental signatures from the detector or the instrument itself.

1. **Bias frames:** Bias frames are basically zero exposure acquisitions, in which the CCD shutter is left closed and the detector is readout. Each detector response is temperature dependent and there is always certain off-set or variation in each pixel of the CCD detector. To take into account the pixel-to-pixel offset, we use bias frames which are then subtracted from all other frames. With advanced cooling systems in CCDs, the dark current is almost negligible, so we can avoid taking dark frames. Several bias images are taken during each observing night to gather detector offset and during the data reduction all bias frames of each night are median combined to form a master bias frame. The master bias is then subtracted from each image of that particular observing night.
2. **Flat frames:** Flat frames are taken with enough signal, but well below the saturation limit of the detector. The telescope optics when pointed at a uniform source of light, often, do not distribute the incoming light uniformly on the detector chip and introduce the light variation in the CCD image. To take care of these non-uniformities, for example, vignetting, shadow effect, light specks due to dust deposition on the optical component and variations in the individual pixel response, flat images are taken. There are two ways to acquire the flat frames— by taking twilight sky images and with the uniform illumination of the dome. We preferred to take twilight sky flat frames throughout our observations. It is to be noted that during each observing night and for each filter, several flat frames are taken (after bias subtraction) which are median combined to form a master flat frame. The final ‘master’ flat frame for a given filter is created by median combining all the bias subtracted individual flats and then dividing the resultant by

the mode value of the frame. This results in the ‘normalized’ master flat frame with values ranging from 0 to 1. This master flat frame is then used for correcting all other object images (so called ‘science’ images). The correction is done by dividing the object images by the master flat frame.

3. **Science frames:** Science frames contains the actual data of our interest, blazars in this case. These images contain instrumental signatures, such as, vignetting, shadow effect, etc. These imperfections are taken care of by the flat fielding procedures as discussed above. Depending upon the optimum signal to noise ratio, we set the exposure time for the science images on each observing night. In case of blazars, we retain some comparison stars in their field in same image. This way, we need not capture the calibration stars separately. In addition, the procedure helps to carry out differential photometry, reducing the effects of changes the atmospheric seeing.

Photometry using IRAF

Photometry is a technique used in astronomy to measure the flux or brightness of the astronomical object. We used this technique in our study to extract the flux of the source of interest and comparison stars using standard routines in IRAF, which are briefly discussed here.

1. The quality check is performed on all images (bias, flats, science images).
2. All bias frames are (median) combined to generate a master bias frame which is subtracted from flats and source images. The procedure is called bias correction.
3. All bias corrected flat frames are combined to generate a master flat for each filter.
4. The bias corrected science frames are divided by the normalized master flat to get the final reduced science images.
5. All the science frames are now corrected for all the instrumental effects, as mentioned in above sections.

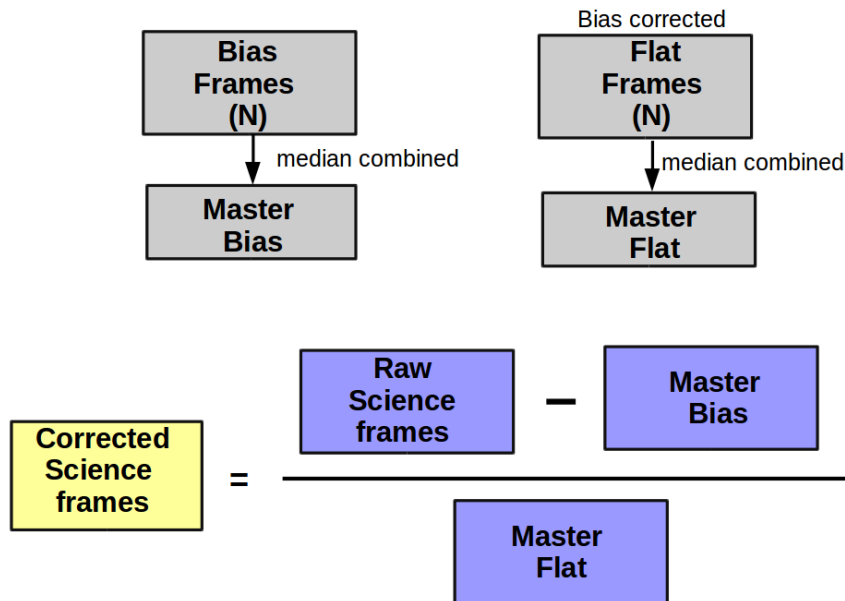


Figure 2.5: Flowchart showing procedure to correct the raw science images using bias and flat frames.

6. Now, the aperture photometry is performed, using DAOPHOT package in IRAF, on the blazar and its comparison stars in the field. We did photometry with several aperture sizes, varying between 1 to 5 times the full-width half maxima (FWHM).
7. The instrumental magnitudes for the source and its comparison stars are calculated to be used for the analysis.

Above procedure is shown in the Figure 2.5.

After obtaining the instrumental magnitudes at different apertures, we needed to choose the optimum value aperture size to be used throughout the analysis. For this, we plotted source instrumental magnitude as a function of the aperture. We found that the aperture with three times the FWHM led to the optimum value of signal-to-noise ratio, following the prescription by Cellone et al. (2000a).

Differential Photometry:

Calibration of the source magnitude is done by differential photometry with respect to the comparison stars in the same field, which reduces the effect of changes in the atmospheric conditions. In order to obtain a reliable photometric sequence for the source, we selected a set of non-variable field stars with brightness closer

to that of the object, as pointed out by [Howell et al. \(1988a\)](#). For each CCD frame, the instrumental magnitudes of the source and its comparison stars were extracted. We used one of the comparison stars closest in brightness to the source, as a comparison star and the rest of the available ones as control stars to check the stability of the sky ([Howell & Jacoby 1986](#)). This way, we obtain the differential magnitudes of the source and comparison/control stars used to perform variability check on the source. In the coming sections, we will describe the procedure to detect the variability in the blazar light curves.

2.2.2 X-rays and UV

The analysis of the X-ray and UV data from Swift is performed using High Energy Analysis Software (HEASOFT) package. The *xrtpipeline* tool provided freely as a part of *heasoft* package, with default parameters are used to extract the cleaned events files. The source discussed in this thesis were bright enough to be observed in WT (window timing) mode. The typical full frame count rates for WT mode observations are always less than 25 c/s which will be pile-up free as recommended by the instrument team at University of Leicester, UK ³ (pile-up occurs at a count rate ≥ 100). Following this, the pile up corrections are not performed in this mode data. For this case, a circular area of 27 pixels (equivalently $\sim 63''$) centred at the position of the source is used as the source region. The background region was extracted as a concentric annulus with inner and outer radii of 80 pixels and 120 pixels, keeping the average half width of annular region at 100 pixel (recommended for a proper background subtraction in WT mode). The photon counting (PC) mode observations are corrected for pile up using the prescriptions suggested by aforementioned team ⁴. The innermost circular area with radius 10 arcsec is excluded (chosen for highly piled up observations) from the source region of 70 arcsec circle around the source. The background, in this case, is taken as an annular region around the source, with inner and outer radii of 150 arcsec and 350 arcsec, respectively. The clean events files are then used to extract the

³<http://www.swift.ac.uk/analysis/xrt/xselect.php>

⁴<http://www.swift.ac.uk/analysis/xrt/pileup.php>

products (spectrum & light-curves) for the source and background regions using the *xselect* tool.

The spectra thus obtained are then fitted with an absorbed log-parabola model with nH value fixed to the galactic value ($1.07 \times 10^{21} \text{ cm}^{-2}$) using *xspec* (version 12.9.0), a standard tool for X-ray spectral fitting provided as a part of *heasoft* package. Using the BACKSCAL keyword in WT mode, source and background spectrum files were edited to the proper values, before importing to the fitting tool, to avoid the wrong background subtraction during the fit. Depending upon the source behavior, either log-parabola or power-law models can be used for the fitting.

The background subtracted count rates extracted for the energy band 0.3-10.0 keV are used to generate the light-curves. The unabsorbed fluxes in 0.3-10.0 keV band are also estimated by adding component “cflux” and fitting after freezing the normalization. The fluxes thus obtained are also used for timing analysis.

The snapshots observations in the filters V (5468 Å), B (4392 Å), U (3465 Å), UVW1 (2600 Å), UVM2 (2246 Å), and UVW2 (1928 Å), for all the OBsIDs, were integrated with the *wotimsum* task and analyzed using the *wotsource* task, with a source region of 5 arcsec, while the background was extracted from an annular region centred on the source with external and internal radii of 40 arcsec and 7 arcsec, respectively. The observed magnitudes from all OBsID are then corrected for extinction according to the model described in [Cardelli et al. \(1989\)](#). A tool, developed in-house, using R-platform⁵, is used to perform the required reddening corrections. The corrected fluxes are then used for the timing analysis to study variability in blazars.

2.2.3 Gamma-rays

We discuss the data reduction procedure of gamma-ray data and mention the procedures briefly how to install required packages along with data reduction and analysis steps.

1. Software requirements: To analyze the Fermi-LAT data, we need the Hea-

⁵<https://www.r-project.org/>

soft package that can be downloaded from HEASARC website and should be installed. After that, one needs to download and install the Fermi Science Tools (FST) from Fermi Science Support Center (FSSC) with the current software version v9r33p0, released Jun 03, 2014. It is highly recommended to use the binary tar distributions of the software which is available for various UNIX systems. The Fermi data products are created daily by the LISOC (the LAT Instrument and Science Operation Center) and sent to the FSSC. In case of any problem in the software installation and setup, a query can be raised with FSSC helpdesk.

2. Download data: After the software installation and setup is done, download the data– to be analyzed, from the LAT data server. This page displays– LAT Photon, Event, and Spacecraft Data Query, under which you have to fill in the details of the source coordinates/name, select coordinate system (J2000 in our case), search radius (by default, 15 degrees), observation dates, Time system, Energy Range, Lat data type (photon, for point like sources) and check the spacecraft data. After that click on Start Search, it will show another page, displaying, Query *<query ID string>* submitted. One has to click on the link provided on the page. The next page will show the photon file (PH) and spacecraft file (SC) details (no. of entries, size), which will be available to download. The file format is FITS, which is open digital standard file system used in astronomy. Download both the files and place them in a separate directory.

3. Download diffuse models and 3FGL catalogue: To process the data files obtained, as described in step 2, we need to download the latest Fermi catalogue, galactic diffuse and isotropic emission models (*gll_iem.v06.fits* and *iso_P8R2_SOURCE_v6.v06.txt*) from the FSSC website.

4. Data Preparation: The detection, flux determination and spectral modeling of the Fermi-LAT sources is accomplished by a maximum likelihood optimization technique. Unbinned likelihood analysis is the preferred method for time series analysis of the LAT data, where the number of events in each time bin

is expected to be small. Data preparation consists of two major steps, `gtselect` and `gtmktime`.

- **gtselect:** This tool is used to make cuts based on columns in the event data file (photon file) such as time, energy, position, zenith angle, instrument coordinates, event class, and event type. The event class is chosen based on the nature of the sources, whether extended or point source etc. We have selected the event class=128, based on the source class in Pass 8 data, (i.e., *P8R2_SOURCE*) as most of our objects studied here are point sources. This is most favored selection, as suggested by the Fermi-LAT team, with good sensitivity for the analysis of moderately extended and point sources on medium to long timescales.
- **gtmktime:** In addition to cutting the selected events, `gtmktime` makes cuts based on the spacecraft file and updates the GTI (Good Time interval) extension.
- **gtbin:** The count maps are generated from the event files to pick up the obvious sources.
- **Generating XML file:** The source model XML file contains the various sources and their model parameters to be fit using the `gtlike` tool. The `gtlike` tool reads the source model from an XML file. The model file contains your best guess at the locations and spectral forms for the sources in your data. A source model can be created using the model editor tool, by using the user contributed tool `make3FGLxml.py`, or by editing the file directly within a text editor.
- **Generating diffuse model response:** Each event must have a separate response precomputed for each diffuse component in the source model. This is computed using command `gtdiffrsp`.
- **Generating Exposure map:** Then, the exposure map is generated which is needed in order to analyze diffuse sources, and to derive the absolute fluxes.

- **Likelihood fitting:** Using the command *gtlike*, the model is fitted to the data and the various parameters are extracted like, flux, errors, spectral indices, and other required information.

For the detailed discussion and help on the Fermi-LAT data analysis, please refer to the standard analysis documentation provided on the FSSC website ⁶.

2.3 Statistical techniques

2.3.1 C-test

The intrinsic variability in the blazar light curves is quantified by using various statistical techniques. One of the classic method used extensively is to check the confidence of variability present in the data-set. This method was first proposed by [Jang & Miller \(1997\)](#) and later generalized by [Romero et al. \(1999\)](#). In the differential light curves of a blazar, the source-control (BC) and comparison-control stars (CC) are plotted, the latter representing the confidence comparison curve. Following this idea, it is assumed that CC light curve are affected only by the instrumental variations because of the selection of non-variable comparison stars. Since source and all the stars used in constructing differential lightcurves are in the same field, the process minimizes the effect of seeing variation. The standard deviation of comparison-control curves are considered as the measurements of the observational errors ([Jang & Miller 1997](#)). This way the scatter (σ), being larger than the obtained photometric errors, provides more accuracy in the determination of the actual errors present in the variability light curve. This conventional method is known as confidence parameter test (or, C-test), represented as follows.

$$C = \frac{\sigma_{(B-C)}}{\sigma_{(C1-C)}}$$

where, $\sigma_{(B-C)}$ and $\sigma_{(C1-C)}$ are scatters in differential magnitude of source and comparison stars([Jang & Miller 1997](#)). The criterion adopted for the variability in the source should be $C \geq 2.57$, with more than 3σ confidence (99% confidence).

⁶<https://fermi.gsfc.nasa.gov/ssc/data/analysis/documentation/>

This way, the intrinsic variability in the source is ensured by using the differential light curve of the source.

2.3.2 F-test

F-test, also known as Fisher-Snedecor distribution test after Ronald Fisher and George W. Snedecor, is a statistical test which measures the sample variances of two quantities i.e, variance of calibrated source magnitude (defines variability between the data values) and between differential magnitude of comparison stars (variability within a data). To test the significance of variability during each night, F-test was employed on data using R statistical package.

$$F = \frac{\sigma^2_B}{\sigma^2_{CC}} \quad (2.1)$$

where σ^2_B , σ^2_{CC} are the variances in the blazar magnitudes and differential magnitudes of the standard stars for nightly observations, respectively. An F-value of ≥ 3 implies variability with significance of more than 90% while an F-value of ≥ 5 corresponds to 99% significance level.

2.3.3 Amplitude of Variability

To determine the extent of intra-night variability of the source in the differential light curve, we calculated amplitude of variation using the definition given by [Heidt & Wagner \(1996\)](#),

$$A_{var} = \sqrt{(A_{max} - A_{min})^2 - 2\sigma^2} \quad (2.2)$$

where, A_{max} and A_{min} are source's maximum and minimum amplitude of intra-night calibrated differential light curve and σ is the standard deviation in the measurement and is given by

$$\sigma = \sqrt{\frac{\sum(m_i - \bar{m})}{N - 1}}$$

where, N is the total number of observational points in each band on a particular

night, m_i is differential magnitude of comparison stars on epoch i and \bar{m} is average of differential magnitudes of entire data set.

Taking these statistical parameters into consideration and to report the observational nights show intrinsic variability, the observational data set need to fulfill the following criterion i.e., $C > 2.57$; F-test value > 3 (90% confidence level); $F > 5$ (99% confidence level) and $A_{var} > 5\%$.

2.3.4 Fractional Variability

The variability amplitudes for all the energies are determined using the fractional root mean square (rms) variability parameter, introduced by [Edelson & Malkan \(1987\)](#); [Edelson et al. \(1990\)](#). Basically, the excess variance was used to compare the variability amplitudes at different energy bands from the same observation ([Vaughan et al. 2003](#)). This methodology, however, has a limitation that it works only for the densely sampled data, having small flux uncertainties, taken from different instruments with different but small sensitivities. The large data gaps or high uncertainties in flux measurements can also introduce larger values of rms variability amplitude. The availability of a good quality data across EMS allows one to infer the variability in the source. The fractional variability and the associated errors were calculated using the relation ([Vaughan et al. 2003](#)),

$$F_{var} = \sqrt{\frac{(S^2 - \sigma^2)^2}{r^2}} \quad (2.3)$$

$$\sigma F_{var} = \sqrt{\left(\sqrt{\frac{1}{2N}} \frac{\sigma^2}{r^2 F_{var}}\right)^2 + \left(\sqrt{\frac{\sigma^2}{N}} \frac{1}{r}\right)^2} \quad (2.4)$$

where, S^2 is the sample variance, σ^2 is the mean square value of uncertainties associated with each observation, and r is the sample mean.

2.3.5 Duty cycle of variation (DCV)

We know that blazars are variable at diverse time scales. But whether a source is variable at intra-night timescales, and if so, how often, can be determined

by observing the source on a number of nights and check on how many nights intranight variability (INV) is detected. Duty cycle of variation (DCV) parameter sheds light on the probability of its INV. For calculating DCV, we obtained the ratio of INV nights to the total number of nights (Romero et al. 1999).

$$DCV = 100 \frac{\sum_{i=1}^n (N_i / \Delta t_i)}{\sum_{i=1}^n (1 / \Delta t_i)} \% \quad (2.5)$$

where, $\Delta t_i = \Delta t_{i,obs}(1+z)^{-1}$ is duration of monitoring of a source which is corrected for redshift and N_i is 0 or 1 if source is non-variable or variable respectively.

2.3.6 Structure function

To explain intrinsic variability timescales like cooling, acceleration or light crossing timescales associated with single emission region, a concept of particle acceleration was invoked by Kirk et al. (1998). One way is to look into the light curves as already mentioned. More sophisticated mathematical formulation to estimate the time scale of variability is using structure function (SF) analysis. Simonetti firstly introduced this method to get an information about characteristic timescale for flat- and steep spectrum radio sources which qualifies C-test and chi-square criteria. For in-depth description, readers are referred to Simonetti, Cordes, & Heeschen (1985) for a general description and Gliozzi, Brinkmann, O'Brien, Reeves, Pounds, Trifoglio, & Gianotti (2001) for implications of SF on blazar light curves. In order to estimate the characteristic variability timescale, we used first order structure function which is defined by the equation,

$$SF(\tau_i) = \frac{\sum [M(t + \tau_i) - M(t)]^2}{N} \quad (2.6)$$

where, $M(t)$ is the magnitude at time t and τ_i is the time lag. The chi-square method was used to fit structure function where minimum variability timescales and corresponding errors were identified (for a reference, see Zhang et al. (2012)).

$$SF(\tau) = \begin{cases} k\tau^\beta, & \tau \leq \tau_o. \\ C, & \tau > \tau_o. \end{cases} \quad (2.7)$$

where, τ_o is characteristic timescale with 1σ uncertainty and $\beta = \frac{d\log(F)}{d\log(\tau)}$ is logarithmic slope in $\tau - SF$ plane characterizing the variability and nature of the processes. If the value of β is 0, it indicates flickering noise and if $\beta \geq 1$, it indicates turbulent process in jet (or shot-noise).

2.3.7 Discrete Correlation Function

Discrete correlation function was first introduced by [Edelson & Krolik \(1988\)](#) and generalized by [Hufnagel & Bregman \(1992\)](#) to include a better error estimate. Since uneven sampling is more often than not a norm in astronomical observations, DCF offers an advantage compared to other correlation methods in this realm. A brief description of the method is given by [Tornikoski et al. \(1994\)](#) and [Hufnagel & Bregman \(1992\)](#). A variant of DCF is the zDCF ([Alexander 2014](#)) which corrects for various biases of the DCF method by employing equal population binning and Fishers z-transform.

The unbinned discrete correlation for the time series is done using the following equation:

$$UDCF_{ij} = \frac{(a_i - \bar{a})(b_j - \bar{b})}{\sqrt{\sigma_a^2 \sigma_b^2}}, \quad (2.8)$$

where a_i and b_j are the individual data points of the two data streams, \bar{a} and \bar{b} are the mean values of the time series. After calculating the UDCF, the correlation function is binned, the bin size is set as average of the interval between consecutive observations for all correlations. The DCF(τ) is given by following equation :

$$DCF(\tau) = \frac{1}{N} \sum_{i=0}^N UDCF_{ij}(\tau) \quad (2.9)$$

Here τ is the center of the bin size $\delta\tau$. The DCF technique was proposed to work for unevenly sampled data, without interpolating in the temporal domain, giving the standard error as:

$$\sigma_{dcf}(\tau) = \frac{1}{N-1} \left\{ \sum_{i=0}^N [UDCF_{ij} - DCF(\tau)]^2 \right\}^{1/2} \quad (2.10)$$

In order to identify quasi-periodicity in the lc 's, autocorrelation is performed using the technique of DCF in which the correlation of the time series(a_i) with itself ($b_j=a_j$) is determined at different points in time. It will have a peak at zero lag, but any other strong peak will indicate the presence of periodicity. $DCF > 0$ implies that two data samples are correlated, $DCF = 0$ stands for no correlation while $DCF < 0$ implies anti-correlated data series.

2.3.8 Lomb-Scargle Periodogram Analysis

Determining periodicities in the unevenly sampled time series is not directly possible with methods like Fast Fourier Transform(FFT) which involves some degree of interpolation to fill in the gaps. This drawback can be overcome by the Lomb-Scargle (hereafter L-S) method ([Lomb 1976](#); [Scargle 1982](#)) which estimates a frequency spectrum based on a least squares fit of sinusoid. We have used this method to verify the periodicities estimated using the structure functions.

The periodogram is calculated with a sampling interval of $1/4T$ in the frequency space, T being the total length of the time series with an upper limit of $N/2T$, N being the total number of observations and the lower limit was set at $1/T$. For more details about the L-S periodogram see [Press et al. \(1992\)](#), and references there-in.

We have extensively used the above mentioned statistical tools in our study. It helped us to investigate the variability from the blazar differential light curves with more than 3σ confidence, the estimation of timescales of variability and their confirmation using structure functions and power spectrum, searching for periodicities, if present, using correlation techniques along with periodogram analysis approach. The results obtained using these techniques are presented in the forthcoming chapters.

Chapter 3

Intra-night and Long-term

Optical Variability in 3C 66A

The long-term continuous optical lightcurves generated from the high temporal resolution, multi-band observations provide wealth of information on blazars. The random and variable, at diverse time scales, patterns in blazar lightcurves help to understand the structure and the dynamics of the relativistic jet which dominates their emission, particularly when in brighter state. The detailed long term behavior of this class of sources has not been studied much to explore their structure, physical processes responsible for the emissions and any relationship between the rapid variations and the long term trends. Such long term studies on some of the blazars have resulted in detection of, for example, the presence of the quasi-periodic variations in OJ 287, explained based on the binary black hole model (Sillanpaa et al. 1988; Pihajoki et al. 2013) and the possibility of the precession of the jet (Nesci et al. 2005) in S5 0716+714. The good quality multi-band light-curves have been used for some sources to study correlated variations which provide information about time lags and spectral behaviour (Stalin et al. 2009; Wu et al. 2012; Bachev et al. 2017). More often, the data interpretation become complex because of the sparse observational coverage, non-simultaneity etc., but a few dedicated long-term blazar monitoring facilities and programs, e.g., Steward Observatory (Arizona), SMARTS (Boston university), Fermi-LAT, Swift-XRT, OVRO (Owens Valley), UMRAO etc., have benefited the astronomers

with continuous data coverage.

One such blazar monitoring program has been going on at Mount Abu InfraRed Observatory (MIRO), Rajasthan, India where a sample of such sources are being observed. Under this program, the optical observations on several blazars, including 3C 66a, are being performed since 2005 in the four different broad-band filters (*i.e.*, B, V, R and I), using MIRO 1.2 meter telescope facility. This chapter details the long-term (> 10 years) behaviour of the blazar 3C 66A, an intermediate BL-Lac object, with synchrotron component peak lying in optical window (for a detailed description of blazar sub-classes and properties, please refer to Chapter 1), exploring the occurrence of optical micro-variability with any possibility of the quasi-periodic variations and the nature of its long-term variability. The motivation behind this study is to understand the reasons behind variations at different time scales, complex spectral behavior of the source and its activity in general.

3.1 Introduction

3C 66A is a radio source (R.A.= 02:22:41.6 (hh:mm:ss), Dec= +43:02:35.5 (dd:mm:ss)), also known as B0219+428, NRAO102, 4C 42.07, firstly identified by [Wills & Wills \(1974\)](#) as a blue stellar object with a featureless optical spectrum with (U-B) and (B-V) colors similar to those found for the quasi-stellar objects. The initial redshift, $z=0.44$, was determined by ([Miller & McGimsey 1978](#)) which was later confirmed by ([Lanzetta et al. 1993](#)) with a detection of Lyman- α line in IUE spectrum. The redshift of this source is still uncertain, even after thirty years of its detection, as the optical spectrum is featureless and has been studied by several authors ([Finke et al. 2008](#); [Shaw et al. 2013](#); [Paiano et al. 2017](#)). The source redshift (z) is still disputed and the upper limit of $z = 0.44$ is adopted in the present work.

The source is studied over wide range of frequencies from radio to γ -rays. The radio study on parsec scale jet in 3C 66A gives an evidence of the presence of non-

stationary core showing *core-jet with bending jet* morphology on the radio maps (Jorstad et al. 2005; Zhao et al. 2015). The flares in the γ -rays has been also studied by several authors Tosti (2008); Abdo et al. (2010b) and is also detected as a TeV candidate. Based on the synchrotron (low-energy component) peak frequency that lies between 10^{14} Hz and 10^{15} Hz, in the spectral energy distribution (SED, hereafter), it is classified as an intermediate BL Lac (IBL, hereafter) (Perri et al. 2003; Abdo et al. 2010b).

An early investigation of this object by Folsom et al. (1976) demonstrated that this object was variable in the optical with the flare amplitudes of approximately 0.5 mag and time scale of variation ranging from a few days to months. The WEBT campaign of 2003-2004 (Böttcher et al. 2005) revealed micro-variability with flux changes of $\sim 5\%$ on a timescale as short as ~ 2 hr. Intra-night variability (INV) has also been addressed by several other authors (e.g. Sagar et al. 2004; Raiteri et al. 1998; Gopal-Krishna et al. 2011; Rani et al. 2011) albeit with limited number of nights over a maximum period of four years. Williamson et al. (2014) used X-ray, γ -ray and optical data during 2008-2012 to discuss spectral behavior in flaring and quiescent states of 3C 66A (also see Abdo et al. 2011) and other blazars. Bach et al. (2007), while studying a larger sample of blazars, found 3C 66A to be variable at months time scale with faster variations superposed on its optical light-curve during 2005-2006.

A typical light-curve of the source is given in Figure 3.1, showing significant variation in R-band at short and long term time scales.

The reason for long-term variability (LTV) is suggested to be due to the large scale relativistic shock moving down the jet, while INV is caused by the interaction of these shocks with small scale particle or magnetic field irregularities present in the jet Romero et al. (1999). If both, INV and STV/LTV, features are related to the processes in the jet then a long term high temporal resolution study of the blazars would be very useful to see if there was any connection between the two.

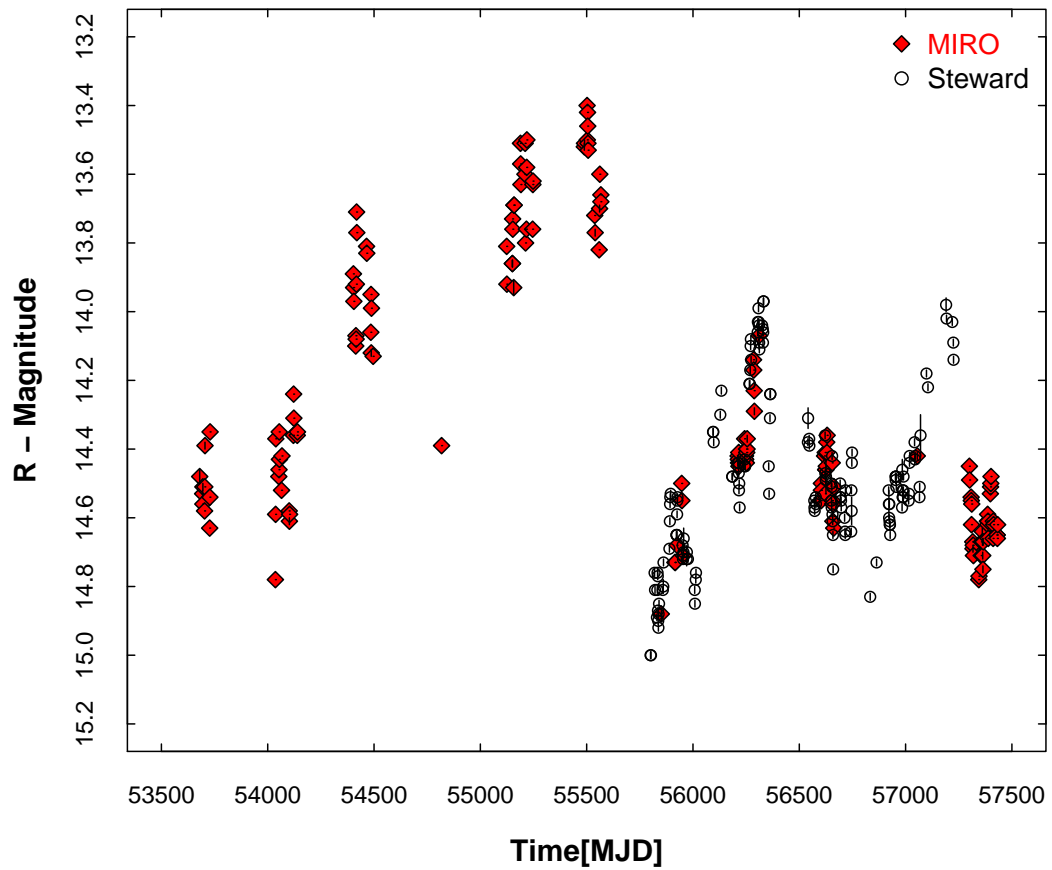


Figure 3.1: The light curve of blazar 3C 66A in the optical R-band is shown. The daily averaged source magnitude are shown by filled diamonds (red) and open circles (black), obtained from MIRO & Steward Observatory from 2005-2016 (Kaur et al. 2017c).

3.2 Observations and Data reduction

The photometric monitoring of 3C 66A was performed using the PIXELLANT liquid Nitrogen (LN₂) cooled CCD-Camera mounted at the f/13 Cassegrain focus of the 1.2m Telescope at Mt. Abu InfraRed Observatory (MIRO), Gurushikhar, Mt Abu, Rajasthan, operated by the Physical Research Laboratory, Ahmedabad, India. The CCD Camera has 1296×1152 pixels, each with 22 micron size and a read out time of about 13 seconds. With 0.29 arcsec per pixel, the total field of view (FOV) is about $6.5' \times 5.5'$. The observations during October 2014 were made with iKon ANDOR CCD camera having 2048×2048 pixels, thermo-electrically cooled to -80°C to keep dark current low. The FOV for the both CCDs is large enough to accommodate the source and several field stars which can be used for the source calibration. The CCD-photometric system is equipped with the Johnson-Cousin UBVRI ([Johnson & Morgan 1951](#); [Bessell 2005](#)) filter set.

3.2.1 Observation strategy

The data over more than ten years have been collected by following a general observation strategy. A few frames in the four broad band filters (B, V, R, and I) are captured to address the long-term behavior of the source while monitoring the source in R filter for minimum one hour for detecting intra-night variability (INV) present in the source. This strategy helps us to collect dense, multi-epoch source information which further explores the various timescales for intra-night, short-term and long-term flux and spectral variations (INV/STV, and LTV).

During each night of the observation, several bias and flat images are taken to perform the background and the sky correction on the source image, called as science image. During the whole observing period of more than 10 years, observations are made with high temporal resolution keeping exposure times to provide good signal to noise ratio; 30-40 seconds in I, 35-45 seconds in R, 40-45 seconds in V and 50 - 60 seconds in B band. Thus separation between consecutive images ranges from 45 (I-band) seconds to 75 (B-band) seconds. All the observations are taken very carefully so as to accommodate at least five comparison (or refer-

ence) stars in the source frame that would help perform differential photometry on single frame simultaneously, i.e., source plus comparison stars. Readers are encouraged to read Chapter 2 of the document for a complete procedure on the data reduction on CCD images.

The comparison stars in the field of the source are captured in the same frame where the source is present. The procedure reduced the errors in calibrating the magnitude/flux of the source. By following this strategy, 3C 66A is observed on total 160 nights out of which on 89 nights it was monitored for INV. A total of 5173, 702, 1187 and 597 photometric frames in R, B, V and I bands, respectively, were obtained during more than ten years of observations.

3.2.2 Data reduction using IRAF

The data obtained is reduced using the standard routines in IRAF¹. Before proceeding to the data reduction, all the CCD frames are inspected to evaluate the quality of the image, the reliability of the data, and existence of any spurious features. After that, the quality checked CCD images are subjected to the data reduction procedure using bias and flat fielding correction. The details of whole data analysis procedure is discussed in the Chapter 2. The photometry is performed on the stars and comparison stars using DAOPHOT package in IRAF. The instrumental magnitudes are obtained through aperture photometry method using several aperture sizes, ranging from 1 to 5 times the FWHM of the source. The instrumental magnitude are plotted against various aperture sizes to pick the suitable aperture throughout the analysis. We have chosen aperture size 3 times the FWHM which led to optimum value of the S/N as prescribed by [Cellone et al. \(2000a\)](#).

Calibration of the source magnitude is done by differential photometry with respect to the comparison stars in the same field, which reduces the effect of changes in the atmospheric seeing. In order to obtain a reliable photometric

¹IRAF is distributed by the National Optical Astronomy Observatories, which are operated by the Association of Universities for Research in Astronomy, Inc., under cooperative agreement with the National Science Foundation.

sequence for 3C 66A we selected a set of non-variable stars with brightness as close to that of the object as possible. For each CCD frame, the instrumental magnitudes of the blazar 3C 66A and five other stars were extracted. Out of the five stars, four were found appropriate to be used as standard comparison stars viz. 1, 2, 4 and 5² for differential photometry. The photometric sequence for these stars was reported by [Smith & Balonek \(1998\)](#); [Fiorucci & Tosti \(1996\)](#); [Craine et al. \(1975\)](#). From here on, these stars are referred to as C1, C2, C4 and C5, respectively. We used one of the four stars closest in brightness to the source, as a comparison star and rest of the available stars as control stars to check the stability of the sky on that particular night. The observed magnitudes of the 3C 66A obtained during the non-INV nights were corrected using the averaged magnitude of all the four stars. Since the color difference between 3C 66A and its comparison stars is low ($\sim 0.5\text{mag}$), the effect of the air mass variation has negligible impact on our photometric results ([Carini et al. 1992](#)).

3.3 Data analysis

To detect the genuine intra-night variability (INV) in our data with at least 90% of significance, we employ several statistical tests. The customized programming scripts in R-package are made to ease the data analysis procedure and the calculations. The basic tests performed for this study are C-statistics, F-test and amplitude of variability estimation. These methods are briefly discussed in the following sections.

3.3.1 INV detection using statistical methods

To ascertain and quantify the presence of the intra-night variability in the source 3C 66A, we performed the *C*-statistical test and F-test on the observed dates when the source was monitored for at least an hour.

²<http://www.lsw.uni-heidelberg.de/projects/extragalactic/charts>

C-test

The variability parameter, C , first employed by [Jang & Miller \(1997\)](#) and generalized by [Romero et al. \(1999\)](#), is defined as:

$$C = \frac{\sigma_{BL-Cm}}{\sigma_{Cn-Cm}}, \quad (3.1)$$

where σ_{BL-Cm} and σ_{Cn-Cm} are the standard deviations of the differential magnitudes of (3C 66A – Comparison star) and (Control star – Comparison star), respectively. The standard deviation σ , has been calculated as

$$\sigma = \sqrt{\frac{\sum_{i=0}^N (m_i - \bar{m})^2}{N - 1}}, \quad (3.2)$$

where $m_i = (m_2 - m_1)_i$ denotes the differential magnitudes of 3C 66A and comparison star (or control star and comparison star), $\bar{m} = \overline{m_2 - m_1}$ is the differential magnitude averaged for a given night and N represents the number of the data points for a given night. For the 99% confidence, $C \geq 2.57$.

For details of the F-test and amplitude of variation please refer to Chapter 2, Section 2.3. Using these aforementioned criteria we have classified a night as variable, subject to the conditions of F-value ≥ 5 , $C \geq 2.57$ and amplitude of variation ≥ 0.05 mag. These are further discussed in the next section.

3.3.2 Quasi-periodic variations (QPV) and variability timescales

The blazar light-curve sometimes shows the presence of rapid variations which appear periodic in nature. Such features in the light-curve may throw some light on the possible emission mechanism, such as micro-lensing effect ([Webb et al. 2000](#)) which is geometric in nature but extrinsic to the source, and lighthouse effect ([Camenzind & Krockenberger 1992](#)) caused by the helical motion of the plasma in the jet, a geometric but intrinsic process etc. To help analyze light-curves for the presence of such features and estimating various timescales of variation, we have used advanced statistical methods on the whole data-set, i.e., structure function for time scales of variation and periodicity, periodogram

and zDCF autocorrelation function for periodicity analysis. All the methods are briefly described in earlier Chapter under Sections 2.3.6- 2.3.8.

In the structure function, factor β (cf. Section 2.3.6) characterizes the variability and hints about the nature of processes. A typical SF consists of two plateaus and a slope in between. For short time scales, the plateau has an amplitude only twice the measurement noise. For larger timescales, the SF will show a power-law rising trend with slope β , which depends on the nature of the intrinsic variation of the source. After rising, the SF will reach another plateau with amplitude equal to twice the variance of the fluctuation. If the SF does not display a plateau, i.e. increases monotonically, then the timescale of the variability is larger than the duration of the observation. In certain cases, there could be more than one plateau (peak) in the SF, which indicate presence of the multiple variability timescales. We identify the characteristic timescale with the shortest timescale. Any periodicity will be seen in form of the more than one minima in the SF.

In order to identify quasi-periodicity in the light-curves using zDCF, auto-correlation is performed in which the correlation of the time series (a_i) with itself ($b_j=a_j$) is determined at different points in time. It will have a peak at zero lag, but any other strong peak will indicate the presence of periodicity. The value of $DCF > 0$ implies that two data series are correlated, $DCF = 0$ stands for no correlation while $DCF < 0$ implies anti-correlation between the two data series. In the L-S Periodogram, any high amplitude variation will be represented as significant periodicity at low frequencies.

3.4 Results & Discussion

The differential light-curves for the source-comparison and the control-comparison stars are constructed using the instrumental magnitudes, obtained from the aperture photometry on the source and the field stars of interest in all the science images. The standard values of all the comparison/control stars are used to calibrate the source magnitudes. The techniques mentioned in the earlier section to detect and confirm intra-night variations are used to calculate variability pa-

rameters, e.g., time scale and amplitude of variation etc. Here, we discuss the intra-night variability using the differential light curves for the source-comparison star and control star- comparison star as obtained for all the INV qualified nights. Also, the daily averaged brightness magnitudes for the source 3C 66A for all the nights and in all the filters are used to generate long-term light curves and the color-magnitude diagrams to study long term flux/spectral behavior of the source.

Table 3.1: Details of the confirmed INV nights for 3C 66A with no. of data points(N), duration of observation, averaged R-band magnitudes, variability parameter (C), amplitude of variation (A_{var}), F-test value, slope of structure function(SF Slope) and variability time scale (t_{var}). All the INV parameters are estimated with more than 99% confidence level.

Date (yyyy-mm-dd)	MJD (start)	N	Duration (mins)	R-band (mag)	σ_R	C	A_{var} (mag)	F-test	SF Slope (β)	$t_{var}(\delta t_{var})$ (mins)
2005-12-23	53727.9075	127	194.85	14.49	0.01	3.26	0.14	10.63	0.76 ± 0.03	118.0(2.5)
2006-11-16	54055.0058	93	85.90	14.49	0.01	4.43	0.11	19.62	1.96 ± 0.07	68.0(1.9)
2009-11-21	55156.9100	103	185.95	14.71	0.01	4.87	0.67	23.72	1.19 ± 0.03	37.0(1.7)
2010-11-07	55507.0109	139	190.35	13.86	0.01	4.62	0.32	21.34	1.40 ± 0.03	187.0(3.7)
2012-11-21	56252.8389	144	226.73	14.40	0.01	3.56	0.17	12.67	1.35 ± 0.05	40.0(1.1)
2015-12-30	57386.6011	198	213.74	14.65	0.01	3.16	0.15	9.98	1.41 ± 0.05	41.0(1.3)

3.4.1 Intra-night flux Variability (INV)

In order to determine the number of INV nights, we use the criterion that source should be monitored for at least 1 hr during that night. We found 89 out of 160 nights to qualify the criterion. Out of these, 13 nights suffered from the bad weather resulting in poor quality light-curves. To verify whether 3C 66A exhibited INV during the remaining 76 nights, we apply conditions that the variability parameter $C \geq 2.57$, F-value ≥ 5 and amplitude of variation more than 0.05mag. The nights which satisfied all these criteria were considered as confirmed INV nights. The observation details and all the parameters estimated for these INV nights are given in Table 3.1. As can be seen from the Table 3.1, we get only 6 out of the 76 nights which qualify for confirmed INV, implying a duty cycle (DCV) of variation for 3C 66A as $\sim 8\%$ only. However, much higher (up to 86%) have been reported for 3C 66A. Raiteri et al. (1998) observed it for two nights and found it variable for both nights (DCV=100%) with 8% and 14% amplitude of variation; Sagar et al. (2004) reported INV on 6 out of 7 nights (DCV >85%) in their 5-10 hrs monitoring during 1998-2002; Rani et al. (2011) found the source DCV for INV $\sim 28\%$ during their 7-night monitoring for more than 3-hrs while Gopal-Krishna et al. (2011) observed the source for 5-7 hrs on 7-nights and reported 47% as duty cycle of variation. We would like to state that the main reasons for our low DCV values for 3C66a are:

- (1) relatively shorter duration of monitoring (1 hour and more) compared to 3-10 hrs as reported by these authors,
- (2) strict criteria for variability set by us as mentioned above.

For example, if we apply the condition of amplitude of variability to be $>5\%$, DCV reported by Sagar et al. (2004) will come down from 86% to 43%. In their studies, Rani et al. (2011) & Gopal-Krishna et al. (2011) found that longer the period of monitoring, higher the DCV for INV.

For our 6- INV nights, amplitude of variation varies between 0.11 to 0.67 mag while C - test parameter lies between 3 to 4.8 and their light-curves are shown in Figure 3.4. The INV light-curves show flux variations which can be broadly classified into following subgroups: (i) a steady rise or fall in the flux

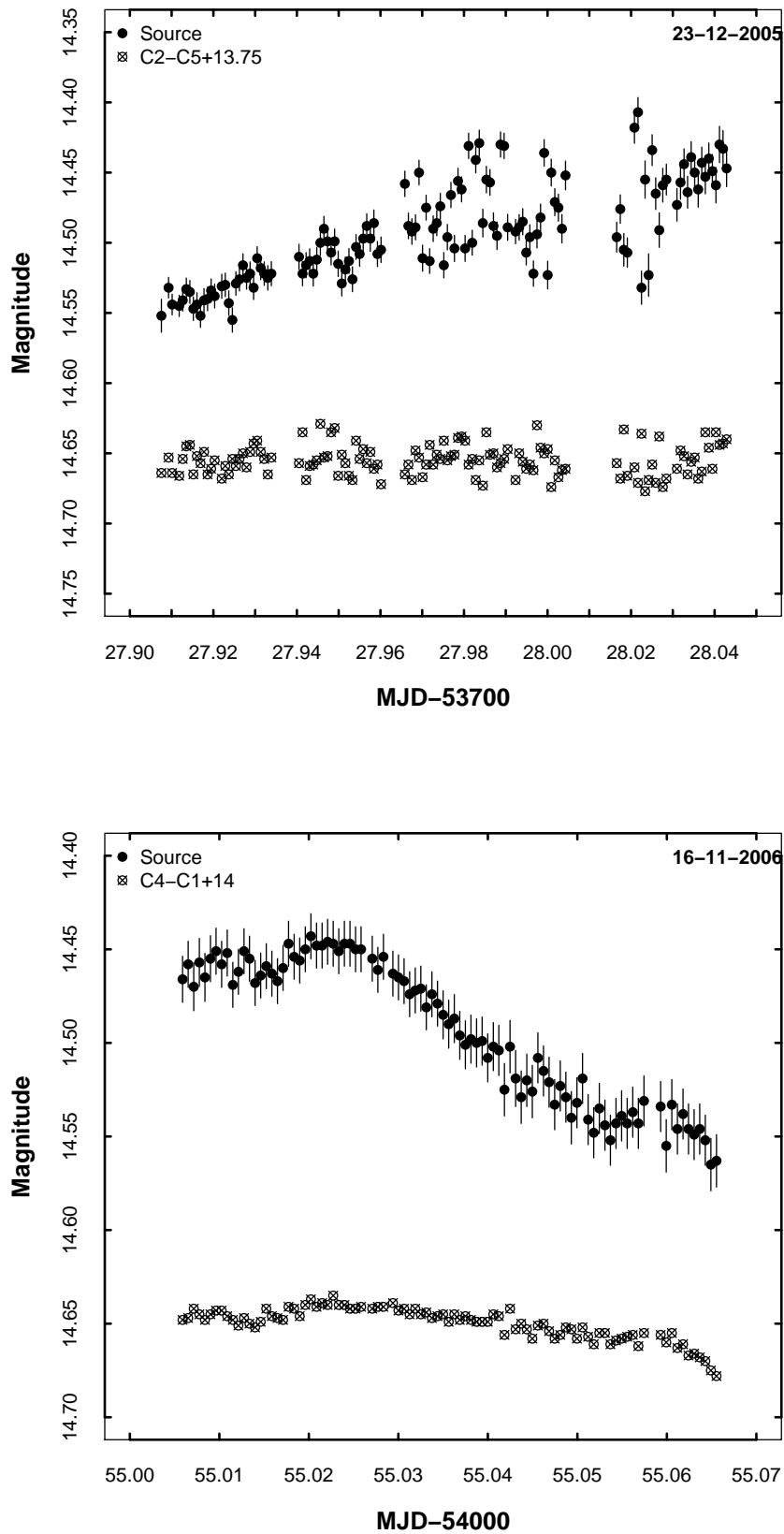


Figure 3.2: Light-curves for the nights showing INV in 3C 66A with the date of observation mentioned in the plots. The statistical results are given in Table 3.1.

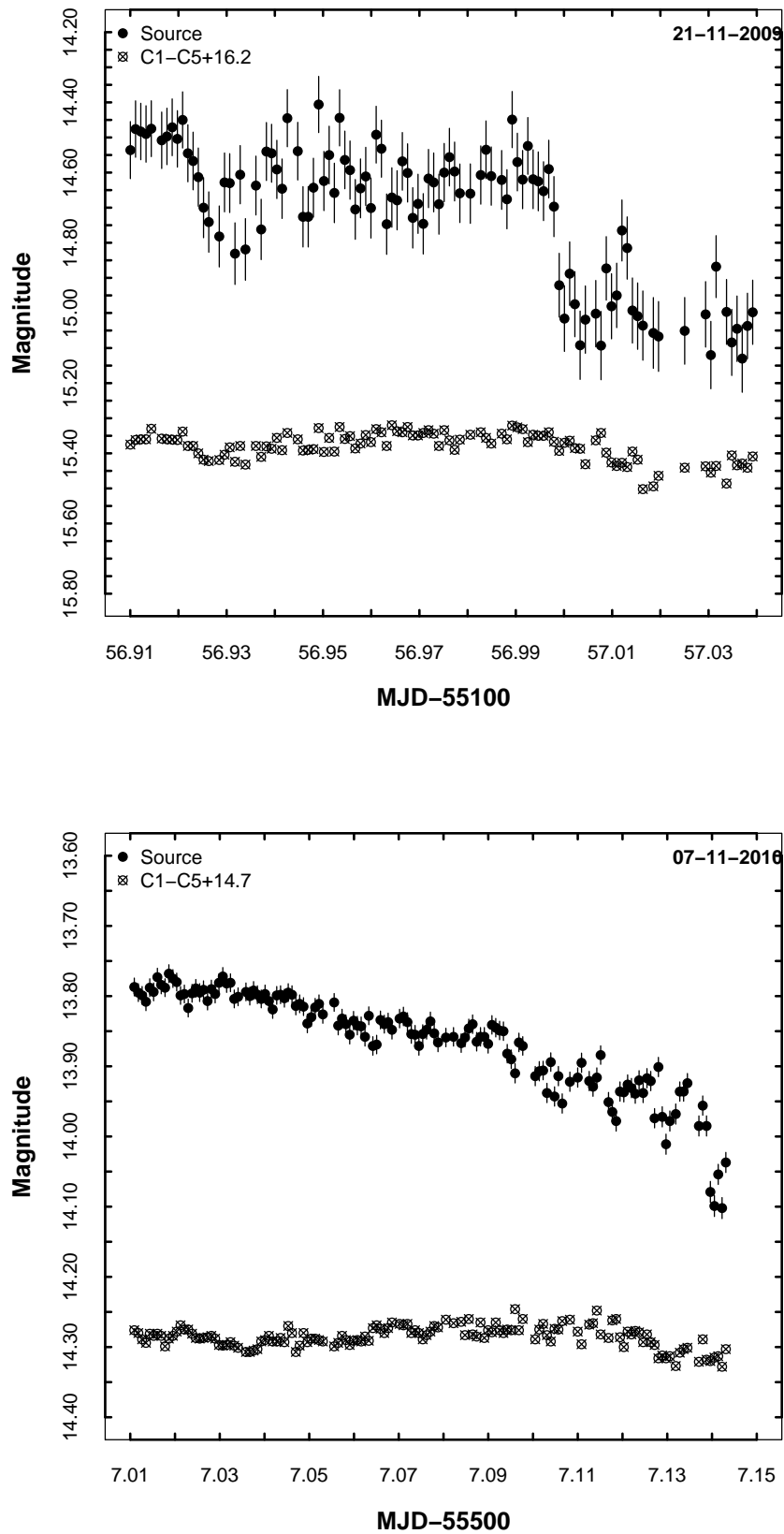


Figure 3.3: Light-curves for the nights showing INV in 3C 66A with the date of observation mentioned in the plots. The statistical results are given in Table 3.1.

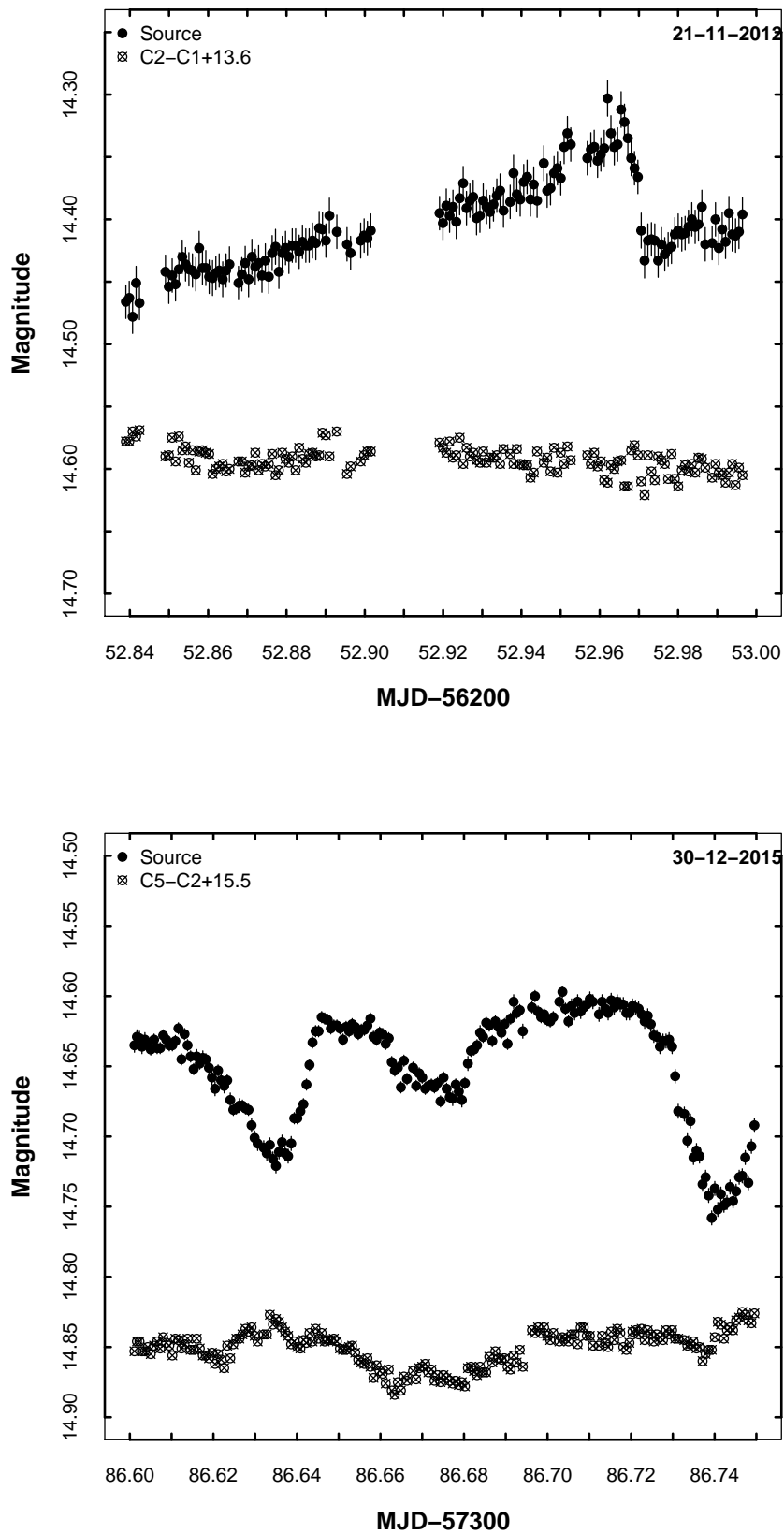


Figure 3.4: Light-curves for the nights showing INV in 3C 66A with the date of observation mentioned in the plots. The statistical results are given in Table 3.1.

during overnight monitoring, (ii) small amplitude fluctuations superimposed over a slowly varying flux and (iii) sharp decline or increase in the flux during the night, giving clear indication of the characteristic time scale of variation. These three types of variations in the light-curves can be attributed to the possibility of the intrinsic differences in the physical mechanisms as well as geometric effects. The continuous rise/fall for a duration of typically few hours may be due to the small scale steady acceleration/cooling of the plasma in the shocked region affecting the synchrotron emission. This can happen if the acceleration/cooling time scales are longer than the light crossing time. Short time scale fluctuations superposed on the slowly varying component might be due to the local inhomogeneities in the blob moving down the jet. The sharp decline or enhancement in the optical flux indicates a violent and evolving nature of the shock formed or sudden injection of the plasma in the emission region. The timescales shorter than few tens of minutes suggest a possibility that the whole cross-section of the jet may not be shocked. Another reason could be the regions of small scale over-densities in the blob passing through a standing or slowly moving core (Chandra et al. 2011). Such standing shocks in the jet can be formed by the pressure imbalance between the jet and the ambient medium. Oscillations in the width of the jet occur as the over-pressured matter in the jet expands until its pressure falls below the ambient pressure. This under-pressured plasma then contracts under the influence of external pressure until high pressure is restored. It leads to the formation of an oblique standing shock terminating into a strong shock wave perpendicular to the jet flow (Sokolov et al. 2004a). In addition, various plasma instabilities leading to the formation of shocks, magnetic reconnection sites, and turbulence (see the recent discussions in Narayan & Piran 2012b; Subramanian et al. 2012; Marscher 2014; Saito et al. 2015; Sironi et al. 2015) can also be responsible for the INV and longer time scale variations. Any constraint on these possibilities can only be imposed by using the simultaneous observations at different wavelengths which is beyond the scope of the present study.

In order to determine various parameters, such as the variability timescale, extent and the rate of the amplitude of variation etc in complex cases, structure

functions (Simonetti et al. 1985; Zhang et al. 2012) have been used extensively (Carini et al. 2011; Wu et al. 2005; Rani et al. 2010; Agarwal et al. 2016; Dai et al. 2015). We have constructed structure functions (SFs) for the variable nights as shown in the Figure 3.5. Using χ^2 – minimization method, fits to the SFs were made to calculate timescales and slope of the SFs (Zhang et al. 2012) as given in Table 3.1. These are then used to discuss the timescales of variation and the nature of the emission process causing such variations. We notice that the SF slope, which characterizes the nature of variability, is close to, or more than 1.0 for all the INV nights, implying that the major cause of the intra-night variations is the turbulent process (Carini et al. 2011) at work in the jet as described above.

3.4.2 Variability time-scales and size of the emission region

All the 6 nights satisfying the criteria of $C \geq 2.57$, amplitude of variation larger than 0.05 mag and $F - value \geq 5$ are used for INV discussion and to estimate the variability time scales. Shortest time scale of variation puts constraints on the size of the emission region. For complex data sets, it is an arduous task to identify the minima and maxima from small amplitude variations in the light-curves. The structure functions shown in Figure 3.5 for the light-curves given in the Figure 3.4, showed minimal variability timescales in the range of 37 min - 3.1 hrs. Among them, the night with the shortest variability timescale was found to be 2009 November 21 (MJD 55156.91) for which the variability timescale estimated from the best fit parameters for the SF is ~ 37 min. The light curve for the night shows indications of multiple small flares almost buried in the noise. The structure function also suggests three plateau and dips but are not pronounced enough to infer periodicity in the INV. For the night of 2015 December 30 (MJD 57386.60), with characteristic variability time scale of 41 minutes, the SF shows signs of quasi-periodicity and is discussed separately. The light curve for the night 2005 December 23 shows increased brightness with a break in the data at MJD 53728.05. The SF indicates a plateau giving a time scale of 118 minutes. On 2006 November 16, after showing some brightening, the source goes fainter by

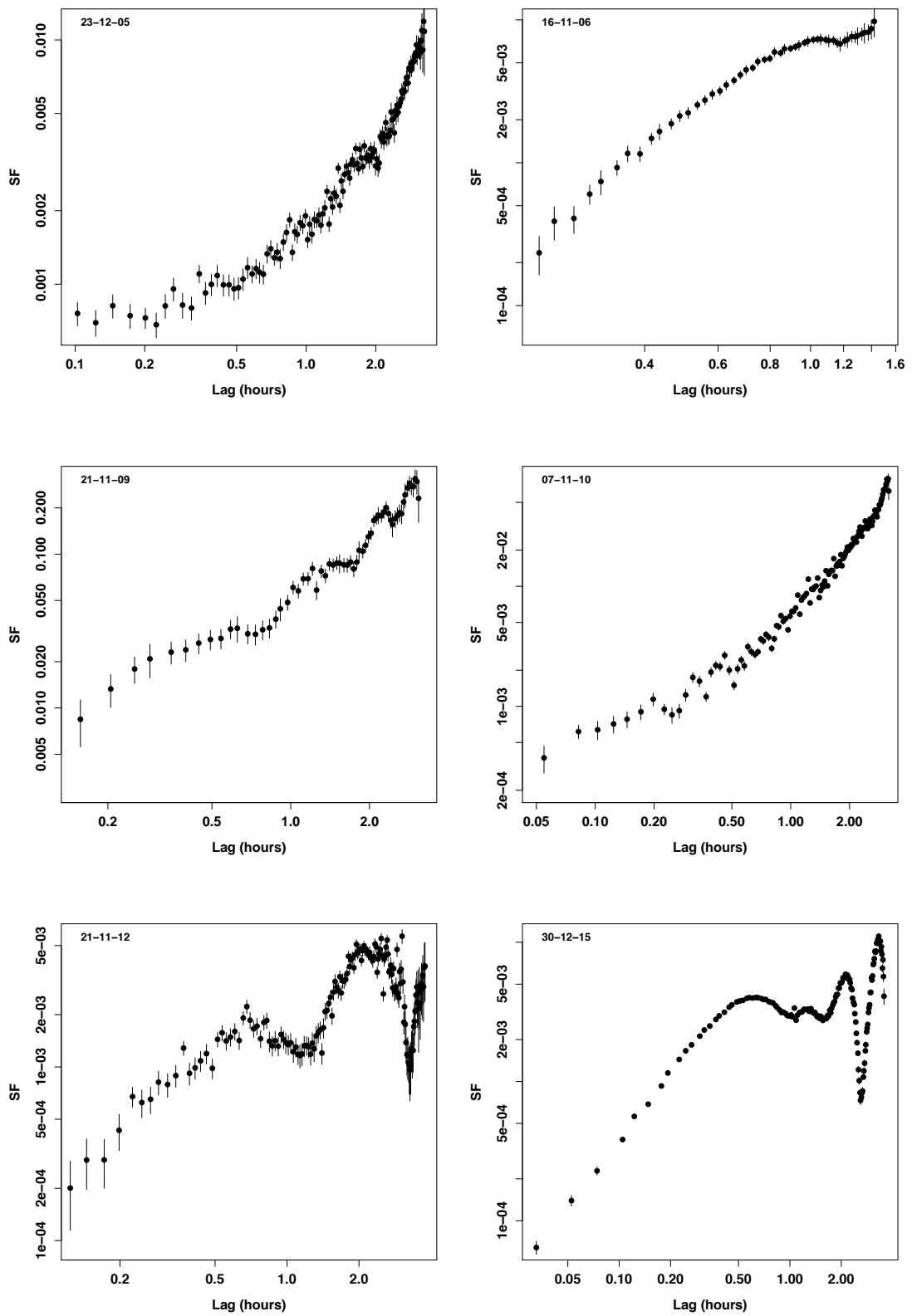


Figure 3.5: Structure functions for the confirmed INV nights during 2005-2016. On 2015 December 30, source shows quasi-periodic variations (QPV).

0.1 mag. The SF gives a time scale of 68 minutes. The blazar 3C 66A goes fainter by about 0.25mag in R-band in a continuous fall on the night of 2010 November 07. The structure function shows a monotonic increase without any detectable plateau. That shows that the variability timescale for this night is longer than the duration of the observation. A continuous increase in the brightness, with a data break at MJD 56252.91 and then sharp drop in brightness by about 0.1 mag characterize the light curve of 2012 November 21 (MJD 56252.84). The structure function shows two peaks and 2-dips, possibly introduced by the data break. It gives a variability time scale of about 40 minutes.

Considering the shortest variability timescale, estimated above, as the time required by the light to cross the emitting region, one can set an upper bound to the size of the emission region, R , given as,

$$R \leq \frac{c\delta\Delta t_{min}}{1+z}. \quad (3.3)$$

Taking Δt_{min} as 37 mins, δ as 15 (Böttcher et al. 2005) and redshift $z = 0.444$ (Lanzetta et al. 1993), we estimate the size of the emission region to be about 6.918×10^{14} cm. Since the variability time scales detected during the 6 INV nights described here range from 37 minutes to 187 minutes, the estimated sizes of the emission regions vary from 6.92×10^{14} cm to 3.49×10^{15} cm, which is about 7 to 35 times the Schwartzchild radii of the SMBH.

The determination of the mass of the central super-massive black holes (SMBH), driving force behind the AGN activity, is very important for understanding the AGN phenomena. There are several methods to determine the black hole mass but they all require very high spatial resolution to either detect the motion of the stars orbiting the central BH or the detection of the variability in the emission lines in the AGN environment (Chandra 2013; Xie et al. 2002). For the BL Lac objects like 3C 66A, which do not show appreciable emission lines in their spectra, determining BH mass is very difficult. Assuming the origin of the rapid variability in blazar flux from the close vicinity of the black hole, several authors have estimated mass of the black hole using variability time scales (Miller et al. 1989; Rani et al. 2010; Zhang et al. 2012; Agarwal et al. 2016; Dai et al. 2015, and

references there-in). [Xie et al. \(2005\)](#) carried out a study to see if the application of the variability timescales was appropriate in estimating the mass of the black hole. They found significant correlation between the masses of the black holes in the blazars estimated using the variability timescales and those derived from the $L_{5100} - R_{BLR}$ relation. The sample size, though, was small (12 sources) and hence the inference can not be claimed as conclusive. Following the assumption that the observed minimum variability time-scale is manifested by the orbital time-scale of the innermost stable orbit around the central Kerr black hole, we estimate the mass of the black hole using the relation ([Abramowicz & Nobili 1982a](#); [Xie et al. 2002](#)):

$$M = 1.62 \times 10^4 \frac{\delta}{1+z} \Delta t_{min} M_{\odot}. \quad (3.4)$$

here, Δt_{min} is the observed minimal time-scale of variability, δ is the Doppler factor and z is the cosmological redshift. Using the above relation, we computed the mass of the black-hole to be $3.7 \times 10^8 M_{\odot}$. This value is in agreement with typical values for such systems.

However, as mentioned earlier, such an estimate of the mass of the black hole holds true only when the variations originate very close to the black hole. [Vovk & Babić \(2015\)](#) suggested that if the time scales of the variability, which are comparable to the rotation period of the last stable orbit, originate close to the black hole, they should correlate with the masses of the black holes calculated by the established methods ([Kaspi et al. 2000](#); [Vestergaard & Peterson 2006](#); [Falomo et al. 2003](#), and references there-in). The study was done for the fast variabilities reported for the γ -ray emission. No significant correlation was found, indicating that the variability could be originated in the jet, away from SMBH, due to small scale inhomogeneities. Therefore, the black hole mass estimated here should be considered with caution.

3.4.3 Quasi-periodic variations in 3C 66A

Several long term studies of the blazars have resulted in the detection of the presence of quasi-periodic variations (QPV). In the case of OJ287, 12-year quasi-

periodicity was explained based on the binary black hole model (Sillanpaa et al. 1988; Pihajoki et al. 2013) while the possibility of the precession of the jet (Nesci et al. 2005) in S5 0716+714 was suggested as the cause for the alternate decrease and increase of the average source brightness over a period of about 10 years. Moreover, quasi-periodicity has also been detected at the intra-night time scales in the blazar optical light-curves (Gupta et al. 2009; Wu et al. 2005; Rani et al. 2010). Rani et al. (2010) detected QPO in optical with a time period of 15 mins. Wu et al. (2005) explained presence of a sine-like feature in the intra-night light-curve of S5 0716+71 based on light-house effect.

During our long-term observation campaign on the 3C 66A, we have detected INV on at least 6 nights (with 99% confidence). Out of these, light-curve and structure function for the night of 2015 December 30 show a possibility of the quasi-periodic variations (QPV). In the structure function analysis, for the time scale of variation, we have taken the interval of time from where the SF begins a steady ascent to its attaining a peak (slope vanishes to zero). For the periodicity, if there are more than one minima in the SF, the interval between consecutive minima is taken as the time period. When the intervals between several such minima are almost similar, their average value is taken as period for the QPV. If the interval values turn out to be much different, periodicity is questionable or there might be more than one period present in the system. The SF for the night of 2015 December 30 (see Figure 3.5) shows maximum at 0.65 hr, first minimum at 1.07 hrs, second at 1.56 hrs and the third one at 2.59 hrs as a deep one, giving the intervals or periods as 1.07 hrs, 0.49 hr and 1.03 hrs, respectively. There appears to be two distinct periods, 1.05 hrs and 0.5 hr in this case, as one value is very different from the rest of the two values. It, therefore, indicates to the possibility of quasi-periodic variations during this night, also reflected in the light-curve for that night.

In order to cross check the SF results we used L-S periodogram (Lomb 1976; Scargle 1982) and discrete correlation function (DCF: Edelson & Krolik (1988); Hufnagel & Bregman (1992); Alexander (2014)) methods to ascertain the existence of QPVs. For this, in order to remove slowly varying component from

the light-curve of 2015 December 30, we subtracted a linear fit. The statistical technique of DCF and L-S periodogram was applied to the resulting data.

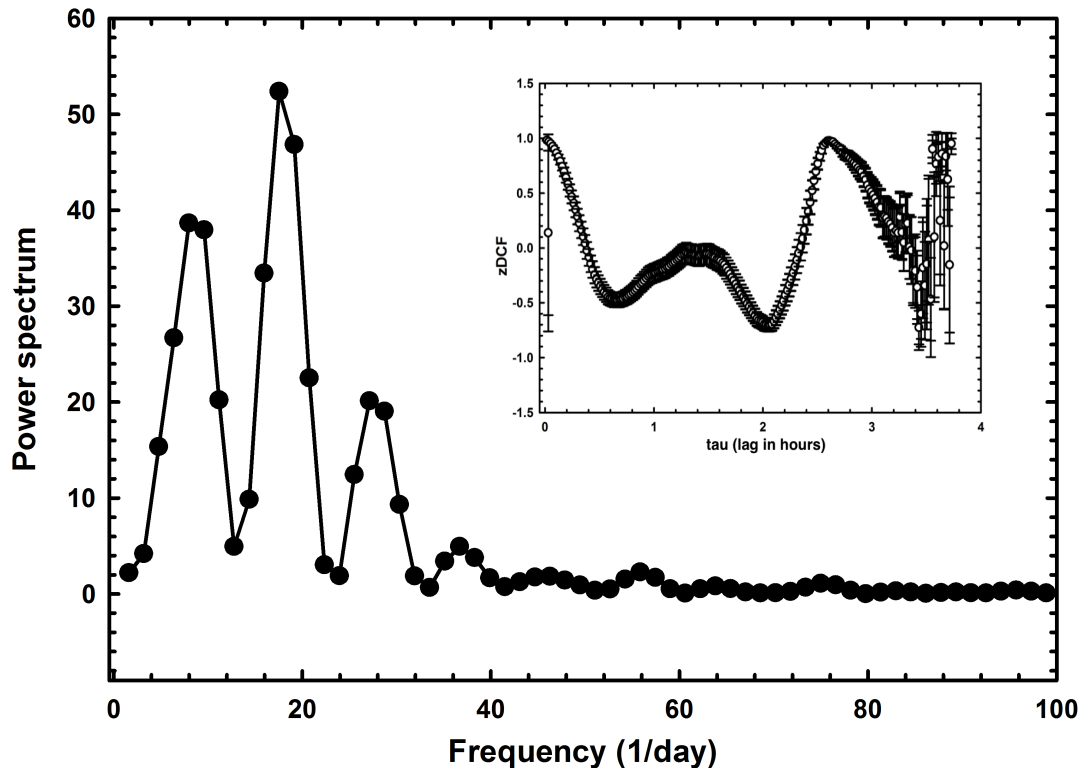


Figure 3.6: LSP and zDCF for the 2015 December 30 INV night showing QPV. The peaks in zDCF and LSP are determined at greater than 99% significance level, showing the possibility of QPV with a quasi-periodic component of about 1.4hr period.

On 2015 December 30 (MJD 53726.99), the periodogram reveals most significant peak at 1.4 hrs and the next significant at 2.6 hrs. The zDCF autocorrelation study also results in two peaks separated by a time lag of about 1.4 hrs and 2.6 hrs. Since data series length on 2015 December 30 is longer than 3.5 hrs, a period of about 2.65 hrs appearing in autocorrelation as well as LSP is also genuine. These values support the suggestion of structure function, thus confirming presence of quasi-periodicity on the night of 2015 December 30 with a period of about 1.4hrs and possibly 2.6 hrs. The periodic variations can be caused by the micro-lensing, a geometrical effect, ([Watson et al. 1999](#); [Webb et al. 2000](#)) which leads to symmetric and periodic features in the lc 's which are achromatic in na-

ture. Also, time scales should be of the order of a day or longer. As indicated by our light-curves, these short time-scale features are not symmetric in nature and hence are not expected to be due to micro-lensing effect. Shock-in-jet model (Marscher & Gear 1985) can also not directly explain these features. Camenzind & Krockenberger (1992) invoked a geometric light-house kind of approach to explain such quasi-periodic behaviour in the frame work of shock-in-jet model. According to it, these intrinsic quasi-periodic variations are caused by the plasma streamlet moving down the jet in a helical motions.

The geometric modulation of the shock-in-jet model can explain QPV observed here. The plasma is injected at a finite radius in the jet. These blobs move relativistically down the jet in the helical trajectory, forward direction of which varies with time (light-house effect: Camenzind Krockenberger 1992). For an observer close to the beamed direction, sweeping beam results in the significant change in the flux due to Doppler boosting of the intrinsic flux variation. Such differential boosting of flux results in the quasi-periodic changes in the observed flux as inferred here. The lightcurves thus formed will be achromatic.

Rise and fall rates of flare brightness

The INV light-curves shown in Figure 3.4, reflect smooth rise or fall in the source brightness over the night. Three nights show slow rise/fall in flux superposed by rapid fluctuations. The rate of change of the flux at different epochs is determined by fitting a line segment to the light-curves. The mean value of the rising rates is approximately 0.06 ± 0.02 mag hr⁻¹. The fastest rate of the change in optical flux (1.38mag/hr) has been seen on 2009 November 21 (MJD 55156.99) when the source decays by 0.40 mag within about 17 mins. Though the error bars are large, trend is very clear (more than 3σ change). Almost a smooth brightening, at a rate of 0.03mag/hr and smooth decline, at the rate of 0.078mag/hr are noticed in the light-curves of 2005 December 23 and 2010 November 7, respectively. Several changes in the source magnitude are seen on the night of 2015 December 30, the night showing QPV, along with a flat trend for a period of about 55 minutes. However, some of the flares on this night lead to rapid changes, varying from

0.12 mag/hr to 0.41mag/hr (errors are within the data points drawn). None of these features appear to be symmetric in nature or having similar rates of flux changes while rising and falling. The flux evolution in such cases is probably not caused by the light crossing time. If the particle injection and cooling were operating at a time scale shorter than R/c (R , size of the emission region), we expect symmetrical rise and fall profiles. Therefore, either injection/acceleration or cooling time scale must be affecting variation, causing different rise and fall rates.

3.4.4 Amplitude of variability and source brightness

In order to investigate the variability activity in different phases of the source brightness, we plotted variability amplitudes, estimated for all the nights (76 nights) considered for the intra-night variability test, as a function of their respective daily mean brightness magnitudes. The nature of the plot revealed larger intra-night variability amplitudes during the nights when the source is relatively fainter. Normally, one would expect larger amplitude of variation during the bright, flaring phases of the source when highly turbulent jet plasma is expected to interact with the frequent shock formations leading to its rapid acceleration and subsequent radiative cooling. During the quiescent phase, the jet is relatively quiet and the blazar emission might have some contribution from other components, for example accretion disk, BLR and host galaxy thermal emission. However, it has been seen that while flat spectrum radio quasars (FSRQ) show contribution from these sources of emission, BL Lac objects show much less such contribution to the optical flux which is dominated by the beamed emission from the jet (Raiteri et al. 2012), even when the source is in the low phase of brightness. One would, therefore, not expect variations with large amplitude during the nights when the source is in low state of brightness. Perhaps, during the bright phase, amplitude of variation is the victim of the overlapping effects of a large number of rapid flares, resulting in the higher base level brightness and reduced effective amplitude of the variation. On the other hand, if we drop a few outliers in the plot, trend would seem to be almost independent of the state of brightness.

That is what one expects if the variability is caused by the processes in the jet. In any case, in order to make a definitive statement on this trend, more such data on a sample of blazars are required.

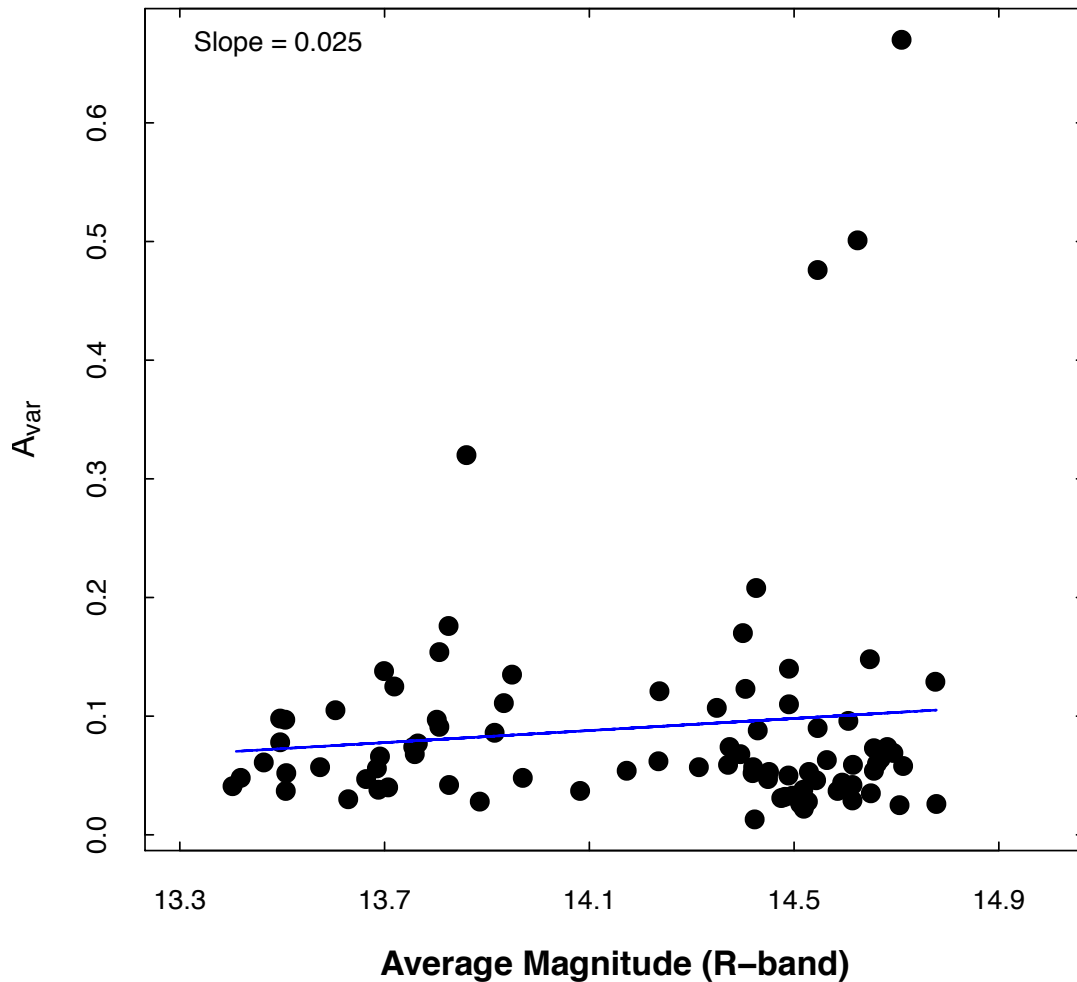


Figure 3.7: Amplitude of variability as a function of the average brightness of BL Lac object 3C 66A. Though a mild trend of larger amplitude of variation with decreasing brightness is seen, it is not significant at 95% confidence level with $p=0.542$ and a Pearson's correlation coefficient 0.068.

3.4.5 Average brightness trend during 2005–2016

To understand the long term behavior of the source and to determine any long-term variability pattern, we used the data for all the nights, averaging the magnitudes on the daily basis and plotted the lc 's for all the optical bands we have

used during 2005 to 2016. We have also used the archival data of the Steward observatory (Smith et al. 2009) available online in R and V bands, to fill the gaps in our daily averaged data set. The R-band light-curve thus plotted shows several flares, superposed over the three outbursts- one major (during MJD 53680 to MJD 56000) peaking somewhere around MJD 55501 (2010 November 1) with $R=13.40$ mag and two minor ones, decaying and rising parts of which could be overlapping. These two outbursts peak at about MJD 56272 and MJD 57192 with almost similar brightness values, 14.08 and 14.02 mag, respectively. From the light curve one can notice the brightness changing by about 0.6 mag within a period of tens of days (STV), by about 1.3 mag in about 700 days and by 1.7 mag within a span of about 1650 days (LTV). There are evidences of the shorter term variations with smaller brightness changes. Thus the light-curves show presence of long-term and short-term variabilities (LTV & STV) during the period of our observation campaign. However, due to the lack of the continuous data set, we are not able to fully resolve and trace these flares and outbursts to be too quantitative. In the course of our decadal observation campaign, 3C 66A has shown a waxing trend reaching its peak brightness (13.40 mag in R band) on 2010 November 1 (MJD 55501.04) and then a waning trend towards later half of the decade. A definite decline in the amplitude of variations in the later half of the decadal observation campaign is noticeable. Similar pattern is reflected in the other optical bands B, V and I as shown in the Figure 3.8, plotted along with R-band data.

During the course of the campaign the average R band magnitude was 14.10 mag, with a maximum as 13.4 mag on 2010 November 1 (MJD 55501.04) and a minimum of 15.01 mag (indicated by the Steward data point in Figure 5) on 2011 August 27 (MJD 55800). The brightness magnitudes for the other bands are as follows (maximum–average–minimum): B-band (14.10–15.10–16.24), V-band (13.41–14.45–15.85) and I-band (12.90–13.49–14.77).

A natural explanation for the flux fluctuations in the blazars, at both long and short term time scales, is the presence of turbulence in the relativistic jet that emits non-thermal synchrotron radiation (Marscher 2014; Romero et al. 1999).

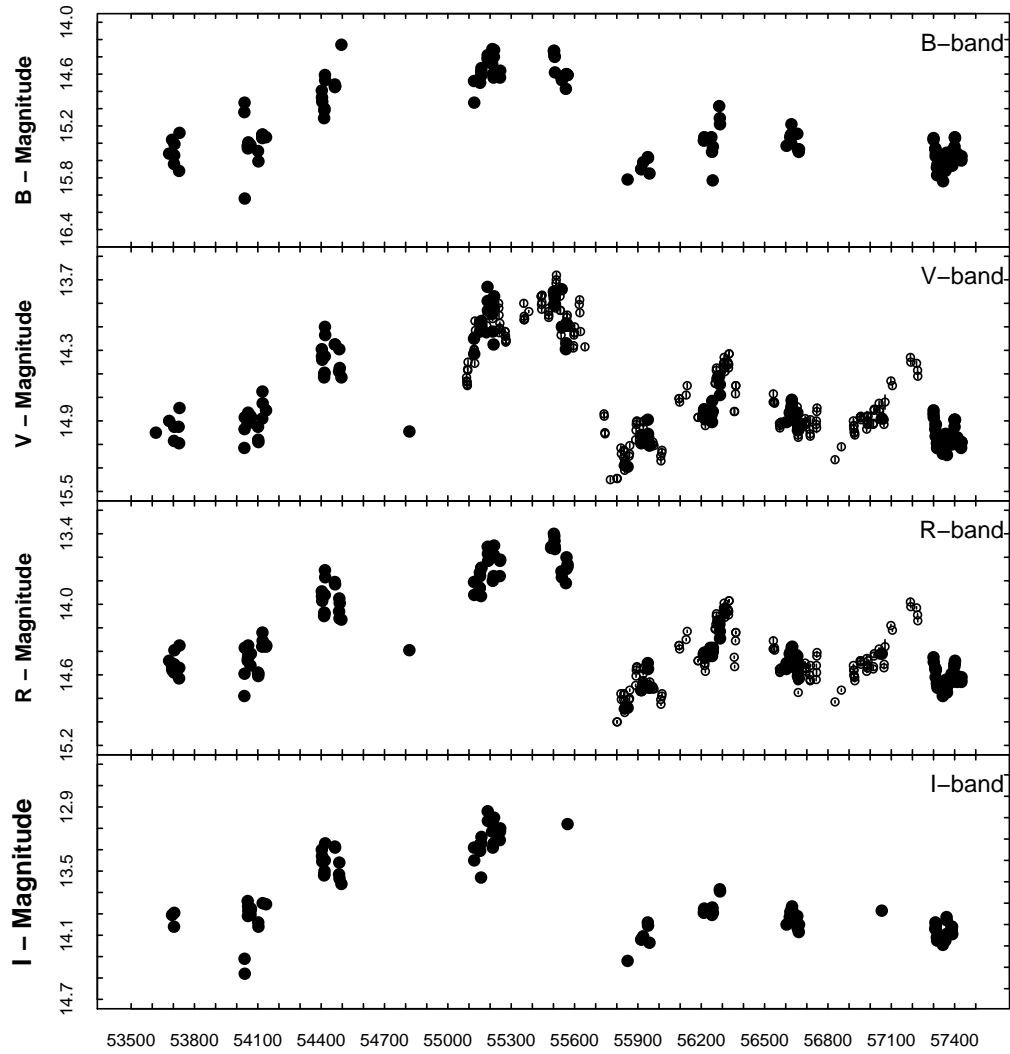


Figure 3.8: Light curves in B, V, R & I bands over the period of monitoring campaign for 3C 66A. Steward Observatory data in R & V bands are shown with open circles.

STVs with timescales of the order of days could be a result of the helical jet model (Marscher & Travis 1996). The source brightness varies with the viewing angle: the source is brighter when the viewing angle is small, but fainter when the viewing angle is large (Lainela et al. 1999a). However, perturbations and or instabilities in the accretion disk could also lead to such variations on longer time scales indicated in our light-curves.

We constructed L-S periodogram from the R-band light-curve data to check whether any quasi-periodicity exists in the long-term data series. We find significant (>99% confidence) power on a time scale of 2.48 years. DCF of the same data set also shows peaks separated by a time interval of about 2.50 years. It means that every 2.5 years or so, a major flare occurs in the jet, caused by, perhaps, a fresh injection of the plasma in the relativistic jet of the source 3C 66A. More data are required to arrive at a better analysis of the long term behavior of the blazar 3C 66A as there are several large gaps, even after including the R-band data from the Steward Observatory.

Considering the issue of whether INV and LTV are related in some way as a result of the processes in the relativistic jet, blazars are the best candidate to study such relationship. Since INV is mainly caused by the interaction of small scale inhomogeneities with the plasma in motion resulting in the enhancement of the synchrotron emission, and/or injection of fresh plasma in the jet, it can very well contribute to the long-term variability. Certainly these processes enhance the jet emission but it is more of a local effect than global. Perhaps it would be meaningful to find LTV time scales of variation and try to see if there was any correlation between short term and long term timescales of the variability . However, for this a well sampled data set is required to un-ambiguously determine the two timescales. In our study, INV amplitudes are inversely correlated to the brightness of 3C 66A but the correlation is not very strong as there are several outliers in the plot. The role of the disk in the long term variability (LTV) is understandable but when it comes to the rapid variations, processes in the jet are the most credible source of the variation. Certainly more study is required to address the interesting issue of a relationship between the short and the long

term variations.

3.4.6 Spectral variability during 2005-2016

In order to understand the spectral behavior of the source in the long term, we used the data obtained in the B, V, R and I bands for all the nights of our 10+ year campaign, irrespective of the duration of observation on a particular night. We take the average value of the brightness magnitude for the nights when it was monitored for intra-night variability in R-band. The light-curves thus generated in B, V, R and I bands are shown in Figure 3.8.

Blazars are known to exhibit varying patterns when it comes to the frequency dependence of the brightness. Most of the blazars show well known bluer-when-brighter (BWB) behavior at most of the epochs while few of them show redder when brighter (RWB) pattern, at least at some of the epochs. A section of blazars shows wavelength independence (achromatism) under the circumstances when external effects are causing the variation, such as micro-lensing. However, it is also seen that same source can exhibit quite different spectral behavior at different epochs. The explanation behind the spectral variations in the same source at different epochs is described by various authors - see, for example [Gu et al. \(2006\)](#); [Fiorucci et al. \(2004\)](#); [Kirk et al. \(1998\)](#); [Mastichiadis & Kirk \(2002\)](#). The change in the Doppler factor, fresh injection of the relativistic plasma interacting with the slowly moving plasma, emission from two different emitting regions could be the cause behind such spectral variations.

The color information for a particular source is important as it helps to discriminate among the various physical processes responsible for the variation. The present spectral analysis is carried out using the data in B, V, R, and I bands for all the observed nights from 2005 November to 2016 February. The colors i.e., (B-I), (B-V), (R-I), (V-R) are determined using the nightly averaged data taken at several epochs. We have plotted color-magnitude diagrams to study the spectral changes with respect to the brightness state of the source. The overall color trend, considering 10+ years of data, in 3C 66A is determined by performing least square fitting on an individual color plot. A straight line in the plot

represents the best fit to the data showing the value of slope on the upper-left corner and significance value (p-value) is shown in upper-left corner of each plot. In Figure 3.9, a mild bluer-when-brighter (BWB) trend is seen in (V-R) vs V and weaker one in (B-V) vs V. The trend seen in (B-R) vs R (cf Figure 3.10) is not significant at 95% confidence level with $p=0.191$. It is to be note that, the source is getting bluer very mildly over whole timeline (V-R color vs time in MJD) and other colors (B-V and V-R) show subdued variation with time, over the whole duration (2005-2016) plotted in Figures 3.11 & 3.12 .

The color trends are also studied by dividing the whole data-set into two parts for the each color-magnitude plot, see Figures 3.13 and 3.14 considering source in bright state i.e., $V < 14.5$ mag (filled black circles) and in faint state i.e, $V > 14.5$ mag (blue open circles). The best-fit line to the respective data is plotted, with the significance value written on the upper-left corner. The red solid line represents the best fit to the data when the source is bright and black solid line is best-fit to the data when the source is in faint state.

To understand the spectral behavior of IBLs over long-term period, we carried out a literature survey on the spectral properties of the 3C 66A and other IBLs which is briefly summarized here.

During the WEBT-ENIGMA multi-wavelength campaign in 2004, the BL-Lac object 3C 66A was extensively monitored which gave a hint of the spectral evolution during an optical flare (see Böttcher et al. 2005). The source showed a very weak positive correlation between the (B-R) color index and the R-band magnitude while in a low phase. A similar trend of the positive correlation was reported by Vagnetti et al. (2003) and Gu et al. (2006). Several studies indicated a significant spectral variation exhibited by 3C 66A when in the low-flux phase. However, there was no hint of any spectral variation during the high-flux phase ($R < 13.5$) of the source (Böttcher et al. 2009; Rani et al. 2010). To understand the spectral variation as a function of the average brightness of the source, we categorized source to be in high state when $R \leq 14.0$ and in low state when $R > 14.0$. Using the Pearson's product moment correlation, we computed correlation and the significance of correlation in the low and high states for V-R and B-V.

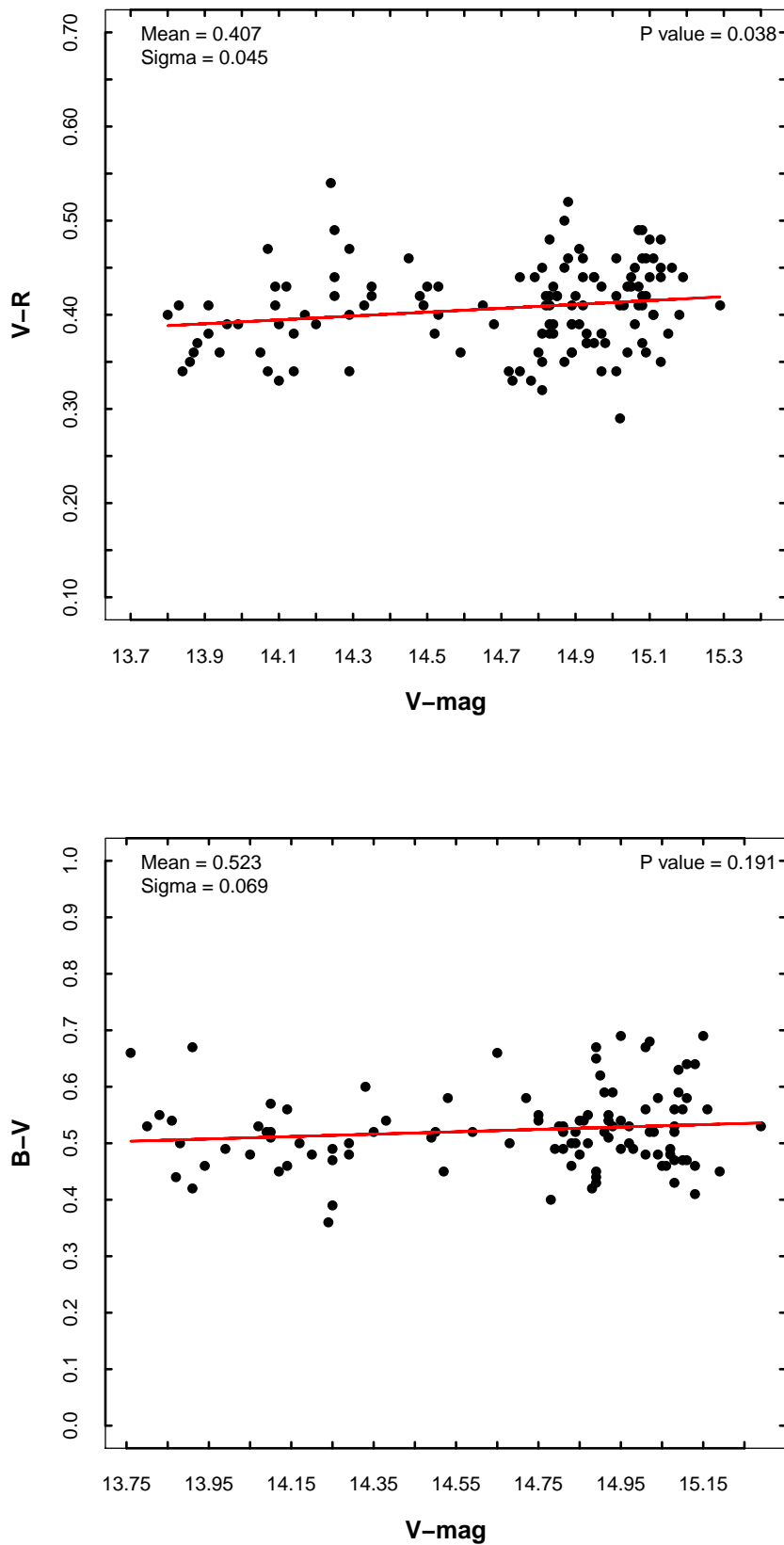


Figure 3.9: Color as a function of the brightness of the source, 3C 66A is plotted. The regression line shows best fit to the data at 95% confidence level.

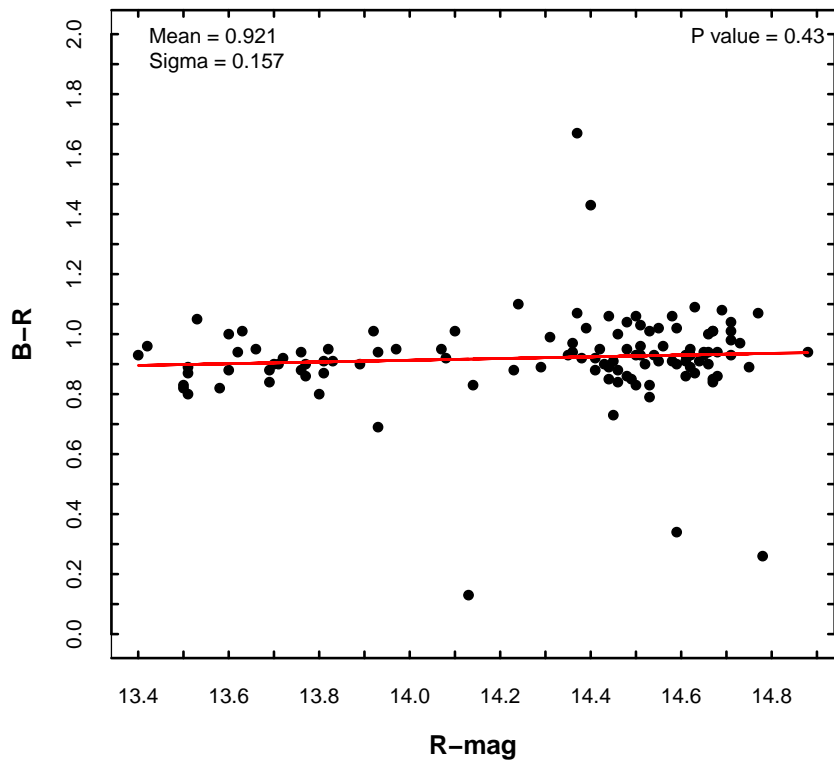


Figure 3.10: Color as a function of the brightness of the source, 3C 66A is plotted. The straight line shows best fit to the data at 95% confidence.

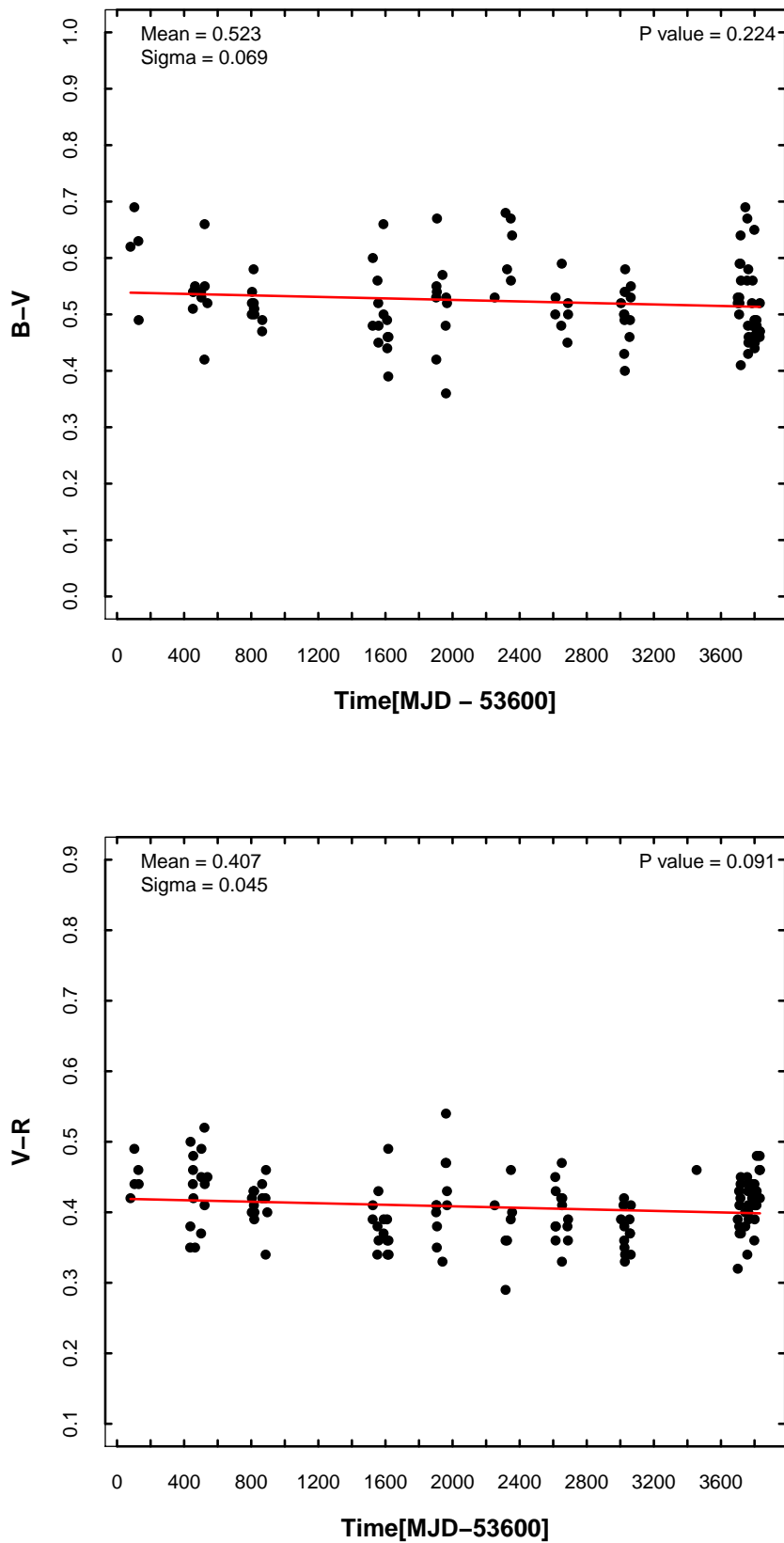


Figure 3.11: Color as a function of the time for the source, 3C 66A. The straight line shows best fit to the data.

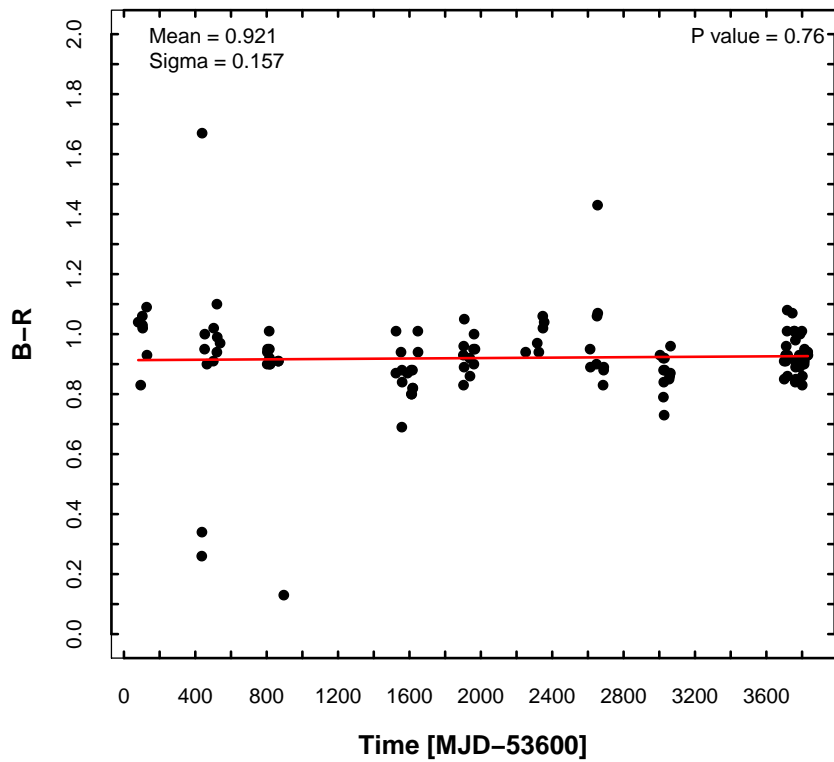


Figure 3.12: Color as a function of the time for the source, 3C 66A. The straight line shows best fit to the data, p value is obtained at 95% confidence.

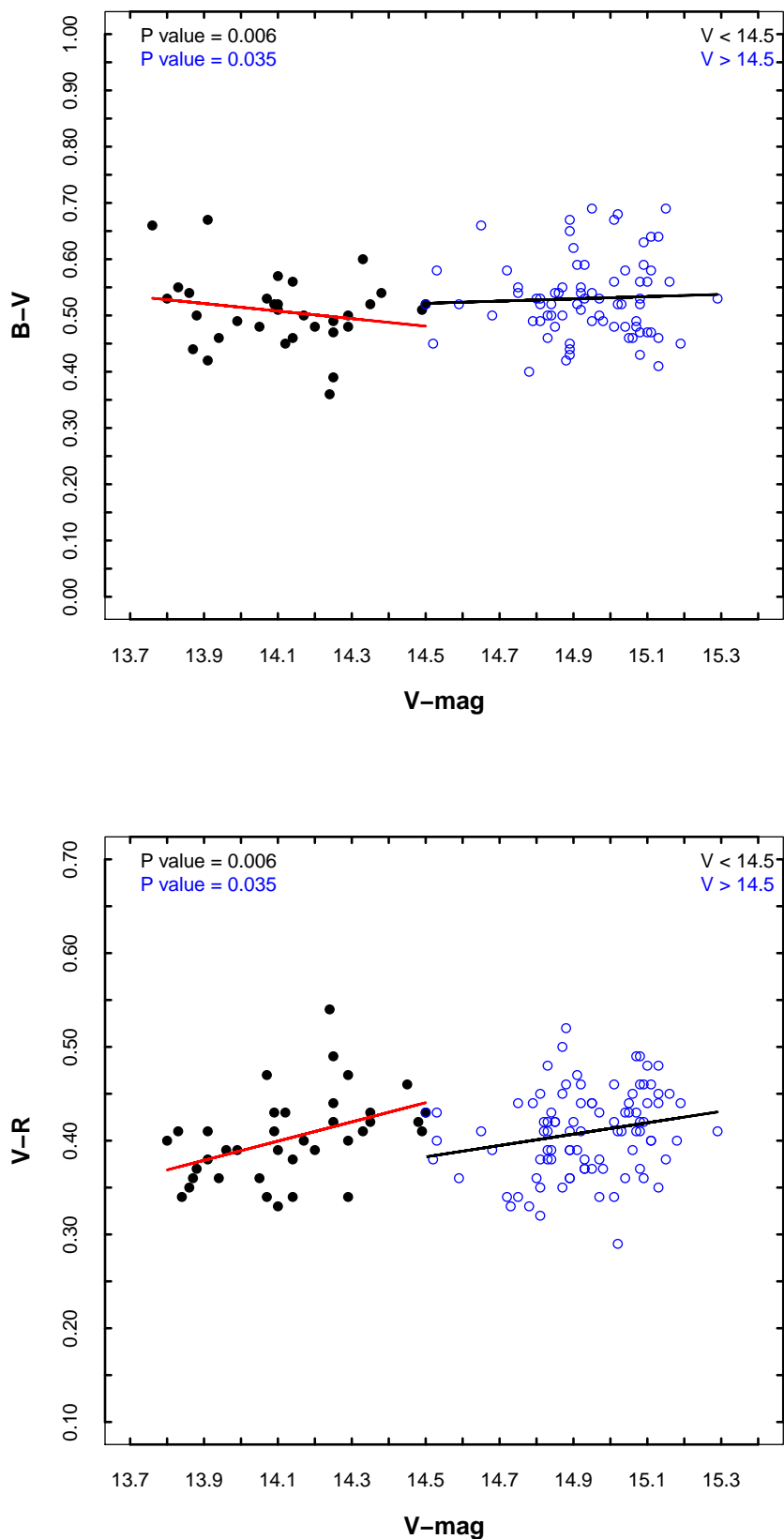


Figure 3.13: Respective colors are plotted along Y-axis and the average magnitude along the X-axis. The regression line fit at 95% confidence level lines show significant trend on the data during the bright state ($V < 14.5$ mag; black) and the faint state ($V > 14.5$ mag; blue) of the source, 3C 66A.

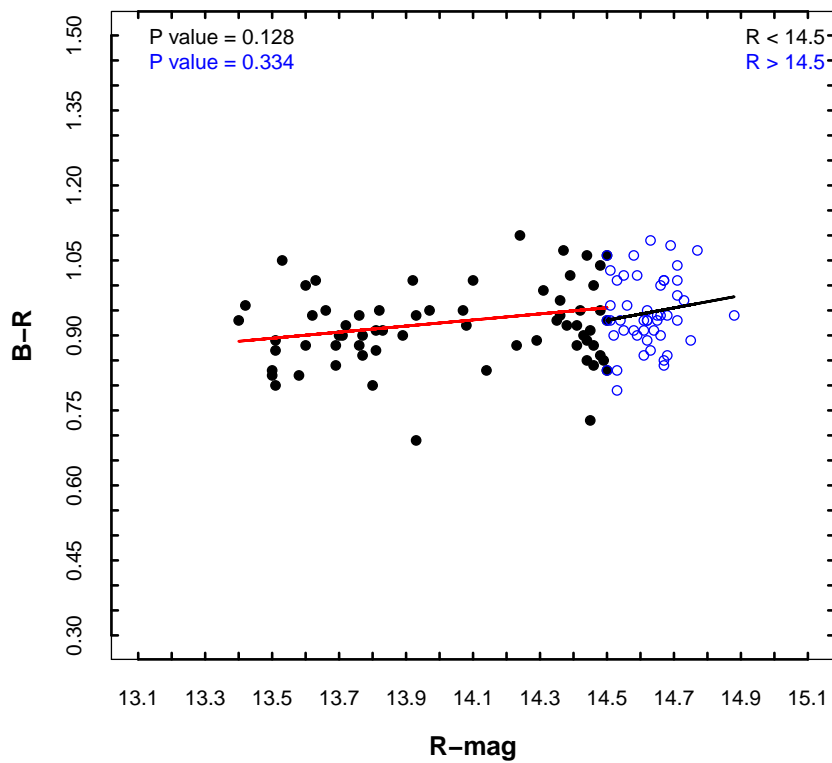


Figure 3.14: Respective colors are plotted along Y-axis and the average magnitude along the X-axis. The straight lines show the least square fitting on the data during the bright state ($V < 14.5$ mag; black) and the fainter state ($V > 14.5$ mag; blue) of the source, 3C 66A. The trends are significant at 95% confidence level.

Our results show almost similar correlations in both the cases, whether source is in the low or high state of brightness. Both show a mild bluer when brighter trend.

Generally, blazars are found to follow a common trend of getting bluer when in brighter phase, but we cannot rule out the observational evidence for a few blazars getting redder when brighter (Stalin et al. 2006). This scenario really needs a careful look on the color index, spectral slope and brightness of the source before drawing any general conclusion about the category of the blazars. Also, Raiteri et al. (2003) reported the different spectral behaviors found at shorter timescales while Gu et al. (2006) found no correlation between color vs brightness of the source during the INV nights. There are reports on different color behavior in a sample of FSRQs and BL-Lacs too (Raiteri et al. 2012). Their study distinctly shows a RWB color for the FSRQs and BWB trend for the BL Lacs, in general.

In the present study, the source 3C 66A showed a mild bluer when brighter trend that could be explained based on the shock-in-jet model (Marscher & Gear 1985). Also, it can occur when an increase in the luminosity of the blazar is caused by the injection of a population of fresh electrons/plasma with a harder energy distribution than the older partially cooled ones (Mastichiadis & Kirk 2002). We have also studied the behaviour of the color as a function of the time during the 10 year period presented here. We notice a very weak trend of decrease in the color with time.

Considering the issue of whether INV and LTV are related in some way as a result of the processes in the relativistic jet, blazars are the best candidate to study such relationship. Since INV is mainly caused by the interaction of small scale inhomogeneities with the plasma in motion resulting in the enhancement of the synchrotron emission, and/or injection of fresh plasma in the jet, it can very well contribute to the long-term variability. Certainly these processes enhance the jet emission but it is more of a local effect than global. Perhaps it would be meaningful to find LTV time scales of variation and try to see if there was any correlation between short term and long term timescales of the variability . However, for this a well sampled data set is required to un-ambiguously determine

the two timescales. In our study, INV amplitudes are inversely correlated to the brightness of 3C 66A but the correlation is not very strong as there are several outliers in the plot. The role of the disk in the long term variability (LTV) is understandable but when it comes to the rapid variations, processes in the jet are the most credible source of the variation. Certainly more study is required to address the interesting issue of a relationship between the short and the long term variations.

3.5 Summary

Long term high spatial resolution data are presented for the duration from 2005 November to 2016 February for the blazar 3C 66A. The data are used to study the variability duty cycle and the extent of the intra-night variability. The intra-night variability is ascertained using the variability test, structure function and the amplitude of variation. Nightly averaged B, V, R and I magnitudes for the whole duration obtained from MIRO along with R and V band data from Steward Observatory, where available, are used to address the long term variability and color behaviour of the blazar 3C 66A during this period. Based on these observational results, following conclusions are drawn:

1. The duty cycle for the intra-night variability in 3C 66A is about 8%, which is relatively lower for BL Lacs, perhaps due to short duration monitoring.
2. The variability time scales for the INV vary from about 37 minutes to about 3 hrs indicating to different sizes for the emission regions. The shortest time scale of variation leads to an upper limit on the size of the emission region as 6.92×10^{14} cm. Consequently, the mass of the central SMBH is estimated to be about $3.7 \times 10^8 M_{\odot}$, assuming the origin of the variability from the region very close to the central engine.
3. Quasi-periodic variations (QPVs) are probably present in the light-curve of one of the INV nights with a period of about 1.4 hrs. This could be the result of the plasma streamlet progressing down the jet in a helical motion, described under the shock-in-jet model.

4. Long term trend in the source brightness shows a large number of flares superposed on the slowly varying pattern. There is an indication of a periodicity of about 2.5 years, however large gaps in the data forbid us to state it confidently.
5. The amplitude of the intra-night variability shows a trend of being larger when the source is fainter. However, more INV data on 3C 66A and many other blazars are required to investigate and confirm it and look for possible processes responsible.
6. A slowly decreasing trend in the average brightness with time and a mild bluer when brighter behavior are noticed, the later supports the shock-in-jet model, typical for BL Lacs.

Chapter 4

Optical Study of Flaring S5 0716+714

One of the most active blazar which is studied extensively to investigate variations, is IBL S5 0716+714. With an aim to explore optical variability at diverse timescales in BL Lac source S5 0716+714, it was observed for 46 nights during 2013 January 14 to 2015 June when it underwent two major outbursts. The observations were made using 1.2-m Mount Abu InfraRed Observatory telescope mounted with CCD camera. On 29 nights, source was monitored for more than two hours, resulting in 6256 data points in R-band, to check for the intra-night variability. Observations in B, V and I bands with 159, 214, and 177 data points, respectively, are used to address inter-night and long term variability and the color behavior of S5 0716+71. The study suggests the source showing significant intra-night variability with a duty cycle of more than 31% and night-to-night variations. The average brightness magnitudes in B, V, R & I bands were found to be 14.42(0.02), 14.02(0.01), 13.22(0.01), 13.02(0.03), respectively, while S5 0716+714 was historically brightest with $R = 11.6$ on January 16, indicating that source was in relatively high state during this period. A mild bluer when brighter behavior, typical of BL Lacs, supports the shock-in-jet model. We notice larger amplitudes of variation when source was relatively brighter. Based on the shortest time scale of variability and causality argument, upper bound on the size of the emission region is estimated as 0.9×10^{15} cm and the mass of the black hole as $10^9 M_{\odot}$.

4.1 Introduction

Since AGN are not resolvable by any existing telescope facility, understanding their structure and emission mechanisms is a big challenge. Blazars, which are variable over diverse time-scales across the whole spectrum, provide a viable tool where their variability time-scales, correlations among multi-frequency light-curves, color variations and SEDs are used as probes (Marscher et al. 2010; Dai et al. 2015; Ciprini et al. 2007, and references there-in). (For details on the blazar properties, please refer to Chapter 1 & 3). Though the mechanisms responsible for the variability remain unclear, long term variability could be due to the disk perturbation/instability or structural changes in the jet, e.g., precession, bending of jet (Marscher & Gear 1985; Kawaguchi et al. 1998; Nottale 1986; Nair et al. 2005). The STV in optical flux, including inter-night variability, could be caused by intrinsic and extrinsic processes, e.g., injection of fresh plasma in the jet, shock moving down the turbulent jet, changes in the boosting factor due to change in the viewing angle, gravitational micro-lensing etc, and sometime results in the spectral changes (Ghisellini et al. 1997; Villata et al. 2002). The INV, also known as microvariability, could be due to shock compression of the plasma in the jet, shock interacting with local inhomogeneities, blob passing through standing core, changing the viewing angle in a jet-in-jet scenario (Narayan & Piran 2012a) or other processes causing small scale jet turbulence (Marscher & Gear 1985; Marscher 2008; Chandra et al. 2011).

The intermediate BL Lac object S5 0716+714 is one of the most active blazars and makes a perfect candidate for variability study on the blazars at diverse time scales (Aliu et al. 2012). It is available in the sky for longer time during the night (due to its high declination), is almost always active, fairly bright, and hence can be observed with moderate facilities. It was discovered by Kuehr et al. (1981) in NRAO 5 GHz radio survey with flux larger than 1 Jy¹ and due to its featureless spectra (Biermann et al. 1981), was categorized as a BL-Lac source. Nilsson et al. (2008) derived a redshift of 0.31 ± 0.08 by taking host galaxy as a standard candle, but recently Danforth et al. (2013) put a statistical upper limit of $z <$

¹1 Jansky = 10^{-23} erg cm⁻² s⁻¹ Hz⁻¹

0.322 (with 99% confidence) on its redshift. The S5 0716+714 shows high duty cycle of variation (DCV) as reported by [Chandra et al. \(2011\)](#), and references there-in). Due to all these properties, it has been the target of several multi-wavelength campaigns around the globe ([Wagner & Witzel 1995](#); [Villata et al. 2002](#); [Raiteri et al. 2005](#); [Nesci et al. 2005](#); [Montagni et al. 2006b](#); [Gupta et al. 2008](#); [Dai et al. 2015](#)), focusing on INV and STV. After being reported in its high phase, the object was followed by [Bachev et al. \(2012\)](#) who claimed historical maxima and minima of 12.27 (MJD 56194) and 12.08 (MJD 56195) in R-band, respectively. [Rani et al. \(2013\)](#) found the γ -ray emission to be correlated with optical and radio, supporting SSC mechanism responsible for the high energy emission. However, an orphan flare in X-ray indicated to the limitation of such simple scenario.

Investigating the long-term variability trend, [Nesci et al. \(2005\)](#), and references there-in) reported a decreasing average brightness of the source during 1961-1983 followed by an increasing one upto 2003, superposed with short term flares. They extracted source brightness data from photographic plates obtained from the Asiago Observatory, POSS1 and Quick V surveys dating back to 1953 to generate long term light curves. It underlined the importance of the astronomical data, even if taken for some other purpose. From all these data, they even predicted a decrease in the mean brightness of the source during next 10 years, i.e., after 2003. In fact the source was inferred, from the data during 2003 to 2014, to be in decreasing brightness phase by [Chandra et al. \(2014\)](#), and the present work, suggesting a precessing jet during which viewing angle started to increase. The blazar S5 0716+714 has undergone several optical outbursts in the past, superposed on average decreasing or increasing trends as reported by many workers ([Raiteri et al. 2003](#); [Nesci et al. 2005](#); [Gupta et al. 2008](#); [Larionov et al. 2013](#)). Micro variability (INV) on the time-scales of a few hours to 15 minutes is reported by ([Chandra et al. 2011](#); [Rani et al. 2013](#); [Man et al. 2016](#), and references there-in) with source showing bluer-when brighter (BWB) behaviour in general. On the other hand, [Raiteri et al. \(2003\)](#) found a weak correlation with color, while others did not find any correlation between color and brightness([Stalin](#)

et al. 2009; Agarwal et al. 2016; Wu et al. 2005). The blazar S5 0716+714 has also been reported to show (quasi-) periodic variations (QPV) in optical at several epochs and at many time scales ranging from hours to years (Raiteri et al. 2003; Gupta et al. 2008). However, Bhatta et al. (2016) did not find 3 and 5 hr QPV genuine.

Recently, S5 0716+714 was reported achieving new historical brightness levels (11.68 in R-band) in optical on 2015 January 20 by Chandra et al. (2015a,b), reassuring that it will never stop to surprise us. It, therefore, justifies a continuous coverage of the source in order to help us understand the nature of blazars in general and S5 0716+714 in particular. Keeping this objective in mind and to understand the variability characteristics, chromatic behaviour and relationship between variability amplitude and brightness of the source, here we present our results obtained from the observations during January, 2013 to June, 2015. Section 2 describes the observations and data analysis, section 3 presents the results and discussions while section 4 summarizes the work.

4.2 Observations and Data Reduction/Analysis

To investigate intra-night and inter-night variability in BL-Lac source S5 0716+714, we carried out the optical observations using 1.2m telescope of the Mount Abu Infrared Observatory(MIRO), operated by the Physical Research Laboratory, Ahmedabad. The observatory is located at Gurushikhar mountain peak, about 1680 m above the sea-level, in Mount Abu (Rajasthan), India, which provides a typical best seeing of 1.2 arcsec. The observations were taken with liquid-nitrogen cooled Pixcellent CCD camera as backend instrument, equipped with Johnson-Cousins optical BVRI filter set. The dimension of CCD array is 1296 x 1152 pixels of size 22 μm each. The field of view (FOV) is about 6.5 x 5.5 arcmin² with a plate scale of 0.29 arcsec/pixel. The CCD readout time is 13 seconds with readout noise of four electrons and negligible dark current when cooled to temperature of about -120°.

In order to study INV (microvariability), as a strategy, we monitored the

source for a minimum of two hours in the Johnsons R-band with a high temporal resolution (less than a minute) to resolve any rapid flare, while for STV and LTV in the source brightness and color, 4/5 images were taken in B, V, I-bands everyday during the campaign period. The source and its comparison/control stars ², – having brightness close to that of the source (Howell & Jacoby 1986) were kept in the same frame. The differential photometry was performed which minimizes the effect of non-photometric conditions, like minor fluctuations due to turbulent sky and other seeing effects. The exposure time was decided by keeping the counts well below the saturation limit and in the linear regime of CCD (Cellone et al. 2000b). Several twilight flat field images and bias images were taken on each observation night to calibrate the science images. By following the above mentioned strategy, a total of 6256, 159, 214 and 177 images in R, B, V and I-band, respectively, with exposure times varying from 30 (I band) to 60 (B-band) seconds, were obtained and subjected to analysis.

The observed data were checked for spurious features, if any, and reduced using IRAF³ standard tasks- bias subtraction, flat fielding, cosmic ray treatment etc. The comparison stars 5 and 6⁴, present in the source field were chosen to perform differential photometry. Other stars (stars 2 and 3) in the field were too bright to be used for differential photometry as they could introduce errors (from differential photon statistics and random noise, like sky) (Howell et al. 1988b). An optimum aperture size, three times the FWHM, was used based on the prescription by Cellone et al. (2000b), as a smaller apertures can give better Signal-to-Noise(SNR), but might lead to spurious variations if the seeing was not good, while a larger aperture would have significant contribution from the host galaxy thermal emission(Cellone et al. 2000a) and might suppress the genuine variations in the blazar flux. Aperture photometry on the blazar S5 0716+714 and comparison stars 5 & 6, using the same aperture size, was performed using

²<http://www.lsw.uni-heidelberg.de/projects/extragalactic/charts/0716+714.html>

³IRAF-Image Reduction and Analysis Facility is data reduction and analysis package by NOAO, Tuscon, Arizona operated by AURA, under agreement with NSF.

⁴Stars taken from the sequence A,B,C,D by Ghisellini et al. (1997) and corresponding sequence, 2, 3, 5, 6 by Villata et al. (1998)

DAOPHOT package in IRAF on photometric nights.

The aperture photometry technique was employed on total 6806 images in BVRI-bands and the source magnitudes were calibrated with the average magnitude of the comparison star 5 and 6, which were also used to check stability of the sky during the observations, as described in equation 1 and equation 2. No correction for host galaxy of S5 0716+714 was applied as the host galaxy is much fainter (R-band >20 mag; Montagni et al. (2006b)) than the central bright sources. The differential light curves (*LCs*) were constructed to detect INV, while BVI & R band long term *LCs* were generated from daily averaged values in each band. To quantify the INV nights, we applied several statistical tests, for example confidence parameter test (C-test), amplitude of variability (A_{var}) test, as discussed in the next section.

4.3 Results and discussion

As already mentioned earlier, the photometric data obtained after the aperture photometry were used to plot the intra-night and inter-night light curves. Though lightcurves themselves are not sufficient to reveal the complexities of the variability and blazar phenomena, these are good indicators of the emission mechanism and can help put constraints on various models. The nature of most of the light curves differ from one night to other, indicating to the emission from random and turbulent process in the jet. Since the physical mechanisms which trigger blazar variability, especially on intra-night time scales, are still debatable, any detailed study of *LCs* should add to our understanding.

In order to identify and characterize the nights showing INV, we performed variability amplitude and confidence parameter (C-test) tests. In the following we also discuss STV, LTV and color behaviour of the source during the period of our observing campaign.

4.3.1 Intra-night variability

The blazars show rapid variability which can sample very compact sizes of emission regions. To determine the number of INV nights, we first excluded the not-so-photometric nights and those with less than two hours of monitoring. We were left with 29 nights to qualify this criterion during 2013 January - 2015 June. The *LCs* for S5 0716+714, being very complex with a number of features, it was very difficult to infer INV from just visual inspection, barring a few cases. To resolve this problem, we used C-test, F-test and amplitude of variation (A_{var}) statistical methods, which have been described in detail in earlier chapters,.

INV light curves and duty cycle of variation (DCV)

After performing statistical tests on the entire data set, we get 9 out of total 29 nights which are found variable based on all the above mentioned criteria i.e., $C \geq 2.57$, $F \geq 5$ for more than 99% confidence level and $A_{var} \geq 0.05$. Figure 1 shows the light curves for these INV nights where time in Modified Julian Date (MJD) is plotted along X-axis and the brightness magnitude in R-band along Y-axis. Lower plot is the differential *LC* for the two comparisons (5 and 6), to check the stability of that particular night, thus providing extent of uncertainty in the source values. The *rms* values of these differential lightcurves for comparison stars indicates to the accuracy of our magnitude measurements. Upper curve (solid circles) shows the calibrated brightness magnitudes for the source. Photometric errors are plotted which are of the order of a few milli-magnitudes.

The INV light-curves (Figures 4.1–4.5) feature monotonic rise or fall, slow rise or decay with rapid fluctuations superimposed on it, alongwith a few *LCs* indicating to a possibility of the quasi-periodic oscillations with short timescale. It can be noted that the shapes of the most of the nightly curves are different, as also reported by several other authors (Chandra et al. 2011; Kaur et al. 2017c, and references there-in) indicating that the emission processes are stochastic and complex in nature. A symmetric flare lightcurve would mean the cooling timescale is much shorter than the light-crossing timescale. On the night of 2013 February 12 (Fig. 4.1), the brightness decays slowly with no distinct peak, with total

change in the amplitude of variation by about 7.5%. In the same figure, a slow increase in flux by about 0.07 mag in about 2.6 hr, with several rapid fluctuations superimposed (including one with 0.04 mag in about 30 min) is noticed on 2013 March 6. Next day *LC* (Fig. 4.2) starts with slight decreasing trend but begins brightening up at MJD 56358.88, with a rapid increase after 1.44 hr leading to 0.06 mag (2σ). The flux decreases up to MJD 56607.0 and then remains stable within errors on 2013 November 11 (Fig. 4.3). The *INV LC* on 2013 March 12 shows interesting features with a brightening by 0.11 mag in about 30 min, followed by a decay of about 0.17 mag in about one hour. It starts increasing again reaching initial level of about 13.41 mag. A slow decrease in flux and then relatively faster increase by about 0.07 mag within about 70 min characterizes the *LC* on 2013 December 28 (Fig. 4.3). A significant increase in flux by 0.13 mag within about 2.9 hr is noticed on 2013 December 30 (Fig. 4.4) while on 2014 December 02 night, brightness decreases continuously, with no peak. On 2014 December 3 (Fig. 4.5), flux rises by 0.08 mag within 2.4 hr during the total monitoring of about 6 hrs.

However, it is difficult to determine variability time scales accurately only from visual inspection of *LCs* and therefore, in the next section we introduce and use structure functions and later analysis them for to estimate required parameters.

Duty Cycle of variation: Most of the blazars show very high probability of variation even on intra-night time scales with an amplitude of variation of a few tenths of magnitude. In order to quantify the probability of variation, duty cycle of variation (DCV) is often used. The DCV is defined as a fraction of the total number of nights the source is monitored (Romero et al. 1999) for, which are found variable. An expression to estimate DCV is given by,

$$DCV = 100 \frac{\sum_{i=1}^n (N_i / \Delta t_i)}{\sum_{i=1}^n (1 / \Delta t_i)} \% \quad (4.1)$$

where, $\Delta t_i = \Delta t_{i,obs} (1+z)^{-1}$ is duration of monitoring, corrected for redshift and N_i is 0 or 1 depending on whether the source is non-variable or variable, respectively.

Several authors ([Wagner & Witzel 1995](#); [Chandra et al. 2011](#); [Dai et al. 2015](#), and references there-in) have reported INV *DCV* for S5 0716+714 ranging from 40% to 100% during their observations, which indicates that the source is almost always active. In our case, 9-nights out of a total of 29 nights monitored for more than two hours, are detected as confirmed variable. Thus based on our observations during 2013-2015, we get a value of 31% as duty cycle, which is on the lower side. Reasons could be that we monitored the source, by chance, when it did not show much activity or our duration of monitoring may not be sufficient. In order to check for any connection between the INV shown by the source and the duration over which it was monitored, we calculated the duty cycle with more than one hour and two hour monitoring period. Out of the total 46 nights of observation during 2013-2015, we find 35 nights and 29 nights monitored for a minimum of one hour and two hours, respectively. Based on these, we obtained INV duty cycle values for the S5 0716+714 as 26% and 31%, respectively, in two cases. It, therefore, indicates that longer the duration of monitoring, more will be the probability of finding a source variable, i.e., a higher DCV.

Rise & fall rates of variation in INV lightcurves: To investigate the extent of the intra-night variability of the source, we determined rate of change in magnitude (rise/fall) on each INV night for S5 0716+714 by fitting a line segment to light curves. During our observations, 2013 February 12 and 2013 December 28 represent the nights with minimum and maximum rates of change in the magnitudes of the source with $0.015 \text{ mag hr}^{-1}$ and $0.381 \text{ mag hr}^{-1}$, respectively. The rate of brightness change on 2013 December 28 happens to be one of the fastest for this source. Earlier, [Chandra et al. \(2011\)](#); [Man et al. \(2016\)](#) have reported 0.38 mag/hr & 0.35 mag/hr rates, respectively. Rate of change in magnitude as high as $0.43/\text{hr}$ has been reported for the PKS 2155-304 ([Sandrinelli et al. 2014](#)). The source showed smooth decline in its brightness by 0.05 mag on February 12 with 7.60% amplitude of variability. On 2013 March 6, S5 0716+71 became brighter by 0.08 mag in 3 hours with rapid fluctuations (few tens of minutes duration) superposed over the day-long trend showing 7.58% amplitude of variation in the light curve. On 2013 March 7, brightness decreases from 13.90 mag to al-

most 13.95 mag within an hour, after which source brightened by more than 0.1 mag in next 3 hours with a rate of change of 0.03 mag hr^{-1} . On 2013 March 12, light-curve shows a sine like feature, with rising (0.1 mag in 30 min) - declining (0.2 mag in 72 mins) - rising (>0.2 in about 72 min approx.) trends in brightness over the duration of more than three hours.

Table 4.1: Details of the rate of rise/fall in the magnitude for INV nights. Δm_+ , Δm_- represent the source brightening or dimming, respectively.

Date	Trend	Rise/Fall mag ($\Delta m_+/\Delta m_-$)	Duration (in minutes)	Rate= $\Delta m/\Delta t$ (mag/hr)
12-02-2013	Fall	0.05 (Δm_-)	198 mins	0.015
06-03-2013	Flickering over	0.08 (Δm_+)	>150 mins	0.02
	Monotonous rise			
07-03-2013	Fall	0.05 (Δm_-)	72 mins	0.03
	Rise	0.12 (Δm_+)	144 mins	
12-03-2013	Sine like	0.1 (Δm_+)	30 mins	0.05
	pattern	0.2 (Δm_-)	72 mins	
		0.2 (Δm_+)	72 mins	
11-11-2013	Fall	0.08 (Δm_-)	> 72 mins	0.04
28-12-2013	Fall with	0.08 (Δm_-)	72 mins	0.38
	Flickering	0.02 (Δm_-)	few tens of minutes	
30-12-2013	Monotonic rise	0.14 (Δm_+)	144 mins	0.07
02-12-2014	Monotonic fall	0.02 (Δm_-)	216 mins	0.05
03-12-2014	Sine like	0.08 (Δm_-)	288 mins	0.02

The light curve on 2013 December 28 showed sharp rise/fall magnitudes over two peaks and again showed rising trend with overall change in magnitude by 0.38 mag hr^{-1} . However, the features in the light curves are asymmetric in nature, which rules out variation being caused by extrinsic mechanisms. The variability in blazars is stochastic in nature at almost all timescales. The flares, therefore, appear to be produced independently and any similarity & difference might reflect different scales of particle acceleration and energy dissipation (Nalewajko et al. 2015). The variations in blazars are caused largely in the jet but it is difficult to ascertain whether these are intrinsic or geometric in nature. Intrinsic variations are dissipative and not reversible in time. Hence they should cause asymmetric flares. The geometric variations, on the other hand, are symmetric in time (Bachev et al. 2012). The intrinsic variability could be due to fast injection of relativistic electrons and radiative cooling or escape of particles or radiation from the emission zone. The symmetric flares, however, might result if cooling time scale is much shorter than the light crossing time (Chatterjee et al. 2012).

The INV *LCs* are, in general, asymmetric and complex indicating the random/turbulent nature of the flow inside the jet. Based on the visual inspection of these curves, we categorized three observed trends:

- a) Rapid intra-night changes in the source flux, indicating to the violent, evolving nature of the shock formed in the jet. It might either be due to presence of oblique shocks or instabilities in the jet.
- b) The steady rise or fall in the light-curve during a night indicates to the light crossing timescale to be shorter than the cooling time scale of the shocked region. It is when data series is shorter than characteristic time scale of variability.
- c) The small-amplitude rapid fluctuations (asymmetric in shape) superimposed over slowly varying light curve suggest small scale perturbations in the shock front or oscillations in the hot-spots downstream the jet and may not be associated with emission region size.

The details of INV nights are provided in Table 4.2, with the date & time of observation, duration of monitoring, number of data points, average magnitude of the source and values of the statistical parameters such as C , A_{var} etc.

Table 4.2: Details of INV nights for the source S5 0716+714 during 2013-2015. The statistical parameters mentioned, i.e., C and A_{var} , have been calculated at 99% confidence level, N is no of data points and σ is standard deviation in nightly averaged magnitude.

Date of observation	MJD	T_{start} (hh:mm:ss)	Duration hrs	N ⁵	$\bar{m} \pm \sigma$	C	A_{var} (%)	t_{var} hrs
12-02-2013	56335.84038	20:10:09	3.28	195	13.94 ± 0.02	2.63	7.60	2.36
06-03-2013	56357.96250	23:06:00	3.47	237	14.10 ± 0.02	2.72	7.58	1.68
07-03-2013	56358.82424	19:46:54	3.72	203	13.90 ± 0.03	4.46	11.38	2.04
12-03-2013	56363.84308	20:14:02	2.83	229	13.50 ± 0.05	8.90	15.61	1.11
11-11-2013	56607.03115	00:44:51	1.88	139	14.08 ± 0.02	4.62	9.75	0.96
28-12-2013	56654.88889	21:20:00	2.48	284	14.72 ± 0.02	2.65	11.89	0.76
30-12-2013	56656.90536	21:43:43	2.27	350	14.30 ± 0.05	7.55	15.38	3.1
02-12-2014	56993.05133	01:13:5	4.58	284	13.41 ± 0.06	12.37	20.50	3.54
03-12-2014	56994.98155	01:13:55	5.97	454	13.27 ± 0.03	5.23	10.07	3.89

Variability timescale, size of emission region and black hole mass

It is important to know the characteristic timescale of intra-night variability which puts constraints on the emission size and structures of the blazar emission zones. The rapid variations with duration of a few hours originate, perhaps, in the close vicinity of the central engine where jets are launched and might be caused by a combination of accretion disk instability, shock propagating within the jet, and, or particle acceleration and consequent radiative cooling at the jet base (Ulrich et al. 1997). Since the INV light curves are complex, we use structure function(SF), as described in Chapter 2, to discuss features in the intra-night light curves and estimate INV timescales and any possible quasi-periodicity.

Figure 4.6 shows these structure functions for the INV night light curves. It is seen that first order SF for several nights does not show any plateau, that means that the characteristic timescale of variability is longer than the length of the observational data (Dai et al. 2015). The local maximum following the smooth rise in the SF- τ plane reveals time-scale of variability introduced by the presence of minimum and maximum or vice-versa in the curve. If the SF consists of more than one plateau with slopes (β) following a power-law trend, presence of multiple timescales is inferred. If periodicity is present, it will be seen as local minima in SF after the local maximum. The difference between two minima gives the time period. The timescale of the variability obtained for all the INV nights are given in Table 4.2.

On several nights (2014-12-02, 2013-03-07, 2013-11-11, & 2013-02-13), SF shows continuous increase with none or feeble plateau, indicating that characteristic time scale of variability is longer than the monitoring period, giving only a lower limit of the variability time scale. While *LC* for the night 2013 March 12 shows several features, SF shows only one plateau and then a dip at about 2.2 hr. On December 13, 2013, SF shows a discernible peak with a time scale of 3.11 hr, followed by a rise again. SF for INV night of 2014 December 14 shows a plateau at 2.89 hr. As can be seen, INV night 2013 December 28 shows a plateau in its SF giving the shortest characteristic timescale of variability of about 45.6 minutes during our observing campaign. The details of the SF parameters for all

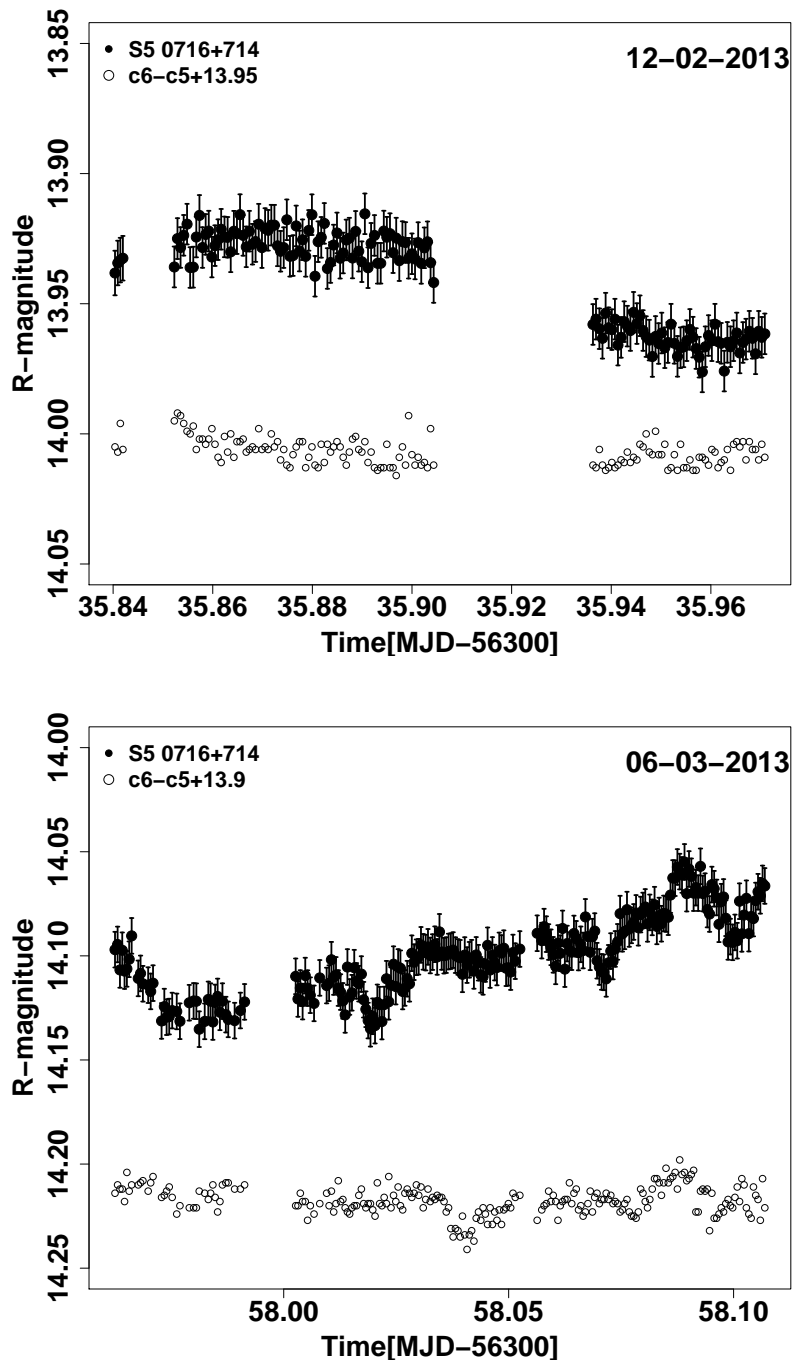


Figure 4.1: Intra-night light curves for the source S5 0716+714 during January, 2013 to June, 2015.

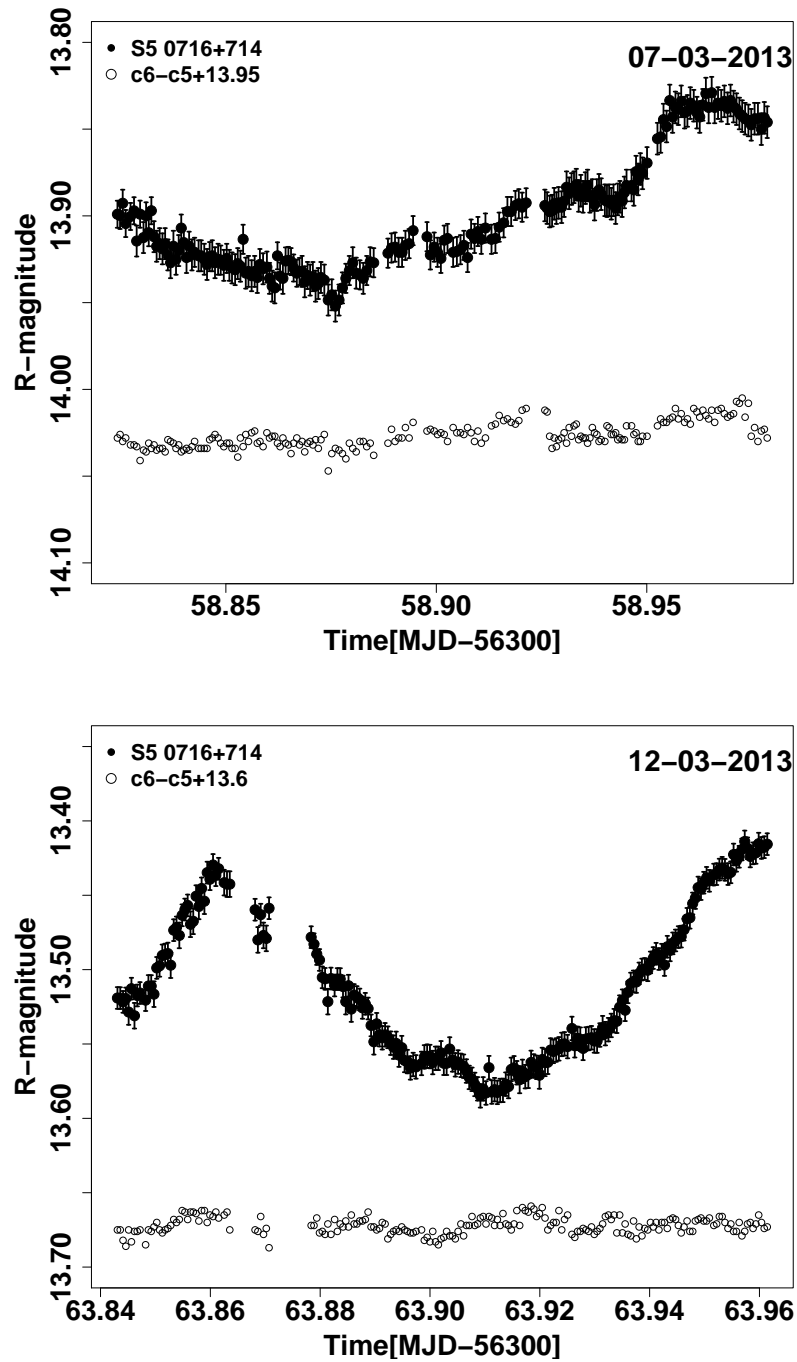


Figure 4.2: Same as for Fig. 4.1, but for 2013 March 7 & March 12 INV nights

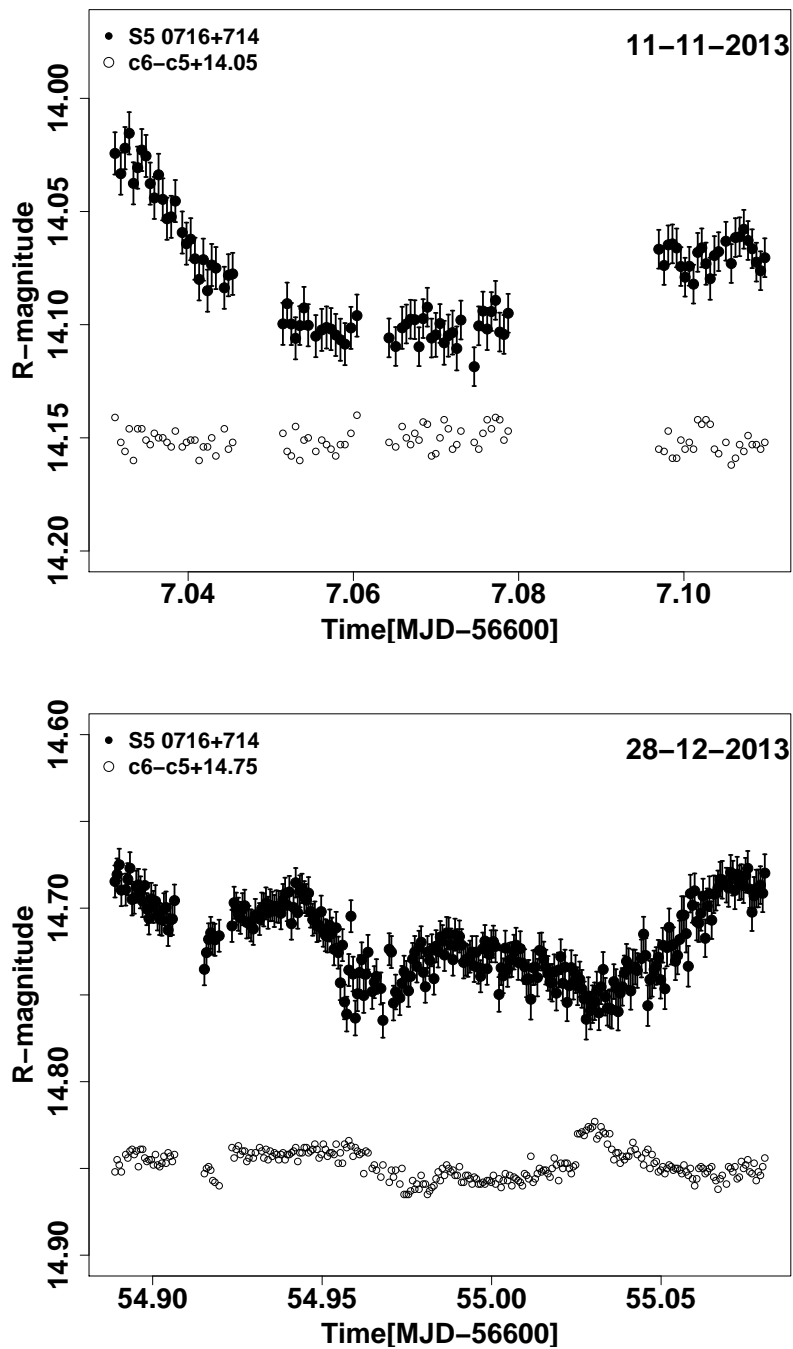


Figure 4.3: Same as for Fig. 4.1, but for 2013 November 11 & December 28 INV nights.

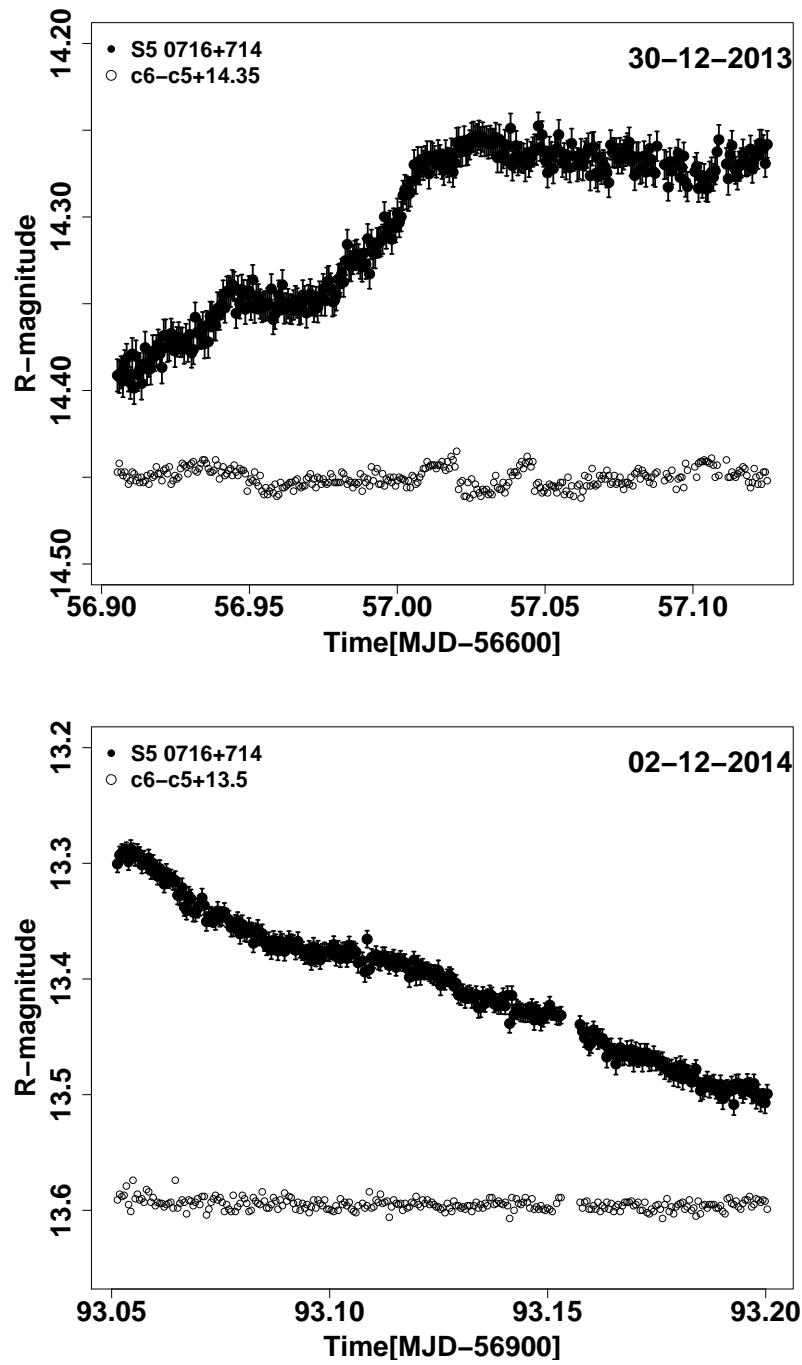


Figure 4.4: Same as for Fig. 4.1, but for 2013 December 30 & 2014 December 02 INV nights.

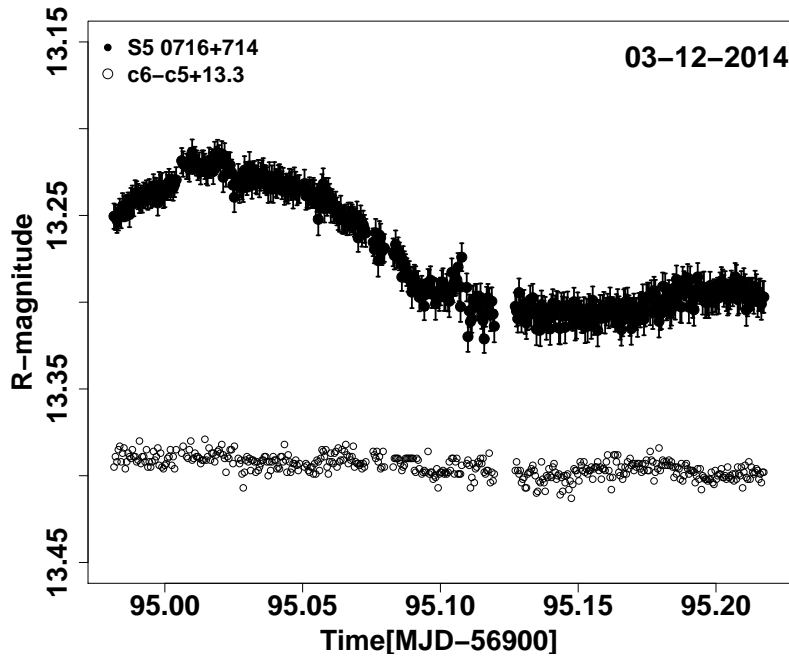


Figure 4.5: Same as for Fig. 4.1, but for 2014 December 03 INV night.

the INV nights are given in Table 4.3.

The INV lightcurves feature several complete events with specific time scales. Applying light travel time arguments, these time scales can be used to put limits on the size of the emission regions responsible for variation in flux. The shortest characteristic timescale puts constraint on the size of emission region (Elliot & Shapiro 1974). Using the characteristic timescales obtained from light curve and SF analysis, the size of the emission region,

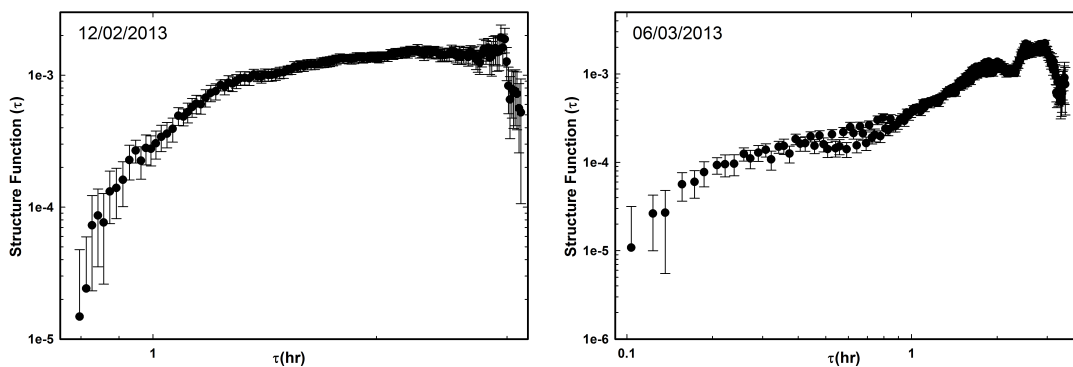


Figure 4.6: Structure functions for the INV nights are plotted for the source S5 0716+714 during 2013-2015.

Table 4.3: The table shows the structure function parameters for INV nights, k and β , along with time scale of variability. All the parameters have been calculated at more than 99% confidence level.

Date (dd-mm-yy)	$k(\delta k)$	$\beta(\delta\beta)$	$t_{var}(\delta t_{var})$ (min)
12-02-13	0.31(0.02)	4.82(0.01)	141.6 (3.5)
06-03-13	0.99(0.01)	1.67(0.01)	100.8 (2.3)
07-03-13	1.71(0.01)	1.81(0.01)	122.4 (2.8)
12-03-13	0.08(0.01)	1.21(0.01)	66.6 (1.1)
11-11-13	3.61(0.03)	1.33(0.01)	57.6 (1.0)
28-12-13	1.14(0.01)	0.97(0.01)	45.6 (1.0)
30-12-13	0.88(0.01)	1.31(0.01)	186.0 (1.6)
02-12-14	2.29(0.01)	2.34(0.01)	212.4 (2.4)
03-12-14	2.32(0.02)	2.41(0.01)	233.4 (2.8)

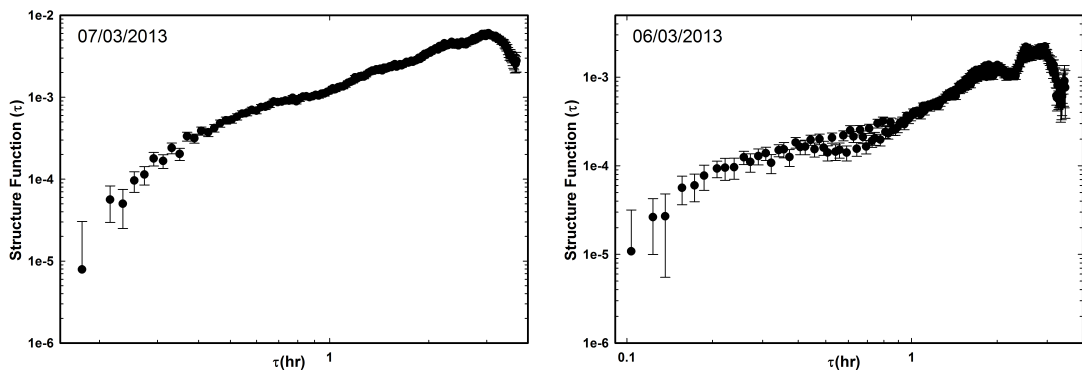


Figure 4.7: Structure functions for the INV nights are plotted for the source S5 0716+714 during 2013-2015.

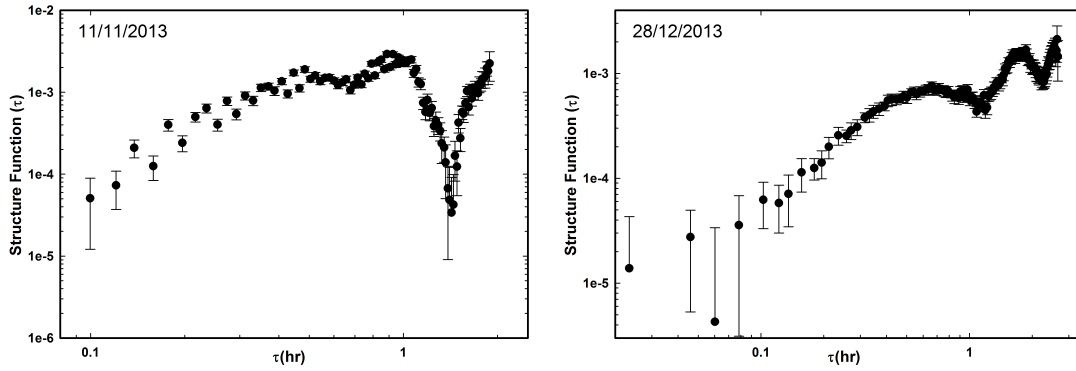


Figure 4.8: Structure functions for the INV nights are plotted for the source S5 0716+714 during 2013-2015.

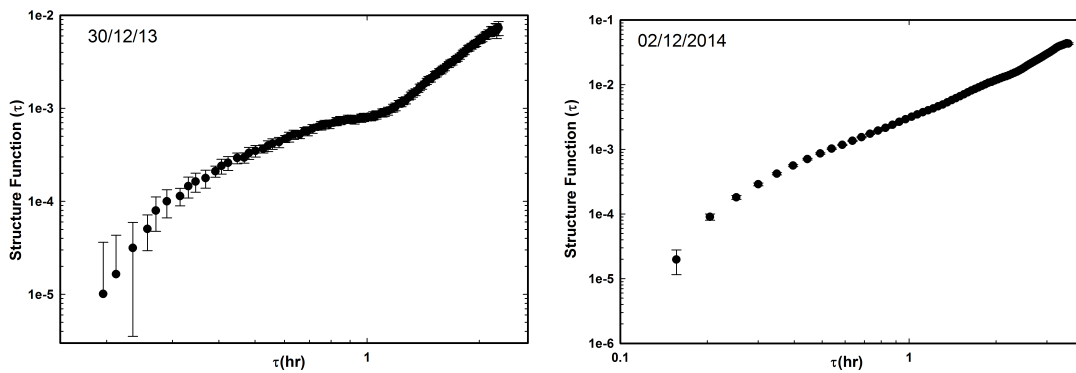


Figure 4.9: Structure functions for the INV nights are plotted for the source S5 0716+714 during 2013-2015.

$$R \leq \frac{\delta c \Delta t_{var}}{(1+z)} \quad (4.2)$$

where, c is speed of light, Δt_{var} is minimum timescale of variability, δ is the Doppler factor (taken as 15) and z is the redshift of the source ($z=0.32$). Using $\Delta t_{var} = 45.6$ minutes, the estimated size of the emission region is of the order of $\approx 10^{15}$ cm. Apart from this shortest time scale of variability, other time scales estimated at all other nights provide multi-sizes emission regions in the jet. The longest time scale of variability detected in the present study is which corresponds to a size of 2.94×10^{15} cm in the source frame.

The mass is one of the most important property of the black hole. There are two categories of the methods to determine mass of a black hole in AGN; primary and secondary. While there are direct, primary methods applicable to nearby black hole systems where motion of the surrounding stars and gas under the influence of black hole, are traceable (Vestergaard 2004), it is very difficult to have an estimate of their masses at high redshifts. In the secondary methods, mass of the black hole is estimated by resorting to approximations, eg, using any parameter to which black hole mass is correlated. There are several methods which fall in this category. However, for the sources which do not show any emission line and host galaxy is also weak, the case of BL Lac type sources, it becomes very very difficult to estimate the mass of black hole. For such systems, the variability time scale can provide a rough estimate for their black hole mass, assuming that the shortest time scale of variation is governed by the orbital period of the inner most stable orbit around a Kerr (maximally rotating) black hole. Miller et al. (1989) claim the origin of microvariability from very close to the central engine, while Marscher et al. (1992) associate their location somewhere in the jet, caused by turbulence. Many authors have used this method to estimate masses of black holes in the BL Lac sources using shortest variability time scales (Fan 2005; Gupta et al. 2008; Rani et al. 2010; Chandra et al. 2011; Kaur et al. 2017c). Here we use this method to estimate the mass of a Kerr black hole at the center of S5 0716+71 using the expression (Abramowicz & Nobili 1982b; Xie et al. 2002)

$$M = 1.62 \times 10^4 \frac{\delta \Delta t_{min}}{1+z} M_{\odot}, \quad (4.3)$$

where, G is universal gravitational constant, c is speed of light and δ is the Doppler factor. Taking the shortest variability time scale, $t_{min} = 45.6$ min and Doppler factor as 15, we estimate the mass of the Kerr black hole as $5.6 \times 10^8 M_{\odot}$, which is in agreement with other values including a value of $1.25 \times 10^8 M_{\odot}$ (Liang & Liu 2003) obtained by using optical luminosity. Bhatta et al. (2016) linked plateau in the LC to the characteristic timescale for developing outflow within the jet base, equivalent to the innermost stable orbit and obtained the value of black hole mass as 4×10^9 (maximally spin BH) and $3 \times 10^8 M_{\odot}$ (lowest spin BH). Agarwal et al. (2016) obtained a value of $2.42 \times 10^9 M_{\odot}$.

Knowing the black hole mass M_{BH} , the Eddington luminosity, upper limit to the luminosity for an accreting object of mass M , can be estimated as (Wiita 1985),

$$L_{Edd} = 1.3 \times 10^{38} (M/M_{\odot}) \text{erg s}^{-1} \quad (4.4)$$

which, in case of the S5 0716+71 comes out to be about $7.28 \times 10^{46} \text{erg s}^{-1}$. It should be noted that due to the lower rates of accretion in BL Lacs, the bolometric luminosity is one to two orders of magnitude less than the Eddington luminosity.

Quasi-periodic variability: Another very interesting albeit highly debatable issue is the possible presence of periodicity in the blazar light curves, Claims for their existence have been made in optical bands (Lainela et al. 1999b; Fan & Lin 2000). A few INV LC s indicate to the presence of possible quasi-periodic variations, also noticed in this source by Wu et al. (2005); Gupta et al. (2008); Rani et al. (2010); Poon et al. (2009); Man et al. (2016), with periods varying from 15 minutes to 1.8 hr. The presence of such features, if genuine, can be explained by light-house effect (Camenzind & Krockenberger 1992), plasma moving in the helical magnetic field or micro-lensing effect etc. In the present case, the variations seen on timescales of few hours with asymmetric profiles rule out the possibility of the micro-lensing as the mechanism. Flares could arise here

by sweeping beam whose direction changes with time due to helical motion. To estimate variability timescales and/or periodicity (if present) in our *LCs*, we use structure function and periodogram analysis.

The SF for the night of 2013-03-12 shows only one minimum at about 2.2 hr while that for 2013-12-28 gives two minima at 1.25 hr and 2.3 hr, giving a possible period of about 1.2 hr. To verify these, we study power spectrum density plot for these two nights as shown in Figure 4.10. Power spectrum density is a common tool to determine the strength of variations as a function of frequency. It is simply computed by using fast Fourier transform (FFT) method and is mostly used for evenly sampled data. For March 12 night, we get a peak at 2.25 hr with maximum power, while next one is with negligible power. There is, therefore a possibility of a quasi-period of 2.25 hr (SF also gives a value of 2.2 hr), albeit closer to total duration of observations (2.8 hr). The December 28 PSD has a major period 4.8 hr (more than data series duration) and next one 1.4 hr with much less power, which might be due to less than 3σ significance in the variation (cf, LC in Fig. 4.3). We, therefore, infer a possibility of the quasi-periodicity on 2013-3-12 & 2013-12-28 nights with periods of 2.2 hr and 1.25 hr, respectively. We also carried out autocorrelation analysis of these two nights data using zDCF. The zero crossing time of the ACF indicates to the possible characteristic time scale of variability while any peak, if exists, indicates to the periodicity in the data series. On the night of 2013 March 12, ACF gives two peaks at 1.2 and 2.2 hrs while SF gives a peak at 2.2 hrs only. On the other hand, ACF has three peaks, 1.2 hr, 2.4 hr and 3.12 hr on 2013 December 28. First two peaks are almost the same as given by SF fitting. The peak at 3.12 hr is close to the time series length. The quality of the light curves presented herein particular its dense sampling is good enough to search for hour-long period QPVs, and we get significant indication for 2.2 hr period on March 12, and 1.2 and 2.24 hr period QPV on December 28, 2013. Still, these QPVs are not at very high significance level to claim with high confidence. It implies no strong persistent periodic signal in the source within the analyzed variability timescale domain.

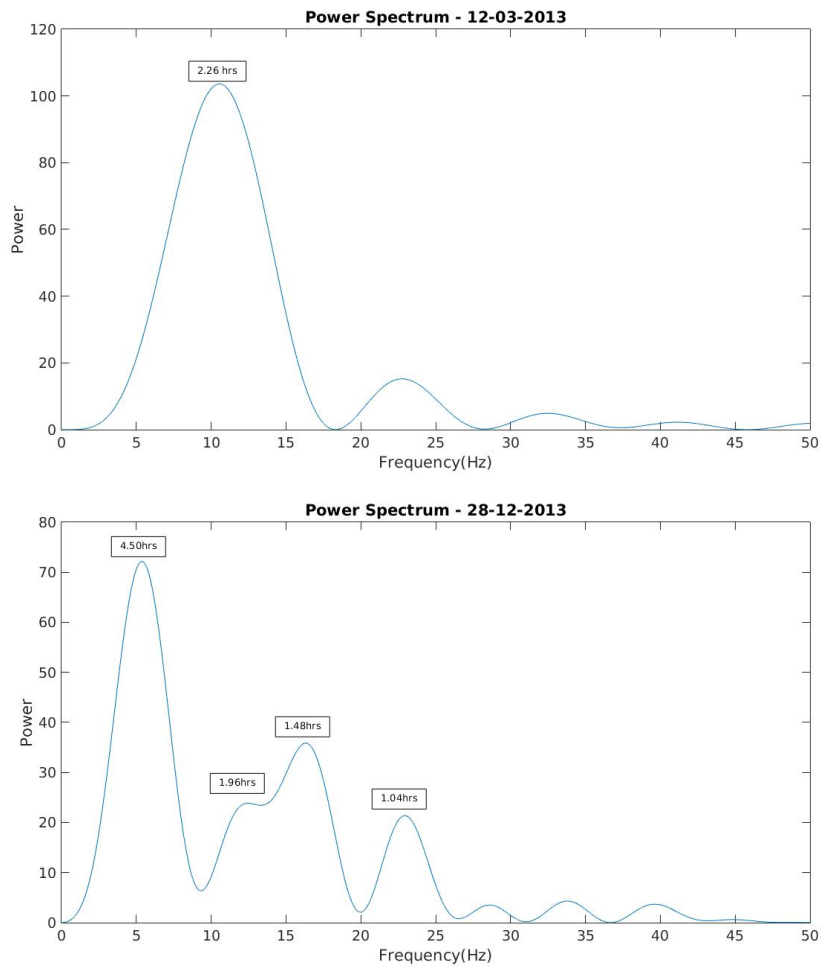


Figure 4.10: Power spectrum density for source S5 0716+714, plotted for the nights showing indication of periodic component in their SFs & LCs.

Variability amplitude (A_{var}) and the brightness state of source

In order to find out whether extent of variability has any dependence on the brightness of the source, we calculated the amplitude of variability (A_{var}) in R-band for all the nights monitored for long enough time to show a minimum of 3% amplitude variation, using equation 2.2. The values of A_{var} are plotted against nightly averaged brightness magnitude in R-band (Figure 4.11) for the duration of 2013 January to 2015 May. We notice larger variability amplitudes when the source was brighter. In blazars, the A_{var} is indicative of the environment where turbulent plasma in the jet interacts with frequent shock formations where relativistic electrons are accelerated in the magnetic field which then cool down leading to synchrotron radiation. During this period (2013-2015), the source was in relatively more active phase showing average R-band magnitude of $13.22 \pm 0.01\text{mag}$ (historical average $R = 14.0$) and therefore one would expect larger amplitude of variation in the active jet. When the source is relatively faint, thermal emission from the host galaxy is expected to dilute the intrinsic variation in the jet emission, resulting in smaller A_{var} . Several authors have reported the similar behaviour to what we have noticed. Agarwal et al. (2016) and Yuan et al. (2017) notice a very mild trend of larger A_{var} when source was brighter. Montagni et al. (2006b) estimated rates of magnitude variation for 102 nights during 1996 – 2003 for S5 0716+71 and found faster ($\sim 0.08/h$) rates when source was brighter ($R < 13.4$), though the dependence was weak, compared to average rate of change ($\sim 0.027\text{mag}/h$) irrespective of the state of the source brightness.

However, just the opposite behaviour has been detected by Kaur et al. (2017c) in another IBL, 3C66A as described in the earlier chapter, i.e., larger amplitude of variability when the source was relatively fainter. Perhaps more extensive study on several blazars is needed to address the issue.

The behaviour of the amplitude of variation as a function of the source brightness also provides a clue to how the LTV and INV could be related. When the source is bright, it indicates that the relativistic shock is propagating through the larger scale jet leading to enhanced flux at the longer time scale (LTV, Romero

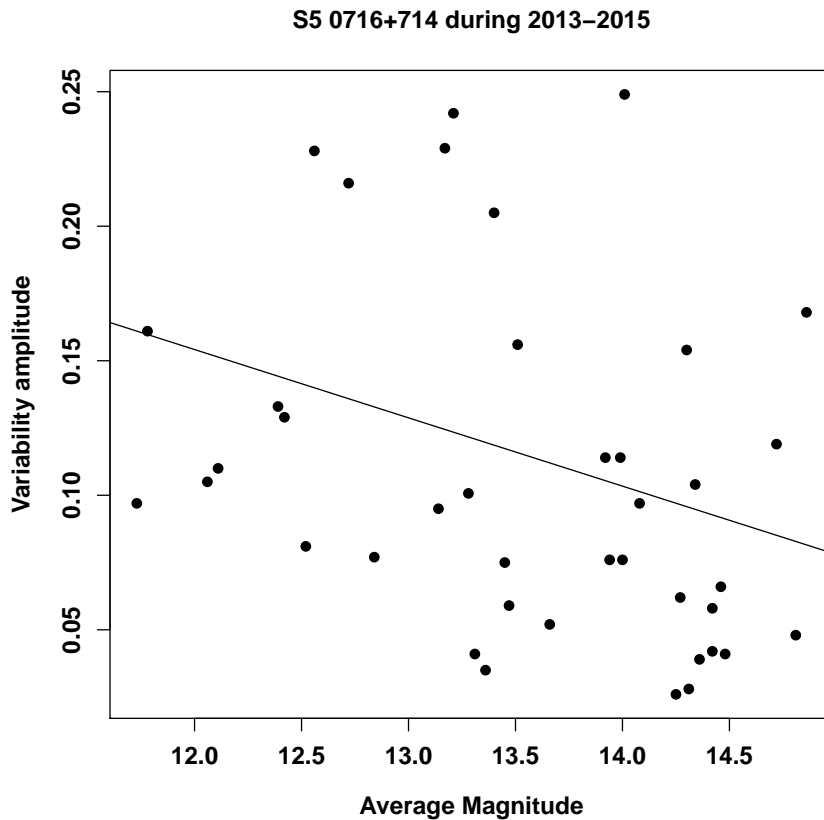


Figure 4.11: The amplitude of variability as a function of the average R-band brightness during 2013-2015. The linear regression fit at 95% confidence level (0.05 significance) gives p value of 0.049 but Pearson correlation coefficient is low (0.313), showing a weak correlation.

[et al. \(1999\)](#). The interaction of the shock with local inhomogeneities (small scale particle or magnetic field irregularities) or turbulence interacting with the shock ([Marscher et al. 1992](#)) is perhaps giving rise to the intra-night variations (INV). Since we notice an increase in the amplitude of INV with an increase in the mean brightness of the source, later being seen due to LTV, there is perhaps a relation between LTV and INV. A statistical study on a number of sources with good quality long term data showing INV, STV and LTV on a large number of nights would, perhaps reveal whether INV amplitudes really have any correlation with the long and short term variability amplitudes. Certainly, S5 0716+71 would qualify as one such candidate for the study.

4.3.2 Long-term variability

The long-term optical light curve constructed for the period 2013 January-2015 May for the S5 0716+714 is shown in Figure 4.12, with time in MJD and B,V,R & I brightness in magnitude. A total of 46 nights with 6256, 159, 214, & 177 data points in R, B, V, & I-bands, respectively, are used in generating these *LCs*. The source was in its faintest state with 15.2 mag in R-band on MJD 56663.08 (2014 Jan 6) and in its brightest state with 11.68 mag, almost one year later on MJD 57040.90 (2015 January 18). The S5 0716+71 has undergone several outbursts and flares during its two & half year journey with two major outbursts peaking in 2013 March and 2015 January, having a duration of about 350 & 510 days. Based on our data plotted here, we estimate long-term variability (LTV) amplitudes of about 2.5 mag and 3.45 mag with time scales of 250 and 360 days, respectively, during these two outbursts. These LTV time scales are estimated with respect to the minimum and maximum brightness values of the source during the two outbursts. During the 2015 January outburst, S5 0716+714 reached its unprecedented brightness level (Chandra et al. 2015a,b). Using multi wavelength data from Fermi-LAT, Swift-XRT, Swift UVOT, MIRO (optical R-band), Steward optical R-band and polarization data, we (Chandra et al. 2015b) detected two sub-flares contributing to this major 2015 January outburst. In optical, the source brightened by 0.8 mag in 6 days (MJD 57035–57041) and, post flare, decayed over next four days at a rate of 0.13 mag per day. Very sharp drop in brightness within a day (MJD 57040–57041) and subsequent rise in brightness the very next day (MJD 57042) indicated to the presence of two sub-flares with almost same peak flux during the outburst. A rapid swing in the position angle of polarization indicated to the magnetic reconnection (Zhang et al. 2012) in the emission region, causing the outburst.

In the long term, the source became fainter within a year from its average brightness, $R = 13.5$ mag in 2013 to $R \sim 15$ mag in 2014 January. It was then in the brightening phase during 2014 to 2015 with intermittent flaring activity. S5 0716+71 attained brightest value in 2015 January and started its journey towards fainter side later as reflected in all the B, V, R, and I-band (from $R = 11.56$ mag

to 13.20 mag, a 1.64 mag decay in five months, c.f., Figure 4.9) *LCs*. In addition to major outbursts, there are at least 9-flares with their duration ranging from 20 days to 30 days leading to changes in brightness of the source from a few tenths of magnitude to as much as more than 1.5 magnitude in R-band. The frequent large gaps in the data restrict us from appropriately characterizing these flares which indicate that the source remains almost always active with substantial brightness changes.

There are several approaches to explain the variation at various time scales- long as well as short. The intrinsic variations could be caused by the instability & hot spots in the disk or its outflow, and activities in the relativistic jet. Variations could also be caused by the causes extrinsic to the source, e.g., interstellar scintillation- which are highly frequency dependent and normally affect long wavelength radio observations, gravitational microlensing - might cause long term variations in some source but will result in achromatic, symmetric lightcurves. The later is less likely to cause INV (Wagner & Witzel 1995). Since S5 0716+714 was in relatively bright phase and emission is strongly jet dominated, most probable source of variation should be processes in the jet. The shock-in-jet model (Marscher & Gear 1985; Marscher 2008) is normally able to explain variety variability events with some modifications (Zhang et al. 2015; Camenzind & Krockenberger 1992), where a shock propagates down the jet interacting with a number of particle overdensities or stationary shocks/cores distributed randomly in the parsec scale jet. Such standing shock are formed due to pressure imbalance between jet plasma and ISM. In trying to maintain a balance, an oblique shock is created perpendicular to the jet axis. The relativistic shock interacting or passing through such regions energize the particles in the presence of magnetic field, which then radiate synchrotron emission while cooling. Either the jet moves in a helical motion slob moves in helical magnetic field and the resultant causes the change in the viewing angle, thus changing the Doppler factor which significantly enhances/reduces the intrinsic flux variation, depending upon the decrease/increase in the angle. The model can explain rapid variations by resorting to jet-in-jet scenario(Zhang et al. 2015; Camenzind & Krockenberger

1992). The small flares before the outburst indicate an acceleration/cooling of relativistic particles due to plasma blobs interacting with shock front and an on-going activity in jet due to the superposition of all the events leading to long term variability in the source. In our study, after the second outburst, the source enters into the faint state again. Several studies have been carried out to address the long term behaviour of the source. (Raiteri et al. 2003; Nesci et al. 2005) used the historical data, including from the literature, during 1953–2003 and noticed alternate trends of decreasing and increasing mean brightness on a tentative period of about 10 years, claiming precession of the jet to be responsible for them. It should be noted that even during these slow trends of increasing/decreasing mean brightness, source was very active with a large number of flares superposed on these. Again, a decreasing trend was noticed by (Sunil Chandra’s Thesis 2014, submitted to the MLS University; private communication) beginning 2003 which continued upto 2012, they also predicted an increase in average brightness after 2014. Agarwal et al. (2016) observed the source for 23 nights during 2014 November– 2015 March and found the source in bright state, showing INV for 7 out of 8 nights and STV with 1.9 mag change during about 28 days (MJD 57013.86 – 57041.34). In their long term work for the period 2004 – 2012, Dai et al. (2015) reported STV at 10 days time scale, 11 INV nights out of 72 nights observed with an average magnitude of $R=13.25$ and an overall change by 2.14 magnitude.

A complete observation log along with daily averaged R band photometric magnitudes for S5 0716+714 are provided in Table 4.4.

Spectral behavior of S5 0716+71

The variation of color with the brightness of the source provides useful clues to constrain the blazar emission models (Hao et al. 2010). To investigate the spectral behavior of S5 0716+714 over long timescale i.e., from 2013 to 2015, the color-magnitude diagrams, (B-V) v/s V, (B-R) v/s R and (V-R) v/s R, are plotted using nightly averaged magnitudes in B, V and R bands with N1, N2 and N3 indices, respectively. The minimum and maximum values of the colour indices

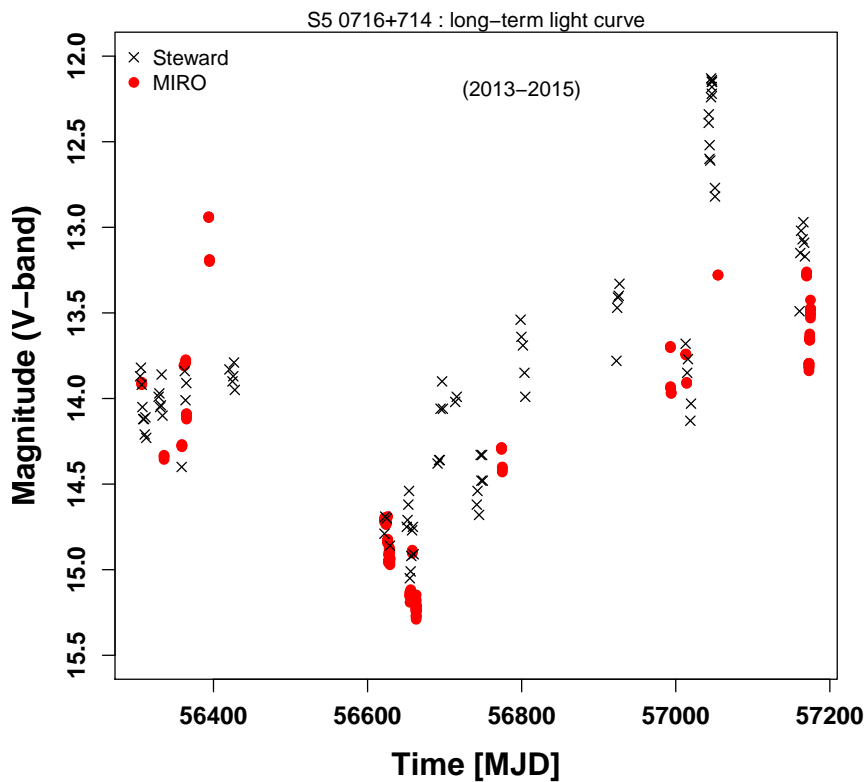
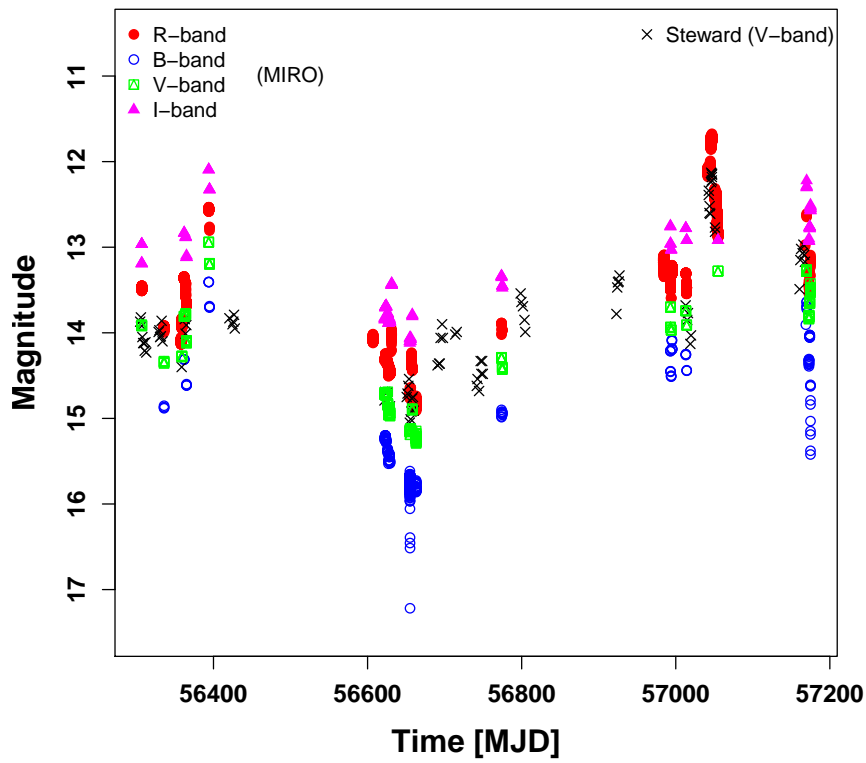


Figure 4.12: Long-term B,V,R & I band light curves of S5 0716+714 for the duration 2013 January - 2015 May. Data used are from MIRO and Steward observatory.

Table 4.4: Observation log and photometric results for S5 0716+714 in R-band during 2013 January-2015 May. Columns are: Date of observation, Time (UT) & MJD, No. of data points, average magnitude with standard deviation & Photometric errors, variable (Y/N)

Date (dd-mm-yyyy)	T_{start} (hh:mm:ss)	MJD	N^6	\bar{m} (Avg mag)	$m(\sigma)$	Error	Variable (Y/N)
14-01-2013	21:30:14	56306.89600	785	13.4788	0.01	0.01	N
12-02-2013	20:10:09	56335.84038	195	13.9430	0.02	0.01	Y
06-03-2013	23:06:00	56357.96250	237	14.0072	0.10	0.03	Y
07-03-2013	00:03:50	56358.00266	203	13.9963	0.10	0.01	Y
10-03-2013	19:37:50	56361.81794	231	13.3565	0.01	0.003	N
12-03-2013	20:14:02	56363.84308	229	13.5055	0.05	0.004	Y
13-03-2013	23:38:51	56364.98531	160	13.6604	0.01	0.005	N
11-04-2013	19:49:09	56393.82580	182	12.5637	0.03	0.02	N
12-04-2013	19:46:43	56394.82411	5	12.78	0.02	0.02	N
11-11-2013	00:44:51	56607.03115	139	14.0787	0.02	0.003	Y
26-11-2013	03:20:25	56622.13918	13	14.3107	0.01	0.003	N
27-11-2013	01:48:39	56623.07545	25	14.2591	0.01	0.01	N
28-11-2013	01:13:25	56624.05098	169	14.2756	0.01	0.01	N
29-11-2013	01:07:09	56625.04663	247	14.3377	0.01	0.01	N
30-11-2013	02:29:12	56626.10361	107	14.3572	0.01	0.008	N
01-12-2013	03:08:06	56627.13063	112	14.4850	0.01	0.02	N
02-12-2013	02:32:13	56628.10571	200	14.4176	0.01	0.04	N
03-12-2013	02:12:03	56629.09170	242	14.4633	0.01	0.03	N
05-12-2013	00:19:24	56631.01347	230	14.0110	0.03	0.02	N
28-12-2013	21:20:00	56654.88889	284	14.7181	0.02	0.007	Y
30-12-2013	21:43:43	56656.90536	350	14.3039	0.04	0.005	Y
01-01-2014	00:18:37	56658.01293	183	14.4229	0.01	0.004	N
05-01-2014	02:10:57	56662.09094	50	14.8162	0.01	0.005	N
06-01-2014	00:43:03	56663.02990	349	14.8554	0.06	0.006	N
26-04-2014	20:26:39	56773.85184	10	13.9236	0.05	0.006	N
27-04-2014	20:08:22	56774.83914	05	13.9689	0.01	0.008	N
22-11-2014	20:08:34	56983.83929	49	13.1434	0.02	0.002	N

Table 4.5: Brightest and faintest magnitudes of the S5 0716+714 during two & half year period.

Source	Brightest mag	MJD (Date)	Faintest mag	MJD (Date)
S5 0716+714	11.72 (0.05)	57046.92 (24-Jan-2015)	14.85 (0.06)	56663.02 (05-Jan-2014)

Table 4.6: The average color values with statistical parameters for color versus magnitude of the source S5 0716+714 during 2013-2015. The plots show a mild bluer when brighter trend.

Color Index	m	c	r^2	r	p
B-R	0.08 ± 0.03	-0.22 ± 0.45	0.26	0.51	0.02
B-V	0.02 ± 0.02	0.16 ± 0.34	0.06	0.25	0.29
V-R	0.05 ± 0.03	-0.37 ± 0.48	0.12	0.35	0.13

m = Slope of regression line, r^2 = square of Pearson correlation coefficient, p = Probability for null hypothesis.

for better sampled case of B-R v/s R are, 0.40 and 1.3, respectively while the color average is $\langle B - R \rangle = 0.6$, with standard deviation $\sigma=0.14$. To determine the correlation between the color v/s magnitude and color v/s time, we performed regression analysis by fitting a straight line, $y = mx + c$ (y = color index, x = average magnitude in Figures ?? & 4.14, and x = time in MJD in Figures 4.13coltime1 & 4.16), using linear model in R software package and extracted various parameters like intercept(c), slope(m), correlation coefficient(r), p-value etc. These are given in Table 4.6.

It is clear from the Figure 4.13 & 4.14 alongwith values of the various parameters obtained from regression analysis (see Table 4.6) that the source showed weak positive correlation for B-V and V-R color indices plotted against brightness magnitudes, with Pearson correlation coefficient (r) of 0.25 and 0.13 along with p-value of 0.29 and 0.13 respectively. However, comparatively stronger positive correlation for B-R color index versus average magnitude of source with Pear-

son coefficient r as 0.5 and null hypothesis probability, $p = 0.02$ are noticed at 95% confidence level. Thus present study suggests a bluer-when-brighter (BWB) color for S5 0716+71 (cf., Figure 4.13 and Figure 4.14) as also reported by many workers (Poon et al. 2009; Chandra et al. 2011; Wu et al. 2009; Man et al. 2016). Li et al. (2017) statistically studied data for S5 0716+71 during 1995-2015 and addressed the issue of long-term, short-term and INV behaviour of the symmetry in flares and color and found flares as asymmetric in general and BWB color on all the time scales considered. The spectral changes in S5 0716+714, and blazars in general, are complicated and difficult to explain. The source was reported with strong BWB trend over long-timescales (Poon et al. 2009) and during its flaring phase (Ghisellini et al. 1997; Wu et al. 2005, 2009; Gu et al. 2006). Wu et al. (2005) and Agarwal et al. (2016) discussed color trends in their studies but did not find any change on intra-night or long-term timescales. Raiteri et al. (2003), on the other hand noticed all possible scenarios, i.e., BWB, RWB and no trend at all, in his studies. Stalin et al. (2009) found source showing no color dependence with brightness on long and short time scales, albeit a BWB color on intra- and inter-night timescales was noticed. The fresh injection of high energy particles in the emission region inside the jet might lead to BWB behaviour (Ghisellini et al. 1997; Raiteri et al. 2003; Gu et al. 2006). It is explained by the shock-in-jet model (Marscher & Gear 1985; Marscher 2008) where the propagation of a disturbance downstream the jet gives rise to shock formation and the lag between different wavelengths emissions provide information on their relative spatial separations. In the case of BL Lacs, the higher frequency electrons close to the shock front undergo faster radiation losses than low-frequency ones. The BWB behavior basically means that the flux enhancements are produced either during the episodes of intense particle acceleration or, alternatively, by the fluctuating magnetic field superimposed on the local, steady electron energy distribution. The redder when fainter trend indicates that when the jet is not dominant, the contribution from disk emission or host galaxy becomes relevant. These cases show the complex color behaviour of the source with the brightness. However, in case of the S5 0716+714 where galaxy is several magnitudes fainter ($R > 20$ mag

Montagni et al. (2006b)), thermal contribution from the host is negligible.

Spectral variation with time: The long-term optical light curves of blazars manifest significant details on the nature of the source as these contain various phases in their brightness, color changes during flares, outbursts and fainter states. Several authors have looked at spectral variations with time on intra-night and inter-night timescales for blazars (Raiteri et al. 2003; Wu et al. 2005; Stalin et al. 2009; Gaur et al. 2012; Rani et al. 2010; Agarwal et al. 2016) and reported a mixed behaviour- some sources showing color dependence while others showed no change in color over considered timescales. Agarwal et al. (2016), during their 130 day study, found a change of about 0.3 in spectral color with no significant dependence on time or brightness phase. Yuan et al. (2017) reported a complex pattern for spectral index with time without any specific trend during the period 2000-2014. The color variations are caused by differential cooling of energetic electrons behind the shock front. The relativistic shock moving down the jet accelerates electrons to high energies at the sites of high magnetic field or electron density giving rise to emission at diverse frequencies. Since the regions of the plasma over-densities or quasi-stationary shocks are randomly distributed in the jet, the interaction of the relativistically moving knot with existing features in the large scale jet gives rise to multiple outbursts which evolve individually and perhaps differently. The processes involve give rise to changes in the spectral behaviour with time. A nicely sampled lightcurve in different optical bands should give a better picture of the temporal evolution of S5 0716+71; our data suffer from substantial gaps and the observations in different bands are not truly simultaneous.

We report a secular change in the color of the IBL S5 0716+714 during the two & half year period (2013 January–2015 May). Figures 4.15 & 4.16 are plotted with color index (B-V), (B-R) and (V-R) against time in MJD for this period. A mild bluer behavior is noticed in (B-V) color-time plot indicating the source to get bluer over long timescales of more than two years i.e., from 2013 January – 2015 May. Other color indices ($B - R$) and ($V - R$) show a weak, or almost no trend in color with time. The source was in relatively bright phase during 2013,

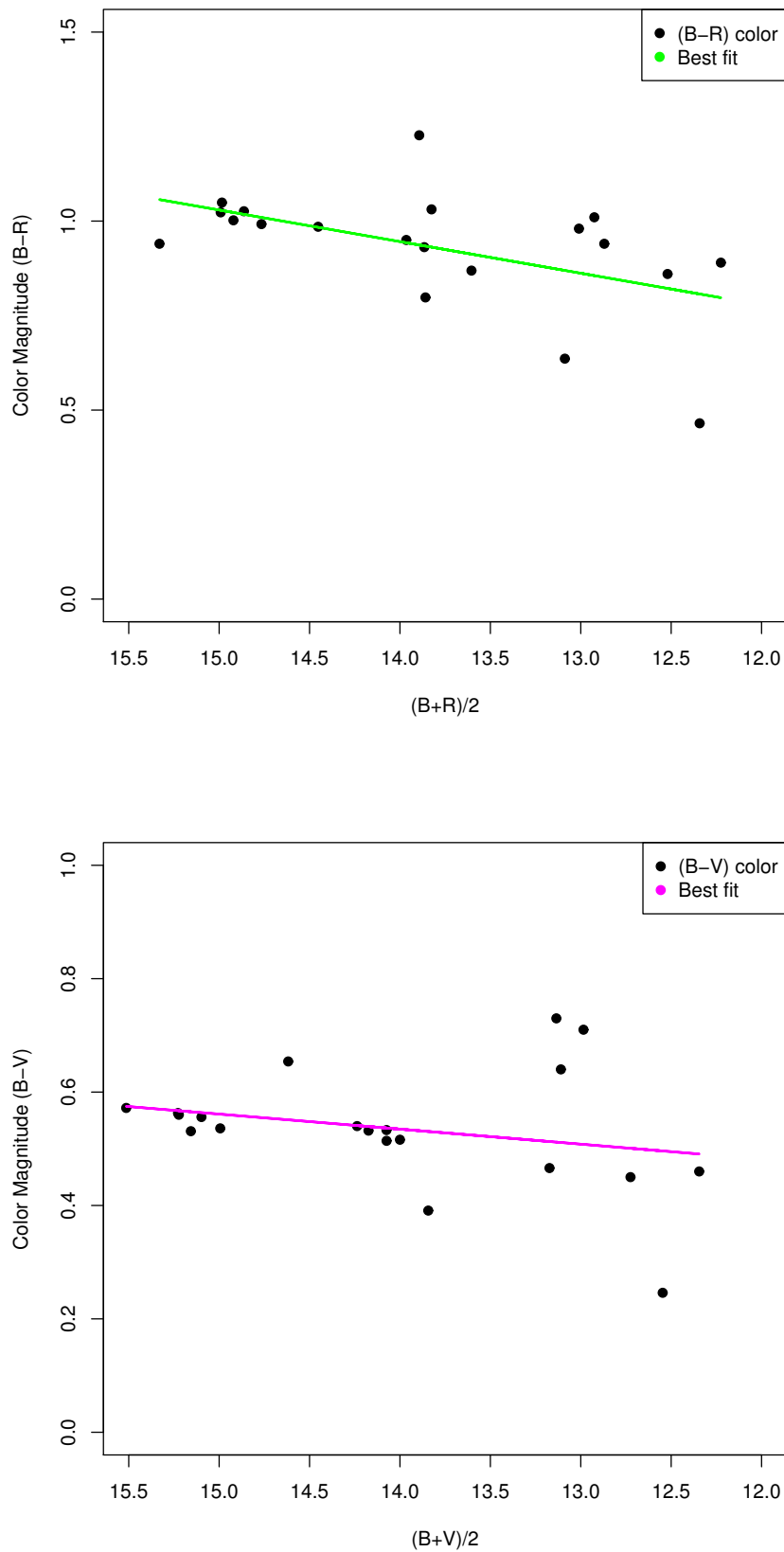


Figure 4.13: Color-magnitude plot for source S5 0716+714 during 2013-2015 showing bluer when brighter trend. The statistical significance parameters are given in Table 4.6

c_{BRV}

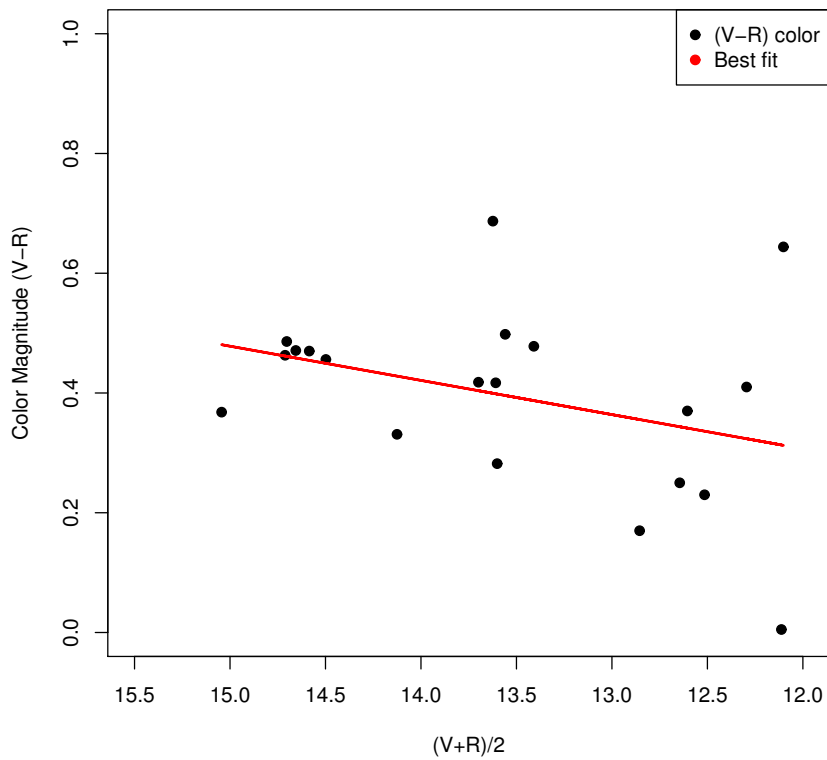


Figure 4.14: Color-magnitude plot for source S5 0716+714 during 2013-2015 showing bluer when brighter trend. The statistical significance parameters are given in Table 4.6.

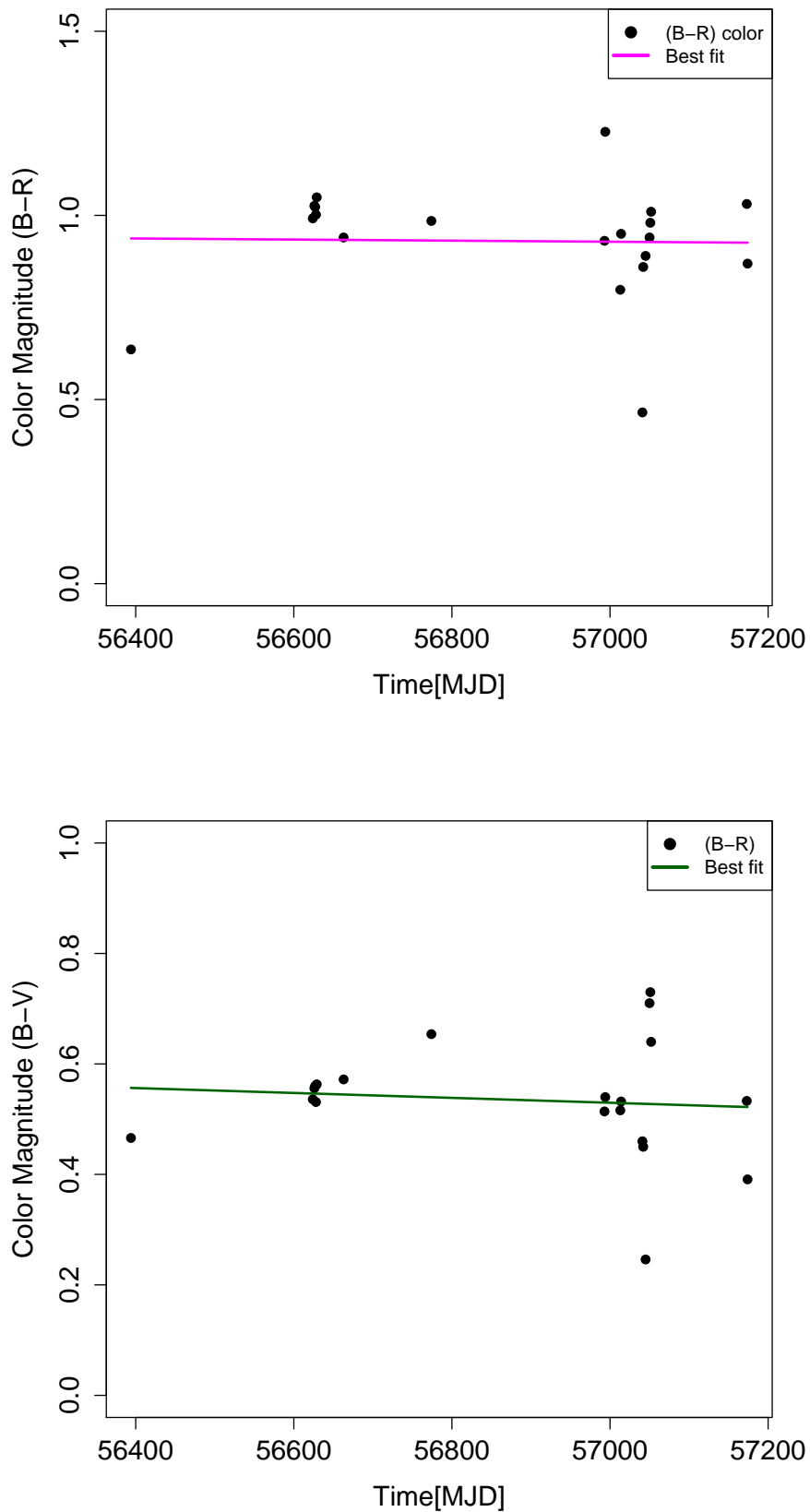


Figure 4.15: The color of source S5 0716+714 is plotted with time (MJD). B-V v/s time shows a bluer trend with time while B-R v/s time trend is not significant.

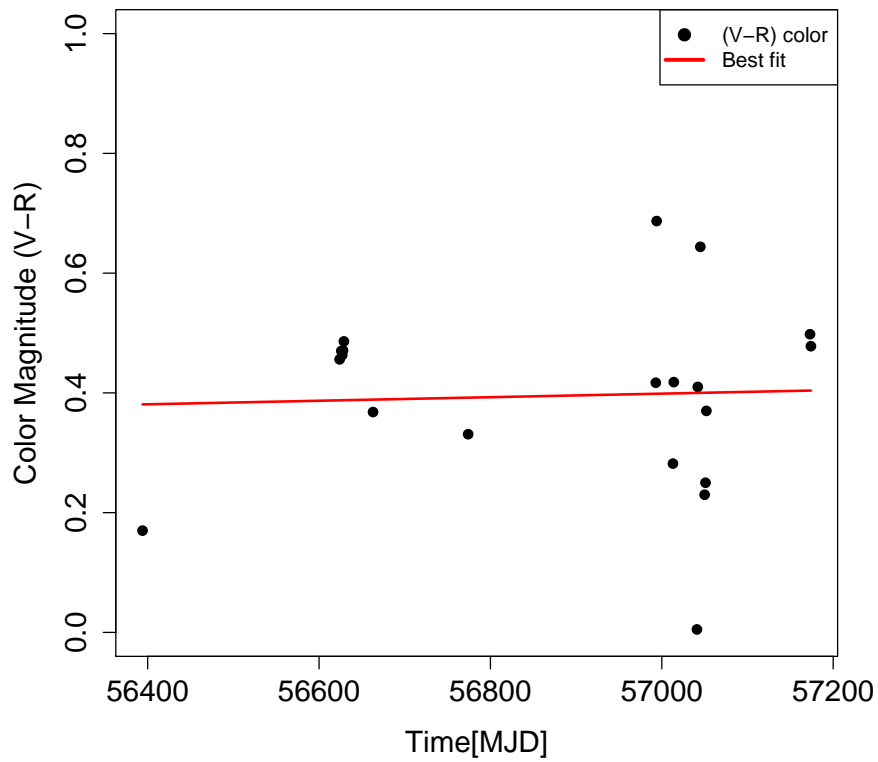


Figure 4.16: The color of source S5 0716+714 is plotted with time (MJD). The trend is not significant at 95% confidence level.

in low-phase during 2014 and entered into its brightest phase in January 2015. Our observational data during the period shows almost no change in the average color during this period albeit with a mild bluer behaviour with time in (B-V) color.

4.4 Conclusions

The IBL blazar S5 716 was observed for 46 nights with high temporal resolution during a period of more than two years (2013–2015) in optical BVRI wavelength bands from Mt. Abu InfraRed Observatory (MIRO). It was monitored for more than two hours during 29 nights to address INV. The nightly averaged B, V, R & I band brightness magnitudes with 6256, 159, 214 & 177 data points, were used to discuss long term variability and color behaviour of the source. The source exhibited intra-night as well as inter-night variability at significant levels. From the present study, following conclusions are drawn:

- Source showed variability over diverse timescales i.e., a few tens of minutes to months and a duty cycle of variation of more than 31%. The DCV appears to be dependent upon monitoring time. Two major outbursts with ~ 370 and 500 days duration superimposed with several flares are noticed.
- The structure function analysis leads to the shortest variability timescale of 45.6 minutes, based on which upper limit on the size of emission region of the order of 10^{15} cm is estimated. There are several time scales longer than this indicating multi-sized emission regions in the jet. Based on the longest time scale, the size of emission region is estimated as 2.94×10^{15} cm.
- Assuming the rapid variations being originated in the vicinity of central engine, black hole mass is estimated to be of the order of $5 \times 10^8 M_{\odot}$ using shortest variability time scale.
- The structure function and power spectrum analysis are used to infer a period of about 1.2 hr on the night of 2013 December 28. However, it could easily be red-noise signature as flux enhancements are within $3\text{-}\sigma$.

- The source exhibited a bluer when brighter (BWB) spectral behaviour in the long term *LC* which supports shock-in-jet model.
- The brightness of the S5 0716+71 shows a mild increase with time during 2013 January–2015 May along with a mild bluer color.
- A larger amplitude of variation when the source was in relatively brighter state is detected, indicating to synchrotron dominated jet emission. It, perhaps, indicates that long term and intra-night variabilities are linked.

It should be noted that these inferences are drawn from the data with large gaps. However, the data presented here should be very useful for other related statistical and modeling studies on this very interesting source.

Chapter 5

HBL 1ES 1959+650 in Outburst: A Multiwavelength Study

Most of the time blazars remain either in quiescent phase or rather in low activity phase. During this phase, they remain below the detection limit in one or more energy bands and therefore, it is not possible to carry out correlated variation study between different energy bands. There are times when these are highly active, showing strong outbursts (with high S/N) which provide opportunity to carry out detailed study on the nature of the source. The elevated flux levels enables to sample shorter timescales which constraints the size of the emission region, flare profile study for acceleration and cooling mechanisms. In the last two chapters, we discussed about the optical properties of two intermediate BL Lac objects (IBL; 3C 66A and S5 0716+71) in context with the flux and spectral variability, using the extensive optical data obtained from Mount Abu InfraRed Observatory (MIRO), India. In the next two chapters, we are presenting a comprehensive multiwavelength variability study on the two blazars that belongs to the different blazar classes (1ES 1959+650–HBL; CTA 102–FSRQ), covering their historical major outbursts that show the unprecedented fluxes across the whole spectrum, The present chapter covers a detailed study of the two major outbursts (or flares) in the high-energy peaked blazar (HBL), i.e., 1ES 1959+650, during its exceptionally bright state in 2015–2016.

5.1 Introduction

It is already known that the blazars are highly luminous and extremely variable across the whole electromagnetic spectrum (EMS). Most of the blazars often show the correlated emission, but not always, between the different bands when in their outburst (flaring) state and/or otherwise also. The outbursts in the blazar are very rare phenomenon and very important to study because they provide us the clues to understand their emission processes and the mechanisms behind that. The observational flare patterns or features throw a light on the jet environment and give hints about the distribution of the material in the jet at different frequencies. Therefore, blazar variability light curves are considered as one of the most important and primitive source of information, as they carry the imprint of the flares, their features and patterns, overall flux trend at different frequencies, their correlations, spectral information etc. The spectral energy distribution of blazars is another useful tool to understand the overall emission mechanism during the flare, pre-flare, post-flare and quiescent period. Generally, their spectral energy distribution (SED) is dominated by two broad peaks imply two different non-thermal emission processes at work, namely synchrotron process, in radio to UV energy regime, and the up-scattering of low energy photons by the relativistic particles via inverse-Compton (IC) process, in the X-ray to TeV γ -ray domain. The origin(s) of the seed low-energy photons is still under debate, whether they come from inside the jet or somewhere, outside the jet, i.e., from broad line regions, narrow line regions, torus etc (Baliyan et al. 2005; Böttcher et al. 2005). In most of the cases, the fluxes at different frequencies are seen to vary in a correlated manner, suggesting that most of the SED is produced by the same electrons in a particular emission zone of the jet (reference: Ghisellini 2016). Thus, blazar SED is another important tool to know more about the overall status of the source, in general, by unveiling the emission and physical processes inside the jet and help to constrain the existing physical theoretical models.

Amongst the blazars, HBLs are found at relatively low redshifts and are less variable than LBLs (Jannuzi et al. 1994). But some of them are very active with flares and outbursts detected almost over the complete accessible EMS, ranging

from the radio to TeV γ -rays (Acciari et al. 2011; Furniss et al. 2015). While almost all the TeV flares are witnessed to have a counterpart in optical and X-rays, barring some orphan flares, the GeV energy region might show weaker activity. Blazars also show significant polarization in optical (Chandra et al. 2011, and references there-in) and radio wavelengths which is a measure of the alignment and the strength of the magnetic field. The changes in the degree of optical polarization (DP) and position angle (PA) are commonly seen during the flares in the blazars. Such rapid variations in DP and PA during a flare have been modeled for many sources (e.g., for 1ES 1011+496 - Aleksić et al. (2016), Mrk 421 - Zhang et al. (2015), for 3C 279 - Kiehlmann et al. (2016); Hayashida et al. (2012); Abdo et al. (2010a)). The outbursts in blazars are mostly thought to be a manifestation of the shock formation and their movement down the jet (Orienti 2015; Marscher et al. 2010), internal inhomogeneities and their interaction with shocks, re-collimation of shocks downstream the jet causing re-acceleration (Spada et al. 2001) or, a new population of the relativistic plasma injected into the jet. In spite of the considerable efforts until now, none of the proposed models are able to explain blazar phenomena. Our understanding of the geometry of the jet, the emission processes responsible for different flaring activities and the behavior of the objects during their quiescent phase are limited by the sample size and the scarcity of simultaneous data over a broad energy range. Therefore, there is need for extensive multi-wavelength studies on a large sample of blazars to enable a comprehensive understanding of the emission processes, in general.

5.2 1ES 1959+650

The HBL 1ES 1959+650, redshift $z=0.048$ (Perlman et al. 1996), was first detected in radio band using NRAO Green Bank Telescope (Gregory & Condon 1991) and observed in X-rays during the slew survey by the Einstein Imaging Proportional Counter (Elvis et al. 1992). The first TeV detection of this source was reported by the Seven Telescope Array group in 1999 (Nishiyama 1999). This source was identified as an optical BL Lac object by Schachter et al. (1993).

Later, a bright ($m_R = 14.9$) elliptical galaxy was confirmed by [Scarpa et al. \(2000\)](#) as its host. The source has undergone various outburst stages, including intense activity at very high energies (GeV-TeV). [Krawczynski et al. \(2004\)](#) reported an "orphan" flare at VHE during an outburst in 2002, in a multi-wavelength campaign (WHIPPLe and HEGRA for TeV, RXTE for X-rays, Boltwood and Abastumani observatory for optical, UMRAO for radio 14.5 GHz) from May 18 - August 14, 2002. The authors reported a correlation between the γ -ray and X-ray fluxes but during orphan TeV flare, no enhancement in X-ray flux was seen and there was no correlation between optical and X-ray/ γ -ray emissions. [Böttcher et al. \(2005\)](#) explained 2002 orphan TeV flare using a hadronic synchrotron mirror model in which the orphan TeV photons originated from the interaction of relativistic protons with an external photon field supplied by synchrotron radiation reflected off a dilute reflector. Another intense flaring activity was seen during 2012 April- June covered in a multi wavelength campaign by [Aliu et al. \(2014\)](#). During the outburst, 1ES 1959+650 emitted enhanced flux in gamma-rays without any significant simultaneous rise at X-ray energies. The authors proposed a reflected emission model to explain elevated γ -ray flux, via pion production with very high energy protons (10-100 TeV).

1ES 1959+650 was reported in unprecedented high flux state across all the energies (gamma-ray, X-ray, UV, Optical and radio) during 2015 which extended to 2016 as well. The source underwent two major outbursts; first, during March 2015 and the second one during October 2015 with exceptionally large count rates (more than 20 counts/sec) in X-rays ([Kapanadze 2015a](#)), making it only the third TeV source with such high X-ray count rate after Mrk 421 and Mrk 501. Such outburst activities provide an opportunity to study the underlying physical processes responsible for emission at different energies. Recently, [Kapanadze et al. \(2016\)](#) reported prolonged X-ray activity in 1ES1959+650 during their 6-month coverage of 2015 October outburst (MJD 57235-57410) along with enhanced γ -ray (0.3-100 GeV) flux at several epochs. They also claimed an orphan γ -ray flare at MJD 57314 with no enhancement at other energy regimes, albeit with a rider that due to sparse data, a rapid X-ray flare might have occurred. To

understand the overall behavior of 1ES 1959+650, we carried out an extensive multi-wavelength study of the outburst activities in 1ES 1959+650 from 2015 January-2016 June (MJD 57040-57570). Optical follow-up observations from Mt Abu InfraRed Observatory (MIRO) were carried out for the source when it exhibited high flux state in X-ray, GeV and TeV energies. This paper is organized as follows. Section 5.3 describes the observations and data analysis techniques in optical, X-ray and Gamma-rays. Results obtained on the light curves and spectral energy distribution (SED) are discussed in Section 5.4 while Section 5.5 presents a brief summary of the work done in this study.

5.3 Multi-wavelength Observations and Data Reduction

Multi-wavelength data from various resources, space-borne observatories, namely, Fermi (γ -rays), Swift (UV, optical & X-rays) and the ground-based facility, MIRO (optical/IR) are used in this study. We have also made use of the publicly available archival data from Steward Observatory, Arizona (Smith et al. 2009) in optical and 15GHz radio data from OVRAO (Richards et al. 2011) to discuss various outburst episodes. In the following the data analysis techniques used for the data from aforementioned resources are summarized briefly.

5.3.1 Gamma-ray : Fermi-LAT

FERMI Large Area Telescope (Fermi-LAT) is a primary instrument on board the Fermi satellite (Atwood et al. 2009). The LAT has an unprecedented sensitivity in the γ -ray band (20 MeV - 300 GeV) and scans the entire sky in approximately 3 hrs except for a few extremely high priority specific pointing mode observations when the observations are taken for 30 minutes for the prioritized sources. It provides a multi-dimensional data base of location, energy and time for each detected event.

We analyzed 1ES 1959+650 Fermi-LAT data from January 01, 2015 (MJD 57023) to June 30, 2016 (MJD 57550) using recommended standard procedure

by making use of the latest ScienceTools (version v10r0p5). The photon class events lying within the region of interest (ROI) of 10° , zenith angle $< 100^\circ$, within the energy range of 0.1 - 300 GeV, are extracted using "gtselect" tool. Here, we have selected the event class=128, based on the source class in Pass 8 data, (i.e., *P8R2_SOURCE*). This is most favourable selection, as suggested by the Fermi-LAT team, with good sensitivity for the analysis of moderately extended and point sources on medium to long timescales. We discarded the data when the rocking angle of the spacecraft was greater than 52° to avoid any photon contamination from the Earth's limb. The unbinned likelihood analysis was performed using gtlake tool with the help of input source model covering a region of 20° around the source position, generated using 3rd FGL catalog ([Acero et al. 2015](#)).

A maximum likelihood analysis using gtlake has been used to reconstruct the source energy spectrum. The background model was constructed using third Fermi LAT catalog (*gllpsc_v16.fit*) that contains 36 gamma-ray sources lying within ROI $< 12^\circ$, as well as diffuse emission with no extended sources within this region. We have made use of a log-parabolic model and a power law model for the sources with significant and without spectral curvature, respectively. The source (1ES 1959+650) spectral parameters within 3° were kept free during spectral fitting, while sources outside of the aforementioned range were held fixed as in the 3FGL catalog. The Galactic diffuse emission and the isotropic emission component was modelled using *gll_iem_v06.fits* and *iso_P8R2_SOURCE_v6_v06.txt*, respectively. Fermi-LAT data was reduced using a Python based package called Enrico (Sanchez & Deil, 2013). A time binning of 2 days was used to extract the source light curve. However, post outburst, we used 2.5 day binning.

5.3.2 X-ray, UV, optical : Swift-XRT/UVOT

We have made use of the 95 observation IDs observed by the instruments XRT and UVOT onboard Swift, during January 30, 2015 to June 06, 2016. The *heasoft* (version 6.17) package along-with the recently updated calibration database (2016 January 21 for XRT & 2016 March 05 for UVOT) is used for the analysis of the

above-mentioned data. However, the data are not available for the duration 2016 March 21 to April 29 (MJD 57462-57507).

The *xrtpipeline* tool provided freely as a part of *heasoft* package, with default parameters is used to extract the cleaned events files. This source, being very bright, is mostly observed in WT mode. The typical full frame count rates for WT mode observations are always less than 25 c/s which will be pile-up free as recommended by the instrument team at University of Leicester, UK ¹ (pile-up occurs for rate ≥ 100). Following this, the pile up corrections are not performed for WT mode data. For this case, a circular area of 27 pixels (equivalently $\sim 63''$) centred at the position of the 1ES 1959+650 is used as the source region. The background region was extracted as a concentric annulus with inner and outer radii of 80 pixels and 120 pixels, keeping the average half width of annular region at 100 pixel (recommended for a proper background subtraction in WT mode). The PC mode observations are corrected for pile up using the prescriptions suggested by aforementioned team². The innermost circular area with radius $10''$ is excluded (chosen for a highly piled up observations) from the source region of $70''$ circle around the source. The background in this case is used as an annular region around the source, with inner and outer radii of $150''$ and $350''$, respectively. The clean events files are then used to extract the products (spectrum & light-curves) for the source and background regions using the *xselect* tool.

The spectra thus obtained are then fitted with an absorbed log-parabola model with nH value fixed to the galactic value ($1.07 \times 10^{21} \text{ cm}^{-2}$) using *xspec* (version 12.9.0), a standard tool for X-ray spectral fitting provided as a part of *heasoft* package. Using the BACKSCAL keyword in WT mode, source and background spectrum files were edited to the proper values, before importing to the fitting tool, to avoid the wrong background subtraction during the fit. The log-parabola was chosen instead of the commonly used absorbed power-law which was giving very poor fit ($\chi_\nu \geq 1.9$). The absorbed broken power-law model was providing similar fit as that using curvature model. We prefer log-parabola because it provides natural turn-over in the spectrum instead of a sudden break as given by

¹<http://www.swift.ac.uk/analysis/xrt/xselect.php>

²<http://www.swift.ac.uk/analysis/xrt/pileup.php>

broken power-law models. The background subtracted count rates extracted for energy band 0.3-10.0 keV are used to generate the light-curves (see Fig. 5.1). The unabsorbed fluxes in 0.3-10.0 keV band are also estimated by adding component “cflux” and fitting after freezing the normalization. The fluxes thus obtained are also used for timing analysis in this paper.

The UVOT data analysis is done in a similar fashion as adopted in [Chandra et al. \(2015b\)](#). The snapshots observations in the filters V (5468 Å), B (4392 Å), U (3465 Å), UVW1 (2600 Å), UVM2 (2246 Å), and UVW2 (1928 Å), for all the OBsIDs, were integrated with the *wvotimsum* task and analyzed using the *wvotsource* task, with a source region of 5”, while the background was extracted from an annular region centred on 1ES 1959+650 with external and internal radii of 40” and 7”, respectively. The observed magnitudes from all OBsID are then corrected for extinction according to the model described in [Cardelli et al. \(1989\)](#). A tool, developed in-house, using R-platform³, is used to perform the required reddening corrections. The corrected fluxes are then used for timing analysis and the results are presented in the following section 5.4 (See Fig. 5.1 for light curve).

5.3.3 Optical observations : MIRO

Following an alert ([Ciprini & Fermi Large Area Telescope Collaboration 2015](#)) about an enhanced γ -ray activity in 1ES 1959+650 on October 20, 2015 (MJD 57315), we made optical photometric observations using two telescope facilities at Mt. Abu InfraRed Observatory (MIRO). The 1.2 m telescope is equipped with LN2-cooled CCD (1296 \times 1152 pixels; pixel size = 22) at its f/13.2 Cassegrain focus, whereas, a thermo-electrically cooled (T \sim -80°C) iKon ANDOR CCD (2048 \times 2048; pixel size =25) is used as backend instrument for 0.5 m telescope. The dark current in both systems is negligible.

The observations were carried out using BVRI Johnsons-Cousins filters for total thirteen nights during October 23 to December 13, 2015 (MJD 57318- 57369). High temporal resolution (exposure time of \approx 40-50 seconds) data with the optimum signal-to-noise ratio (S/N > 5) are obtained. The flat field images were

³<https://www.r-project.org/>

taken during twilight and dawn on daily basis whereas bias frames were taken whenever telescopes were slewing to change the source. During 2015 November-December, we also monitored the source to look for intra-night variability (INV).

The data were reduced using standard data reduction procedures using IRAF package (Image Reduction and Analysis Facility) and locally developed pipelines (Chandra et al. 2011; Kaur et al. 2017b). On each night, master bias and master flat frames were generated by combining all bias and flat field images, respectively. The science images were then corrected with bias and flat field and aperture photometry was performed on the source as well as on comparison stars using DAOPHOT package. The source magnitudes thus obtained were calibrated using two comparison stars 4 and 6 (Villata et al. 1998) having similar brightness as that of the source.

Table 3.1 gives the details of photometry data obtained from MIRO where column 1 and 2 represent the date and MJD of observations, third and fourth column are nightly averaged R- and V-band magnitudes along with photometric errors, column 5 shows the telescopes used. In order to look for INV in 1ES 1959+650, we monitored the source for more than an hour on 9 nights during October - December 2015.

5.3.4 Supplementary data : Optical (Steward Observatory); Radio(OVRO)

We have used optical photometry and polarimetry data available online from the Steward Observatory⁴ during October 2015 to look for the polarization behavior during the flaring state of 1ES1959+650. In order to discuss source behavior in the low energy domain and any possible correlated variation with respect to those in other energy regimes, we have utilized the publicly available radio data from Owens Valley Radio Observatory (OVRO)⁵ at 15 GHz frequency for the duration 2014 December 15 (MJD 57053) to 2016 June 30 (MJD 57569).

⁴<http://james.as.arizona.edu/~psmith/Fermi/>

⁵<http://www.astro.caltech.edu/ovroblazars/index.php?page=home>

5.4 Results and Discussion

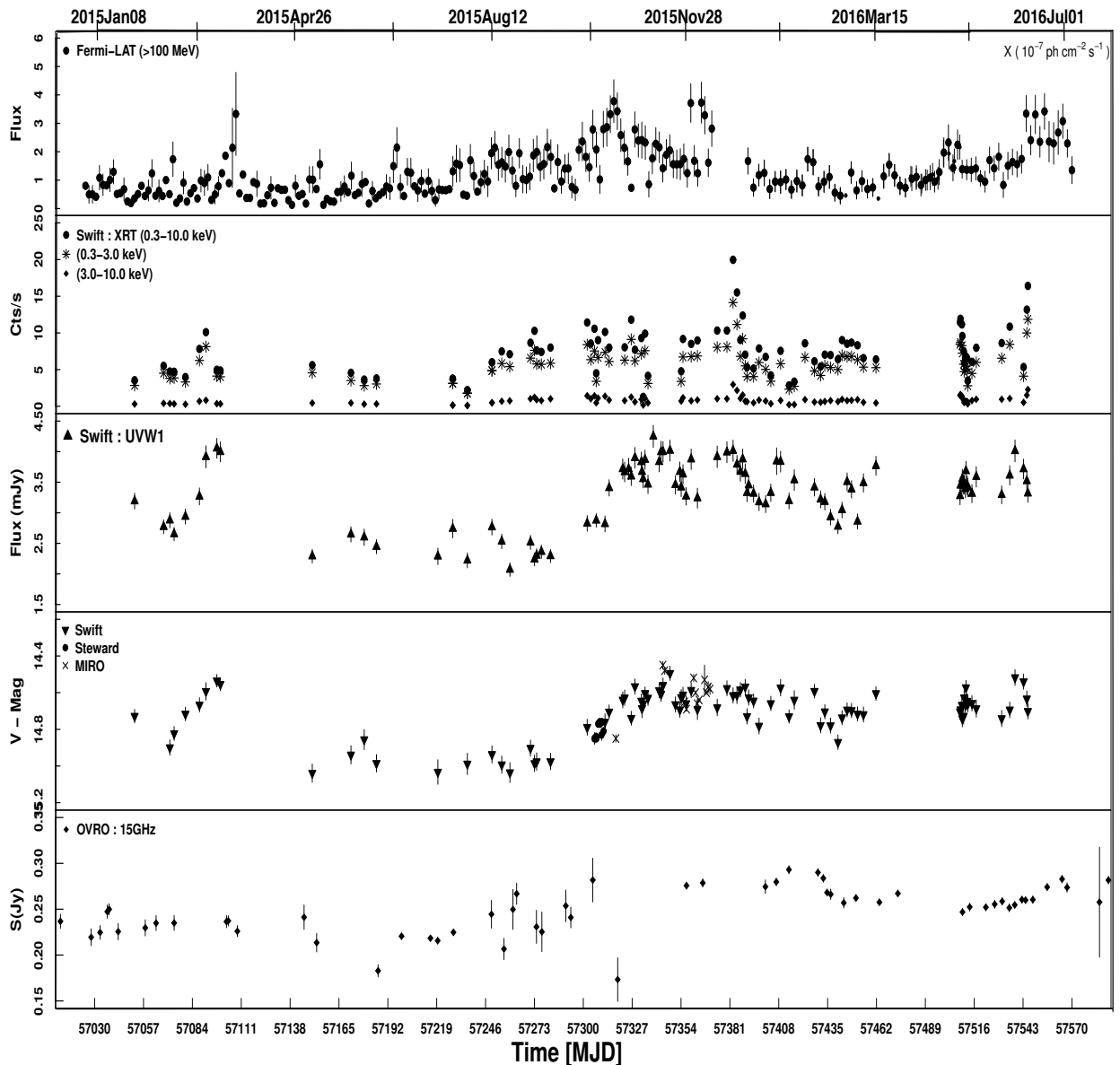
Multi-wavelength light curves (MWLC) are constructed using analyzed data as described in the previous section (section 2) and are shown in Figure 5.1 where X-axis represents the time in MJD (Modified Julian Day) and Y-axis shows respective flux or magnitude values at various energies. In Figure 5.1 (from the top), the first panel: Fermi-LAT γ -ray (0.1 to 300 GeV) flux, second panel: Swift-XRT flux at three X-ray energy bands i.e., (0.3 - 3.0 keV: X1 band), (3.0 - 10.0 keV : X2 band), and (0.3 - 10.0 keV : X3 band), third panel: Swift-UVOT UV (UUVW1-band) light-curve, fourth panel: Swift-UVOT, MIRO and Steward Observatory V-band optical light-curve, fifth panel: OVRO 15 GHz radio light-curve.

5.4.1 Multi-wavelength light curve

As can be noticed from the Figure 5.1, the light curves across all the energy bands (Gamma-rays – X-rays – UV – Optical – Radio) appear very complex in nature, especially during the two major outbursts, with a number of flares, sub-flares with diverse rates and periods of quiescence appearing through out the entire electromagnetic spectrum (EMS). Such random trends are typical in blazar light-curves (Chatterjee et al. 2012). The shape and duration of the flares in the light-curve along with polarization information reveal the emission mechanisms at work, strength of the magnetic fields, etc., in the jet. A rising trend in MWLC corresponds to the acceleration of the relativistic particles as a dominant process while a declining trend indicates to their subsequent cooling.

The flux at GeV energies (0.1 - 300 GeV) for 1ES 1959+650 remained at the level of ($F_{\gamma} \approx 1.3 \times 10^{-08}$ ph cm $^{-2}$ s $^{-1}$) most of the time super-imposed with a number of flares during 2015-16. It should, however, be noted that it is more than double the average flux level reported in 3FGL catalogue ($F_{\gamma} = 5.83 \pm 0.18 \times 10^{-09}$ ph cm $^{-2}$ s $^{-1}$). During the October 2015 outburst, the source showed flux level as high as 3.8×10^{-07} ph cm $^{-2}$ s $^{-1}$ with 2-day binning, highest ever reported for this source in the (0.1-300 GeV) range. Kapanadze et al. (2016) (hereafter, K16) reported γ -ray flux as 1.2×10^{-07} ph cm $^{-2}$ s $^{-1}$ at this epoch in the (0.1-100)

Figure 5.1: Multi-wavelength light curve (MWLC) for 1ES 1959+650 from January 2015 to June 2016, showing three major flaring episodes. Flare 1 (March 2015), Flare 2 (October 2015) and Flare 3 (June 2016) in γ -rays are clearly visible in the MWLC. Time is in MJD, plotted along X-axis and Y-axis has the fluxes/magnitudes. Top panel shows Fermi-LAT fluxes with 3σ statistical error bars. The second panel is soft X-ray (XRT-Swift) with three energy bands (0.3-3.0 KeV, 3.0-10 KeV, and 0.3-10 KeV). Third panel shows UV flux (in mJy; W1 band) from UVOT onboard Swift. Fourth panel display optical V-band magnitudes obtained from Swift, MIRO and Steward Observatory. Last panel shows radio flux at 15 GHz taken from OVRO public archive.



GeV range with a 3 day binning. The difference in maximum flux level might have arisen due to different binning, energy range covered (0.3-100 GeV) and analysis method used in K16.

Several sub-flares, with varying rise/fall rates, have been noticed before and after the onset of major outbursts - March 2015 (outburst 1) and October 2015 (outburst 2) which is extended to 2016 June. On the other hand, X-ray flux was seen to behave erratically during the whole period with significantly enhanced flux when the source was in outburst in γ -ray, UV, optical and radio. A flare beginning at MJD 57070 (outburst 1) appears truncated due to lack of data in X-ray; UV and optical met the similar fate while a clear flare is noticed in γ -ray light-curve, peaking at about MJD 57109 (2015 March 28) with ($F \approx 3.2 \times 10^{-07}$ ph cm $^{-2}$ s $^{-1}$). The trend shows that a complete data set could have led to correlated flaring in all these energy bands.

In soft X-ray band (0.3-3.0 keV; X1 band) counts varied from 3-13 cts sec $^{-1}$, but for X2-band (3.0-10.0 keV; relatively hard flux state), the counts remained between 1-2 cts sec $^{-1}$. During the outburst phase, the total number of counts in X-ray reached as high as 10 - 20 cts sec $^{-1}$. However, K16 report maximum count rate as 22.95 in 0.3 - 2.0 keV range at MJD 57382.8, same as reported in [Kapanadze \(2015b\)](#). Such high X-ray count rate makes it only the third TeV source after Mrk 501 & Mrk 421. The UV light curve (3rd panel from the top) showed significant variation during the outburst period. A consistently high flux is seen starting around MJD 57245 (2015 August 11: onset of outburst 2), with signatures of various flares spanning a few days, super-imposed over an already high flux. Almost similar trend is seen in optical V-band light curve but with less flux modulations superimposed on the increased flux level. These elevated flux levels, almost double the base value, continued for more than 200 days due to intense flaring activity. The radio light curve at 15 GHz shows slowly decreasing flux up to MJD 57184 after which it starts increasing again, showing strong flare and then crossing 2.5 Jy level on MJD 57305 (2015 October 10: outburst 2). After this, radio flux drops sharply, reaching lowest value in the whole duration, just when optical degree of polarization and position angle had undergone rapid

changes (cf Figure 5.2, right panel). Though there are very limited data on DP and PA, their rapid variations are interesting in that these are immediately followed by a major *gamma*-ray flare. Subsequently, optical, UV and X-ray emissions also peak in their respective light-curves. The details of the second outburst will be discussed in the context of γ -rays, in the next section.

Apart from these major flaring activities, several mini-flares spanning a few days in γ -rays can be seen in the light-curve, e.g., flare peaking at about MJD 57070; a drop of flux ($1.7-0.2 \times 10^{-7} \text{phcm}^{-2} \text{s}^{-1}$), 57152; with simultaneously enhanced emissions at radio, UV & X-rays, 57191; no data in X-ray/UV/Optical but 15GHz flux is significantly enhanced, 57340 etc. The detailed investigation of the light-curves reveals twin peaks in γ - ray *lc*, spanning almost 6 days each, just after the major outburst-2 peaks. Both the flares are at almost the same flux level as that of the outburst-2 flare.

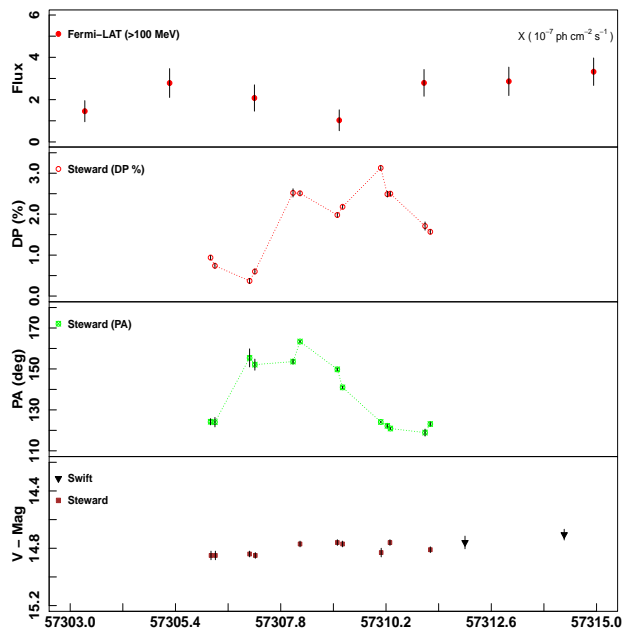
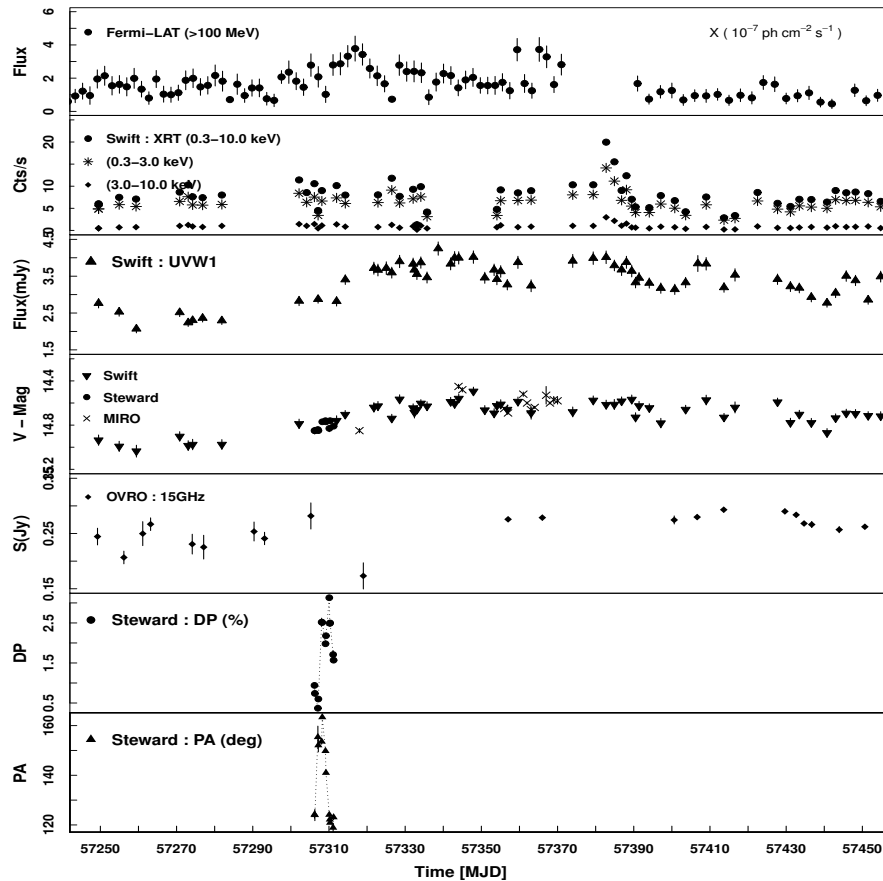
In the following section, we will discuss various features in the light-curve and SED of the source.

5.4.2 MWLC: Outburst 1 (March 2015)

The duration of March 2015 outburst in γ -ray flux was roughly of 29 days (MJD 57094 - 57123) with a peak flux value reaching $F_\gamma = 3.25 \times 10^{-07} \text{ph cm}^{-2} \text{s}^{-1}$ on MJD 57109 (2015 March 28 OR 23 March). During the peak outburst, source brightened by more than 10 times the quiescent state flux value ($F_\gamma > 0.3 \times 10^{-07} \text{ph cm}^{-2} \text{s}^{-1}$). The outburst is temporally almost symmetric with rise time and decay time as 15 and 14 days, respectively. It has several pre-burst flares contributing to it with diverse rates. Similarly, outburst in X-ray has a duration of about 17 days, peaking around MJD 57091 with 10.1 counts s^{-1} . The rising rate for X-rays is $4.4 \pm 1.61 \times 10^{-12} \text{ergs cm}^{-2} \text{s}^{-1}$ with a rather sharp decline. However, it is quite possible that it could have been truncated due to lack of the data, the peak still to occur, just like what we see in UV and optical bands. In that case, all the emissions are likely to peak simultaneously, indicating to having almost same origin.

Notice the similar enhancement in the form of a mild outburst in radio band

Figure 5.2: (Top): Detailed light curves in γ -ray, X-ray, UV, optical and radio with optical polarization (DP) and position angle (PA) for the duration between MJD 57250 - 57450 (August 2015 to March 2016). (Bottom) : Zoomed version of the light curve in γ -ray and optical showing rapid changes in DP and PA occurred within five days (MJD: 57306.5 - 57311.5) before the onset of major outburst in γ -ray.



lasting for about 14 days with a sharp decay. It appears that March 2015 outburst activity first started in radio band, then in X-rays, UV, optical and later in γ -ray. However, there are some pre-outburst flares seen in optical, UV and gamma-rays as well. The γ -ray outburst starts when X-ray emission has almost peaked and UV/optical are in the process of reaching peak values (Figure 5.1). X-ray peak leads UV/optical and γ -ray ones by about 7 and 8 days, respectively. Since 1ES 1959+650 is an HBL, X-ray emission (dominated by soft X-rays) is expected to come from synchrotron process which is also responsible for UV and optical emissions. High energy particles giving rise to X-ray emission cool faster and hence X-ray emission leads optical/UV. However, 7-days lag between X-ray and optical/UV appears to be a bit long and perhaps emission regions are also aligned differently to line of sight (LOS). It could also be that UV and optical peaks could not be exactly located due to the truncated data. In SSC, the γ - ray emission is produced by IC process where synchrotron seed photons take time to travel to high-energy (γ - ray) emission region (light travel time), where these are up-scattered (Sokolov et al. 2004b). It is possible that the emissions are generated when the emitting plasma passed through a standing or slowly moving shock down the jet and below the sub-mm core. Jorstad et al. (2001) reported that γ -ray flares were associated with ejection of super-luminal radio knots into the jet, which initiates flare in radio and γ -ray flare followed.

All the four flares in the light-curve upto MJD 57220 rise slowly while decay very fast. The variations during the outbursts clearly follow a common trend across all the energies, indicating that acceleration timescales for electrons are longer than their cooling timescales.

5.4.3 MWLC: Outburst 2 (October 2015- June 2016)

The build up to the second major outburst (outburst-2: MJD 57285 - 57370) started much earlier, due to the lack of data in other bands (X-ray, UV and optical), we consider the period from MJD 57225, which marks significant enhancement in the fluxes in all energy bands, particularly 15GHz radio band and X-ray, as shown in Figure 5.2. While fluxes in optical, UV and γ -ray start rising

gradually, radio and X-ray band fluxes rise sharply, reaching a plateau at about MJD 57246, when even γ -ray flux has also increased significantly, while optical and UV are still rising. These two bands reach plateau when radio and γ -ray fluxes have already peaked.

The rise and fall rates for γ -rays during 2nd outburst were estimated as $-9.01 \pm 2.21 \times 10^{-09}$ ergs cm $^{-2}$ s $^{-1}$ (MJD 57285 - 57317) and $-3.31 \pm 1.08 \times 10^{-09}$ ergs cm $^{-2}$ s $^{-1}$ (MJD 57317 - 57326). For X-rays the estimated rise rate is $3.44 \pm 0.82 \times 10^{-12}$ ergs cm $^{-2}$ s $^{-1}$ (MJD 57249 - 57382). The main outburst showed sudden flux enhancement, supported by sub-flares, spanning 41 days in γ -rays (MJD 57285 - 57326) reaching its peak value on MJD 57316.8 (2015 October 22). A prolonged, erratic flaring activity (with more than twice the average flux) with duration of about 145 days in X-ray flux is clearly seen, in which a flare peaks around MJD 57382 with largest ever 20 cts s $^{-1}$, followed by four other significant flares, each of them detected with >10 cts s $^{-1}$. Note that we have selected X-ray data-sets to estimate flare duration when the source count rate was above 5 cts s $^{-1}$.

Let us discuss the major flares in the light-curve where γ -ray flux is normally above 10^{-7} phcm $^{-2}$ s $^{-1}$. The flare at MJD 57237 (2015 August 3) decays by 1×10^{-7} phcm $^{-2}$ s $^{-1}$ in 2d, rising again by about 1.2×10^{-7} phcm $^{-2}$ s $^{-1}$ to 1.7×10^{-7} phcm $^{-2}$ s $^{-1}$. The flux in two other flares at MJD 57247 and 57262 rise by more than two-fold to about 2.0×10^{-7} phcm $^{-2}$ s $^{-1}$ in 2d. The pre-outburst flux of flare at MJD 57297 changes from 0.7×10^{-7} phcm $^{-2}$ s $^{-1}$ to 2.14×10^{-7} phcm $^{-2}$ s $^{-1}$ and rises further to 2.4×10^{-7} phcm $^{-2}$ s $^{-1}$ at MJD 57302. It is followed by peak flux (0.28Jy) in radio at MJD 57305 (2015 October 10) and a 26σ detection of VHE by VERITAS (Mukherjee 2015), accompanied by a significant enhancement in optical, UV and X-ray flux. After two more flares contributing to the flux, October 2015 outburst reaches its peak flux 3.75×10^{-7} phcm $^{-2}$ s $^{-1}$ at MJD 57316.88 (2015 October 22) in the (0.1-300 GeV) energy range. The peak in γ -ray flux is followed by delayed peaks in optical, UV, and X-ray bands showing significant variability at about MJD 57322. However, radio flux is at its lowest after a sharp decay. It should be noticed that this major flare in γ -rays happened just after

the rapid changes in optical polarization and position angle followed by peak in radio flux. All these activities signal that the emissions were correlated and were perhaps caused by passage of a blob through the sub-mm core as around the same time significant VHE emission and noticeable radio emission (Mukherjee 2015; Trushkin et al. 2015) were detected. We, therefore, feel that the occurrence of an orphan flare in the (0.3-100 GeV) γ -ray range at this epoch as claimed by Kapanadze et al. (2016), while discussing the X-ray flux variations with other bands appears very doubtful.

After the major flare, the γ -ray flux drops to $0.7 \times 10^{-7} \text{phcm}^{-2} \text{s}^{-1}$ in 10d, rising again to $2.7 \times 10^{-7} \text{phcm}^{-2} \text{s}^{-1}$ in 2d. This flare at MJD 57328 (2015 November 2) is followed by X-ray (K16), UV and optical. The γ -ray flare at MJD 57342 is accompanied by E1-event in X-ray as reported in K16 (ToO observation: we do not have data) with 20 cts/second, followed by first of the twin peak flare in optical (discussed later) and flare in UV. FACT also reported 3σ detection of VHE emission at this epoch. The first twin γ -ray flare at MJD 57360, flux $3.5 \times 10^{-7} \text{phcm}^{-2} \text{s}^{-1}$, is followed by, after one day, second optical twin peak and preceded by E3 event in X-ray (19 cts/s; K16). Radio emission is also enhanced with enhancement in UV flux. All the emissions appear to be nicely correlated. After this, there is break in our γ -ray data, but there are significant flares in optical, UV and X-ray. In fact this was also ToO slot as reported in K16, where a γ -ray flare is accompanied with E2 event in X-ray along with enhanced flux in optical and UV.

A nicely correlated flare in radio, optical, UV, X-ray and γ -ray fluxes is noticed peaking at MJD 57421 (2016 February 3), in the light-curve followed by a Swift data break upto MJD 57507. Just before that, a large outburst occurs (flux change $(1 - 2.2) \times 10^{-7} \text{phcm}^{-2} \text{s}^{-1}$) at MJD 57506 (2016 April 28), decaying part of which is captured by all other bands. A clean flare in UV, optical, followed by X-ray and γ -ray flares at MJD 57540, with 0.25 mag brightness in V and a change in UV flux 2.5-3.5 mJy is seen. A number of flares contribute to the last outburst in γ -ray flux centred at MJD 57544.72 when flux increases almost three fold to $3.34 \times 10^{-7} \text{phcm}^{-2} \text{s}^{-1}$, the outburst lasting about 25 days. X-ray counts

increase from 5 to 15, radio also shows correlated enhancement in the flux while UV and optical are decreasing.

As evident from the 15GHz radio light-curve, the source was active much before the enhancement started in X-ray/UV/optical emissions, i.e., around MJD 57185 and exhibited slow rise, peaking around MJD 57305 with a flux value of 0.28 ± 0.02 Jy, and a sharp fall reaching to half of its peak flux in 14 days, i.e., 0.17 ± 0.02 Jy on MJD 57319 (2015 October 24), extinguishing the 134 days of activity in radio. This sudden ‘‘shut off’’ of activity in radio happened just 7-days prior to the highest peak in γ -ray flux and just after the rapid changes in the optical polarization (see, Figure 5.2) had taken place. [Lähteenmäki & Valtaoja \(2003\)](#); [Jorstad et al. \(2001\)](#) also noticed flaring of radio emission at 37 GHz just before a flare in γ -ray flux occurred. With a break in the data, enhanced flux, by a factor of two ($F_{radio} = 0.250 \pm 0.002$ Jy), is noticed in 15GHz radio band.

Therefore, across the whole spectrum, an outburst with significant high flux levels and slow rising/decaying trend spanning over a few months (long-term variation) is noticed along with flux variations lasting for a few days (short-term variations). Rapid variability in γ -rays with clear mini-flares lasting over a few days is seen, in general, but not always, showing slow rise and fast decrease, with 2-day binned data-set. A slow rising trend in flares suggests fast cooling of electrons and a less stochastic acceleration process ([Kapanadze et al. 2016](#)). A prolonged activity in X-ray band showing chaotic behavior in the light-curve is noticed, when the source was peaking at GeV, γ -ray energies. UV and optical peaks were seen to occur later as compared to X-rays.

Correlation in the flux variations

It is clear from Figures 5.1 & 5.2 that while flux starts rising first at lower energies (V, UV, X-ray) during outburst 2, it peaks first at γ -rays followed by X-ray, UV & V bands. To check if the variations in these bands are correlated, we used discrete correlation function (DCF) which was first introduced by ([Edelson & Krolik 1988](#)) and generalized by ([Hufnagel & Bregman 1992](#)) to include a better error estimate. A brief description of the method is given by [Tornikoski](#)

et al. (1994) and Hufnagel & Bregman (1992). The zDCF (Alexander 2014), a variant of DCF which corrects for various biases in the DCF method by employing equal population binning and Fishers z-transform, is used to look for correlated variations. Lags have been computed based on maximum likelihood criterion satisfying one sigma confidence interval.

Figures 5.3 & 5.4 show three columns consisting of three panels each. Top two panels show light curves at two different energies while bottom panel show discrete correlation between them. In the correlation study on the present data sets, we notice that due to multiple overlapping flares in almost all the bands, and particularly erratic, elevated flux in X-rays, the correlations between various fluxes are not very strong. We could not get a clear correlation with X-ray vis-a-vis other bands and it is now shown here. However, as is reflected in the light-curves also, UV and optical fluxes are correlated with more than 95% confidence level (0.5 significance), with UV leading optical by about a 2 hr 20 mins (Fig. 5.4). Similarly, γ -ray versus V and UV are correlated with γ -ray leading by 20 and 18 days, respectively. It can be clearly seen that events in γ -rays are well correlated with events in UV and optical and fairly with X-ray variations. Therefore, the high energy γ -ray emission was followed by emissions at lower frequencies, X-ray, UV and optical, in general. However, there are instances when γ -ray emission lags behind low energy emissions, which can be explained based on light-travel time arguments and/or differentially aligned emission regions with respect to LOS.

In case of HBLs, low energy emissions (IR to soft X-rays) are produced by the relativistic electrons as synchrotron radiation while the high energy emission is expected to be generated through Inverse Compton (IC) process under which synchrotron photons are up-scattered by the same population (synchrotron) of electrons which produced them. Generally, it is the most preferred scenario known as one-zone SSC that is capable of explaining SED of the high energy peaked blazars (HBL) and has been used in many other studies (Bottacini et al. 2010, and references there-in). In SSC, both, low and high energy SED components are expected to show similar temporal evolution.

Figure 5.3: Discrete correlation plots for 1ES 1959+650, during October 2015 outburst between (Left) γ -ray & UV, (Right) γ -ray & V-band. Top two panels show light curves in respective energies (X-axis : MJD; Y-axis : Flux/Mag) while the bottom panel shows correlation between them (X-axis: Lag in days; Y-axis: zDCF).

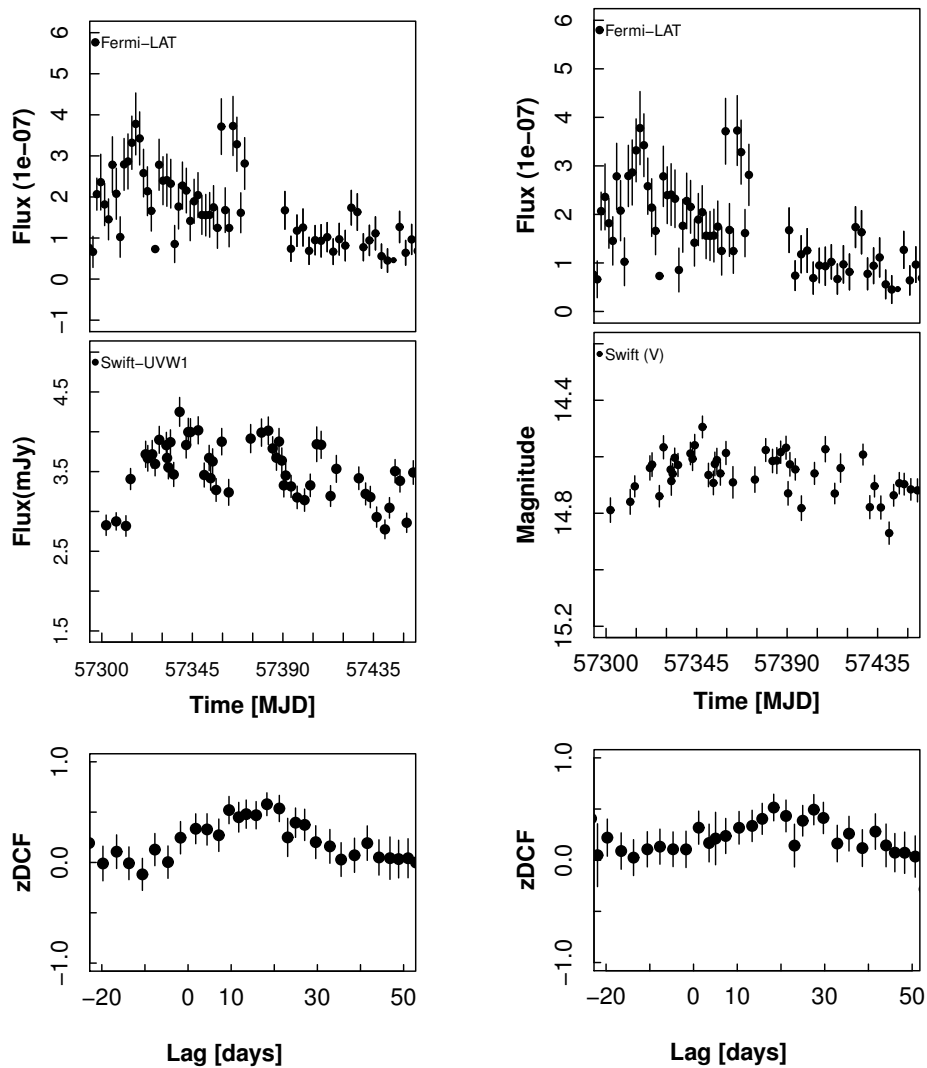
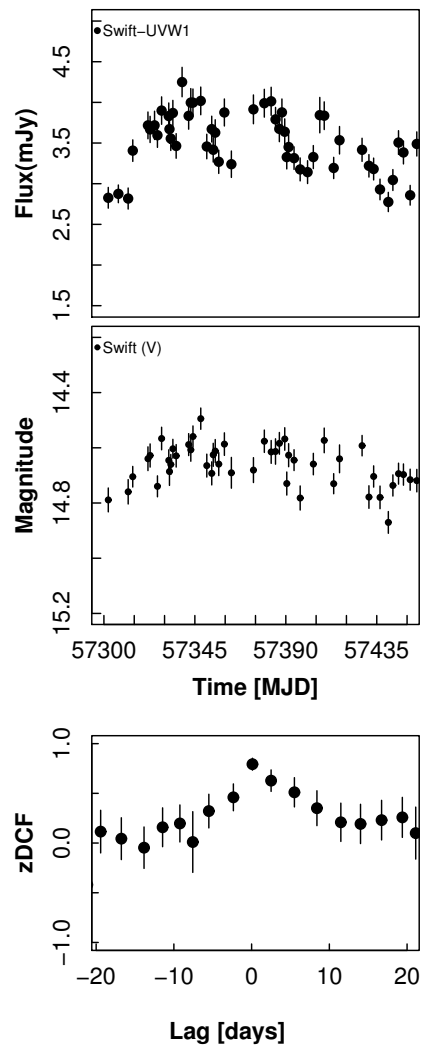


Figure 5.4: Discrete correlation plots of 1ES 1959+650, during October 2015 outburst between UV (UVW1 band) & optical (V-band). Top two panels show light curves in respective bands (X-axis : MJD; Y-axis : Flux/Mag) while the bottom panel shows correlation between them (X-axis: Lag in days; Y-axis: zDCF). Correlation is significant at 95% confidence.



Since significant lags were noticed between high energy γ -rays and other low energy emissions, opacity effects of the turbulent medium inside the jet could be responsible. In this case, the higher energy emission would occur first followed by low energy emission, as longer wavelengths are more susceptible to opacity effects compared to shorter ones. The second explanation could be if the emissions are generated in different regions and/or are aligned differently to the line of sight of an observer. For example, if emission region emitting at higher energy is oriented closer to observer's line of sight as compared to other regions emitting at lower frequencies, then high energy emission would be more strongly Doppler boosted (due to relativistic effects) and will show faster variations in the light-curve (Mastichiadis & Kirk 1997; Finke et al. 2008). The low-energy emitting region being slightly away from observer's line of sight, would show delayed emission. This could be the reason that an activity is first seen at higher energies followed by lower energies and still appears to be correlated.

A strong correlation between soft X-ray and hard X-ray is seen as displayed in figure 5.5 in which we have plotted temporal variation of X-ray fluxes in 0.3-10 keV (first panel from top), 0.3-3.0 keV (third panel) and 3.0-10 keV (fourth panel) ranges. The spectral index is plotted in the second panel showing the harder when brighter trend. In the bottom panel, we also plot x-ray hardness ratio as a function of time. Overall the hardness ratio increases with time. Interestingly, hardness ratio increases rapidly in the run up to the maximum flux while flaring. After that, it remains range bound between -0.6 to -0.55. The strong correlation between soft and hard X-ray fluxes is also confirmed in figure 5.6 suggesting the common origin of the X-ray emission via same energy processes or a co-spatial nature of the emitting regions in two energy domains. The later one is more probable as softer side is supposed to be emitted in synchrotron process but both, soft and hard x-ray fluxes share the same population of relativistic electrons. The emissions at different X-ray energies did not show any lag between them (cf. Fig. 5.5). However, to check how strongly these emissions are correlated, we carried out first order and second order polynomial fitting on the whole data and results are plotted in the Figure 5.6. We found that the quadratic function provided a

better fit, with the regression coefficient of $R^2=0.91$, in comparison to the linear fit ($R^2=0.88$). The results suggest that when the source was brightening, there were more number of hard X-ray photons as compared to softer ones. This means that when the source was in active phase, either there were more number of seed photons available which are then reprocessed (from inside or outside the jet), or a large number of hard X-ray photons themselves were generated by the internal shocks in the jet. On the other hand, lower energy hard X-ray photons might be contributed by synchrotron process itself, adding to hard X-ray flux. Our study found that the source showed harder when brighter (cf Fig. 5.5) behaviour, which is typical in case of blazars.

Nevertheless, the origin and prolonged activity in X-rays, as mentioned above, is still intriguing. The lack of connection between optical/UV and X-rays, very low degree of polarization (random), longer cooling timescales in X-ray light curves as noticed for Mrk 421 (Baloković et al. 2016) suggest contributions from multiple emission regions. Raiteri et al. (2015) suggested a complex UV and X-ray behavior for PG 1553+113 using multi-wavelength WEBT campaign data. A recent study by Cavaliere et al. (2017) suggested the presence of an extra keV synchrotron component during particle progressive acceleration along with canonical optical to GeV emissions. It would, therefore, be very interesting to look for the processes and regions leading to the origin of X-rays and their relationship with other energy-bands during outburst and longer quiescent states to understand emission mechanisms at work inside the jet.

Quantifying fractional variability amplitude, F_{var}

The source showed different sampling patterns at different energies that leads to different timescale to probe in different sources (Edelson 1992). In order to perform variability study, the first check is to determine whether the source is truly variable or not. The variability amplitude at all the energies could be determined using the fractional root mean square (rms) variability parameter, introduced by Edelson & Malkan (1987); Edelson et al. (1990). Basically, the excess variance was used to compare the variability amplitudes at different energy bands from

Figure 5.5: The X-ray light curve (Time in MJD along X-axis; Counts/sec along Y-axis) shows the similar flux trend in blazar 1ES 1959+650 using three different energy bins, i.e., 0.3–10keV: first panel (from top); 0.3–3keV: third panel; 3–10keV: fourth panel. The second panel shows the spectral index in 0.3-10 keV range. The bottom panel shows the hardness ratio obtained from fluxes at 3.0-10.0 keV and 0.3-3.0 keV.

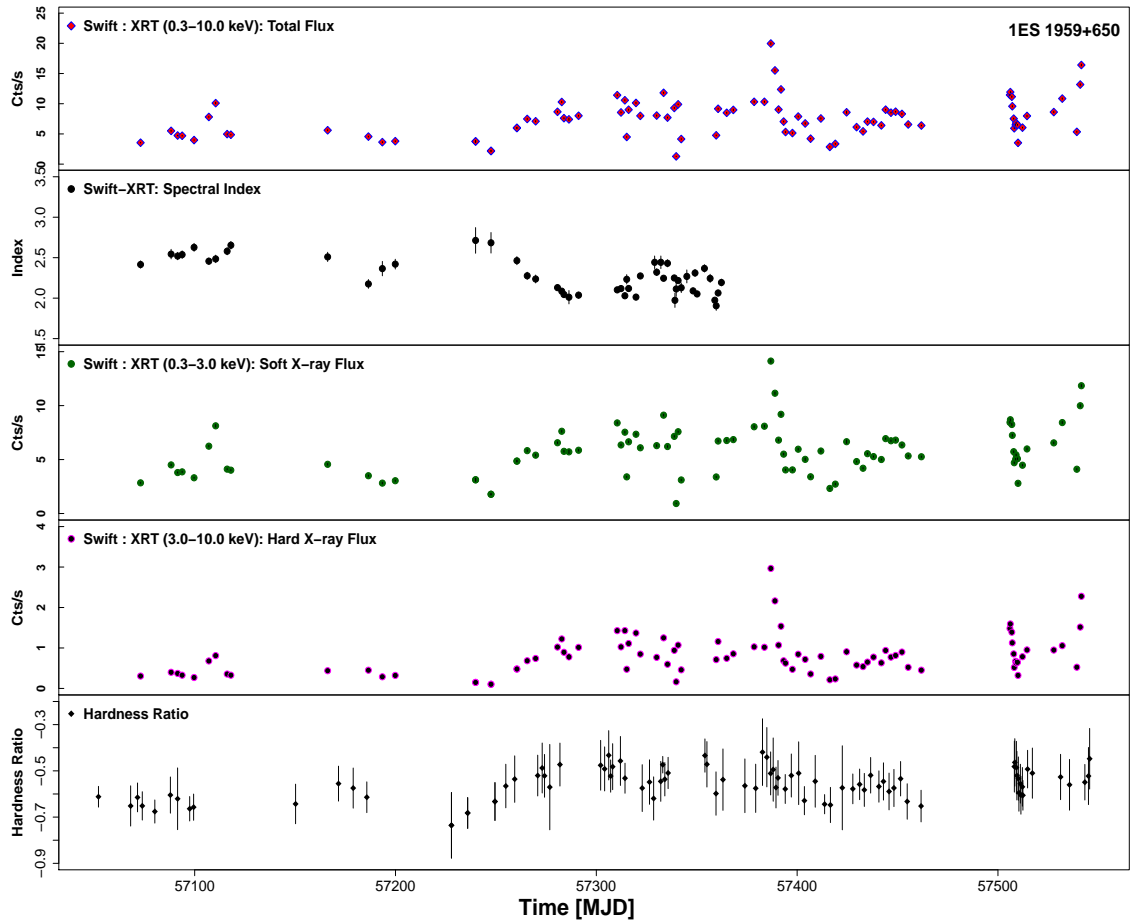
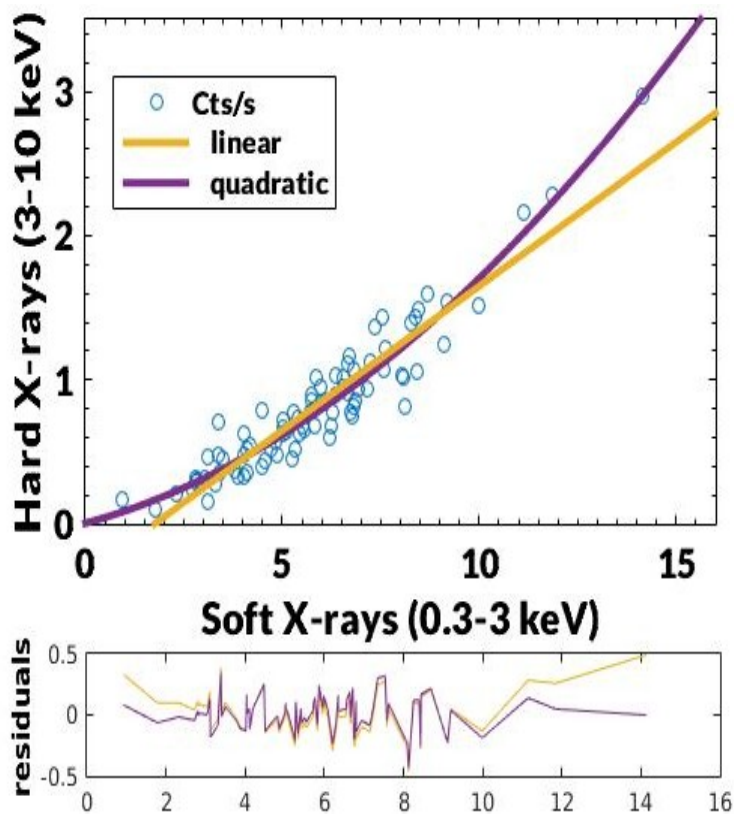


Figure 5.6: The plot shows correlation between the soft X-rays (0.3–3 keV) and the hard X-rays (3–10 keV) flux in 1ES 1959+650 during its bright state. A strong correlation is seen using the quadratic fit in violet ($R^2 = 0.91$) along with linear fit indicating to common origin of two emissions. The lower panel shows residuals of the fitting.



the same observation (Vaughan et al. 2003). This methodology has some caveats that suggest the densely sampled data having small flux uncertainties at different energies, taken from different instruments with different sensitivities. Otherwise, large data gaps or high uncertainties in flux measurements can also introduce larger values of rms variability amplitude. In the present case, the availability of good quality data across EMS allowed us to infer the variability in the source. The fractional variability and the associated errors were calculated using the relation from Vaughan et al. (2003),

$$F_{var} = \sqrt{\frac{(S^2 - \sigma^2)^2}{r^2}} \quad (5.1)$$

$$\sigma F_{var} = \sqrt{\left(\sqrt{\frac{1}{2N}} \frac{\sigma^2}{r^2 F_{var}}\right)^2 + \left(\sqrt{\frac{\sigma^2}{N}} \frac{1}{r}\right)^2} \quad (5.2)$$

where, S^2 is the sample variance, σ^2 is the mean square value of uncertainties associated with each observation, and r is the sample mean.

The table 5.1 shows that the fractional rms variability amplitude, for the blazar 1ES 1959+650, increases towards higher frequencies. The large variability towards higher frequencies could be due to the large number of particles producing very high energy emission from a very compact region. The jet emission dominates over a slowly varying yet steady thermal component from the disk, and any thermal contribution from disk will be diluted by the non-thermal emission component inside the jet. Therefore, the larger rms variability is seen towards higher frequencies. Other studies on several blazars have been reported to show the larger fractional variability towards the higher energies (Abdo et al. 2010a; Ramakrishnan et al. 2015). But, Bonning et al. (2009) reported the decrease in fractional rms variability amplitude towards higher frequency for the source 3C 454.3. They argued that it could be due to the presence of stable thermal component which is also noticed by Villata et al. (2006). According to the internal shock model, the variability should show increasing trend of rms variability amplitude, for intrinsic variability in the source, at higher frequencies. It is because when the shock is formed, large number of high energy particles emits from a very compact region just behind the shock. And, the lower-energy emission escapes

Table 5.1: Column 1 represents the different energy regime and the energy ranges are given in column 2. The fractional root mean square variability estimate for each energy range is calculated in column 3 along with the associated errors in column 4, using the prescription given in [Vaughan et al. \(2003\)](#).

Energy	Frequency range	F_{var}	Error (F_{var})
Gamma-rays	0.3-300 GeV	0.538	0.021
X-rays	0.3-10.0 keV	0.424	0.004
	0.3-3.0 keV	0.394	0.005
	3-10.0 keV	0.571	0.020
UV-W1	at 4.76 eV (2600 Å)	0.104	0.014
Optical-V	at 2.27 eV (5468 Å)	0.091	0.008

from much extended region behind the shock, which also acts as a reservoir and show variations less profound and longer compared at higher energies.

Synchrotron cooling time scale and magnetic field strength

In the earlier section, we noticed that during second major outburst, the optical emission was delayed by a few hours with respect to the emission in UV band. Now, since 1ES 1959+650 is an HBL, both the emissions are generated by synchrotron process in which electrons are accelerated to the relativistic velocities, which then cool down, radiating at various frequencies- higher frequency emission being emitted first due to faster cooling rate. Therefore, the time lag between emissions at two frequencies can be taken as the difference in the radiative cooling time scales of the population of electrons emitting at those frequencies ([Urry et al. 1997](#); [Baliyan et al. 1996](#)). We can, therefore use the delay between the UV and optical emissions as cooling timescale of the synchrotron electrons and estimate the magnetic field. Using the expression for cooling time scale ([Urry et al. 1997](#)),

$$t_{lag} \approx t_{cool} = 2.0 \times 10^4 \sqrt{\frac{\delta}{(1+z)}} B^{-3/2} (\nu_{15}^{-1/2})_{sec} \quad (5.3)$$

where, B is magnetic field in Gauss, ν_{15} is the frequency in 10^{15} Hz, $\delta = 15$ (Mastichiadis & Kirk 1997) and $t_{lag} = 140$ minutes. This gives us a magnetic field estimate of ≈ 4 G which is on the higher side in such systems.

Estimation of the sizes of emission regions

The central regions of the AGN are very compact in size and can not be resolved by any existing facility. The variability property provides a tool to explore those innermost regions. We have noticed that there are several flares with short time scales. The shortest time scale of variation provides an upper limit to the size of emission region at that particular waveband, based on the light-travel time arguments. In γ -rays, doubling time scale is the time period when flux doubles its initial value with more than 3σ significance. We use it to estimate the upper bound on the size of the emission region, R_γ (Saito et al. 2015). Based on the light-travel causality relation, we estimated R using the relation,

$$R \leq \frac{\delta c \tau_d}{(1+z)} \quad (5.4)$$

where, R is the radius of the emission region, δ is Doppler factor, taken here as 40 (Aliu et al. 2014) for γ -rays, $\tau_d = 1$ day, is the flux doubling timescale and $z = 0.048$, redshift of the source. The γ -ray emission size is estimated as $R_\gamma \leq 9.89 \times 10^{16}$ cm. For the optical emission region, we used variability timescale of 4.5 hrs as a characteristic timescale and $\delta = 15$, to estimate the upper limit to the size of the emission region as $R_{op} \leq 3.71 \times 10^{16}$ cm. The γ -ray emission region estimated here is of the same order but about 3 times larger in size than the optical region size. The emission region sizes obtained suggest that the γ -ray and optical emission might be co-spatial in nature. However, one has to be cautious as due to the larger bin size in case of γ -rays as compared to optical, it is difficult to get an accurate value for the doubling time scale.

The location of the γ -ray production site is not very well known for all the sources, in general. But, for a few sources many authors reported location of

γ -ray emission region based on VLBI and high energy (GeV to TeV) simultaneous data-sets (Agudo et al. 2011; Marscher 2014). Based on these observations, respective models predict that the γ -rays are produced close to the standing radio core (at 1-10pc) as γ -rays cannot escape from the vicinity of black hole due to photon absorption effects.

To determine the distance of the γ -ray emitting region from the central source, we need to know the opening angle close to the base of the jet, Doppler factor (δ), flux doubling time scale (τ_d) and redshift (z). The jet opening angle for blazars is generally less than 1 degree due to small viewing angle (Jorstad et al. 2005), in general. Therefore, using the jet opening angle close to 1 degree, which is the upper limit of opening angle for BL Lacs (Pushkarev et al. 2012), we estimate the distance to the location of γ -ray emission from central engine, using following equation as,

$$d = \frac{\delta c \tau_d}{(1+z)\theta_j} \quad (5.5)$$

The location of high energy γ -ray emission region from central SMBH is estimated as $d = 1.72$ pc. The result indicates that the location of γ -ray production site is close to the standing shock (sub-mm core) inside the jet. Since the jet opening angle for BL Lacs is difficult to measure due to several reasons, eg., jet bending at parsec scale or faint emission where the jet bends etc. (Rector et al. 2003), and the different values reported by many authors (Rector et al. 2003; Jorstad et al. 2005; Lister et al. 2011), the present value for the location should be considered with caution.

5.4.4 Twin flares during October 2015 outburst: Optical/ γ -ray light-curve

Figure 5.2 (left side; top to bottom) shows γ -ray to radio band light-curve with optical polarization for 1ES 1959+650 during MJD 57250 - 57460 constructed using data from space-based instruments (LAT/XRT/UVOT), from MIRO and Steward Observatory (R band converted to V-band as given in Tagliaferri et al. (2003)). On a careful look, a twin peak structure is noticed in optical as well as in

γ -ray light-curve during outburst and post-outburst phase, respectively. Optical twin flares peak around 2015 November 18, MJD 57344 ($R = 14.45 \pm 0.02$ mag) and December 5, MJD 57361 ($R = 14.52 \pm 0.02$ mag); whereas γ -ray twin flares were recorded around 2015 November 30, MJD 57360 and December 5, MJD 57365.5, both showing similar flux levels. It appears that the emission in γ -rays and optical are correlated, peaking almost at the same time.

From the onset of outburst, 1ES 1959+650 brightened gradually during October 2015 with $V = 14.85 \pm 0.02$ mag on MJD 57306 (2015 October 11). On October 13, it brightened by 0.08 mag within a day, decaying by 0.06 mag during MJD 57309 and MJD 57310. On the later date, it brightened by 0.07 mag in about four hours, to 14.76 ± 0.02 mag. After that, the source went into low-flux state and started dimming, reaching 14.81 (0.02) mag on MJD 57311 (October 16, 2015). However, on MJD 57344 (November 17, 2015) our observations detected the source in its brightest level during whole 2015 with 14.45 ± 0.02 mag.

The twin peaks in optical have been reported in a few HBLs (Sokolov et al. 2004b). The flux enhancement in the sources like blazars is well explained by shock models, kink models etc. A propagating shock in plasma with a random magnetic field (Blandford & Königl 1979; Marscher & Gear 1985) hits the Mach disk which leads to the formation of double structured feature in the light-curve. HBLs 1ES 0229+200, 1ES 0502+675, 1ES 2344+514 etc. are seen with such double peaks in optical, with or without periodicity present in their light curves (Kapanadze 2010). On the other hand, in the shock-in-jet model, at the shock front, two regions contribute to the emitted radiation - emission from forward and reverse shocks which could be responsible for short duration twin structures in the optical light curve. On the other hand, in sufficiently magnetized environments, kink instabilities can efficiently convert the magnetic energy into bulk kinetic and thermal energy in the jet. When the shock propagates down the jet through kinky nodes, it illuminates them along its path before getting dissipated as described by Zhang et al. (2016) using relativistic magneto hydrodynamic simulations.

5.4.5 DP and PA change during October 2015 outburst

It is interesting to see how the polarization behaved during multi-frequency outburst during October 2015 in 1ES 1959+650. The Steward observatory optical polarization and position angle (DP and PA) data are plotted in the bottom two panels of Figure 5.2 along with other fluxes, and, with more clarity, in Figure 5.2 (on the right) along with R-band data for October 11 - 17, 2015 (MJD 57306 - 57312). During 2015 October 12 -13, DP along with R-band brightness increased sharply (DP: 0.3% to 2.5%, R mag: 14.37 to 14.31) followed by 10 degree change in PA to 153 degree . While brightness and DP remained at higher levels (DP: 3.13 - 1.57, R-mag: 14.3 -14.37), PA, after successive rotations by 20 degree on next two days, settled down around a value of 120 degree. DP is maximum when the source is brightest during these observations. Variations in DP and R-band magnitudes are also seen at intra-night time scales as well. On October 15, 2015, 1ES 1959+650 brightened by 0.07 mag in R (about 3σ) in about 4.8 hrs, while DP changed by 0.64% ($> 8\sigma$) within 3.6 hrs.

Here, we discuss multi-wavelength flare patterns with changes in optical polarization features. Figure 5.2 clearly shows that DP and PA significantly changed during October 2015 outburst when the source was in very high flux state across the whole electromagnetic spectrum (EMS). While the source was slowly brightening in optical, X-ray and γ -ray, the degree of polarization changed by 2.8 % within 4 days i.e., from MJD 57307 (DP: 0.3 %) to MJD 57310 (DP: 3.0 %). This increase in DP is followed by a change in the position angle of polarization by almost 80 degrees within six days duration. The 15 GHz radio flux reached its peak and then decreased sharply during these changes in optical polarization features, after which flux in γ -rays, followed by optical, UV and X-rays peaked. All this, perhaps, coincided with injection of fresh plasma in the jet which led to flaring in radio, γ -rays and other bands. The situation well suits for the case of emission feature moving down the jet, interacting with the standing shock which results in compression of plasma, alignment of magnetic field resulting in changes in polarization properties and acceleration of charged particles. These physical processes lead to enhanced emission at all the frequencies and increased degree of

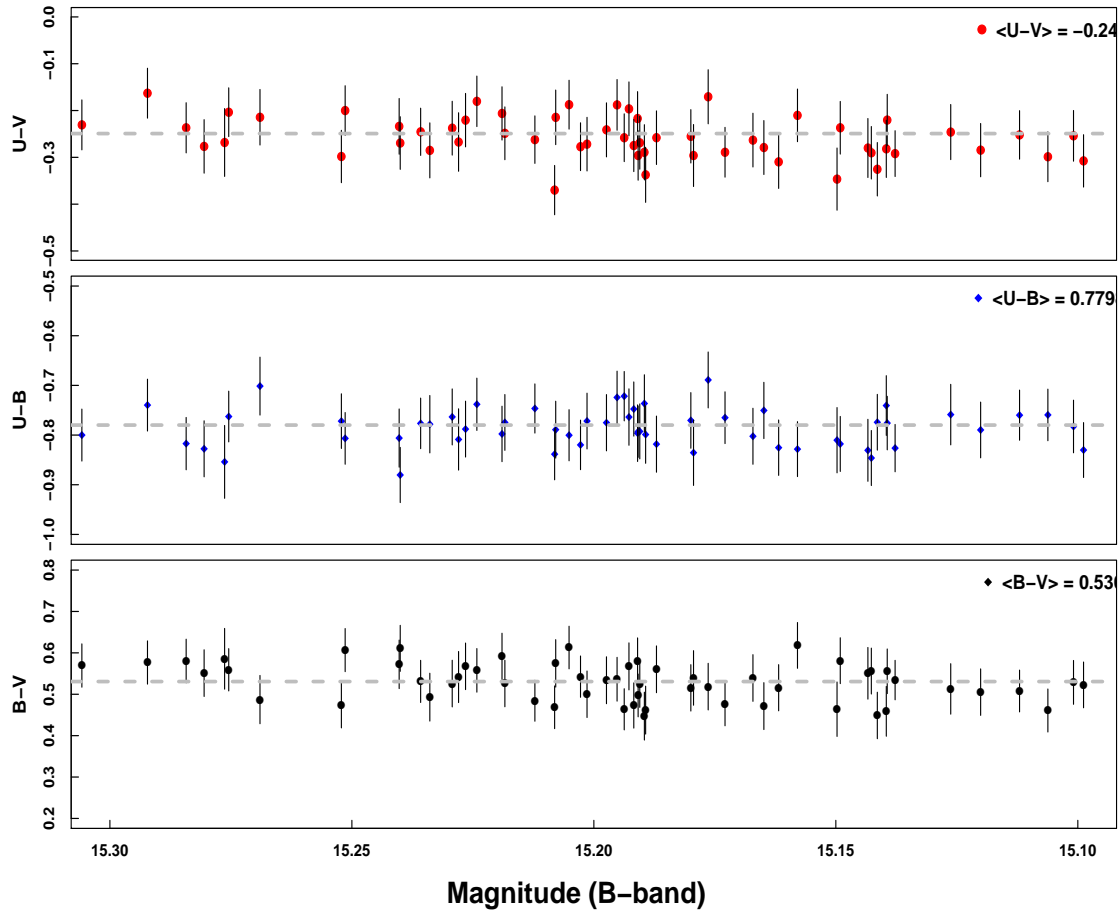
polarization (Marscher 2014). Unfortunately, the polarization data do not cover the complete outburst, including the peak period.

5.4.6 Injection of a new component in the jet

In order to understand the multi-frequency connection of the major outburst activity in 1ES 1959+650 during 2015 October, 15 GHz OVRO data and Astronomers Telegrams (ATels) on TeV activity reported during this outburst are analyzed. During MJD 57303-57304 (2015 October 8/9), the onset of TeV activity (Mukherjee 2015) showing much harder spectra, $\alpha_{TeV} = 2.5$, was followed by a significant enhancement in 15 GHz radio flux, $F_{radio} = 0.28 \pm 0.02$ Jy and γ -ray ($> 100 MeV$; $F_{\gamma} = (2.27 \pm 0.68) \times 10^{-07}$ ph cm $^{-2}$ s $^{-1}$). After six days of flux rise in radio and γ -rays, the source showed historically highest X-ray flux on MJD 57311.99 i.e., (10.13 ± 0.10) cts/s in (0.3-10.0) keV and (7.34 ± 0.09) cts/s in (0.3-3.0) keV energy range. A quasi-simultaneous enhancement in GeV, $F_{\gamma} = (2.86 \pm 0.67) \times 10^{-07}$ ph cm $^{-2}$ s $^{-1}$ on MJD 57313; $F_{\gamma} = (3.77 \pm 0.75) \times 10^{-07}$ ph cm $^{-2}$ s $^{-1}$ on MJD 57316.86 and (7.99 ± 0.06) cts/s in X-ray (0.3-10.0) keV on MJD 57314.28 were reported. The source was detected with highest ever X-ray flux on MJD 57326.48 with exceptionally high count rates i.e., (11.81 ± 0.09) cts/s in (0.3-10.0) keV and (9.12 ± 0.08) cts/s in (0.3-3.0) keV. 1Es1959+650 was dimming in GeV ($F_{\gamma} = (2.05 \pm 0.54) \times 10^{-07}$ ph cm $^{-2}$ s $^{-1}$ on MJD 57347.80) but brightening up in optical, showing $V = 14.94 \pm 0.03$ mag on MJD 57347.91. We also noticed flux enhancement in radio by almost 0.1 Jy, showing $F_{radio} = (0.275 \pm 0.003)$ Jy on MJD 57357 (2015 December 1), followed by GeV activity on MJD 57365.20 ($F_{\gamma} = (3.73 \pm 0.72) \times 10^{-07}$ ph cm $^{-2}$ s $^{-1}$).

The almost continuous enhancement in flux during October 2015 outburst, at different frequencies, suggests a scenario of continuous injection of fresh relativistic particles near the origin of the jet, that accelerates the particles (electrons/positrons) up to the relativistic energies, which, in turn cool down by emitting higher energy photons followed by the emissions at lower frequencies. This can also explain a mild bluer when brighter color seen in the present study 5.7. However, color remains same with time, within errors, except during flaring when

Figure 5.7: Optical color-magnitude plot of 1ES 1959+650 during 2015–2016. The X-axis shows the B-magnitude and the colors, U-B (top panel), U-V (middle panel) and B-V (bottom panel), are plotted along Y-axis. The legend on the top-right corner shows the average color and the grey dashed line shows the best fit to the data.



it shows a stronger BWB behavior, typical of HBLs. A quasi-simultaneous enhancement in the high energy γ -ray and radio flux, perhaps, may be associated with the presence of a standing shock feature or core. The emission in γ -rays is supposed to arise from the seed photons in the acceleration and collimation zone inside the jet, where all particles spiral in helical magnetic field and emit in VHE γ -rays (Marscher 2008). The radio emission is opaque upstream the stationary core due to synchrotron self absorption effects, and becomes transparent only when the emission feature interacts with the radio-core.

During 2015 October outburst, publicly available data and a few published re-

ports suggest correlated variations in radio and TeV fluxes. A quasi-simultaneous flux variability is also noticed by [Tagliaferri et al. \(2008\)](#) and [Hayashida et al. \(2008\)](#) along-with many other authors who reported a correlated activity between highly variable strong γ -rays and radio frequencies ([Ramakrishnan et al. 2015](#)) with an evidence of the ejection of a super-luminal knot from radio core using VLBI images ([Jorstad et al. 2001](#); [Schinzel et al. 2012](#); [Jorstad et al. 2015](#)). Their study suggests that if the origin of seed photons responsible for enhanced γ -rays is from the region near radio core (mm-core), then it would, most probably, be due to the interaction of the moving shock with the standing core.

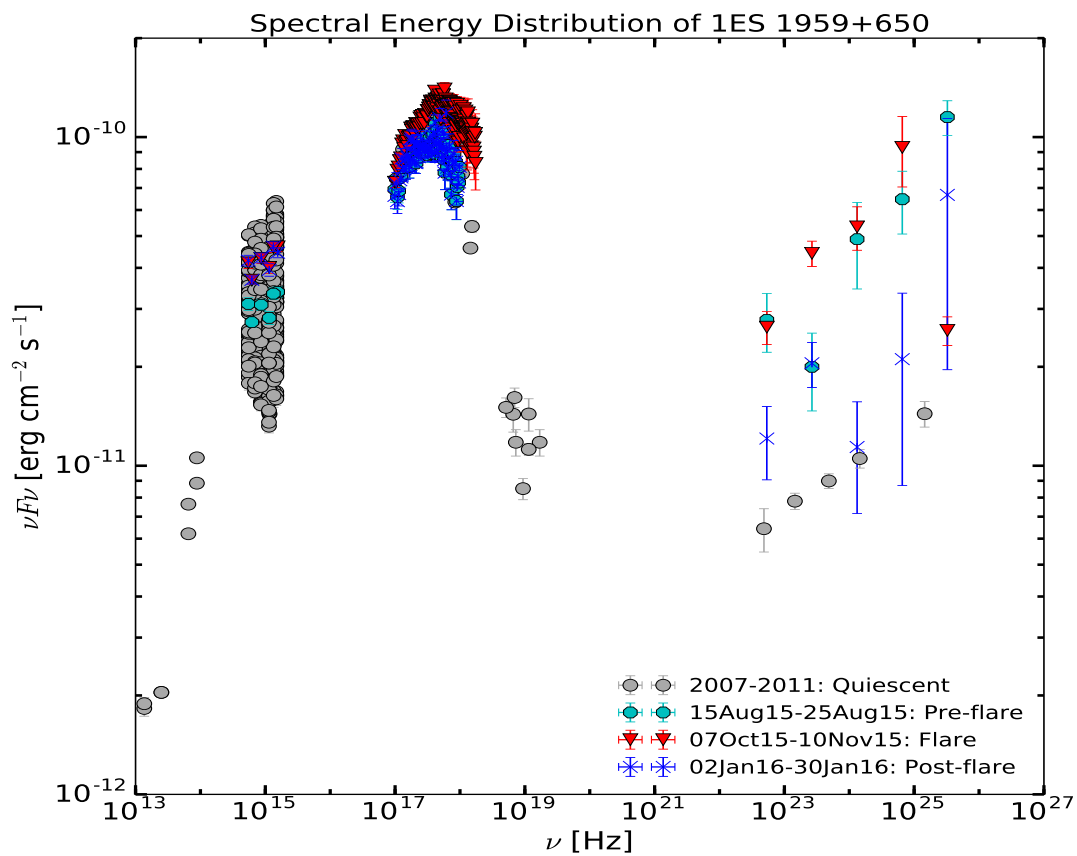
5.4.7 Time-averaged Spectral Energy Distribution

In order to study the spectral behaviour of the HBL 1ES 1959+650 during various flux states, broad band SEDs are constructed using the multi-wavelength data. The figure [5.8](#) shows the complete spectra of 1ES 1959+650 with the frequency (ν ; in Hz) plotted along X-axis and the flux (νF_ν ; in $erg\ cm^{-2}s^{-1}$) along Y-axis. The time averaged spectra are constructed for three different epochs when the source was in different γ -ray flux states, e.g., pre-flare (15 August - 25 August, 2015; cyan), during flare (07 October - 10 November, 2015; red) and post-flare (02 January - 30 January, 2016; blue). The data representing the low state (grey) of the source for the duration 2007 to 2011⁶ are used in the SED to provide a comparison of the spectral features in various flux states.

The optical data is corrected for the effects of the extinction ([Cardelli et al. 1989](#)), de-reddening and the fluxes are converted into proper units ($erg\ cm^{-2}s^{-1}$). The X-ray spectra are generated combining all the observation IDs and fitted with broken power law and the log-parabola models in *Xspec*. However, the results are presented using log-parabola model as it gives a natural turnover to the spectral curvature. The gamma-ray flux is integrated for the different epochs and the spectra are extracted for several energy bins for three epochs as mentioned above, centered around 0.2 , 1.1 , 5.4 , 27 and 134 GeV. The complete likelihood analysis is performed using gtlake tool and the analysis is re-run on each energy

⁶The non-simultaneous data are retrieved from ASDC

Figure 5.8: Time averaged spectral energy distribution for HBL 1ES 1959+650 during 2015-2016. The combined spectra during different epochs covering the flare (filled down-triangles; red), pre-flare (filled circles; cyan) and post-flare (cross symbols; blue) periods. The low-flux phase data collected over the period 2007-2011 are plotted with grey filled circles.. The low energy synchrotron component during pre-flare and post-flare periods are seen to overlap (for details, see the text).



bin, for all the epochs.

The nature of spectra shown in SEDs indicates to the complex emission processes at work in different brightness phases of the source. The spectra at these epochs confirm that the source is more variable across the whole energy spectrum when in high state as also inferred from the light curves (see figure 5.1). During the flaring, the spectrum of the source shows that the synchrotron component peak is mildly shifted towards the higher energies and the X-ray spectrum becomes relatively harder. At the same time, the γ -ray spectra becomes softer with a photon index of -1.78. The steepening of the γ -ray spectrum and the shift in the synchrotron peak location towards higher energy in HBLs have been reported by several other authors (Lichti et al. 2008; Tagliaferri et al. 2008; Aliu et al. 2014; Pian et al. 2014, and references there-in).

When comparing the post-flare and the low-flux (quiescent) states activity, the synchrotron component of the source spectra appears almost similar with similar fluxes and the spectral shape. On the other hand, the IC component shows the enhanced fluxes during the post-flare epoch as compared to those in the low-flux state. During the pre-flaring epoch also the synchrotron spectrum does not change much from its low-flux status, but the high energy component (IC) becomes steeper (see figure 5.8) showing the significant elevated fluxes. This behavior could be due to already elevated flux state of the source as compared to post-flare epoch fluxes. Alternative to it could be an increase in the particle density which can explain increase in γ -ray flux during an enhanced phase. But in SSC, such increase should accompany an increase in X-ray (synchrotron) flux which is not seen. However, activity could be driven by an increase in the particle density, which will cause a decrease in the associated magnetic field, thus resulting almost no increase in low energy component (synchrotron part) (Paggi et al. 2009). This could explain lack of any change in the synchrotron component and IC component showing significant increase during pre- and post-outburst phase.

An interesting case of the shift in the synchrotron peak frequency location in another HBL, Mrk 421, is reported by Baloković et al. (2016). The authors

have noticed that the synchrotron peak frequency location gets shifted, by more than one order (from 0.1-5 keV to 0.04 keV), towards the lower energies during its low flux state and the X-ray spectra hardens when the source is in the bright phase. Pian et al. (2014) reported that the X-ray and γ -ray spectrum, in case of Mrk 421, gets steeper when the source is in its bright flux state. While studying another HBL, Mrk 501 in the flaring state, Pian et al. (1998) noticed the X-ray spectrum getting harder and high energy (γ -ray) spectrum becoming softer with the synchrotron peak frequency located in hard X-ray region during the flare (BEPPOSAX 0.1 - 200 keV observations). One can, therefore, state that relativistic blobs advancing down the jet have peculiar physical conditions that result in different emission features as observed in a source at different epochs.

Such a random spectral behavior, especially synchrotron X-ray component, reflects the complexity in describing the overall emission behavior of the HBLs, in general. In our study, spectral behavior of IC component during pre- and post-flaring is just opposite and, perhaps, indicates to a change in the particle energy distribution that leads to the harder IC spectrum in the post-flaring state.

5.5 Summary and conclusions

In this work, we have presented the analysis of the multi-wavelength data from Fermi and Swift, available publicly, MIRO and Steward Observatory optical data for HBL 1ES 1959+650 during the year 2015-2016, covering two major outbursts. We also made use of the available optical polarization data to discuss 2015 October outburst in detail. The source was active in all the energy bands and showed significant flux enhancements during most of the period covered in this study. It is worth noting that 1ES 1959+650 exhibited highest ever flux in γ -rays and more than 20 counts per second in X-ray emission, making it third source after Mrk421, Mrk501 having such high counts. MIRO data showed the source in its brightest state ($V = 14.45 \pm 0.03$) during 2015.

The optical intra-night variability is detected on one of the nights during 2015 October when the source brightened by 0.07 mag in 4.5 hrs. Also, the

source exhibited short-term variability (over a few days) with a significant (> 0.3 mag in V band) variability amplitude.

The first outburst (March 2015) was characterized by the enhancement in γ -ray emission, perhaps, to follow those at lower frequencies with origin from synchrotron radiation, which is explainable via SSC mechanism, considering light travel time effects. The second outburst (October 2015) was rather complex with the 15GHz radio emission peaking first, just around the time optical polarization features changed rapidly. It was followed by the peaks in γ -ray flux, X-ray, UV and optical emissions, in that order. UV and optical variations were delayed by about 20 days with respect to those in γ -rays. It appears that various emission regions were aligned differently resulting in varying Doppler boosting of the flux and variability time scales. However, since γ -ray flux peaked just after radio, followed by emissions at lower frequencies, the processes could be related to the injection of fresh plasma in the jet.

We estimated magnetic field strength ($B = 4.2$ G) by using time lag between UV and optical emission as synchrotron cooling timescale. The emission region sizes for γ -ray and optical were estimated using shortest time scales of variability and were found to be of the order of $\approx 10^{16}$ cm. The γ -ray emission region appears to be located at a distance of 1.72 pc from central SMBH, which is close to the standing shock feature in the jet. As per the Astronomers' Telegrams (quasi-) simultaneous enhancement in radio and TeV flux were noticed during MJD 57303-57304, indicating to, perhaps, the fresh injection of a new plasma component in the jet which propagates down the jet interacting with standing conical shock (or radio core). It leads to quasi-simultaneous emissions at almost all the frequencies. The long term multi-frequency study suggests a mild bluer-when-brighter trend in the flux, which is relatively stronger during flaring.

The Spectral energy distribution (SED) of the source reveals that during the flaring phase, a minor shift in the synchrotron peak frequency towards higher energies and the steepening of the γ -ray IC spectrum occurs. It could be due to the increase in the particle density, either from inside or outside the jet, during the flaring episode. While IC spectra show contrasting behavior during the pre-flare

and post-flare epochs, the synchrotron component of SED shows a consistent behavior in the both phases. An efficient particle acceleration/cooling process just before the flare or a change in the particle energy distribution due to the external particle fields can lead to such effect without any change in low energy part.

Chapter 6

Unprecedented Outbursts in FSRQ CTA 102

Blazars, when in outburst, provide a unique opportunity to study their spectral behaviour, correlated variations at different frequencies, and structure of the jet. The unprecedented flaring activity in FSRQ CTA 102 is used for a detailed study to understand flaring mechanisms at short and long time scales, spectral behaviour in different energy regimes and to estimate sizes and location of the high-energy emitting region in the jet. Multiwavelength data (γ -ray, X-ray, UV, optical and radio) for CTA 102 during its outburst period, 2016 November to 2017 January, are obtained from Fermi-LAT, Swift-XRT/UVOT, Mt Abu InfraRed Observatory (MIRO) & Steward Observatory, and OVRAO are analyzed to construct multiwavelength light curves, to extract the spectral information, and to perform the correlated variability studies. The CTA 102 attained the highest flux levels across the electromagnetic spectrum (EMS) while flaring and otherwise also, with rapid and prolonged activities at all the frequencies. In optical it became brighter than 11.5 mag in V band. Had it been at a distance of, say, M31 nearby galaxy (CTA 102 is at $z=1.037$), it would have been the brightest source in our night sky. A number of short term (3 to 8 days) and long term ($>$ month) variability events are noticed across the EMS. We infer a mild redder when brighter trend in general and a bluer when brighter one during a few optical flares. Based on the flux doubling timescale, the size of the γ -ray emitting region

is estimated as $\approx 7 \times 10^{15}$ cm, located at a distance of about 1.47×10^{15} cm from the central engine. The bright phase during 2016-17 could possibly be due to successive high energy particle injections into the jet, creating shocks traveling down the jet which lead to the overall flux enhancement across the EMS. As an alternative, a decreasing viewing angle might be responsible for the enhanced flux. The study reveals correlated variations in all the energy bands, with lags within time bins, indicating to the co-spatial origin of most of the emissions. During the flaring event, a bluer-when-brighter color in optical, harder when brighter trend in X-ray and a softening of the γ -ray spectra are noticed.

6.1 Introduction

Flat spectrum radio quasar (FSRQ), CTA 102, at the redshift 1.037 (Paturel et al. 2002) was first detected in γ -rays by the EGRET instrument on-board the *Compton Gamma-Ray Observatory* (Nolan et al. 1993), and then was observed extensively at other wavelengths. The detection of optical variability and the optical-IR correlated emission, during the high-flux state of the source, were reported by Raiteri et al. (1998) and Bach et al. (2007), respectively. Osterman Meyer et al. (2009) detected the optical micro-variability (about 15 min time scale), with rates as high as 2 mag/day and a redder when brighter (RWB) spectral behaviour during the 2004 activity in the source. The total flux and spectral study by Williamson et al. (2014) reported CTA 102 in 12 periods of quiescence, 7 of active and 4 periods of γ -ray flaring state during 2008–2012. A strong correlation between γ -ray and optical flaring events was reported by Cohen et al. (2014), suggestive of the leptonic origin of γ -rays. Before the 2012 outburst, source was rather faint with average R-band brightness about 17 mag but peaked during the 2012 outburst with R= 13.7 mag. The WEBT campaign during 2012 huge outburst in CTA 102 captured the source in its, at that time, highest flux values across the spectrum (e.g., R< 14.6 mag, $F_\gamma = 8.0^{-6} ph cm^{-2} s^{-1}$) and a co-spatial origin of the optical and γ -ray emissions (Larionov et al. 2016b). Casadio et al. (2015) used multiwavelength data, including 43 GHz VLBA images,

and found that the correlated optical and γ -ray flares occurred at more than 12 pc away from the central source. [Bachev et al. \(2017\)](#) addressed intranight variations in blazar CTA 102 during the two extreme outbursts, in 2012 and 2016 and found the brightness changes by a few tenths of magnitude on a time scale of a few hours. The fastest variation were noticed within 30 minutes, resulting in a brightness change by 0.2 mag in R. The multiband optical lightcurves were found by the authors to have strong correlation with no time lag. Just recently, [Zacharias et al. \(2017\)](#) explained the prolonged 2016 outburst in CTA 102 on the basis of a gas cloud entering and leaving the relativistic jet, causing ablation of the gas and hence gradual increase in the the emissions across the EMS.

Recently, CTA 102 underwent unprecedented activity in all the electromagnetic spectrum (EMS) bands during 2016–17 ([Larionov & Kopatskaya 2016](#); [Bulgarelli et al. 2016](#); [Carrasco et al. 2016](#); [Verrecchia et al. 2016](#); [Ciprini & Verrecchia 2016](#), etc.), significantly surpassing 2012 flare levels. The enhanced activity first started in optical, reaching R=14.33 mag on 2016 June 8 ([Larionov & Kopatskaya 2016](#)), while the IR fluxes were significantly increased showing J=9.97 mag ([Carrasco et al. 2016](#)), which was more than 2 mag brighter than that recorded by [Larionov et al. \(2016b\)](#). Since it is difficult to understand the multi-band emission behaviour of these sources when in low phase, such outbursts provide opportunity to study correlated variations between various EMS bands and to determine the locations of the emitting regions ([Raiteri et al. 2012](#); [Marscher et al. 2010](#)).

In this Chapter, we present a multiwavelength investigation of the blazar CTA 102 in its brightest phase in optical, UV, X-ray and γ -ray energy bands, during 2016–2017 and try to understand its variability behaviour. The next section reports multiwavelength observations and data analysis, section 3 discusses the results and the last section concludes the present study.

6.2 Multiwavelength Observations and Data Analysis

6.2.1 Fermi-LAT Observations

The LAT is a pair-production telescope onboard the Fermi satellite (Atwood et al. 2009) with a large effective area ($\simeq 6500 \text{ cm}^2$ on axis for 1 GeV photons) and a large field of view (2.4 sr), sensitive in the energy range 20 MeV to 300 GeV. The Fermi-LAT data for the duration 2016 November 1 (MJD 57693) to 2017 January 21 (MJD 57774) were analyzed using ScienceTools software package version v10r0p5 with the instrument response function P8R2_source_V6. We used the standard LAT-analysis recipe, on PASS 8 SOURCE class events (using `gtselect`) and made use of the third Fermi-LAT catalogue (*gll_psc_v16.fit*) to generate the background model for maximum likelihood analysis (using `gtlike`). The source spectrum was generated using a simple power-law model while we used *gll_iem_v06.fits* and *iso_P8R2_SOURCE_v6_v06.txt* to model the Galactic diffuse emission and the isotropic emission component, respectively. All the analysis steps were performed using publicly available Python package, Enrico (Sanchez & Deil 2013). More details on the data reduction and analysis procedure are given in Chapter 2. We generated the light curves (*lcs*) using 3hr, 6hr and 1 day time bins, corresponding to $\text{TS} > 10$ ($> 3\sigma$ confidence level).

6.2.2 Swift X-ray, UV & optical Observations

We used *Swift*-XRT publicly available data from HEASARC database¹ from 2016 November 14 to 2017 January 18. The data was processed using *xrtpipeline* v.0.13.0 by following the standard analysis steps². The source and background spectra were extracted using *xselect* tool and the pile-up corrections were applied in a few cases when the source was extremely bright. The obtained spectra is fitted with a simple power-law model in XSPEC and the fluxes were calculated (using $n_H = 5.0 \times 10^{20} \text{ cm}^{-2}$; Dickey & Lockman (1990)). The Swift-UltraViolet

¹<http://heasarc.gsfc.nasa.gov/cgi-bin/W3Browse/swift.pl>

²<http://www.swift.ac.uk/analysis/xrt/>

Optical Telescope (UVOT; [Roming et al. \(2005\)](#)) data for 2016 November 14 to 2017 January 18 were reduced using FTOOLS, *wotimsum* and *wotsource*. The details of the analysis procedure are given by [Kaur et al. \(2017a\)](#); [Chandra et al. \(2015b\)](#) and the Chapter 2 of this document.

6.2.3 Optical Observations from MIRO

We monitored the source CTA 102 on total eight nights in December 2016, when it was in unprecedented outburst across all energy regimes. The optical broadband filters (BVRI) were used to carry out high temporal resolution (30–40 seconds per exposure) observations from the Mount Abu InfraRed Observatory (MIRO) telescope facility– 1.2 m telescope equipped with ANDOR CCD camera with 2048×2048 pixels, for details about the instruments and detector, see Chapter 2. The standard procedures were followed to reduce and analyze the data obtained as also described in Chapter 2 in detail.

6.2.4 Steward Optical Observatory data

We also used the optical V-band data and polarization data (DP: Degree of polarization and PA: Position angle) from the public archive at Steward Observatory, Arizona ([Smith et al. 2009](#))³, available only for the duration from 2016 November 3 to 2017 January 13 for CTA 102.

6.3 Results & Discussion

Figure 1 presents the multiwavelength light curve (MWLC) for CTA 102 during 2016 November 1 - 2017 January 21. The time in MJD is plotted along X-axis while the respective brightness fluxes/magnitudes are along Y-axis. The top panel in Figure 6.1 shows the γ -ray flux (in $ph\ cm^{-2}s^{-1}$), using 1d binning, with an average flux of $2.39 \times 10^{-6} ph\ cm^{-2}s^{-1}$ over the period of the outburst. The second panel shows the X-ray (2.0-10.0 keV) Swift-XRT flux (in $ergs\ cm^{-2}s^{-1}$), varying between $(4.81- 0.96) \times 10^{-11} ergs\ cm^{-2}s^{-1}$ with average flux of 2.75×10^{-11}

³<http://james.as.arizona.edu/~psmith/Fermi/>

$\text{ergs cm}^{-2}\text{s}^{-1}$. The third panel displays X-ray photon index. The Swift-UVOT fluxes in all UV bands i.e., W1, M2, W2, are shown in the fourth panel while fifth panel gives the optical UBV-band magnitudes obtained from Swift-UVOT along with Steward Observatory V-band data. The bottom two panels display the polarization data (DP and PA) taken from the Steward Observatory. The correlation study between various energy regimes are performed, using statistical technique zDCF described by Alexander (2014), and the correlation plots are discussed in a later section.

For more clarity on the strong γ -ray outbursts and multiple prominent flares superposed on these outbursts, we plot γ -ray(Fermi-LAT) lightcurve in a separate figure (Figure 6.2), with time in MJD and 1d binned flux in $\text{ph cm}^{-2} \text{s}^{-1}$. During this period (2016 November 1 - 2017 January 21), the average γ -ray flux ($2.39 \times 10^{-6} \text{ ph cm}^{-2} \text{ s}^{-1}$) is more than 300 times of that listed in 2FGL catalog which is about $2.9 \pm 0.2 \times 10^{-9} \text{ ph cm}^{-2} \text{ s}^{-1}$ (Nolan et al. 2012). To estimate the duration of outburst, we have to first define the outburst. We call the source to be in outburst if the γ -ray flux calculated with 1 day binning within the γ -ray energy range 0.1–300 GeV is larger than $2.0 \times 10^{-6} \text{ ph cm}^{-2} \text{ s}^{-1}$. It leads to detection of a big flare at about MJD 57714, lasting just three days and the main outburst which started at MJD 57735 and continued for about next thirty days. Such strong and prolong outburst in this source is unprecedented and contributes enormous power to the overall energy flux of CTA 102. There are a number of rapid but strong flares superimposed on the already much enhanced base level flux. Interestingly, CTA 102 was so active that during the period considered here, the total flux of the source surpassed the already high average γ -ray flux level ($F_{\gamma,avg} = 2.39 \times 10^{-6} \text{ ph cm}^{-2} \text{ s}^{-1}$) at least nine times. In order to determine extent of the power content in the prominent flares, we calculated the FWHM of each flare profile and multiplied it by the duration of the flares. We found the power contained in the flare peaking at MJD 57739 to be approximately $2.25 \times 10^{-5} \text{ ph cm}^{-2}$; for the flare at MJD 57745 about $1.40 \times 10^{-5} \text{ ph cm}^{-2}$. The power contained in the major flare at MJD 57751, is $3.0 \times 10^{-5} \text{ ph cm}^{-2}$ while for another major flare at MJD 57760, it is $2.25 \times 10^{-5} \text{ ph cm}^{-2}$. The source has

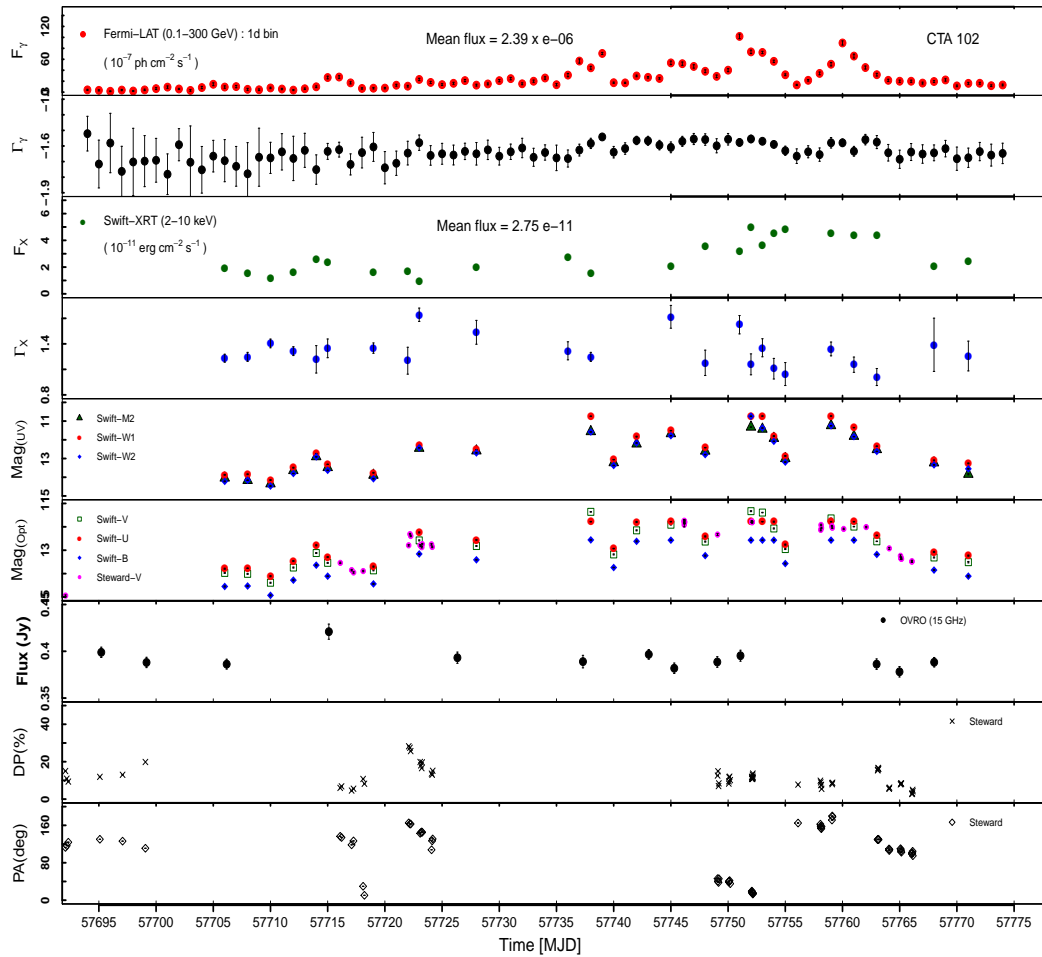


Figure 6.1: Multi-wavelength light curves for CTA 102 during the 2016 Nov - 2017 Jan outburst. From top to bottom: 1d binned Fermi-LAT γ -ray flux ($E > 100$ MeV); Swift-XRT flux (2.0-10.0 keV) ; X-ray photon index (Γ) Swift-XRT; Swift-UVOT UV-band magnitudes (W1, M2, W2); Swift-UVOT and Steward Observatory optical magnitudes; Degree of Polarization (DP%) and position angle (PA in degrees) taken from Steward Observatory.

not experienced such strong flare with so much power in its history.

6.3.1 Multiwavelength light curves

As clearly seen in Figure 6.1, the average fluxes of γ -rays and X-rays are already substantially elevated and any activity over and above these levels represent a significant enhancement on their past historical flux values. It is clearly noted that CTA 102 remained very active across all the energies considered here and exhibited a zoo of almost symmetric γ -ray flares, spanning from 3d to 8d, with significantly high flux levels. At lower energies (UV and optical), an outburst (>1 month), superposed by several flares of a few days duration, is noticed.

CTA 102 experienced a huge outburst of 70d duration, beginning MJD 57694, across EMS after being in the quiescent state for a long time. The activity started with a short γ -ray flare (3d long) on MJD 57701, followed by the next flare on 2016 November 13 (MJD 57705) showing a five fold enhancement in the flux in just 2d ($F_{\gamma}^{peak} = (1.44 \pm 0.25) \times 10^{-6} ph cm^{-2} s^{-1}$).

The γ -ray flare with double peaks (1d apart) peaking at MJD 57715/16 (2016 November 23/24) surpassed the average flux level. The corresponding activity at lower-energies, i.e., in optical, UV and X-ray, also started on MJD 57712, peaking one day early (on MJD 57714), with a flux drop when γ -ray flux was at the peak (on MJD 57716).

Around MJD 57723 (2016 December 1), the overall base level flux kept increasing slowly. While the X-ray flux was low, optical/UV fluxes got enhanced and rapid polarization changes took place (DP: 28% to 13%; PA: 165° to 127°). The changes in DP and PA during γ -ray flaring have been studied by Marscher (2014) extensively, who explained these to be associated with a blob passing through a quasi-stationary core, resulting in the significant emissions at all frequencies under shock-in-jet scenario. The blob/shock compresses the plasma in the dense medium of the core, aligning the magnetic field which results in change in polarization and position angle. We noticed a significant delay between optical/UV and γ -ray fluxes. The low X-ray flux could either be the victim of differential alignment of respective emission regions w.r.t. LOS (Raiteri et al.

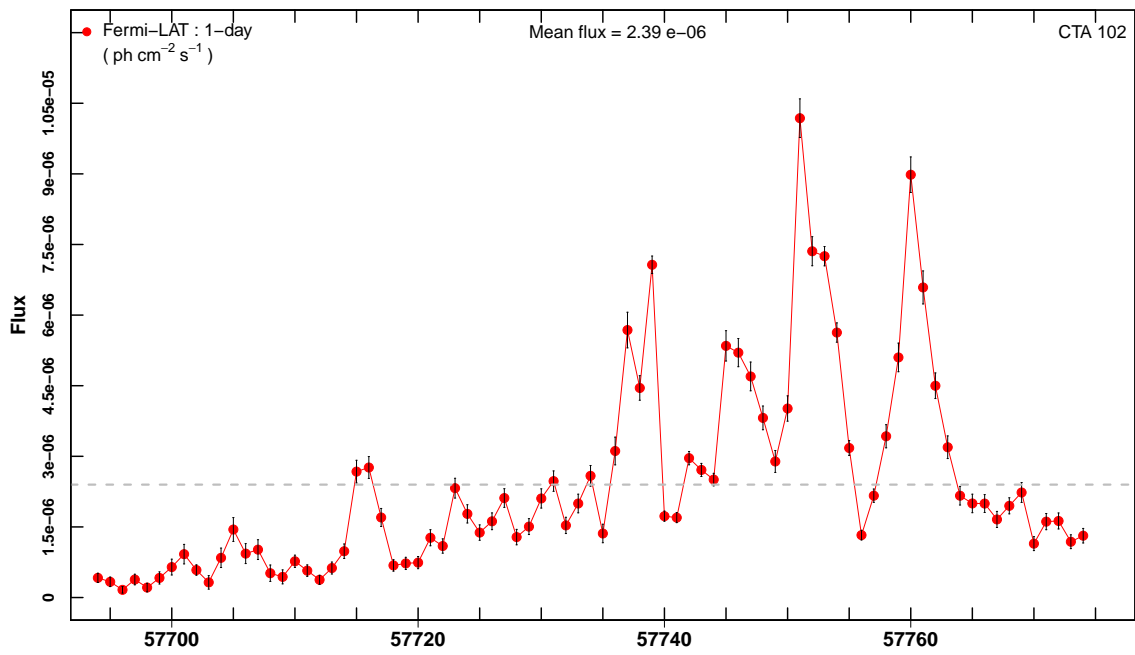


Figure 6.2: γ -ray light curve of FSRQ CTA 102 showing flaring activity during November 2016–January 2017. Time in MJD is plotted along X-axis and flux along Y-axis. The grey dashed line shows the average flux level.

2011), or its origin itself could be different (Cavaliere et al. 2017). Due to large data gaps in X-rays on these epochs, it is difficult to draw any definite conclusion.

A host of rapid γ -ray flares, with the "saw-tooth" features (slow rise-fast decay), were peaking close to the average flux level on MJD 57727, 57731 and 57734 (2016 December 5, 9 & 12).

Figure 6.1 clearly shows the twin γ -ray flares on MJD 57737 & 57739, with the flux levels of $(5.68 \pm 0.37) \& (7.06 \pm 0.18) \times 10^{-6} ph cm^{-2} s^{-1}$, respectively. The X-ray flux increased by more than 50% relative to the flux on MJD 57736, followed by a γ -ray flare (at MJD 57337). Before the second γ -ray peak (at MJD 57739), the X-ray flux dropped by about 44%, followed by the decay in UV & optical. On MJD 57739, when the fluxes at lower energies were slowly declining, a γ -ray flare (second peak) indicated to a possible orphan flare. The cause behind such flare could be upscattering of the ambient photons at the boundary of the jet without any change in the optical flux. There are other explanations based on hadronic scenario for the high energy emission production.

During MJD 57740-57749 we detect a triple-flare, successive constituent flares showing increased amplitudes. Out of these, the major flare peaked at MJD 57745 (2016 December 23) with a fast rise (1d) and slow decay (4d). The X-ray showed subdued activity, peaking 3d later while the optical and UV fluxes were enhanced by 1 mag & 1.7 mag, respectively.

Historical outburst with sub-day variability

In the past, CTA 102 showed rapid variations in optical with time scales as short as 15 min to 3.6 hrs (Osterman Meyer et al. 2009; Raiteri et al. 1998; Bachev et al. 2017). Very recently, Zacharias et al. (2017) also claimed sub-day variability in optical window with a brightest magnitude of 10.98 in R band on 2016, December 29. The optical observations from MIRO show that the source has undergone a significant flux variability over short timescales (day-to-day) also. We calculated the nightly averaged R-band magnitudes for CTA 102 from our 8-nights observations and the results in R-band are tabulated in the table 6.1, where columns

Table 6.1: Nightly averaged R-band optical magnitudes for the blazar CTA 102 obtained using 1.2 m telescope of MIRO, during December 2016.

Date (dd:mm:yyyy)	MJD	R-band (mag)	σ_R
18-12-2016	57740.66	12.68	0.01
19-12-2016	57741.60	11.55	0.01
20-12-2016	57742.57	11.84	0.01
21-12-2016	57743.58	11.99	0.01
22-12-2016	57744.57	11.88	0.01
27-12-2016	57749.62	11.23	0.01
28-12-2016	57750.53	10.98	0.01
29-12-2016	57751.57	10.92	0.01

1 and 2 represent the epoch of observations in date-format and in MJD format, respectively. Column 3 shows the nightly averaged R-band magnitudes and their photometric errors are listed in column 4.

The source, as on December 18, 2016 was having a brightness in R-band as, $R=12.67\pm 0.01$ mag, but brightens suddenly, within a day, by a factor of more than 2.5, with a magnitude of $R=11.55\pm 0.01$. After that, the source brightness decreases during next three days with respective magnitudes as 11.84 ± 0.01 (December 20, 2016), 11.99 ± 0.01 (December 21, 2016), 11.88 ± 0.01 (December 22, 2016). As per our observations on December 27, 2016, the source enters into the extreme flaring phase with 0.6 mag enhancement from the previous brightness value, with the nightly averaged magnitudes of $R=11.23\pm 0.01$. The CTA 102 continues brightening further with $R=10.98\pm 0.01$ on December 28, 2016. Next day, on December 29, 2016, the source attains the optical magnitude of $R=10.92\pm 0.01$, which represents the historically brightest level ever achieved by the source. During this period, the source shows a significant intranight variability (INV), which is recently reported by [Bachev et al. \(2017\)](#). The source, therefore, shows strong day-to-day variations, as shown by our observations.

The γ -ray flux also exhibited significant intra-day and day-to-day variations.

The most pronounced 5d γ -ray flare, with unprecedented flux levels in the history of CTA 102, occurred around MJD 57751 (2016 December 29). The γ -ray flux, $F_\gamma = 1.02 \times 10^{-5} ph \text{ cm}^{-2} s^{-1}$, larger by about 40% than the 2012 flare as recorded by Larionov et al. (2016a), increased by >2.5 times in two days. It is the largest flux reported in the history of CTA 102. This flare, along with its shoulder flare almost overlapped with it, cooled down in the next 5d. The counterparts of this flare in the optical, UV and X-ray show lag by one day (cf. Figure 6.1). The X-ray flux doubled in 1d forming a sharp flare over already enhanced X-ray flux while optical and UV brightness increased by more than 1.5 & 2 mags, respectively, making these flares unprecedented across EMS.

An almost symmetric major γ -ray flare of 8d duration took place, centered around MJD 57760 (2017 January 7), with a peak flux of $8.98 \pm 0.37 \times 10^{-6} ph \text{ cm}^{-2} s^{-1}$ (higher than 2012 levels) and $\Gamma = -1.57 \pm 0.02$ following, with 1 day lag, the optical and UV flares with 1 mag and 2.8 mag enhancements. The X-ray was still showing a plateau while UV decayed slowly; the optical flux remained high for another three to four days followed by a rapid, albeit smooth, flux decrease. Not much activity was seen in polarized flux, but the position angle changed by more than 150° . After this high activity, γ -flux dropped with a minor flare (on MJD 57769; 2017 January 16) towards the end, with a slightly enhanced X-ray flux.

The extreme flux levels reached during present outbursts prompted us to use smaller time bins, i.e., 6 hr and 3 hr ($TS > 10$) in the data in order to investigate rapid variability at shorter timescales during the two major γ -ray flares, centered at MJD 57751 (2016 December 29) and MJD 57760 (2017 January 7). Figure 6.3 shows the γ -ray *lcs* for the major flares during 2016 December (top-left) and 2017 January (top-right), with the upper panel showing 6 hrs and lower one 3 hrs binned data. Clearly, the source showed significant flux variability at sub-day time scale. The variability amplitudes were estimated using the relation,

$$A_{var} = \sqrt{(A_{max} - A_{min})^2 - 2\sigma^2} \quad (6.1)$$

where, A_{max} and A_{min} are the maximum and minimum γ -ray fluxes respectively, and σ is the standard deviation.

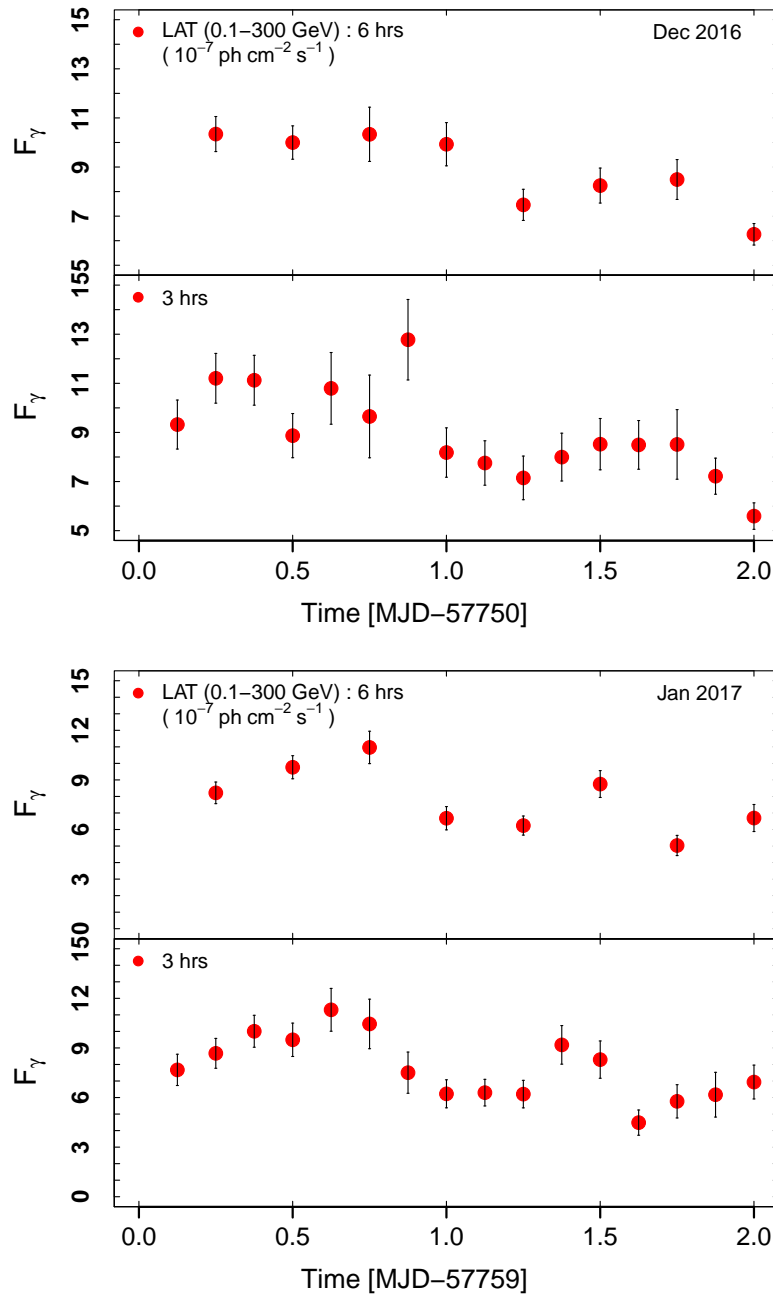


Figure 6.3: γ -ray intra-day flux variability in CTA 102 using 3 hrs and 6 hrs binned data, for the two major flares on MJD 57750-57752 (December 2016) and MJD 57759-57761 (January 2017).

The amplitude of variability, A_{var} , is estimated as $6.70 (1.93) \times 10^{-6} ph cm^{-2} s^{-1}$ on MJD 57751 and $6.25(1.82) \times 10^{-6} ph cm^{-2} s^{-1}$ on MJD 57760, with $>3\sigma$ confidence. To estimate the size of the γ -ray emission region, we used the doubling/halving timescales as calculated from,

$$F(t) = F(t_0)2^{\frac{t-t_0}{|\tau|}} \quad (6.2)$$

where, $F(t)$ and $F(t_0)$ represent the fluxes at time t and t_0 and $|\tau|$ is the halving time scale. Using the above expression, we have estimated the shortest time scale of variability as $\tau=4.72$ hrs.

The shortest time scale of variability provides important information about the size of the emitting region. The timescale, calculated above, is used to constrain the γ -ray emission region size,

$$R < \frac{\delta c \tau}{(1+z)} \quad (6.3)$$

where c , δ , and z are the speed of light, Doppler factor and redshift, respectively. The size of the γ -ray emission region is estimated as $4.6 \times 10^{15} cm$.

One of the major issue facing the blazar jet study is poorly understood structure of the jet– the manner in which matter responsible for energy dissipation is distributed along the jet. The estimates on the location of high energy emission is possible, when the source is highly variable at those energies (preferably, in flaring state). The flaring or outbursts in blazars are rare phenomenon as most of the time they remain in quiescent or low flux state. Therefore, there are very less number of sources for which the location of the high energy emission is determined. The rapid variability in γ -rays, with a time scales of a few minutes to a few tens of minutes, suggest the emission region to lie close to central engine, within a parsec (Tavecchio et al. 2010). However, Marscher et al. (2010) claim that the rapid variability could also be produced in the jet far away from black hole if the emission region occupies only small fraction of the jet instead of the whole cross section (jet-in-jet scenario). The strong correlations detected between γ -ray and mm-wave emissions are suggestive of the emitting regions more than parsec away from the base of the jet, well beyond BLR. It has been

seen in several sources that the γ -ray outburst are triggered by the passing of superluminal blobs (knots) through the mm VLBI cores. Casadio et al. (2015) reported such trend but only when motion of emitting regions coincided with the LOS. The flares in this case were accompanied by increased flux in X-ray and optical energy bands of CTA 102.

Recently Yan et al. (2017) estimated distances from the black holes to the dissipation regions from where γ -ray emission originated for the two blazars (PKS 1510-089 and BL Lac), based on the variability time scales. Here, we use doubling time scale as shortest characteristic time scale of variability obtained for the γ - emission. To have an estimate of the distance to the γ -ray emitting region from the central supermassive blackhole, we need the information about the opening angle close to the base of the jet, Doppler factor (δ), flux doubling time scale (τ_d) and the redshift (z). The jet opening angle for blazars is generally less than 1 degree, as discussed by Jorstad et al. (2005), in general. Therefore, using the jet opening angle close to 1.0° , which is the upper limit of opening angle for BL Lacs (Pushkarev et al. 2012), we estimate the distance to the location of γ -ray emission from central engine, using following relation,

$$d = \frac{\delta c \tau}{(1+z)\theta_j} \quad (6.4)$$

where, the jet opening angle is, $\theta_j \approx 0.7^\circ$ (Jorstad et al. 2005). We find that the γ -ray emitting region is located at a distance of $d = 9.5 \times 10^{14} \text{ cm}$ from SMBH, which is well within BLR dissipation region.

Fromm et al. (2015) estimated distance of the black hole from 86 GHz core in CTA 102 as about 7 pc using an opening angle of 2.6° and a value of 35 for the Doppler factor, while γ -ray emission was produced at a distance of 12 pc away from black hole (Casadio et al. 2015).

Fractional variability amplitude:

In blazars, the variability is largely stochastic event in nature at all frequencies and timescales, particularly at shorter one. The similarities and differences among flare profiles reflect varying extents of the particle acceleration and energy

dissipation. The amplitudes of variation would depend upon the strength of magnetic field, viewing angle particle density and the efficiency of acceleration. The availability of good quality data across the EMS makes it possible to determine the variability amplitude at all the energies. This could be determined using the fractional root mean square (rms) variability parameter, introduced by [Edelson & Malkan \(1987\)](#); [Edelson et al. \(1990\)](#). Basically, the excess variance was used to compare the variability amplitudes at different energy bands from the same observation ([Vaughan et al. 2003](#)). This methodology has some limitations as it works nicely for the densely sampled data having small flux uncertainties at different energies, obtained from different instruments with different but high sensitivities. The large data gaps or high uncertainties in the flux measurements can also introduce larger values of rms variability amplitude and the methods fails. In the present case, the availability of good quality data across EMS allowed us to infer the variability in the source. The fractional variability and the associated errors were calculated using the relation from [Vaughan et al. \(2003\)](#),

$$F_{var} = \sqrt{\frac{(S^2 - \sigma^2)^2}{r^2}} \quad (6.5)$$

$$\sigma F_{var} = \sqrt{\left(\sqrt{\frac{1}{2N}} \frac{\sigma^2}{r^2 F_{var}}\right)^2 + \left(\sqrt{\frac{\sigma^2}{N}} \frac{1}{r}\right)^2} \quad (6.6)$$

where, S^2 is the sample variance, σ^2 is the mean square value of uncertainties associated with each observation, and r is the sample mean.

We find that the source exhibits larger fractional variability (F_{var}) towards higher energies *i.e.*, 0.87 in γ -rays, 0.45 in X-rays, 0.82 in UVW2-band, 0.059 in optical B-band. The large fractional variability towards higher frequencies could be due to large number of particles producing high energy emission. The internal shock model also predicts the high intrinsic amplitude of variability towards higher frequencies.

Spectral features

The optical spectral analysis showed a mild redder when brighter (RWB) color, in general and a bluer when brighter (BWB) trend during the flares. Figure

Energy	F_{var}	$\text{err}(F_{\text{var}})$
Gamma-ray	0.873	0.009
X-ray	0.459	0.001
UVOT - W1	0.089	0.002
UVOT - M2	0.077	0.002
UVOT - W2	0.082	0.002
UVOT - V	0.073	0.003
UVOT - U	0.063	0.002
UVOT - B	0.059	0.002

Figure 6.4: The fractional variability amplitudes of CTA 102 in various energy bands.

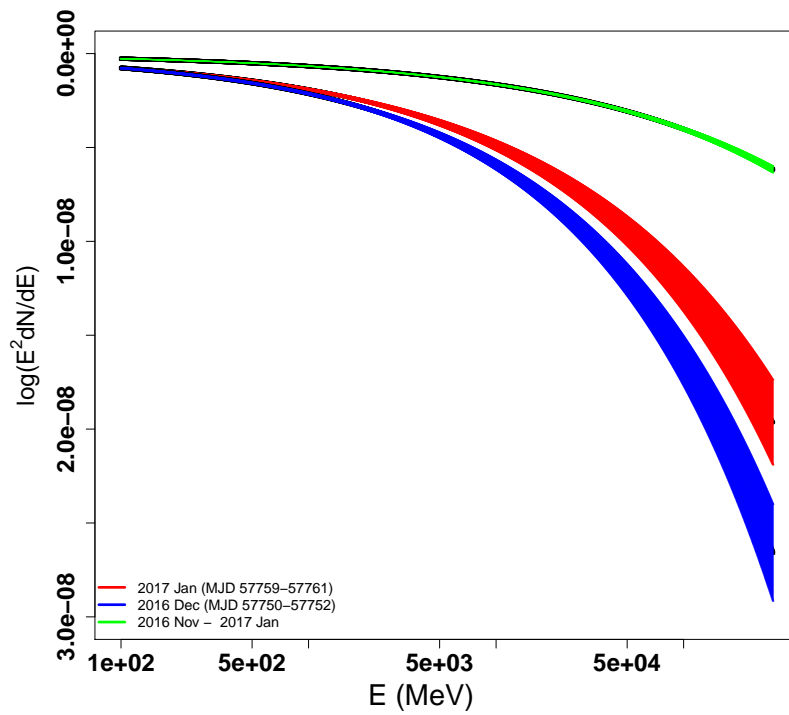


Figure 6.5: γ -ray spectra fitted with a simple power-law ($E > 100\text{MeV}$) for whole duration, 2016 November - 2017 January (green), during the MJD 57751 (red) and the MJD 57760 (blue) major flares.

6.5 shows the γ -ray spectra, with energy on X-axis and counts/bin on Y-axis, for complete duration (green) and during the two historical flares (blue, red). The spectral variability is more profound at higher energies i.e., X-ray becomes harder while γ -ray spectra become softer during the flaring period as compared to the whole period considered here. Using the luminosity distance (d_L) and the brightest X-ray flux value (F_X), we estimated the X-ray jet isotropic luminosity to be $L_{X,jet}^{iso} = 2.68 \times 10^{47}$ erg/s, which exceeded the Eddington luminosity ($L_{Edd} = 1.11 \times 10^{47}$ erg/s; Fromm et al. (2015)), with $\eta = L_{X,jet}/L_{disk} = 6.4$ in the source during its brightest phase, requiring a larger Lorentz factor.

6.3.2 Correlated variations using zDCF

We have also studied the correlated flux variations between two LC s obtained for different energy regimes. It provides the information on how well the variability in two energy bands matches and allows one to measure the time it takes for one emission region to respond to the changes in the other. From the Figure 6.1, it can be noticed that, broadly, all the fluxes in different energy regimes vary in-tandem. To investigate it further, zDCFs between γ -ray and other energy bands are computed. The Figure 6.6 shows the correlation plots for γ -ray & X-ray, γ -ray & UV and γ -ray & optical V-band light curves. As can be noticed from these zDCF plots, strong correlations are seen in all the cases with small lags (within errors/bin sizes). The correlation exhibited between γ -ray and optical in the 2016–17 outburst is similar to the one reported by Larionov et al. (2016b) during 2012 outburst. They, however, reported 1 hr as the time lag between γ -ray and optical emissions in the post-outburst phase and claimed the high energy emission produced under SSC process. During the outburst, a linear relationship between the variations in the two energy bands were noticed which was explained based on viewing angles which results in change in Doppler boosting (Larionov et al. 2016b). During this phase, they also notice harder when brighter trend in both, optical and γ -ray nonthermal emissions. With no significant lags in our case, all the emission regions, therefore, appear to be at least co-spatial and can be explained by the inhomogeneous jet model in which a shock

propagates down the jet, interacting with the plasma over densities or stationary cores distributed randomly in the jet, leading to emission at progressively longer wavelengths (Blandford & Königl 1979; Marscher & Gear 1985). Such strong correlation between high energy emission and those at lower ones suggests that low energy emission is dominated by synchrotron emission, with minor contribution from accretion disk/host galaxy, while the higher energy emissions are due to upscattering of synchrotron photons with a possible contribution from external population of the seed photons, by the high energy electrons responsible for synchrotron emission (Jorstad et al. 2013).

Such strong correlation between γ -ray and optical variations has been noticed for many other sources as well (Cohen et al. 2014; Bonning et al. 2009; Raiteri et al. 2011; Vercellone et al. 2009; Jorstad et al. 2013) and their co-spatial origin was inferred. Bachev et al. (2017) carried out multiband optical study of 2012 and 2016 flares in CTA 102. The authors found no variability in Mg II lines over few years duration. Any correlation between the nuclear flux variations and line emission would indicate nuclear emission being reprocessed by BLR. A time delay between the variations in the nuclear flux and flux in the Mg II line would enable estimation of the mass of the central black hole. The authors report brightest state of the blazar with intra-night variability of 0.2 mag within about 30 minutes. The variations are reported to be due to change in the Doppler factor of the blobs.

The zDCF between γ -ray and X-ray flux shows significant correlation with the former leading the later by couple of days but considering the binning of the data, data gaps resulting in larger errors, it is safer to say that these are correlated. Apart from this, the X-ray shows rather strange behaviour if one looks at the flare-to-flare behaviour of X-ray lightcurve. The rapidly rising γ -ray flare centered around MJD 57745 (2016 December 23) has counter-parts in optical and UV but X-ray flux shows decreasing trend. The slow decay of the flare was also traced well in these two bands, while the X-ray started rising and peaked when γ -ray flux reached minimum. Even after the major γ -ray flare at MJD 57751 (2016 December 29), while all the fluxes decayed slowly, X-ray flux started increasing again, peaking when all the fluxes reached their minima. The last

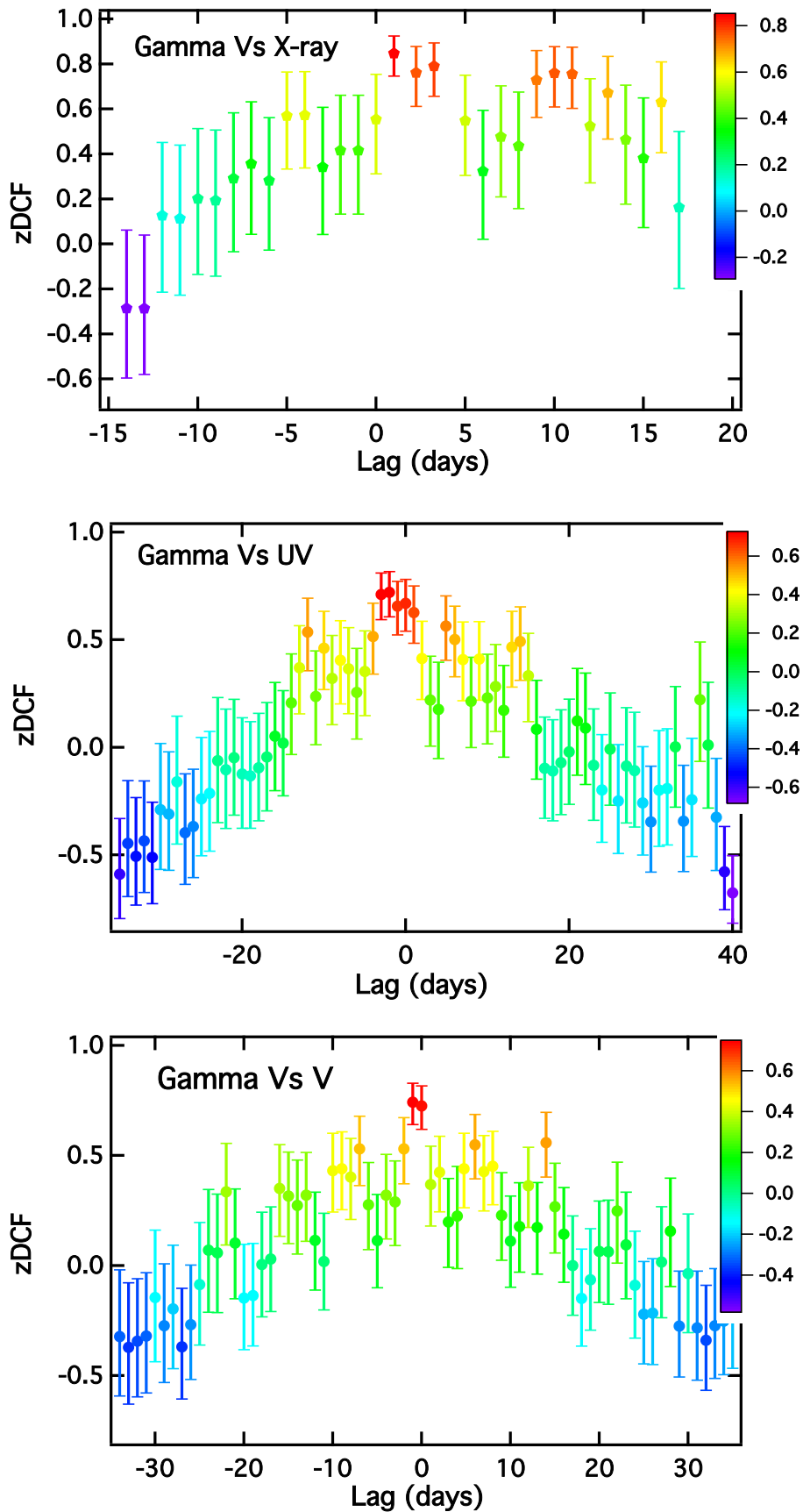


Figure 6.6: Discrete correlations (zDCF) for CTA 102 between γ -rays and X-ray, UV and optical fluxes, respectively, during 2016 November- 2017 January.

major flare in γ -rays on MJD 57760 (2017 January 7) peaked with one day lag w.r.t. optical/UV bands while X-ray flux formed a plateau. Such an intriguing behavior of the X-ray flux during the high flux state in this source has been noticed earlier for several sources (Cavaliere et al. 2017; Kaur et al. 2017a; Carnerero et al. 2017).

Average flux levels in CTA 102 during 2016 outburst

The optical outburst activity during November 2016–January 2017, in CTA 102 is recently reported by Bachev et al. (2017) showing the brightest magnitude as R=11.43 mag as on December 23, 2016. The authors reported the averaged R-band magnitude during the flaring period as 12.56 mag. It is to be noted that unprecedented flare fluxes apart, the average flux levels detected in the present study on CTA 102 are the highest ever reported. We report the average brightness levels for γ -ray, X-ray, UV and optical as $2.39 \times 10^{-6} \text{ ph cm}^{-2} \text{ s}^{-1}$, $2.75 \times 10^{-11} \text{ erg cm}^{-2} \text{ s}^{-1}$, 12.45 mag (W1), 13.44 mag & 11.63 (R; MIRO), respectively. However, the brightest values achieved by the blazar CTA 102 during 2016 outburst are unprecedented as noted here, $1.04 \times 10^{-5} \text{ ph cm}^{-2} \text{ s}^{-1}$ (γ -ray), $5.1 \times 10^{-11} \text{ erg cm}^{-2} \text{ s}^{-1}$ (X-ray;XRT), 12.45 mag (W1;UVOT), 13.44 mag(B;UVOT), 10.92 (R; MIRO). The long-term consistent increase in the optical flux could be due to a systematic increase in the magnetic field strength, particle density or a systematic decrease of the external radiation energy density that reduces the probability of energy losses. Alternatively, these could result from a decrease in the viewing angle, which leads to stronger Doppler boosting (Bachev et al. 2017; Larionov et al. 2016b) at higher frequencies.

6.4 Conclusions

After the 2012 huge optical flare, FSRQ CTA 102 flared up again, beginning 2016 June 8. This outburst with several flares covering EMS, is discussed using the data from Fermi-LAT, Swift-XRT/UVOT and ground based observatories, Steward & MIRO. The study reveals that the source was in its historically brightest phases in the γ -ray, X-ray, optical and UV bands. There were several instances when the

flux increased manifolds due to strong flaring events which lead to short term (3d to 10d) and long-term (30d or longer) variability trends. The MIRO data suggest the source to show strong day-to-day variations. We noticed correlated, quasi-simultaneous emissions, with a delay of not more than a few days, indicating to their co-spatial origins. The larger values of fractional variability towards higher frequencies suggest more activity at higher energies. Based on the halving time scale in γ -ray flux ($\tau = 4.72$ hrs), the emission region size is estimated as 4.6×10^{15} cm. Taking the jet opening angle as 0.7° (Jorstad et al. 2005), we estimate the distance of γ -ray emission region from the central super-massive black hole as 9.5×10^{14} cm.

It is proposed that the consistent flaring activity, which kept the flux levels high, is caused by the frequent injection of plasma into the jet and its interaction with quasi-stationary core. The strong shocks lead to the subsequent gain in the particle energy, on either side of the shock, leading to the enhanced flux levels. As an alternative explanation, viewing angle could be decreasing which will lead to enhanced emission through EMS. The base flux could be enhanced by perturbation or as a series of discrete, possibly overlapping flares, originating at shock fronts as shocks travel down the jet.

We detect a harder when brighter & softer when brighter spectral behavior in X- and γ -ray flux, respectively. A relatively softer trend during major γ -ray flares suggests an efficient cooling mechanism due, perhaps, to the high particle density in the vicinity of BLR (Sikora et al. 2002) leading to the rapid quenching of particles before their attaining higher energies. On the other hand, higher energy radiation/particles might be escaping the emitting region. Rapid flares could be the result of interaction of blobs with the plasma inhomogeneities/irregularities in the emission region.

In the multiwavelength *lcs*, X-ray emission behaves rather strangely at times, which could be due to its differential orientation with respect to LOS or different origin of the X-ray emission.

Chapter 7

Summary and Future Scope

7.1 Summary

Blazars, a sub-class of AGN, are the jet dominated sources and largely show featureless spectra. Their radiation processes are highly complex and non-thermal in nature, characterized by a power-law distribution of the accelerated particles in the jet, unlike the normal galaxies emitting the black-body radiation. These offer important probes to study the events occurring very close to the central engine as rapid variations across the electromagnetic spectrum (EMS) are detected in these sources. In fact blazars show variability at diverse time scales, a few minutes to tens of years. The correlated variations in the multiwavelength light curves provide wealth of information on the structure of the jet and emission processes there-in. The emission is highly boosted due to relativistic motion of the emitting regions seen at a very small angle to the line of sight (LOS). Our present understanding about their enigmatic energy phenomenon is based on the efforts from the enormous amount of observational data, several multiwavelength campaigns using ground- and space-based telescopes and extensive theoretical modeling. In case of blazars, broad picture of their spectral energy distribution is that while low energy emission is from synchrotron emission by relativistic electrons, the high energy emission is produced by the up-scattering of low energy photons by the particles emitting synchrotron emission. But how these particles are accelerated to emit at such high energies, where from the low energy photons

are coming, what exactly triggers the strong long outbursts and rapid flares across EMS, how and why the jet remains collimated even at kpc scales, etc., are very poorly understood issues. There is a broad understanding that the particles in the jet are accelerated by the relativistic shocks or magnetic reconnection during the interaction with slowly moving plasma or the stationary shocks distributed randomly in the parsec scale jet. Such interactions lead to the emissions across the EMS that carry the information to decode the energetics and morphology of the jet.

7.2 Work carried out in this thesis

There are a number of issues related to the energetics and structure of the AGN which remain un-resolved even after decades of extensive work using the best possible facilities across the spectrum and current theoretical understanding, due mostly to, the lack of consistent long term good quality multiwavelength data and theoretical models which appear in-adequate to deal with the complexities in the AGN environment. The highly compact nature and large redshifts of these sources add to the problem as these can not be resolved across the spectrum- albeit VLBI is able to resolve sub-parsec scale features (radio core at 43 and 86GHz) only in the nearby AGN, but upstream of the core, radio emission is self absorbed. There is a need to have better resolution at higher frequencies to probe the regions closer to the black hole. That is where the variability in the flux and polarization comes to the rescue, at least partly. The rapid variability being detected across the EMS is able to probe regions in the vicinity of the central engine from where relativistic jet is supposed to be launched.

In the work presented in this thesis we have tried to address the issues related to the structure and emission processes in AGN using this tool- variability in blazars. Since the shortest variability timescales put constraints on the size of the emission regions located in the jet, it helps to understand the jet structure. The correlated flux variations between various energy bands, with information on the lags/leads provide the spatial separation of the regions emitting at different

frequencies, indicating to how the material is distributed in the jet. In addition, broad band spectral energy distribution, in conjunction with multiwavelength light curves, provides crucial clues on their energy production mechanisms, from radio to very high energy γ -rays.

A brief overview about the AGN phenomena, blazars variability along with various emission models are presented in the Chapter 1, while Chapter 2 details the various observing facilities used to obtain multi-wavelength data, data analysis procedures and statistical tools employed to extract science from the data.

The optical window is very crucial to any study in astronomy in general and AGN is particular as it is the most equipped part of the EMS with a large number of observatories around the world monitoring a set of blazars. It is also important for addressing the production of high energy emission as it provides the seed photons for their production. The correlation between optical and other energy bands provides crucial information for the study of blazar behaviour. Keeping this in mind, we have taken up the study of the long-term and intra-night optical variability of the two blazars with their synchrotron peak lying in this energy domain- 3C 66A and S5 0716+714 discussed in Chapters 3 & 4, respectively. The high temporal resolution data in the four optical broadband filters (B,V,R,I) from the Mount Abu InfraRed Observatory (MIRO) and elsewhere, whenever available, are used.

Our results suggest that the 3C 66A is much less active in comparison to S5 0716+714, reflected in their duty cycles of variation (DCV) of 8% and 31%, respectively. For 3C 66A, the intranight variability (INV) timescales ranging from 37 min to 3 hr, are determined showing presence of the multiple emission regions in the jet. Using the shortest variability timescale, the mass of the central supermassive black hole is estimated to be about $3.7 \times 10^8 M_{\odot}$ assuming the origin of the rapid variability from the region very close to the central engine. A possible quasi-periodic variation of about 1.4 hr is detected on one of the INV nights (December 30, 2015), which could be the result of the plasma streamlet (jet-in-jet) progressing down the jet in a helical motion under shock-in-jet scenario. The long-term light curve of the source shows a number of flares (few months duration)

superposed on the slowly varying outbursts. A possible characteristic timescale of about 2.5 yr is inferred (though the data gaps are large), using periodogram analysis. The average brightness of the source decreases with time and a mild bluer when brighter (BWB) behavior is noticed. The second source, S5 0716+714 was observed in the optical broadband filters, for two and half years, from MIRO. S5 0716+71 has shown the dramatic INV and higher DCV as discussed and shows that the source is almost always active. It is noticed that DCV depends upon the length of its monitoring; longer the observation time, higher would be the probability to find the source variable. The estimated emission region size is of the order of 10^{15} cm, based on the characteristic timescale of 45.6 min, that puts an upper bound on the black hole mass to be $5 \times 10^8 M_{\odot}$. In the long term light curve, two major outbursts are noticed spanning about 360 days and 500 days, superposed by several small flares lasting a few weeks. The periodogram analysis reveal the possible periodic signature of about 2.26 yr (LTV; 2013–2015) and 1.2 hr (INV; December 28, 2013). The source exhibits bluer when brighter behavior (BWB) and a mild bluer trend with time. The high amplitude of variability is found when the source is in bright state, which is the expected behaviour as emission is dominated by the jet activity.

The blazars mostly stay in their low or quiescent phase. However, there are times when they show huge outbursts emitting across the spectrum and provide valuable information for understanding the physical processes behind the acceleration of particles responsible for these emissions. These are the times one can analyze whether the shock compression of the plasma or magnetic reconnection are responsible for acceleration, how the various emitting regions are located inside the jet and how the spectral nature of the source unfolds. Chapter 5 presents the multiwavelength study of outbursts in the γ -ray bright blazar, 1ES 1959+650 (HBL), during 2015–2016. The source was in the unprecedented flux state, with two major outbursts, i.e., during March 2015 and October 2015. Our study found the October 2015 outburst to be really complex. The radio (15 GHz) leads gamma-rays (GeV) with the rapid changes in the optical polarization, indicating to the fresh injection of plasma that interacts with the stationary feature in the

jet. From the correlation analysis, we could estimate the magnetic field strength as, $B = 4.2$ G- slightly on higher side for such systems. Based on characteristic timescales, the optical and γ -ray emission region sizes are found to be of the order of 10^{16} cm, which are co-spatial in nature. The jet expansion criterion allowed us to determine the location of the γ -ray emitting region from the central engine, as 1.72 pc. The spectral energy distribution (SED) shows a minor shift in the synchrotron peak frequency towards higher energies and the steepening of the γ -ray IC spectrum, during the flaring.

Chapter 6 presents the recent outburst activity in the flat spectrum radio quasar, CTA 102, in detail. We carried out a multiwavelength flux and spectral study on its unprecedented flaring activity during MJD 57693 - 57774 (2016 November 11 - 2017 January 21). The flux values calculated in this work are the historically largest for CTA 102 ever reported in the γ -ray, X-ray, optical and UV bands. For example, the average γ -ray flux during the period of study is 300 times larger than the average flux value reported in the 3FGL catalog. The larger values of fractional variability towards the higher energies suggest rapid injection of the large number of higher energy particles in the increasingly compact emitting regions. Based on the halving time scale in γ -ray flux ($\tau = 4.72$ hr), the emission region size is estimated as 7.2×10^{15} cm. The distance of γ -ray emitting region from the central super-massive black hole is estimated as 1.02×10^{15} cm, which is within the BLR. The spectral study shows the harder when brighter trend in X-rays & softer when brighter spectral behavior in γ -rays.

7.2.1 Main findings of the study

The present work helps to improve our understanding of the blazar phenomena using the rapid variability, which probes very compact regions and long term trends which provide clues to their long term behaviour and emission from large scale jet. Following are the main findings:

1. Our detailed optical long-term study on two sources, 3C 66A and S5 0716+71, suggests that the DCV for intranight variability depends upon the duration

of the observations. Longer the observation time, higher would be the possibility of detecting the source variability.

2. The trend of the amplitude of variation as a function of brightness is found to be opposite in the two sources, belonging to the same blazar class, IBL. The larger variability amplitude when the source is fainter is observed in 3C 66A which is difficult to explain as the emission is dominated the jet. It needs further study using larger sample.
3. The detection of several variability timescales suggests the possibility of multiple dissipation regions in the jet.
4. The two IBL discussed show strong outburst at longer time scales superposed by the frequent flares, showing STV. The shocks propagating down the jet and interacting with plasma inhomogeneities or stationary cores result in LTV and STV.
5. The extensive multiwavelength study on two sources, 1ES 1959+650 (HBL) and CTA 102 (FSRQ), reports their historically bright flux states across EMS and the complex behavior of their outbursts in October 2015 and December 2016, respectively.
6. The characteristic timescales, obtained from the doubling/halving timescales, in 1ES 1959+650 ($\tau = 1\text{d}$) and CTA 102 ($\tau = 4.72\text{ hr}$) are used to constrain the size of γ -ray emission region as, $\approx 10^{16}\text{ cm}$ and $7.2 \times 10^{15}\text{ cm}$, respectively.
7. The location of the γ -ray emission region from the central engine is estimated as 1.72 pc, close to the stationary bright feature in the jet, and $1.02 \times 10^{15}\text{ cm}$, which is within BLR, for 1ES1959+650 and CTA 102, respectively.
8. The trend of fractional variability, larger towards the higher frequencies, is found to be similar in both the sources, 1ES 1959+650 and CTA 102.

9. Our multiwavelength study confirms the intriguing behavior of the X-ray emission, in both 1ES 1959+650 and CTA 102, and requires more detailed study, especially during flaring episodes.
10. During the outbursts in 1ES 1959+650 and CTA 102, the γ -ray spectra tends to be softer, which could be due either to the higher energy particles escaping the dissipation region or Klein-Nishina effect.

7.3 Challenges and Scope of the AGN Research

The present study, as well as works carried out by others, has underlined the requirement of continuous, simultaneous good quality data across the electromagnetic spectrum. The large gaps in the data series often faced, seriously limit the scope of inferences to be drawn with high confidence. On the other hand, it is very challenging to sustain the long observing campaigns with simultaneous observations across the EMS beyond a few weeks at the best, as such efforts are threatened by a number of parameters- in UV/optical and near IR, it is sky conditions, while in shorter wavelengths, the availability of the space platforms, in addition to the problems of proper functioning of the instruments, which affect observations in all the windows. The resulting large gaps severely affect the applicability and ability of the theoretical models also to extract best possible science from the observational data. Our study also underscores the requirement of archiving the astronomical data being obtained in various programs addressing diverse issues, as such data could be very important for other studies. The authors need to be encouraged to put their data in archives accessible to the larger community as astronomical data is precious and can not be obtained again at that epoch. The importance of this effort has been demonstrated in the studies of, say, OJ 287 and S5 0716+714, where significant amount of data have been extracted from the photographic plates obtained more than 100 years ago, when AGN as a research field did not exist. It is a big challenge to put all the data at one place, contributed by all the observers for the benefit of future studies, efforts, for example, at NASA ADS are worth mention.

Even after more than 6-decades of intensive work in the field of AGN, a large number of outstanding problems remain unsolved, in spite of immense development in almost all windows of the study, which has of course led to considerable understanding of the field. In the present study, while it helped understand some of the issues, some new issues have surfaced. It is but natural to believe that when a blazar is in active phase, the variability amplitude should be larger as compared to when it is in relatively fainter stage, as the emissions are dominated by the jet activity. However, we notice the opposite for IBL 3C 66A. Whether it is due to large data gaps or some intrinsic process is responsible, can only be settled by further studies in this direction. Similarly, the detection of very rapid variations poses a challenge to the theoretical models, which in turn try to fit the data by using patches in their models. Such attempts fail to explain the observational data on other sources or features in the same source observed at different epochs. These problems have been noticed more frequently in addressing the correlated variations in different bands, color behaviour- both short and long term etc. Another challenge has been understanding the behaviour of the x-ray emission, which more often than not, does not follow any pattern. It is perhaps due to our lack of understanding of their origin. There are challenges in fixing whether leptonic or hadronic scenario should be used to explain higher energy emissions, the source of seed photons and the location of the emission regions etc. Whether long term variations in the flux are caused by the disk instabilities, precession of the jet, shocks moving down the jet or OJ 287 kind of scenario where dynamics of binary black hole system is responsible for such variations, is still to be established. There are studies which challenge the particle acceleration by the shocks, claiming that shocks can not accelerate the particles beyond thermal energies, proposing particle acceleration by magnetic reconnection!

The present day observing facilities across the spectrum; radio telescopes from meter to sub-millimeter (VLA, OVRO, SMA, ALMA), IR observatories (WISE, Spitzer, Herschel, 2MASS), optical observatories with 8-10m class largest aperture (GTC¹, Keck etc), UV/X-ray (Swift, Chandra, XMM-Newton, Suzaku, NuS-

¹<http://www.gtc.iac.es/>

TAR, INTEGRAL), GeV γ -rays (Fermi-LAT, AGILE) and very high energy facilities (MAGIC, VERITAS, TACTIC, H.E.S.S., HEGRA) have served tremendously adding to our knowledge of cosmic phenomena.

The very first Indian multiwavelength space observatory, AstroSat, measured high polarization in the X-ray emission from Crab pulsar with high precision, as well as detection of polarization in a few GRBs. However, it is limited to very bright sources. It is hoped that the next generation facilities will be able to measure X-ray polarization in blazars which will help understand how much emission is thermal (disk related) and how much is non-thermal, largely caused by synchrotron or IC processes.

In coming years, the issues which remain still unanswered and unexplored would hopefully be addressed with the upcoming sophisticated and more sensitive observational facilities. The imaging at shorter wavelengths with more sensitive and better resolution instruments like, VLBI-ALMA (Atacama Large Millimeter Array), VLBI-SKA (Square Kilometer Array) would provide the sensitivity of about a few tens of micro arcseconds. Other upcoming telescope facilities, a few are soon to be operational and others are under construction, would join the venture to address the unresolved issues, for example, SKA, VLBI-ALMA, TMT, E-ELT, LSST, JWST, eROSITA, Athena, IXPE, CTA, IceCube, e-LISA etc appear to be very promising. A few such burning issues, where AGN study plays significant role, as briefly mentioned in the following.

7.3.1 AGN & origin of VHE γ -rays, neutrino and cosmic rays

The future belongs to multiwavelength and multi-messenger astronomy when it will be essential and fruitful to use all available facilities at our disposal to solve some basic but outstanding problems, eg, production of VHE gamma-ray, source(s) of neutrinos and high energy cosmic rays. The γ - ray astronomy provides an important tool to probe the physics of high energy particles in space. These are produced by the acceleration of charged particles, leptons or hadrons, in the high energy environments. It is possible in shocks where particles are

accelerated to as high as TeV and PeV energies in a sudden energy burst, such as supernovae, γ -ray bursts, AGN etc. These particles interact with ISM or dense media (e.g., dense clouds), where secondary particles, such as charged and neutral pion, η mesons, are produced due to collisions, quickly decaying into γ -rays and neutrinos. The background seed photons for the production of these high energy neutrinos and γ -rays have energies above a few keV. Thus AGN are efficient accelerators of particles through shock or diffusive Fermi acceleration processes where protons can reach ultra high energies (UHE) producing high energy γ -rays and neutrinos through proton-proton and/or photo-hadronic interactions.

On the other hand, all mechanisms producing high energy neutrinos will also produce gamma rays of similar energies, pointing back to their sources. Thus, observations of these two messengers are complementary. Gamma-ray telescopes, e.g. the atmospheric Cherenkov one, can precisely point towards the accelerators and even localize acceleration sites in nearby objects. Neutrino telescopes, on the other hand, are less able to precisely pin-point the origin of neutrinos. But the neutrinos they detect are the only completely unambiguous tracer of hadronic acceleration, even out to high redshifts and above PeV energies which is not possible for gamma-ray telescopes due to photon-photon absorption. However, situation in the VHE neutrino experiments has changed with the evidence for astrophysical neutrinos above the MeV band. The IceCube collaboration has announced the detection of a diffuse astrophysical neutrino signal at PeV energies. Out of 37 neutrino events observed by IceCube Collaboration in the $30 \text{ TeV} < E < \text{a few PeV}$ range, 12 were seen to have their error circle coincident with 10 HBLs. It is proposed that photo-hadronic interaction of accelerated high energy protons with the synchrotron/SSC background photons in the nuclear region of these high energy blazars and AGN are probably responsible for some of the observed IceCube events. Though no significant correlation was found between the two events (IceCube event location and HBLs), the process of neutrino production by HBLs can not be refuted. Much more monitoring of these sources are required, which will benefit from these new facilities.

Blazars as sources of high-energy neutrinos have been explored in other recent

studies (Mücke et al. 2003; Dermer et al. 2014; Kistler et al. 2014). The studies to determine how the neutrino emission of blazars contributes to the cosmic neutrino background (Dermer et al. 2014; Padovani et al. 2015) and detection of neutrino flux during blazar flaring events in different wavelength bands should provide signatures for the hadronic origin of the γ -ray emission. Blazar observations will benefit greatly from the enhanced CTA, with access to low-frequency peaked sources (FSRQs, LBLs, IBLs & NLSy1s) due to its wider energy coverage and improved sensitivity.

Exploring AGN as source of cosmic rays, CTA is expected to provide clues to the origin of ultra-high energy cosmic rays (UHECR) through precise observations of extragalactic sources. The evidence for the production of gamma rays and perhaps neutrinos, through cosmic acceleration in these sources appears to be the only way to resolve this problem. It is because of the difficulties of direct searches for UHECR sources due to the low event statistics and the effect of Galactic and extra-galactic magnetic fields on the charged particles. The AGN sources are to be captured when flaring as well as detection of variability during low states, which will constrain current hadronic emission models. The multi-wavelength, simultaneous observations using state of the art telescopes will be required for this. The only signature of UHECRs in γ -rays is a hard spectrum at energies higher than characteristic γ -ray absorption energy by the EBL(extragalactic background light). The interaction of UHE cosmic rays with EBL and CMB photons in intergalactic medium produces UHE photons and leptons, triggering electro-magnetic cascades.

With a number of outstanding problems and challenges, few mentioned above, in the field of AGN, it is but obvious that the AGN field will remain abuzz with hectic activities for decades to come. There is bright future for those involved in the studies of AGN phenomena!

Chapter 8

List of Publications

8.1 Publications in Journals

1. *FSRQ CTA 102: Un-precedented multi-wavelength outburst during 2016-17*, **Navpreet Kaur** and K.S.Baliyan, Under Review, A&A, (2017).
2. *Optical Intra-day and short term variability in S5 0716+71 during 2013-2015*, **Navpreet Kaur**, K S Baliyan, S Ganesh, S Chandra, Submitted to AJ (2017).
3. *Multi-wavelength study of flaring activity in HBL 1ES 1959+650 during 2015-16*, **Navpreet Kaur**, S. Chandra, Kiran S. Baliyan, Sameer, S Ganesh, ApJ, 846, 158 (2017).
4. *Optical intra-day variability in 3C 66A: A decade of observations*, **Navpreet Kaur**, Sameer, Kiran S. Baliyan and S. Ganesh, MNRAS, 469, 2305 (2017).
5. *Multi-wavelength Study of Blazars Using Variability as a Tool*, K.S. Baliyan, **Navpreet Kaur**, S. Chandra, Sameer, S. Ganesh, Journal of Astronomy Space Sciences, 177-183 (2016).
6. *Multi-wavelength flaring activity in BL Lac object S5 0716+714 during 2015 outburst*, Chandra S., Zhang H., Khushwaha P., Singh K.P., Bottcher M., **Navpreet Kaur**, Baliyan, K.S., ApJ 809, 130 (2015).

7. *Multiwavelength observations of a VHE gamma-ray are from PKS 1510-089 in 2015*, M. L. Ahnen, S. Ansoldi, L. A. Antonelli, et al, including, **Navpreet Kaur**, &KS Baliyan, A&A, 603A, 29A (2017).
8. *Primary black hole spin in OJ287 as determined by the General Relativity centenary*, M. J. Valtonen, S. Zola, S. Ciprini, et al, including, Baliyan KS, **Navpreet Kaur**, Sameer, S Ganesh, ApJ, 819, L37 (2016).
9. *Search for QPOs in the Light Curve of the Blazar OJ287: Preliminary Results from 2015/16 Observing Campaign*, S. Zola, M. Valtonen, G. Bhatta, et al, including, KS Baliyan, **Navpreet Kaur**, Sameer, Galaxies (doi : 10.3390/galaxies4040041), (2016).
10. *MAGIC observations of variable very high-energy gamma-ray emission from PKS1510-089 during May 2015 outburst*, Julian Sitarek, et al, including, KS Baliyan, **Navpreet Kaur**, Sameer, ICRC Proceedings (2017).

8.2 Published Reports (ATels)

1. *Optical:NIR Observations of HBL 1ES 1959+625 from Mt Abu IR Observatory(MIRO)*, KS Baliyan, Sunil Chandra, **Navpreet Kaur**, S.Ganesh, Sameer, et al, ATel 9070 (2016).
2. *Brightening of FSRQ 3C 454.3 with an intense optical micro-variability*, **Navpreet Kaur**, KS Baliyan, CM Mukesh, S Ganesh, Janaka J, ATel 9723.
3. *Near Infrared aring of the blazar FSRQ PKS 1510-089 MIRO Observations*, Sameer, **Navpreet Kaur**, S.Ganesh, V. Kumar, K.S.Baliyan, ATel 7495.
4. *FSRQ B2 1156+29: NIR follow up observations from MIRO*, Sameer, Shashikiran Ganesh, **Navpreet Kaur**, Kiran S. Baliyan, ATel 7494.
5. *Unprecedented brightening of blazar S5 0716+714 and a brighter CGRABS J0510+1800*, Sunil Chandra, Pankaj Kushwah, S. Ganesh, **Navpreet Kaur**, Kiran Baliyan, ATel 6962.

References

- Abdo, A. A., Ackermann, M., Ajello, M., et al. 2010a, *Nature*, 463, 919
- Abdo, A. A., Ackermann, M., Agudo, I., et al. 2010b, *Astrophys. J.*, 716, 30
- Abdo, A. A., Ackermann, M., Ajello, M., et al. 2011, *Astrophys. J.*, 726, 43
- Abramowicz, M. A., & Nobili, L. 1982a, *Nature*, 300, 506
- . 1982b, *Nature*, 300, 506
- Acciari, V. A., Aliu, E., Arlen, T., et al. 2011, *Astrophys. J.*, 738, 169
- Acero, F., Ackermann, M., Ajello, M., et al. 2015, VizieR Online Data Catalog, 221
- Agarwal, A., Gupta, A. C., Bachev, R., et al. 2015, *Mon. Not. Roy. Astron. Soc.*, 451, 3882
- . 2016, *Mon. Not. Roy. Astron. Soc.*, 455, 680
- Agudo, I., Marscher, A. P., Jorstad, S. G., et al. 2011, *Astrophys. J. Lett.*, 735, L10
- Aharonian, F., Akhperjanian, A. G., Bazer-Bachi, A. R., et al. 2007, *Astrophys. J. Lett.*, 664, L71
- Aharonian, F. A. 2000, , 5, 377
- Aleksić, J., Ansoldi, S., Antonelli, L. A., et al. 2016, *Astron. Astrophys.*, 591, A10

- Alexander, T. 2014, ZDCF: Z-Transformed Discrete Correlation Function, Astrophysics Source Code Library, ascl:1404.002
- Aliu, E., Archambault, S., Arlen, T., et al. 2012, *Astrophys. J.*, 759, 102
- . 2014, *Astrophys. J.*, 797, 89
- Atwood, W. B., Abdo, A. A., Ackermann, M., et al. 2009, *Astrophys. J.*, 697, 1071
- Bach, U., Raiteri, C. M., Villata, M., et al. 2007, *Astron. Astrophys.*, 464, 175
- Bachev, R., Semkov, E., Strigachev, A., et al. 2012, *Mon. Not. Roy. Astron. Soc.*, 424, 2625
- Bachev, R., Popov, V., Strigachev, A., et al. 2017, *Mon. Not. Roy. Astron. Soc.*, 471, 2216
- Baliyan, K. S., Joshi, U. C., & Deshpande, M. R. 1996, *Astrophys. Space Sci.*, 240, 195
- Baliyan, K. S., Joshi, U. C., & Ganesh, S. 2005, *Bulletin of the Astronomical Society of India*, 33, 181
- Baliyan, K. S., Kaur, N., Chandra, S., Sameer, S., & Ganesh, S. 2016, *Journal of Astronomy and Space Sciences*, 33, 177
- Baloković, M., Paneque, D., Madejski, G., et al. 2016, *Astrophys. J.*, 819, 156
- Begelman, M. C., & Sikora, M. 1987, *Astrophys. J.*, 322, 650
- Bessell, M. S. 2005, *Annual Review of Astronomy and Astrophysics*, 43, 293
- Bhatta, G., Stawarz, L., Ostrowski, M., et al. 2016, *Astrophys. J.*, 831, 92
- Biermann, P., Duerbeck, H., Eckart, A., et al. 1981, *Astrophys. J. Lett.*, 247, L53
- Blandford, R. D., & Königl, A. 1979, *Astrophys. J.*, 232, 34

- Blandford, R. D., & Znajek, R. L. 1977, *Mon. Not. Roy. Astron. Soc.*, 179, 433
- Błażejowski, M., Sikora, M., Moderski, R., & Madejski, G. M. 2000, *Astrophys. J.*, 545, 107
- Bloom, S. D., & Marscher, A. P. 1996, *Astrophys. J.*, 461, 657
- Boettcher, M. 2010, ArXiv e-prints, arXiv:1006.5048
- Bonning, E. W., Bailyn, C., Urry, C. M., et al. 2009, *Astrophys. J. Lett.*, 697, L81
- Boroson, T. A. 2002, *Astrophys. J.*, 565, 78
- Bottacini, E., Böttcher, M., Schady, P., et al. 2010, *Astrophys. J. Lett.*, 719, L162
- Böttcher, M. 2006, *Astrophys. J.*, 641, 1233
- Böttcher, M., Harvey, J., Joshi, M., et al. 2005, *Astrophys. J.*, 631, 169
- Böttcher, M., Fultz, K., Aller, H. D., et al. 2009, *Astrophys. J.*, 694, 174
- Bulgarelli, A., Verrecchia, F., Lucarelli, F., et al. 2016, The Astronomer's Telegram, 9788
- Burrows, D. N., Hill, J. E., Nousek, J. A., et al. 2005, *Space Sci. Rev.*, 120, 165
- Camenzind, M., & Krockenberger, M. 1992, *Astron. Astrophys.*, 255, 59
- Cardelli, J. A., Clayton, G. C., & Mathis, J. S. 1989, *Astrophys. J.*, 345, 245
- Carini, M. T., Miller, H. R., Noble, J. C., & Goodrich, B. D. 1992, *Astron. J.*, 104, 15
- Carini, M. T., Walters, R., & Hopper, L. 2011, *Astron. J.*, 141, 49
- Carnerero, M. I., Raiteri, C. M., Villata, M., et al. 2017, ArXiv e-prints, arXiv:1709.02237

- Carrasco, L., Miramon, J., Recillas, E., et al. 2016, The Astronomer's Telegram, 9801
- Casadio, C., Gómez, J. L., Jorstad, S. G., et al. 2015, *Astrophys. J.*, 813, 51
- Cavaliere, A., Tavani, M., & Vittorini, V. 2017, *Astrophys. J.*, 836, 220
- Cellone, S. A., Romero, G. E., & Combi, J. A. 2000a, *Astron. J.*, 119, 1534
- . 2000b, *Astron. J.*, 119, 1534
- Cerruti, M., Benbow, W., Chen, X., et al. 2017, *Astron. Astrophys.*, 606, A68
- Chandra, S. 2013, Multi-Wavelength Study of Variability in Blazars, PhD Thesis, ,:Not Available
- Chandra, S., Baliyan, K. S., Ganesh, S., & Foschini, L. 2014, *Astrophys. J.*, 791, 85
- Chandra, S., Baliyan, K. S., Ganesh, S., & Joshi, U. C. 2011, *Astrophys. J.*, 731, 118
- Chandra, S., Kushwah, P., Ganesh, S., Kaur, N., & Baliyan, K. 2015a, The Astronomer's Telegram, 6962, 1
- Chandra, S., Zhang, H., Kushwaha, P., et al. 2015b, *Astrophys. J.*, 809, 130
- Chatterjee, R., Bailyn, C. D., Bonning, E. W., et al. 2012, *Astrophys. J.*, 749, 191
- Ciprini, S., & Fermi Large Area Telescope Collaboration. 2015, The Astronomer's Telegram, 8193
- Ciprini, S., & Verrecchia, F. 2016, The Astronomer's Telegram, 9841
- Ciprini, S., Takalo, L. O., Tosti, G., et al. 2007, *Astron. Astrophys.*, 467, 465
- Cohen, D. P., Romani, R. W., Filippenko, A. V., et al. 2014, *Astrophys. J.*, 797, 137

- Craine, E. R., Johnson, K., & Tapia, S. 1975, *Pub. Astron. Soc. Pac.*, 87, 123
- Dai, B.-z., Zeng, W., Jiang, Z.-j., et al. 2015, *Astrophys. J. Supplement.*, 218, 18
- Danforth, C. W., Nalewajko, K., France, K., & Keeney, B. A. 2013, *Astrophys. J.*, 764, 57
- Dermer, C. D., Cerruti, M., Lott, B., Boisson, C., & Zech, A. 2014, *Astrophys. J.*, 782, 82
- Dermer, C. D., & Schlickeiser, R. 1993, *Astrophys. J.*, 416, 458
- Dickey, J. M., & Lockman, F. J. 1990, *Annual Review of Astronomy and Astrophysics*, 28, 215
- Edelson, R. 1992, *Astrophys. J.*, 401, 516
- Edelson, R. A., & Krolik, J. H. 1988, *Astrophys. J.*, 333, 646
- Edelson, R. A., Krolik, J. H., & Pike, G. F. 1990, *Astrophys. J.*, 359, 86
- Edelson, R. A., & Malkan, M. A. 1987, *Astrophys. J.*, 323, 516
- Elliot, J. L., & Shapiro, S. L. 1974, *Astrophys. J. Lett.*, 192, L3
- Elvis, M., Plummer, D., Schachter, J., & Fabbiano, G. 1992, *Astrophys. J. Supplement.*, 80, 257
- Falomo, R., Kotilainen, J. K., Carangelo, N., & Treves, A. 2003, *Astrophys. J.*, 595, 624
- Fan, J.-H. 2005, *Chinese Journal of Astronomy and Astrophysics Supplement*, 5, 213
- Fan, J.-H., Huang, Y., He, T.-M., et al. 2009, *Pub. Astron. Soc. Japan*, 61, 639
- Fan, J. H., & Lin, R. G. 2000, *Astrophys. J.*, 537, 101
- Finke, J. D., Shields, J. C., Böttcher, M., & Basu, S. 2008, *Astron. Astrophys.*, 477, 513

- Fiorucci, M., Ciprini, S., & Tosti, G. 2004, *Astron. Astrophys.*, 419, 25
- Fiorucci, M., & Tosti, G. 1996, *Astron. Astrophys. Suppl.*, 116, 403
- Folsom, G. H., Miller, H. R., Wingert, D. W., & Williamon, R. M. 1976, *Astron. J.*, 81, 145
- Fossati, G., Maraschi, L., Celotti, A., Comastri, A., & Ghisellini, G. 1998, *Mon. Not. Roy. Astron. Soc.*, 299, 433
- Fromm, C. M., Perucho, M., Ros, E., Savolainen, T., & Zensus, J. A. 2015, *Astron. Astrophys.*, 576, A43
- Furniss, A., Noda, K., Boggs, S., et al. 2015, *Astrophys. J.*, 812, 65
- Gaur, H., Gupta, A. C., Strigachev, A., et al. 2012, *Mon. Not. Roy. Astron. Soc.*, 420, 3147
- Gaur, H., Gupta, A. C., Bachev, R., et al. 2015, *Astron. Astrophys.*, 582, A103
- Ghisellini, G. 2012, *Mon. Not. Roy. Astron. Soc.*, 424, L26
- Ghisellini, G., Maraschi, L., & Treves, A. 1985, *Astron. Astrophys.*, 146, 204
- Ghisellini, G., Tavecchio, F., Maraschi, L., Celotti, A., & Sbarrato, T. 2014, *Nature*, 515, 376
- Ghisellini, G., Villata, M., Raiteri, C. M., et al. 1997, *Astron. Astrophys.*, 327, 61
- Giozzi, M., Brinkmann, W., O'Brien, P. T., et al. 2001, *Astron. Astrophys.*, 365, L128
- Gopal-Krishna, Goyal, A., Joshi, S., et al. 2011, *Mon. Not. Roy. Astron. Soc.*, 416, 101
- Gregory, P. C., & Condon, J. J. 1991, *Astrophys. J. Supplement.*, 75, 1011
- Gu, M. F., Lee, C.-U., Pak, S., Yim, H. S., & Fletcher, A. B. 2006, *Astron. Astrophys.*, 450, 39

- Guo, F., Liu, Y.-H., Daughton, W., & Li, H. 2015, *Astrophys. J.*, 806, 167
- Gupta, A. C., Srivastava, A. K., & Wiita, P. J. 2009, *Astrophys. J.*, 690, 216
- Gupta, A. C., Cha, S.-M., Lee, S., et al. 2008, *Astron. J.*, 136, 2359
- Hao, J.-M., Wang, B.-J., Jiang, Z.-J., & Dai, B.-Z. 2010, *Research in Astronomy and Astrophysics*, 10, 125
- Hayashida, M., Bigongiari, C., Kranich, D., et al. 2008, *International Cosmic Ray Conference*, 3, 1021
- Hayashida, M., Madejski, G. M., Nalewajko, K., et al. 2012, *Astrophys. J.*, 754, 114
- Hayashida, M., Nalewajko, K., Madejski, G. M., et al. 2015, *Astrophys. J.*, 807, 79
- Healey, S. E., Romani, R. W., Cotter, G., et al. 2008, *Astrophys. J. Supplement.*, 175, 97
- Heidt, J., & Wagner, S. J. 1996, *Astron. Astrophys.*, 305, 42
- Howell, S. B., & Jacoby, G. H. 1986, *Pub. Astron. Soc. Pac.*, 98, 802
- Howell, S. B., Warnock, III, A., & Mitchell, K. J. 1988a, *Astron. J.*, 95, 247
- . 1988b, *Astron. J.*, 95, 247
- Hufnagel, B. R., & Bregman, J. N. 1992, *Astrophys. J.*, 386, 473
- Hughes, E. B., Hofstadter, R., Rolfe, J., et al. 1980, *IEEE Transactions on Nuclear Science*, 27, 364
- Jang, M., & Miller, H. R. 1997, *Astron. J.*, 114, 565
- Jannuzi, B. T., Smith, P. S., & Elston, R. 1994, *Astrophys. J.*, 428, 130
- Johnson, H. L., & Morgan, W. W. 1951, *Astrophys. J.*, 114, 522
- Jones, T. W., O'dell, S. L., & Stein, W. A. 1974, *Astrophys. J.*, 188, 353

- Jorstad, S. G., Marscher, A. P., Mattox, J. R., et al. 2001, *Astrophys. J.*, 556, 738
- Jorstad, S. G., Marscher, A. P., Lister, M. L., et al. 2005, *Astron. J.*, 130, 1418
- Jorstad, S. G., Marscher, A. P., Larionov, V. M., et al. 2010, *Astrophys. J.*, 715, 362
- Jorstad, S. G., Marscher, A. P., Smith, P. S., et al. 2013, *Astrophys. J.*, 773, 147
- Jorstad, S. G., Marscher, A. P., Morozova, D. A., et al. 2015, in IAU Symposium, Vol. 313, Extragalactic Jets from Every Angle, ed. F. Massaro, C. C. Cheung, E. Lopez, & A. Siemiginowska, 33–38
- Kapanadze, B. 2010, , 81, 235
- . 2015a, The Astronomer’s Telegram, 8289
- . 2015b, The Astronomer’s Telegram, 8468
- Kapanadze, B., Dorner, D., Vercellone, S., et al. 2016, *Mon. Not. Roy. Astron. Soc.*, doi:10.1093/mnrasl/slw054
- Kaspi, S., Smith, P. S., Netzer, H., et al. 2000, *Astrophys. J.*, 533, 631
- Katarzyński, K., Ghisellini, G., Tavecchio, F., et al. 2005, *Astron. Astrophys.*, 433, 479
- Kaur, N., Chandra, S., Baliyan, K. S., Sameer, & Ganesh, S. 2017a, ArXiv e-prints, arXiv:1706.04411
- Kaur, N., Sameer, Baliyan, K. S., & Ganesh, S. 2017b, ArXiv e-prints, arXiv:1705.00810
- . 2017c, *Mon. Not. Roy. Astron. Soc.*, 469, 2305
- Kawaguchi, T., Mineshige, S., Umemura, M., & Turner, E. L. 1998, *Astrophys. J.*, 504, 671

- Kellermann, K. I., Lister, M. L., Homan, D. C., et al. 2003, in *Astronomical Society of the Pacific Conference Series*, Vol. 299, *High Energy Blazar Astronomy*, ed. L. O. Takalo & E. Valtaoja, 117
- Kiehlmann, S., Savolainen, T., Jorstad, S. G., et al. 2016, *Astron. Astrophys.*, 590, A10
- Kirk, J. G., Rieger, F. M., & Mastichiadis, A. 1998, *Astron. Astrophys.*, 333, 452
- Kistler, M. D., Stanev, T., & Yüksel, H. 2014, , 90, 123006
- Kolb, U. 2010, *Extreme Environment Astrophysics* (Cambridge: Cambridge University Press)
- Konigl, A. 1981, *Astrophys. J.*, 243, 700
- Krawczynski, H., Hughes, S. B., Horan, D., et al. 2004, *Astrophys. J.*, 601, 151
- Kuehr, H., Pauliny-Toth, I. I. K., Witzel, A., & Schmidt, J. 1981, *Astron. J.*, 86, 854
- Lähteenmäki, A., & Valtaoja, E. 2003, *Astrophys. J.*, 590, 95
- Lainela, M., Takalo, L. O., Sillanpää, A., et al. 1999a, *Astrophys. J.*, 521, 561
- . 1999b, *Astrophys. J.*, 521, 561
- Lanzetta, K. M., Turnshek, D. A., & Sandoval, J. 1993, *Astrophys. J. Supplement.*, 84, 109
- Larionov, V. M., & Kopatskaya, E. N. 2016, *The Astronomer's Telegram*, 9130
- Larionov, V. M., Jorstad, S. G., Marscher, A. P., et al. 2013, *Astrophys. J.*, 768, 40
- Larionov, V. M., Villata, M., Raiteri, C. M., et al. 2016a, *Mon. Not. Roy. Astron. Soc.*, 461, 3047
- . 2016b, *Mon. Not. Roy. Astron. Soc.*, 461, 3047

- Li, Y. T., Hu, S. M., Jiang, Y. G., et al. 2017, *Pub. Astron. Soc. Pac.*, 129, 014101
- Liang, E. W., & Liu, H. T. 2003, *Mon. Not. Roy. Astron. Soc.*, 340, 632
- Lichti, G. G., Bottacini, E., Ajello, M., et al. 2008, *Astron. Astrophys.*, 486, 721
- Lind, K. R., & Blandford, R. D. 1985, *Astrophys. J.*, 295, 358
- Lister, M. L., Aller, M., Aller, H., et al. 2011, *Astrophys. J.*, 742, 27
- Lomb, N. R. 1976, *Astrophys. Space Sci.*, 39, 447
- Lynden-Bell, D. 1969, *Nature*, 223, 690
- Madejski, G., Nalewajko, K., Madsen, K., et al. 2017, in APS April Meeting Abstracts
- Man, Z., Zhang, X., Wu, J., & Yuan, Q. 2016, *Mon. Not. Roy. Astron. Soc.*, 456, 3168
- Mangalam, A. V., & Wiita, P. J. 1993, *Astrophys. J.*, 406, 420
- Mannheim, K., & Biermann, P. L. 1992, *Astron. Astrophys.*, 253, L21
- Marscher, A. P. 1979, in , Vol. 11, Bulletin of the American Astronomical Society, 458
- Marscher, A. P. 2008, in Astronomical Society of the Pacific Conference Series, Vol. 386, Extragalactic Jets: Theory and Observation from Radio to Gamma Ray, ed. T. A. Rector & D. S. De Young, 437
- Marscher, A. P. 2014, *Astrophys. J.*, 780, 87
- Marscher, A. P. 2016, *Galaxies*, 4
- Marscher, A. P., & Gear, W. K. 1985, *Astrophys. J.*, 298, 114
- Marscher, A. P., Gear, W. K., & Travis, J. P. 1992, in Variability of Blazars, ed. E. Valtaoja & M. Valtonen, 85

- Marscher, A. P., & Travis, J. P. 1996, *Astron. Astrophys. Suppl.*, 120, 537
- Marscher, A. P., Jorstad, S. G., Larionov, V. M., et al. 2010, in Bulletin of the American Astronomical Society, Vol. 42, AAS/High Energy Astrophysics Division #11, 709
- Marziani, P., Sulentic, J. W., & D’Onofrio, M. 2012, in *Astrophysics and Space Science Library*, Vol. 386, Fifty Years of Quasars: From Early Observations and Ideas to Future Research, ed. M. D’Onofrio, P. Marziani, & J. W. Sulentic, 1
- Mastichiadis, A., & Kirk, J. G. 1997, *Astron. Astrophys.*, 320, 19
- . 2002, , 19, 138
- Miller, H. R., Carini, M. T., & Goodrich, B. D. 1989, *Nature*, 337, 627
- Miller, H. R., & McGimsey, B. Q. 1978, *Astrophys. J.*, 220, 19
- Montagni, F., Maselli, A., Massaro, E., et al. 2006a, *Astron. Astrophys.*, 451, 435
- . 2006b, *Astron. Astrophys.*, 451, 435
- Mücke, A., & Protheroe, R. J. 2001, *Astroparticle Physics*, 15, 121
- Mücke, A., Protheroe, R. J., Engel, R., Rachen, J. P., & Stanev, T. 2003, *Astroparticle Physics*, 18, 593
- Mukherjee, R. 2015, *The Astronomer’s Telegram*, 8148
- Nair, S., Jin, C., & Garrett, M. A. 2005, *Mon. Not. Roy. Astron. Soc.*, 362, 1157
- Nalewajko, K., Giannios, D., Begelman, M. C., Uzdensky, D. A., & Sikora, M. 2011, *Mon. Not. Roy. Astron. Soc.*, 413, 333
- Nalewajko, K., Uzdensky, D. A., Cerutti, B., Werner, G. R., & Begelman, M. C. 2015, *Astrophys. J.*, 815, 101
- Narayan, R., & Piran, T. 2012a, *Mon. Not. Roy. Astron. Soc.*, 420, 604

- . 2012b, *Mon. Not. Roy. Astron. Soc.*, 420, 604
- Nesci, R., Massaro, E., Rossi, C., et al. 2005, *Astron. J.*, 130, 1466
- Netzer, H. 1990, in *Active Galactic Nuclei*, ed. R. D. Blandford, H. Netzer, L. Woltjer, T. J.-L. Courvoisier, & M. Mayor, 57–160
- Nilsson, K., Pursimo, T., Sillanpää, A., Takalo, L. O., & Lindfors, E. 2008, *Astron. Astrophys.*, 487, L29
- Nishiyama, T. 1999, *International Cosmic Ray Conference*, 3, 370
- Nolan, P. L., Bertsch, D. L., Fichtel, C. E., et al. 1993, *Astrophys. J.*, 414, 82
- Nolan, P. L., Abdo, A. A., Ackermann, M., et al. 2012, *Astrophys. J. Supplement.*, 199, 31
- Nottale, L. 1986, *Astron. Astrophys.*, 157, 383
- Oke, J. B. 1967, *Astrophys. J.*, 147, 901
- Orienti, M. 2015, ArXiv e-prints, arXiv:1504.03119
- Osterman Meyer, A., Miller, H. R., Marshall, K., et al. 2009, *Astron. J.*, 138, 1902
- Ostorero, L., Villata, M., & Raiteri, C. M. 2004, *Astron. Astrophys.*, 419, 913
- Padovani, P., Petropoulou, M., Giommi, P., & Resconi, E. 2015, *Mon. Not. Roy. Astron. Soc.*, 452, 1877
- Padovani, P., Alexander, D. M., Assef, R. J., et al. 2017, *Astron. Astrophys. Rev.*, 25, 2
- Paggi, A., Massaro, F., Vittorini, V., et al. 2009, *Astron. Astrophys.*, 504, 821
- Paiano, S., Landoni, M., Falomo, R., et al. 2017, *Astrophys. J.*, 837, 144
- Papadakis, I. E., Samaritakis, V., Boumis, P., & Papamastorakis, J. 2004, *Astron. Astrophys.*, 426, 437

- Paturel, G., Dubois, P., Petit, C., & Woelfel, F. 2002, *LEDA*, 0 (2002)
- Perlman, E. S., Stocke, J. T., Schachter, J. F., et al. 1996, *Astrophys. J. Supplement.*, 104, 251
- Perri, M., Massaro, E., Giommi, P., et al. 2003, *Astron. Astrophys.*, 407, 453
- Pian, E., Vacanti, G., Tagliaferri, G., et al. 1998, *Astrophys. J. Lett.*, 492, L17
- Pian, E., Türler, M., Flocchi, M., et al. 2014, *Astron. Astrophys.*, 570, A77
- Pihajoki, P., Valtonen, M., Zola, S., et al. 2013, *Astrophys. J.*, 764, 5
- Poon, H., Fan, J. H., & Fu, J. N. 2009, *Astrophys. J. Supplement.*, 185, 511
- Press, W., Teukolsky, S., Vetterling, W., & Flannery, B. 1992, *Numerical Recipes in C* (Cambridge: Cambridge University Press)
- Pushkarev, A. B., Hovatta, T., Kovalev, Y. Y., et al. 2012, *Astron. Astrophys.*, 545, A113
- Qian, B., Tao, J., & Fan, J. 2000, *Pub. Astron. Soc. Japan*, 52, 1075
- Raiteri, C. M., Ghisellini, G., Villata, M., et al. 1998, *Astron. Astrophys. Suppl.*, 127, 445
- Raiteri, C. M., Villata, M., Tosti, G., et al. 2003, *Astron. Astrophys.*, 402, 151
- Raiteri, C. M., Villata, M., Ibrahimov, M. A., et al. 2005, *Astron. Astrophys.*, 438, 39
- Raiteri, C. M., Villata, M., Aller, M. F., et al. 2011, *Astron. Astrophys.*, 534, A87
- Raiteri, C. M., Villata, M., Smith, P. S., et al. 2012, *Astron. Astrophys.*, 545, A48
- Raiteri, C. M., Stamerra, A., Villata, M., et al. 2015, *Mon. Not. Roy. Astron. Soc.*, 454, 353

- Ramakrishnan, V., Hovatta, T., Nieppola, E., et al. 2015, *Mon. Not. Roy. Astron. Soc.*, 452, 1280
- Rani, B., Gupta, A. C., Joshi, U. C., Ganesh, S., & Wiita, P. J. 2011, *Mon. Not. Roy. Astron. Soc.*, 413, 2157
- Rani, B., Krichbaum, T. P., Lott, B., Fuhrmann, L., & Zensus, J. A. 2013, *Advances in Space Research*, 51, 2358
- Rani, B., Gupta, A. C., Strigachev, A., et al. 2010, *Mon. Not. Roy. Astron. Soc.*, 404, 1992
- Rector, T. A., Gabuzda, D. C., & Stocke, J. T. 2003, *Astron. J.*, 125, 1060
- Rees, M. J. 1966, *Nature*, 211, 468
- . 1984, *Annual Review of Astronomy and Astrophysics*, 22, 471
- Richards, J. L., Max-Moerbeck, W., Pavlidou, V., et al. 2011, ArXiv e-prints, arXiv:1111.0318
- Romani, R. W., Healey, S., Michelson, P., & Sadler, E. 2005, A Southern Gamma-Ray Blazar Survey, NOAO Proposal
- Romero, G. E., Cellone, S. A., & Combi, J. A. 1999, *Astron. Astrophys. Suppl.*, 135, 477
- Roming, P. W. A., Kennedy, T. E., Mason, K. O., et al. 2005, *Space Sci. Rev.*, 120, 95
- Sagar, R., Stalin, C. S., Gopal-Krishna, & Wiita, P. J. 2004, *Mon. Not. Roy. Astron. Soc.*, 348, 176
- Saito, S., Stawarz, L., Tanaka, Y. T., et al. 2015, *Astrophys. J.*, 809, 171
- Sanchez, D. A., & Deil, C. 2013, ArXiv e-prints, arXiv:1307.4534
- Sandrinelli, A., Covino, S., & Treves, A. 2014, *Astron. Astrophys.*, 562, A79
- Sandrinelli, A., Treves, A., Falomo, R., et al. 2013, *Astron. J.*, 146, 163

- Scargle, J. D. 1982, *Astrophys. J.*, 263, 835
- Scarpa, R., Urry, C. M., Padovani, P., Calzetti, D., & O'Dowd, M. 2000, *Astrophys. J.*, 544, 258
- Schachter, J. F., Stocke, J. T., Perlman, E., et al. 1993, *Astrophys. J.*, 412, 541
- Schinzl, F. K., Lobanov, A. P., Taylor, G. B., et al. 2012, *Astron. Astrophys.*, 537, A70
- Shaw, M. S., Romani, R. W., Cotter, G., et al. 2013, *Astrophys. J.*, 764, 135
- Sikora, M., Begelman, M. C., & Rees, M. J. 1994, *Astrophys. J.*, 421, 153
- Sikora, M., Błażejowski, M., Moderski, R., & Madejski, G. M. 2002, *Astrophys. J.*, 577, 78
- Sikora, M., Janiak, M., Nalewajko, K., Madejski, G. M., & Moderski, R. 2013, *Astrophys. J.*, 779, 68
- Sikora, M., & Madejski, G. 2000, *Astrophys. J.*, 534, 109
- Sikora, M., Rutkowski, M., & Begelman, M. C. 2016, *Mon. Not. Roy. Astron. Soc.*, 457, 1352
- Sillanpaa, A., Haarala, S., Valtonen, M. J., Sundelius, B., & Byrd, G. G. 1988, *Astrophys. J.*, 325, 628
- Simonetti, J. H., Cordes, J. M., & Heeschen, D. S. 1985, *Astrophys. J.*, 296, 46
- Sironi, L., Petropoulou, M., & Giannios, D. 2015, *Mon. Not. Roy. Astron. Soc.*, 450, 183
- Sironi, L., & Spitkovsky, A. 2014, *Astrophys. J. Lett.*, 783, L21
- Smith, P. S., & Balonek, T. J. 1998, *Pub. Astron. Soc. Pac.*, 110, 1164
- Smith, P. S., Montiel, E., Rightley, S., et al. 2009, ArXiv e-prints, arXiv:0912.3621
- Sokolov, A., Marscher, A. P., & McHardy, I. M. 2004a, *Astrophys. J.*, 613, 725

- . 2004b, *Astrophys. J.*, 613, 725
- Spada, M., Ghisellini, G., Lazzati, D., & Celotti, A. 2001, *Mon. Not. Roy. Astron. Soc.*, 325, 1559
- Stalin, C. S., Gopal-Krishna, Sagar, R., et al. 2006, *Mon. Not. Roy. Astron. Soc.*, 366, 1337
- Stalin, C. S., Kawabata, K. S., Uemura, M., et al. 2009, *Mon. Not. Roy. Astron. Soc.*, 399, 1357
- Subramanian, P., Shukla, A., & Becker, P. A. 2012, *Mon. Not. Roy. Astron. Soc.*, 423, 1707
- Tagliaferri, G., Ravasio, M., Ghisellini, G., et al. 2003, *Astron. Astrophys.*, 412, 711
- Tagliaferri, G., Foschini, L., Ghisellini, G., et al. 2008, *Astrophys. J.*, 679, 1029
- Tavani, M., Vittorini, V., & Cavaliere, A. 2015, *Astrophys. J.*, 814, 51
- Tavecchio, F., Ghisellini, G., Bonnoli, G., & Ghirlanda, G. 2010, *Mon. Not. Roy. Astron. Soc.*, 405, L94
- Tornikoski, M., Valtaoja, E., Terasranta, H., et al. 1994, *Astron. Astrophys.*, 289, 673
- Tosti, G. 2008, *The Astronomer's Telegram*, 1759
- Trushkin, S. A., Sotnikova, J. V., & Mingaliev, M. G. 2015, *The Astronomer's Telegram*, 8337
- Ulrich, M.-H., Maraschi, L., & Urry, C. M. 1997, *Annual Review of Astronomy and Astrophysics*, 35, 445
- Urry, C. M., & Padovani, P. 1995, *Pub. Astron. Soc. Pac.*, 107, 803
- Urry, C. M., Treves, A., Maraschi, L., et al. 1997, *Astrophys. J.*, 486, 799
- Vagnetti, F., Trevese, D., & Nesci, R. 2003, *Astrophys. J.*, 590, 123

- Valtonen, M. J., Zola, S., Ciprini, S., et al. 2016, *Astrophys. J. Lett.*, 819, L37
- Vaughan, S., Edelson, R., Warwick, R. S., & Uttley, P. 2003, *Mon. Not. Roy. Astron. Soc.*, 345, 1271
- Vercellone, S., Chen, A. W., Vittorini, V., et al. 2009, *Astrophys. J.*, 690, 1018
- Verrecchia, F., Munar-Adrover, P., Pittori, C., et al. 2016, The Astronomer's Telegram, 9840
- Vestergaard, M. 2004, *Astrophys. J.*, 601, 676
- Vestergaard, M., & Peterson, B. M. 2006, *Astrophys. J.*, 641, 689
- Villata, M., & Raiteri, C. M. 1999, *Astron. Astrophys.*, 347, 30
- Villata, M., Raiteri, C. M., Lanteri, L., Sobrito, G., & Cavallone, M. 1998, *Astron. Astrophys. Suppl.*, 130, 305
- Villata, M., Raiteri, C. M., Kurtanidze, O. M., et al. 2002, *Astron. Astrophys.*, 390, 407
- Villata, M., Raiteri, C. M., Balonek, T. J., et al. 2006, *Astron. Astrophys.*, 453, 817
- Vittorini, V., Tavani, M., Cavaliere, A., Striani, E., & Vercellone, S. 2014, *Astrophys. J.*, 793, 98
- Vovk, I., & Babić, A. 2015, *Astron. Astrophys.*, 578, A92
- Vovk, I., & Neronov, A. 2016, *Astron. Astrophys.*, 586, A150
- Wagner, S. J., & Witzel, A. 1995, *Annual Review of Astronomy and Astrophysics*, 33, 163
- Watson, D., Hanlon, L., McBreen, B., et al. 1999, *Astron. Astrophys.*, 345, 414
- Webb, J. R., Howard, E., Benítez, E., et al. 2000, *Astron. J.*, 120, 41
- Wierzcholska, A., & Siejkowski, H. 2015, *Mon. Not. Roy. Astron. Soc.*, 452, L11

- Wiita, P. J. 1985, *Physics Reports*, 123, 117
- Williamson, K. E., Jorstad, S. G., Marscher, A. P., et al. 2014, *Astrophys. J.*, 789, 135
- Wills, B. J., & Wills, D. 1974, *Astrophys. J. Lett.*, 190, L97
- Wu, J., Böttcher, M., Zhou, X., et al. 2012, *The Astronomical Journal*, 143, 108
- Wu, J., Zhou, X., Ma, J., Wu, Z., & Jiang, Z. 2009, in *Astronomical Society of the Pacific Conference Series*, Vol. 408, *The Starburst-AGN Connection*, ed. W. Wang, Z. Yang, Z. Luo, & Z. Chen, 278
- Wu, J., Zhou, X., Peng, B., et al. 2005, *Mon. Not. Roy. Astron. Soc.*, 361, 155
- Xie, G.-Z., Chen, L.-E., Xie, Z.-H., Ma, L., & Zhou, S.-B. 2005, *Pub. Astron. Soc. Japan*, 57, 183
- Xie, G. Z., Liang, E. W., Zhou, S. B., et al. 2002, *Mon. Not. Roy. Astron. Soc.*, 334, 459
- Yan, D., Wu, Q., Fan, X., Zhang, L., & Wang, J. 2017, ArXiv e-prints, arXiv:1711.05939
- Yuan, Y.-H., Fan, J.-h., Tao, J., et al. 2017, *Astron. Astrophys.*, 605, A43
- Zacharias, M., Böttcher, M., Jankowsky, F., et al. 2017, ArXiv e-prints, arXiv:1711.06117
- Zackrisson, E. 2005, PhD thesis, Department of Astronomy and Space Physics, Uppsala University, Sweden
- Zdziarski, A. A., & Böttcher, M. 2015, *Mon. Not. Roy. Astron. Soc.*, 450, L21
- Zel'dovich, Y. B., & Novikov, I. D. 1964, *Soviet Physics Doklady*, 9, 246
- Zhang, H., Li, H., Guo, F., & Taylor, G. 2016, ArXiv e-prints, arXiv:1612.03943
- Zhang, J., Liang, E.-W., Zhang, S.-N., & Bai, J. M. 2012, *Astrophys. J.*, 752, 157

- Zhang, J., Xue, Z.-W., He, J.-J., Liang, E.-W., & Zhang, S.-N. 2015, *Astrophys. J.*, 807, 51
- Zhang, Y.-H., & Li, J.-C. 2017, *Mon. Not. Roy. Astron. Soc.*, 469, 1682
- Zhao, G.-Y., Chen, Y.-J., Shen, Z.-Q., Sudou, H., & Iguchi, S. 2015, *Astron. J.*, 149, 46

